A Model for the Simulation of Sidescan Sonar

Judith M. Bell

Thesis submitted
for the
Degree of Doctor of Philosophy

Heriot-Watt University

Department of Computing and Electrical Engineering

September 1995

Table of Contents

List of Figures

List of Tables

Symbols

Chapter 2

c	velocity of sound
T	temperature
S	salinity
z	depth
r	range
α	logarithmic absorption coefficient
∇^2	Laplacian
δ	Dirac delta function
$g(x, y, z, t)$	velocity potential of field at (x,y,z) and time t
ω	angular velocity
$G(x, y, z)$	velocity potential at position (x,y,z)
I	branch line integral
$H_0^1()$	Hankel function of first kind of zero order
K_m	eigenvalues of m^{th} mode
G_m	normal modes
$S(r)$	range dependance of velocity potential
$\psi(r, z)$	approximate parabolic velocity potential
k	wavenumber
n	index of refraction
σ	scattering cross section
A	area of scattering
I_s, I_i	scattered and incident intensity
S	scattering strength

θ	incident grazing angle
ϕ	scattering grazing angle
μ	Lambert's empirical reflectivity coefficient
$H(x, y)$	surface height function
r_c	radius of curvature

Chapter 3

c	velocity of sound
h	height of towfish above seafloor
I_r	reflected intensity
I_i	incident intensity
μ	empirical reflectivity coefficient
θ_g	grazing angle
$H(z)$	transfer function of filter
$h(k)$	impulse response coefficients
$x(n)$	discrete input signal to filter
$y(n)$	discrete output signal to filter
N	number of filter coefficients
m	decimation factor
F_s	original sampling rate
δ_s	stopband deviation
δ_p	passband deviation
f_s	stopband cutoff frequency
f_p	passband cutoff frequency

Chapter 4

$S(f)$	spectral density
f	frequency
β	frequency exponent
D	fractal dimension
E	Euclidean dimension
ρ_1, ρ_2	density in sediment layers 1 and 2
m	ratio of density of sediment to density of water
n	refractive index
α_s	absorption in sediment
S_b	bistatic scattering strength
σ_{br}	roughness scattering cross section
σ_{bv}	volume scattering cross section
θ_i	incident grazing angle
θ_s	scattering grazing angle
ϕ_s	bistatic azimuthal angle
ρ	density ratio
v	sound speed ratio
δ	loss parameter
γ_2	spectral exponent
w_2	spectral strength
μ	fluctuation ratio
Δ_t, Δ_z	transverse and vertical components of change of acoustic wavevector
$W(K)$	two dimensional roughness spectral density
h_0	reference length
$J_0()$	zeroth order Bessel function

$R(\theta)$	Rayleigh coefficient
σ_{kr}	bistatic Kirchhoff cross section
σ_{pr}	bistatic perturbation cross section
α, C_h	roughness structure parameters
Γ	gamma function
κ	complex wavenumber
$W_{\rho\rho}$	density fluctuation in sediment
W_{KK}	compressibility fluctuation in sediment

Chapter 5

G	acoustic velocity potential
S	eikonal
A	envelope function
k	wavenumber
c	velocity of sound
g	velocity gradient
Δd	vertical distance in velocity layer
R_c	radius of curvature
c_0	vertex velocity
α	absorption
r	range
f	frequency
S_h	horizontal distance
I	intensity

Chapter 6

r_0	near field distance
A	area of transducer
λ	wavelength
$R(\theta, \phi)$	response of transducer
$v(\theta, \phi)$	normalised response function
$B(\theta, \phi)$	transducer beam pattern
n	number of transducer elements
d	distance between elements in array
L, a	length of linear array
θ	beam angle in vertical plane
ϕ	beam angle in horizontal plane
ϕ_{yaw}	yaw offset angle in horizontal plane
ϕ_{pitch}	pitch offset angle in horizontal plane
θ_{pitch}	pitch offset angle in vertical plane
ψ_{pitch}	pitch angle of transducer

Chapter 7

χ^2	chi-square statistic
N_i	observed number of events in i^{th} bin
n_i	expected number of events in i^{th} bin
R_i	observed number of events in i^{th} bin of first data set
S_i	observed number of events in i^{th} bin of second data set
$g_i(t)$	windowed amplitude function
n	number of lines in data sample
f_{NY}	Nyquist frequency

$P_i(f)$	power spectrum of i^{th} line
$P(f)$	average power spectrum
$P_L(f)$	log power spectrum
$P_{NL}(f)$	normalised log power spectrum
$D_{f_1}, D_{f_2}, D_{f_3}$	power spectral features

Acknowledgements

I would like to thank the members of staff of the Department of Computing and Electrical Engineering at Heriot Watt who have assisted during the period of this work. In particular, I would like to thank Dr. Laurie Linnett and Professor George Russell for their encouragement, guidance and supervision.

I am also indebted to the Defence Research Agency for their financial assistance with this project, and to Mr. J. Wickenden for his encouragement and support.

I would also like to thank my family and friends for their help and encouragement. In particular, I would like to thank my parents for their continued belief in me, because without them this work could not have been completed.

Abstract

This thesis presents the development of a computer model for the simulation of the sidescan sonar process. The motivation for the development of this model is the creation of a unique and powerful visualisation tool to improve understanding and interpretation of the sidescan sonar process and the images created by it. Existing models tend to generate graphical or numerical results, but this model produces synthetic sidescan sonar images as the output. This permits the direct visualisation of the influence of individual parameters and features of the sonar process on the sidescan images.

The model considers the main deterministic aspects of the underlying physical processes which result in the generation of sidescan sonar images. These include the propagation of the transmitted pulse of acoustic energy through the water column to its subsequent interaction and scattering from the rough seafloor. The directivity and motion characteristics of the sonar transducer are also incorporated. The thesis documents the development of the model to include each of these phenomena and their subsequent effect on the sidescan sonar images. Finally, techniques are presented for the investigation and verification of the synthetic sidescan images produced by the model.

Chapter 1

Introduction

1.1 Introduction

Almost three quarters of the earth's surface is covered by water, yet comparatively little is known about the complex underwater environment. In particular, many regions of the ocean and seafloor remain unexplored due to their inaccessibility and the problems of remotely sensing and imaging areas underwater.

Light and electromagnetic radiation are severely attenuated underwater and can propagate only over short distances. Water tends to be murky and turbid, and light is scattered and absorbed by the suspended sediments and crustaceans. Sensors, such as cameras, which rely on light to produce images, have very limited applicability underwater. Therefore, following the example of many marine animals which use sophisticated acoustic systems for communication and active ranging, devices based on the transmission and reception of acoustical energy have been developed to investigate the oceanic environment. This is because sound has the advantage over light of being able to propagate over long ranges underwater, irrespective of the water clarity. The history of the application of sound for underwater investigation, from the initial observations of Leonardo de Vinci in 1490 to post war acoustical developments, is summarised by Urick [1].

Devices which use underwater sound for communication or observation are generally referred to as *SONAR* systems. This term was coined after the Second World War to

provide an analogy to the equivalent electromagnetic echo-location system of radar and is an acronym for "SOund Navigation And Ranging".

One type of sonar which has found increasing application in military, commercial and environmental sectors is the sidescan sonar. This is an acoustic imaging device which is towed through the water behind a survey vessel to provide wide area, large scale pictures of the seafloor. The images are generated sequentially as acoustic signals are transmitted to the side of the sonar and the sound which is reflected back to the device is subsequently used to produce an image of the seabed. The sidescan image generated in this manner provides a qualitative representation of the seafloor topography and sediment characteristics. The principles of operation of the sidescan sonar will be explained in greater detail in chapter three.

The objective of the research reported in this thesis is to develop a computer based model for the simulation of the sidescan sonar process. The model will calculate the acoustic phenomena influencing the generation of the images by modelling the underlying physical processes. These are dependent on the physical characteristics of the ocean volume, its surface and its bottom, in addition to the transducer characteristics. The model will produce an image as its output, in the same form as the output of the actual sonar system it represents.

1.2 Motivation

Although sound is superior to light in that it can propagate over long ranges, it is an inferior carrier of information. This is related to its lower velocity of propagation, approximately $1500 ms^{-1}$ compared to $3 \times 10^8 ms^{-1}$ for light, and its lower resolving capacity, as a result of its correspondingly longer wavelength.

The properties of acoustic transmission, and the subsequent method of generation of sidescan sonar images, produce sonar images that are not of a visual quality and do not

provide a direct representation of the seabed. As a result of the relatively low velocity of propagation, the time taken for the acoustic signal to travel from the source to the seabed and return is significant with respect to the capture time of the signal; the sonar therefore displays the returned signal as echo intensity against time. The images are distorted because of this time-based display and the motion of the transducer during the capture process. The actual resolution of features on the seabed determinable from the images is dependent on the sonar operating characteristics, in particular the frequency, pulse length and directivity. In addition, the images are not unique as completely different features on the seabed can appear similar on the sidescan record.

Sidescan images are therefore difficult to interpret and obtain any quantitative information from. It is intended that the model presented in this thesis will aid the interpretation process by providing a training and visualisation tool. The model will permit the simulation of many complex environments and can be used to simulate sonar artifacts and train users to understand the physical phenomena which contribute to the generation of the images. This will result in improved interpretation skills, both by the operator, or as part of an on-line automated classification system [2].

The model will also permit the isolation of individual parameters and the subsequent determination of their effect on the sidescan image. Therefore, the use of this model by sophisticated users is also envisaged, as it can provide a suitable platform for this isolation procedure or for the testing of complex algorithms, such as those for motion compensation [3].

Although many models exist within the field of underwater acoustics, they tend to concentrate on individual aspects of the sonar process. This can provide detailed and accurate information about certain parameters, but it does not permit the direct visualisation of the effect of these parameters on the sidescan sonar process. Existing sonar prediction models which do combine the individual models generate only numerical and graphical results for one particular instance of the transmitted signal. The typical outputs do not

bear any direct resemblance to the sonar image generated by an actual sidescan system and it can be difficult to correlate the predicted numerical results with the sidescan image. The existing sonar prediction and associated sub-models will be reviewed in greater detail in chapter 2.

The aim of the simulation model developed within this thesis is therefore to fulfill the requirement of accurately modelling the sonar process with numerical models, but producing as its output an image which resembles the sidescan sonar image which would be generated under the specified operating conditions.

1.3 Author's Contribution

The simulation model developed within this thesis is felt to provide a significant contribution towards the modelling of the sidescan sonar process. The model is one of the first to produce realistic simulated sidescan sonar images based on the calculation of the actual physical process. Synthetic sidescan sonar images have been generated previously but these have relied entirely on image processing and statistical techniques to replicate texture in existing sidescan images without consideration of the actual physical process [4].

The model considers the main physical processes, including acoustic propagation through the water medium, seabed reverberation and transducer characteristics. The second main contribution is in the linking together of these various sub-models to form the simulation model. This allows the exploration of the effects of many variables, both separately or in any combination, on the sidescan sonar process, providing a valuable tool for the identification of the major influences on the formation of the images. The subsequent development of improved seabed classification and motion compensation algorithms to obtain quantitative information from the sidescan sonar images is also envisaged.

Only one other model is known to have been developed under a similar basis. This is the SWAT model (Shallow Water Acoustic Toolset) which was developed at the US Naval Coastal Systems Station, as the direct extension to a target strength model to produce synthetic sonar images of the target, in addition to the target strength characteristics [5]. The model concentrates on target simulation and does not provide a general sonar simulation model comparable to the work in this thesis.

It is felt that the work contained within this thesis is more advanced than the SWAT model in terms of the seabed representation and the modelling of the medium characteristics. The model developed in this thesis has the ability to model complex topographic features without the limiting assumptions of a flat seabed contained within the SWAT model. Mathematically defined objects can also be incorporated to represent man-made features or targets on the seabed. The model also calculates the acoustic propagation through the water column using a horizontally stratified media, rather than the constant velocity assumption of SWAT. Further details on the comparison and limitations of the two models is provided in chapter two.

In summary, this thesis develops the fundamental structure for a general sidescan simulation model, which produces qualitative sidescan sonar images from a quantitative description of the environment and operating characteristics. The model is unique in that it provides the pictorial visualisation of sidescan sonar images of complex environments by consideration of the underlying physical processes.

1.4 Thesis organisation

The fundamental concept of this thesis is the description of the model for the simulation of the sidescan sonar. Prior to the discussion of the model development, chapter two will present a review of models available within the underwater acoustic community and will highlight the requirement for a model in this form.

Chapter three will initially describe the basic principles of operation of sidescan sonar, to provide a basis of understanding for the development of the simulation model. The fundamental structure of the model will then be proposed with the introduction of several simplifying assumptions. This lays the foundations for the expansion of the model and the removal of these assumptions in subsequent chapters.

One of the assumptions was the existence of a totally flat seabed. Although providing an initial starting point for the model development, this assumption is very limiting, as it is the imaging of the topographic features of the seabed which provides the primary motivation for the majority of sidescan sonar surveys. Chapter four will discuss the incorporation of models for the seabed which can provide sufficiently complex and realistic data. The model is also extended to include objects on the seabed or in the water column, to provide a general purpose simulation model. Chapter four will then investigate the three dimensional scattering of the acoustic signal from the seabed.

Prior to interacting with the seabed, the acoustic signal propagates through the water with a velocity dependent on the salinity, temperature and pressure of the water. This influences the actual path of propagation and the losses incurred by the signal. Chapter five will further extend the model to include the effects of the water environment on the propagation and the subsequent effect on the transmission loss.

The sound is transmitted and received by the sonar transducer, the directivity properties of which influence the images produced. Chapter six will consider the effect on the sidescan sonar images of incorporating the three dimensional directivity response of the transducer into the sonar simulation model. In addition, the effect of the complex motion incurred whilst towing the transducer though the water is investigated. The towing results in instabilities which can alter the trajectory, speed and orientation of the transducer and produce further distortions in the sidescan sonar image.

Chapters three to six concentrate on the development of the sonar simulation model with little consideration to determining the accuracy of the model output. Chapter seven discusses the problems of testing and verifying the qualitative output of the sonar simulation model and will consider the application of visual, statistical and spectral techniques for verification.

The final chapter of this thesis, chapter 8, consists of a summary of the work and conclusions drawn from it. Potential shortcomings and advantages of the simulation model are discussed, and possible areas for future work are indicated.

Chapter 2

Modelling Techniques in Underwater Acoustics

2.1 Introduction

This chapter will review some of the models already in existence within the field of underwater acoustics. The aim of this summary is to illustrate the requirement for, and the role of, the simulation model developed within this thesis. It will also serve to illustrate the use of some of the currently available models in the development of the new simulation model.

A diversity of models already exists for the calculation of underwater acoustic phenomena. Many of these models consider individual features and aspects of the sonar process, such as the acoustic propagation or reverberation. Within each of these broad categories, several types of model have emerged and the range of models for the computation of the propagation and reverberation will be discussed within this chapter.

Aspects of propagation and reverberation models have also been combined to create active sonar models. These models provide numerical and graphical predictions of the energy levels present in a particular sonar situation. The current state of these models, and their advantages and limitations, will also be discussed to highlight the need for the model for sonar image synthesis developed within this thesis.

Finally, the chapter will investigate other models capable of the synthesis of sonar images. Apart from the texture based models which simply replicate the statistics of the

sonar image with no consideration of the underlying physical processes, only one model (the SWAT model) was discovered to have been developed on a similar basis to that developed within this thesis. A comparison of the advantages and limitations of the SWAT model and the model developed in this thesis will be presented.

Prior to the discussion of the models, the chapter will outline the principle reasons for the development of the models and the roles they fulfill within the underwater acoustics community. The background models for the representation of the complex underwater environment will also be considered.

2.2 Why Model?

The first point to address is the motivation for the development of this broad range of models. Models have been created to fulfill a variety of different roles and have been applied to both the prediction and analysis of underwater acoustic phenomena.

Within their role as a prediction tool, models can provide a systematic means of designing experiments, whether they are to investigate the complex environment itself or the effect of the environment on the acoustic signals. The output from the prediction may simply be the effective sonar range or may be a forecast of the actual results of the experiment. The model can be a valuable prediction tool as it is imperative to properly design experiments and be aware of their expected outcome, in order to minimise experimental costs, as ship time can be very expensive, costing £10K to £50K per day. It is also foreseen that more advanced simulation models could be developed to investigate the acoustic phenomena and eventually minimise the requirement for expensive sea trials.

Models may also be used to increase the effectiveness of data analysis and interpretation, providing information on the oceanographic features and the effects of the complex environment on the acoustic signals. The requirement also exists for sophisticated inverse models, which will permit the derivation of the parameters required to describe

the ocean from the experimental data.

To produce the optimum performance for the application, the sonar designer requires knowledge of how the sound will propagate in the ocean as a function of frequency and pulse characteristics for a variety of source/receiver configurations and for different environmental conditions. Detailed simulation and analysis of theoretical considerations will increase this capability.

Acoustic models exist at a range of complexities for use either in operational field activities or for complex research and investigative studies. Lauer [6] divides the field into pure applications models, pure research models and applications research models. The pure applications, or operations models, are used to support field activities, including the prediction of the performance of Naval Fleet sonars. The main requirement of these models is their ability to generate results rapidly, often under demanding conditions, with the minimal amount of operator experience. Pure research models, on the other hand, are designed for investigative studies within the research environment. Here they are employed for more sophisticated purposes where accuracy is important and not run-time. These models tend to be complicated to operate, requiring the operator to select or input a variety of geoacoustical parameters to adequately describe the environment. The intermediary class of applications research models tend to be more generally available and are a trade-off between the research and applications models, combining the automated features of the pure applications models with the flexibility and input options of the pure research models.

As the level of available computing power continues to increase, it becomes possible to translate more of the theory to operational models, and many of the computational limitations may be removed from the existing models. This is leading to a growth in both the range of available models and in the complexities of these models, which will eventually result in the application of modelling techniques to an even greater range of underwater acoustic problems.

2.3 Ocean Environments

The majority of acoustic models require inputs describing the ocean environment; these are often derived from the more fundamental category of environmental models. Environmental models are usually empirically derived and include relationships for the sound speed, absorption and sediment characteristics.

The only parameter which affects the path of propagation of sound through the water column is the speed of sound, which has a nominal value of $1500ms^{-1}$. The speed of sound in the ocean is a function of three variables: temperature, salinity and depth (or pressure). It therefore changes significantly with season, time of day, weather, geographical position and proximity to rivers and melting ice. Many empirical equations have been formulated to explain this relationship. A simple expression for the sound speed, c, in ms^{-1}, which has found widespread practical application was proposed by Medwin [7],

$$c = 1449.2 + 4.6T - 0.055T^2 + (1.34 - 0.010T)(S - 35) + 0.016z \qquad (2.1)$$

where T is the temperature in degrees centigrade, S is the salinity in parts per thousand and z is the depth in metres. Equation 2.1 was proposed by Medwin for realistic combinations of the variables within the temperature range 0° to 35° centigrade, the salinity range 0‰ to 45‰ and for depths within 1km of the surface.

The formula proposed by Wilson [8] is generally regarded as the most accurate, although it is a complicated expression containing many higher order, cross product terms. Leroy [9] formulated a similar, but simpler, equation which is valid over a more limited range of conditions, but which provided a good fit to Wilson's data.

The variation of sound speed with depth is known as the sound velocity profile (SVP). If the sound velocity profile is independent of range, the environment is horizontally stratified. Several of the acoustic models assume horizontal stratification in order to simplify the calculations, as the horizontal variations in sound speed are usually quite

weak compared with the vertical changes.

The fluidity of water and the stability of less dense over more dense water causes oceans and lakes to be nearly horizontally stratified in local regions. In the open ocean the dimensions of the stratified region may be several hundred kilometres. The horizontal stratification assumption breaks down in the presence of oceanic fronts and eddies, where the environment is range dependent.

The ocean is often broadly categorised as deep or shallow water. Shallow water is rather arbitrarily defined as that part of the ocean lying over the continental shelf where the water depth is less than 200 metres. The velocity profiles of the two areas differ. Deep water has the typical velocity profile illustrated in figure 2.1, where below the ocean surface the temperature decreases sharply with depth causing the main thermocline. Beneath the thermocline there is a region of constant temperature, which results in an increasing velocity profile, as the speed of sound increases with increasing depth. In shallow water wind induced mixing often produces a near isothermal water column which results in a linear sound velocity profile with a positive gradient.

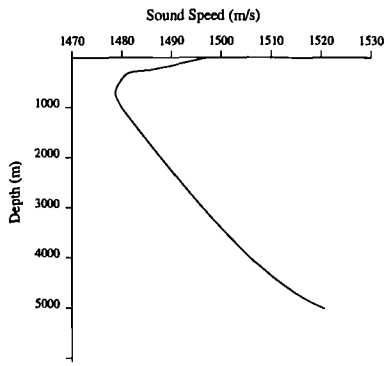

Figure 2.1: Typical sound speed profile of deep ocean

Due to the significant number of bottom interactions in shallow water, the bottom boundary is usually the dominant factor in determining the character of the acoustic field. Therefore the properties of the seabed must also be taken into account. The seafloor

characteristics vary across the differing environments of the continental shelf, the abyssal hill and the abyssal plains. Hamilton [10] discusses the generation of geoacoustical models for the seafloor, and the relevant properties which must be considered. These include information on the sediment type, the thickness and shape of the sediment layers, the density and the velocities and attenuation of the compressional and shear waves.

As well as the bulk properties of the sediments, the actual seabed topography must also be included; this topography can be considered on several scales. Information on the large scale topographic features of the seafloor can be obtained from echo sounders or bathymetric sonar. Briggs [11] discusses the measuring of the small scale roughness of the seabed and its characterisation using power spectral density classifications. The characterisation of larger scale topography by a similar method has also been investigated by Fox and Hayes [12]. The modelling of the seabed topography will be considered in greater detail in chapter 4.

Sound waves are absorbed whilst they propagate through the water column as well as in the sediment layers. Absorption involves the conversion of energy into heat due to the non-ideal nature of the medium and results in a loss of energy as the wave propagates. This loss of energy is proportional to the distance travelled and is expressed in terms of α, the logarithmic absorption coefficient, usually with units of decibels per kilometre.

The absorption of acoustic energy by sea water is caused by three main effects: the shear viscosity, volume viscosity and ionic relaxation. It is the ionic relaxation which results in different absorption coefficients for pure water and sea water. This is largely due to the magnesium sulphate ions in sea water which disassociate when acoustic pressure is applied, and then after a finite relaxation time, reassociate. An empirical model including this effect was developed by Schulkin and Marsh [13]. Fisher and Simmons [14] later proposed a different form of this expression which also included the effects of the ionisation process of boric acid, which is present in small quantities in seawater.

This discussion illustrates the complexity of the ocean environment, and the empirical models required to represent it. Details of these models and their application will be expanded throughout the text.

2.4 Acoustic Propagation Models

The objective of acoustic propagation modelling is to estimate the intensity and phase of the acoustic field in various types of ocean channel. The computed field is a function of frequency, depth and range from the source, and is dependent on the environmental parameters described in section 2.3.

Acoustic propagation models have a variety of applications. One of the major uses of propagation models is to investigate the loss of energy as the field propagates, and the prediction of transmission loss with range is therefore one of the commonest outputs from a propagation model. The output in this case can be used as one of the fundamental building blocks for an active sonar model, as discussed in section 2.6. Propagation models can also be used to investigate ocean processes to provide an understanding of the complex oceanic environment. In this form it is possible to use them in inverse applications to derive information on the parameters influencing the propagation of the sound field.

There is no single method capable of calculating the acoustic field for all possible environmental conditions, frequencies and transmission ranges of interest and hence several types of solution have evolved. These include ray tracing, a high frequency approximation producing a very graphical picture of the field; normal mode techniques, which present an alternative to rays; coupled modes, which are accurate but computationally demanding and parabolic equations, which provide an approximation to the wave equation. A brief discussion of these models will be presented in this section to justify the approach taken in the model developed in this thesis. More extensive reviews of the field of acoustic propagation modelling are given in [15],[16],[17],[18],[19],[20].

2.4.1 The Wave Equation

The solution of the three dimensional wave equation provides the starting point for all propagation models. The wave equation is a partial differential equation relating the space and time derivatives of the acoustic parameters which describe the wave motion as it propagates [21] and is presented in cartesian form in equation 2.2 for the propagation from a point source of strength $s(t)$.

$$\nabla^2 g(x,y,z,t) - c(x,y,z)^{-2} \frac{\partial^2 g(x,y,z,t)}{\partial t^2} = -s(t)\delta(x-x')\delta(y-y')\delta(z-z') \quad (2.2)$$

where ∇^2 is the Laplacian, g is the velocity potential of the field at receiver position (x, y, z) and time t, $c(x, y, z)$ is the sound speed at point (x, y, z) in the the medium, δ is the Dirac delta function and (x', y', z') is the source point.

The majority of propagation models assume that the source generates a continuous, harmonic signal with angular frequency ω, and time dependence $\exp(-i\omega t)$. The wave equation can then be reduced to the Helmholtz (or reduced wave) equation.

$$\nabla^2 G(x,y,z) + \left\{ \frac{\omega}{c(x,y,z)} \right\}^2 G(x,y,z) = -\delta(x-x')\delta(y-y')\delta(z-z') \quad (2.3)$$

where

$$g(x,y,z,t) = G(x,y,z)\exp(-i\omega t) \quad (2.4)$$

To solve the wave or Helmholtz equation it is necessary to specify the boundary conditions. At the ocean surface, the density of air can be considered negligible compared with that of water; therefore, the pressure must vanish at the ocean surface (a pressure release surface). Many of the propagation models consider this boundary to be planar and neglect the effect of the sea-state.

The bottom boundary is more difficult to specify since it may consist of several layers. At each interface between two media, the balancing of forces requires that the pressure and the normal component of the particle velocity be continuous across the boundary. If the ocean bottom is treated as an elastic medium, which is capable of supporting shear, the tangential stress across the interface must also be continuous. Since the water column cannot support shear waves, this requires that the tangential stress in the ocean bottom vanishes at the interface. Many of the models discussed in this chapter consider the bottom boundary as a two fluid interface, which is incapable of supporting shear waves. This can be a reasonable assumption if the bottom is composed of softer sediments, where the upper few centimetres tend to be unconsolidated. As high frequency acoustic waves will be severely attenuated within the sediment, they will be unable to penetrate to the depths of the underlying basement rock, but low frequency waves can penetrate further and the effects of shear should then be considered.

Due to the complex nature of the environment and its boundaries, there is no direct solution to the wave equation and it is necessary to make a variety of simplifying assumptions in order to solve it. These approximations result in a range of different types of solution, which will be discussed in the following sections.

2.4.2 Ray Models

Ray theory is a high frequency solution to the Helmholtz equation. The basis of ray theory is the postulate of wavefronts, along which the phase or time function of the solution is constant. Rays, which are everywhere perpendicular to the wavefronts, describe the propagation of sound in space.

The ray solution is derived by separating the amplitude and phase components of the Helmholtz equation by applying the geometric optics approximation. This assumes that the amplitude varies more slowly with position than does the phase. The physical implications of this approximation, which limits the method to the high frequency

domain, are :-

1. The curvature of a ray over a wavelength must be small.

2. The fractional change in the sound speed must be small over a wavelength.

If the environment is horizontally stratified, the solution can be further simplified by the application of Snell's Law, which describes the refraction of sound rays through a layered media [1]. This permits the direct calculation of the range and travel time, resulting in a solution which is fast to compute. This technique will be described further in chapter 5.

One of the principal advantages of ray tracing is that it provides a quantitative and easily visualised description of the propagation of sound in the form of ray diagrams. Further advantages include the ease with which the directionality of the source and the receiver can be incorporated through the use of suitable weighting factors; and the rays can be easily traced through range dependent environments with varying velocity profiles and over complicated bathymetry.

Ray theory is as yet unable to handle wave effects such as diffraction, focal points and caustics and tends to produce abrupt changes in the ray diagram when a transition in the field occurs. It may even generate false caustics or produce unrealistically sharp shadow zones. This limits the usefulness of this technique for investigating low frequency propagation. Ray tracing is sometimes known as a "shooting method", because the end points of the rays are found by trial and error. It is not evident, in advance, whether a ray with a given launch angle will intersect a receiver at a known position and it is therefore necessary to trace many rays. It is also necessary to perform the computations at all ranges from the source to the receiver to determine the ray path.

One ray model, GRASS (Germinating Ray Acoustics Simulation System), was developed in 1973 by the Naval Research Laboratory [22], and has been widely used within the ocean acoustics community. Most of the features of GRASS are in common

with other ray tracing models as mentioned above. The intensity calculations in GRASS may be either coherent, which allows for some frequency dependence, or incoherent. In principle, ray tracing should be capable of dealing with bottom reflections and bottom refracted paths, but GRASS cannot handle both correctly [20].

The technique of ray tracing can also be applied to a medium where the sound speed and ocean currents vary in three dimensions. HARPO [23] has been developed as a general purpose, three dimensional underwater acoustic ray tracing program. HARPO (Hamiltonian Acoustic Ray tracing Program for the Ocean) traces the path of the rays by numerically integrating Hamilton's equations of motion. It permits the modelling of the oceanic temperature and current fields as continuous closed form three dimensional fluctuations. This has provided a tool for exploring out of plane refraction and scattering of rays, and has been used to investigate acoustic fields in the presence of mesoscale eddies [24]. The model has been extended to include more realistic oceanography and boundary conditions and used to calculate long range propagation, over hundreds of kilometres, through complex environments such as the Gulf Stream [25].

Several modifications have been introduced to ray theory, in an attempt to overcome some of the limitations. In order to remove the perfect shadows and infinite energy at caustics, the method of Gaussian beam tracing has been introduced [26]. This is based on the concept of "fuzzy" rays. Each ray is associated with a beam, which has a Gaussian intensity profile normal to the ray. The beamwidth and curvature are integrated along the ray to compute the beam field in the vicinity of the ray. In general, though, conventional ray tracing is unable to accurately calculate the acoustic field in the vicinity of caustics and shadows, but it does provide a simple graphical representation of the propagation.

2.4.3 Normal Mode Models

Normal mode theory describes the propagation in terms of characteristic functions called *normal modes*, each of which is a solution to the Helmholtz equation. Each mode

represents a wave travelling outward from the source with an amplitude that is a function of the source and receiver depths. The normal modes are combined additively to satisfy the boundary and source conditions of interest.

This normal mode solution can then be expressed in equation 2.5, as an infinite sum of uncoupled normal modes plus one or more branch line integrals. The branch line integrals can be considered as having negligible effect, except in the vicinity of the source where the modes are not yet balanced. The acoustic field is expressed as:

$$G = I + \frac{i}{4}\sum_{m} G_m(z_s)G_m(z_r)H_0^1(K_m r) \tag{2.5}$$

where G_m are the normal modes evaluated at the source and receiver depths, z_s and z_r, and K_m are the eigenvalues or horizontal wave numbers of the m^{th} mode. $H_0^1()$ is the Hankel function of the first kind of zero order and I is the branch line integral representing the continuous modal spectrum.

The solution for the normal modes is evaluated using iterative numerical techniques, such as Runge-Kutta [27], to determine the eigenvalues, K_m. The iteration begins with a trial value and proceeds until the boundary conditions are matched at the sea surface and bottom. This iterative technique is suitable for low frequency or shallow water problems where the number of modes is small, and is the basis of the normal mode model SNAP [15]. An alternative technique has been proposed by Porter and Reiss [28], which is based on the finite difference approach, and has been used in SUPERSNAP, an extension to the SNAP model.

Since the normal mode method is based on the separation of range and depth variables, it cannot be used unless the medium is horizontally stratified. However, if the range variations in the velocity profile and depth are only slight, the energy in each mode remains constant as the mode propagates. This adiabatic approximation allows the method to cope with slight range dependence. The other disadvantage of the normal

mode technique is its limited accuracy in the near field of the source.

One advantage of normal modes is that the mode functions do not have to be calculated at all intermediate ranges between the source and the receiver. It is also possible to calculate the acoustic field as it penetrates the sea bottom. The effects of different bottom types can be incorporated through the velocity profile, density and absorption. The r.m.s. roughness of the sea surface and bottom can also be treated. Shear wave effects can be handled in some normal mode programs provided that the contribution of the branch line integral is included.

In summary, the normal mode technique provides a solution of the wave equation suited to low frequency and shallow water situations. The output of normal mode programs is usually in the form of contour plots of the acoustic field with range, or direct transmission loss plots.

To overcome the limitations of the range dependence problem and the adiabatic approximation, coupled mode modelling can be used [29]. This technique consists of subdividing the environment into a number of range segments, in which the acoustic parameters are constant with range but may vary with depth. Across the segment boundaries the pressure and horizontal particle velocity are required to remain constant, allowing the normal modes for each segment to be computed. The full solution is energy conserving and includes both forward and backscattered energy.

COUPLE is an example of a coupled mode solution, and has been found to produce excellent agreement against exact analytic solutions of range dependent problems [30]. The code for this technique is very complex and according to Jensen and Ferla [30] the use of COUPLE to generate accurate numerical solutions is a "*non trivial exercise*".

2.4.4 The Parabolic Equation

If the environment varies with both range and depth, the wave equation cannot be separated and therefore direct numerical integration is required. At present there are no practical methods to perform the direct integration of the three dimensional wave equation. An alternative approach is to derive an approximate wave equation that can be solved numerically. This parabolic equation technique was introduced into underwater acoustics in1973 by Tappert and Hardin [31].

For waves travelling predominantly within a small range of angles, the elliptic wave equation (in cylindrical coordinates) can be approximated to a parabolic equation by removing the main oscillating part of the solution to a function $S(r)$. Thus the velocity potential, $G(r, z)$, can be expressed in terms of a slowly varying function of range and depth, $\psi(r, z)$, and the function $S(r)$ representing the range dependence.

$$G(r, z) = \psi(r, z)S(r) \tag{2.6}$$

The parabolic wave equation, equation 2.7, is then obtained.

$$\frac{\partial^2 \psi}{\partial z^2} + 2ik_0 \frac{\partial \psi}{\partial r} + k_0{}^2(n^2 - 1)\psi = 0 \tag{2.7}$$

where the wavenumber $k = k_0 n$ is expressed in terms of the arbitrary constant k_0. This *reference wavenumber*, k_0, is related to the reference sound speed by $k_0 = \frac{\omega}{c_0}$. The index of refraction, n, is equal to $\frac{c_0}{c(r, z)}$, which is assumed to be slowly varying.

Unlike the wave equation, only the range derivative in equation 2.7 is of first order. Hence if the field, ψ, is defined over a vertical line, at a given range, then its second derivative with respect to z is also known; consequently $\frac{\partial \psi}{\partial r}$ can be deduced. This allows ψ to be calculated at the next range step, $r + dr$, for all values of z. This "marching solution" permits the calculation of the field as it propagates through the medium. A

limitation of the technique is that it requires an initial starting solution. For this purpose a normal mode program is often used. An alternative is to approximate the point source by two Gaussians which are anti-symmetric about the sea surface, hence including the pressure release boundary condition at the sea surface.

In order to implement numerically the marching solution to equation 2.7, two different techniques have been formulated. The first was proposed by Tappert [31] as a split step Fourier algorithm. The second exploits finite difference techniques, which can more easily accommodate rapid variations in the sound speed and density.

The main limitation of the parabolic equation is that it is valid only over a very narrow range of angles. Most of the standard parabolic equation (P.E.) codes are quoted as valid over an angular range of ±20°, although some have been extended to the wider limits of ±40°. A further weakness is that if this angular range is exceeded, the output contour and loss plots continue to look realistic, although they are in fact inaccurate. The other main limitation is that the parabolic equation is a one way solution. It is capable of handling only outgoing waves and therefore cannot cope with backscattered energy. This was shown to introduce errors of up to 2dB in standard benchmark tests [30].

The advantages of parabolic equation codes are that they can compute the field in range dependent environments, with variations in both the sound speed profiles and in the bathymetry. They can also give the field over the entire water column with no additional effort. However, the parabolic equation technique is more applicable to low frequency propagation, since the computation time is proportional to the frequency squared.

In recent years Collins [32][33] has formulated higher order parabolic equations. This approach reduces the narrow angle restrictions and produces a code capable of handling propagation in elastic media. The code is still limited to one way propagation.

2.4.5 Other Propagation Modelling Techniques

Several other techniques for obtaining a solution to the wave equation exist. These include fast field models and finite element models, which will now be briefly discussed.

Fast field programs, or Green's function solutions [15], provide an exact full wave solution for acoustic fields in horizontally stratified media. The numerical solution is exact for complex environments consisting of both fluid and solid media, as it is capable of computing both the compressional and shear waves generated at such interfaces.

The limitation of this technique arises as a result of the horizontal stratification assumption, because the interfaces between layers are assumed to be totally flat, no bathymetric information can be included. It also assumes the sound velocity profile remains constant with range.

The basis of the fast field technique is the reduction of the elliptical Helmholtz equation, which is dependent on range and depth, to an ordinary differential equation with only one variable. A Hankel transform is applied to the Helmholtz equation to produce the ordinary differential equation, which can be integrated numerically to yield a Green's function. An inverse transform is then applied to the Green's function to obtain the field. The inverse transform is reduced to a Fourier transform by the use of the far field assumption for the Hankel function. The main burden computationally is the calculation of the Green's functions, as the Fourier transform can be easily implemented using FFT (Fast Fourier Transform) techniques. The only limitation of this method is the far field assumption, which reduces the accuracy of the result within a few wavelengths of the source.

The fast field solution is similar to normal mode techniques; the difference is that the branch line integral, for computing the continuous part of the spectrum, is automatically included in the fast field solution.

To implement this technique Schmidt has developed the SAFARI fast field program [34][35], which uses an efficient matrix solution to calculate the Green's functions. The program is complex and computationally demanding, but can calculate fields in elastic media. It can also handle multiple sources, arranged either vertically or horizontally to generate complex beam patterns.

Finite element models (FEM) [15] can be used to combat the horizontal stratification assumption. These models permit the calculation of the acoustic field in environments where both the sound velocity and the bathymetry alter with range. They are also capable of handling solid and fluid media, as finite element models can calculate both compressional and shear waves.

Finite element analysis initially segments the ocean and sea bottom into different fluid and solid domains. The domains are then further divided into a mesh of regularly shaped, triangular and rectangular elements, with node points at each vertex. The field can be determined at any node of the mesh using algebraic equations, which are formed from the wave equation and boundary conditions.

The finite elements of the mesh typically have dimensions of one tenth of a wavelength, or less. This technique is therefore limited to low frequencies due to the computation required. The other problem of the finite element method is the termination of the mesh at the lowest boundary. A discussion of this problem and a summary of the technique is provided by Kalinowski, in chapter 3 of [36].

2.4.6 Three Dimensional Propagation Models

The majority of the models discussed have been two dimensional and are capable of calculating the acoustic field in range and depth only. Due to computational limitations very few full three dimensional codes exist. Some two dimensional codes have been extended to 2½D or $N \times 2D$ codes, by applying the two dimensional solution, to

calculate the field in range and depth, over a variety of azimuthal angles.

Although $N \times 2D$ codes can incorporate changes in bathymetry and sound velocity profile over three dimensions they assume negligible bending of the ray paths in the horizontal. Using the ray analogy, the assumption in their application is that a ray launched in a particular vertical plane remains in that plane over its entire propagation path. This is a reasonable assumption except in the vicinity of oceanic fronts and eddies, such as those commonly encountered around the Gulf Stream in the Atlantic Ocean. The other limiting situation occurs in shallow water environments with sloping bottoms, when the wavelength is comparable to the water depth, the phenomena of "horizontal refraction" occurs [37]. This effect, which is actually due to reflection not refraction, is the result of the rays being reflected out of the plane by successive bottom reflections.

A few three dimensional modelling programs have recently been generated. The majority of these are based around ray tracing. The most common of these codes is HARPO, which was discussed in section 2.4.2. Most of the other three dimensional codes are derived from the parabolic equation technique. These codes have the same limiting assumptions, regarding their applicable angular range and lack of backscatter calculations, as the two dimensional parabolic equation models.

2.4.7 Verification of Propagation Models

An initial indication of the accuracy of propagation models can be obtained from an understanding of the approximations used in deriving their solution. However, it is difficult to devise a means of verifying propagation models.

One method is to compare the results of the model against transmission experiments in the ocean. However, it is difficult to compare the results, as anomalies between the model and data may not necessarily be due to faults in the model. Differences may arise as a result of the limitations in specifying the environment or in measuring the

parameters. Experiments designed to test models have also been conducted in the laboratory, using appropriately scaled experiments in tanks [38].

It has also been proposed that models can be tested against each other, or against standard benchmarks, rather than experimentally. To investigate the use of benchmark situations, the Acoustical Society of America formulated a set of benchmark exercises to investigate propagation models [39]. Two scenarios were devised. The first of which was the upslope propagation over a wedge-like sea bottom with a perfect reflecting boundary, a penetrable boundary and a lossy penetrable boundary. The other benchmark was a plane parallel waveguide with a varying sound velocity profile. The specification of these problems is given in greater detail by Jensen and Ferla [30]. Several models were applied to the benchmarks to obtain both analytical and numerical solutions. Analytical solutions were proposed for the ideal wedge by Buckingham and Tolstoy [40]; a ray solution by Westwood [41]; and a mode solution in the parallel waveguide by Thomson *et al* [42]. Parabolic equations were applied by Thomson [43], both for the split step and finite difference techniques, and for higher order parabolic equations by Collins [33]. Jensen and Ferla [30] illustrated the use of a coupled mode code, which was later used as a secondary benchmark.

No model can be validated as the exact solution to a propagation problem. Instead, the reliability of a model can be investigated both experimentally and computationally, and the most applicable model for the circumstances chosen. Care must always be taken to ensure that the model is only applied to situations where the limiting assumptions in its derivation are applicable.

2.4.8 The Selection of a Propagation Model

The selection of a propagation model for a particular application is not always simply a matter of accuracy. Instead, the choice of model can be a subjective process dependent on availability, computer power required, ease of implementation and execution

times. A method for the quantitative comparison of models is discussed by De Santo [36].

For the application required in this thesis, to simulate sonar images, the choice of propagation model is relatively straightforward, as many of the models are not suitable due to the limiting assumptions of their derivation. The parabolic equation is unsuitable because of its inability to model backscatter, the fundamental process by which sidescan sonar images are generated. Fast field programs cannot handle changes in bottom topography, which is the main feature of sidescan sonar images. Finite element models can only cope with low frequencies outside the range of commercial imaging sonar systems. Normal mode techniques are also more applicable to low frequencies and tend to be range dependent, apart from the coupled mode models which tend to be very complex. The ray tracing technique provides a relatively simple, intuitive model which is capable of dealing with the frequency ranges of interest for sonar modelling. The limitations of this technique, as discussed in section 2.4.2, must still be considered in its application. Further details of the modelling of propagation loss using ray tracing are presented in Chapter 5.

2.5 Scattering/Reverberation Models

The scattering of sound from the seabed can be regarded as either a major source of interfering reverberation during acoustic propagation or as a means of remotely measuring properties of the seafloor. It is as a result of the latter case that seabed reverberation is discussed here, since it is the backscattering of acoustic signals from the seafloor which provides the fundamental principle of the operation of sidescan sonar.

The scattering of waves from a random rough surface, such as acoustic waves from the seafloor, is a complex phenomena which occurs in many diverse areas including optics, electromagnetics, sonar and radar. Many reviews of scattering theory are applicable to any of these fields [44][45], as the same theory has been exploited for a variety of applications. No complete solution to the problem of calculating the scattering from

random rough surfaces has been formulated and several approaches exist which will be discussed in this section.

A large proportion of the theory and many of the models for scattering from the seabed have been developed from models for sea surface reverberation. Indeed, the topic of high frequency sea surface scattering has received more attention than sea bottom scattering. A review of reflection and scattering of sound at the sea surface is presented by Fortuin [46], in which a variety of theories, model predictions and comparisons with experimental observations are discussed. Similar models, with a change of boundary conditions, are applicable to sea bottom scattering.

It can be noted that the scattering of sound from the seabed is influenced by the sediment type, and hence the particle size of the sediments. This is only partially true, as the dominant characteristic in determining the scattering is actually the roughness of the seabed, which is partially dependent on the sediment type.

Roughness is a very subjective term to use in describing a surface, as the roughness is dependent on the properties of the wave incident on the surface. The angle of incidence and the frequency of the wave will determine how *rough* a surface appears. The same surface will appear smoother to a wave with a shorter wavelength or a wave with a greater angle of incidence.

The sound wave incident on a surface is both reflected and scattered over a range of angles. The scattered energy distribution for a relatively smooth surface and a rougher surface are illustrated in figure 2.2. The smoother surface results in a greater reflection of energy in the specular direction. For a totally smooth surface, with only specularly reflected energy the relationship for the reflection coefficient of this specular energy is summarised in [47], where the transmission of energy into the sediment layer is also discussed. It is this reflected energy which is considered in propagation modelling, whenever forward reflection from boundaries occurs.

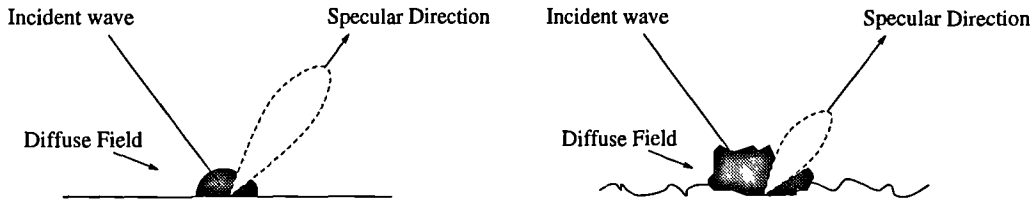

Figure 2.2: Schematic diagrams of scattering from (a) smooth surface (b) rough surface

The incident energy is also scattered diffusely in all directions. The magnitude of the diffuse field is dependent on the roughness of the surface.

A variety of approaches to quantifying the magnitudes of the scattered energy exist. Some models can only calculate the monostatic reverberation, in that they can only calculate the energy backscattered in the same direction as the incident wave. Other models are bistatic and can compute the scattered field in any direction. The concept of a *scattering cross section*, is also fundamental to this discussion. This term is defined by Urick [1] and is expressed in equation 2.8, where σ is the scattering cross section per unit solid angle per unit area.

$$\sigma = \frac{r^2}{A}\frac{I_s}{I_i} \tag{2.8}$$

In this relationship A represents the area over which the scattering is measured and r is the reference range at which the intensities are calculated. The ratio provides a measure of the ability of a surface to scatter energy. The term σ is actually a dimensionless parameter although it is referred to as the scattering cross section. The quantity $10\log_{10}\sigma$ is then defined as the *scattering strength.* The scattering strength can also be defined as the logarithmic ratio of the scattered intensity from a unit area to the incident intensity, when both values are referred to a unit distance. A brief description of the approaches available for describing and quantifying the scattering strength will be presented in the following sections.

2.5.1 Lambert's Law

Lambert's law of diffuse reflectivity is one of the simplest empirical methods of calculating the scattering strength. The scattering function is assumed to be dependent on the angular variation but is independent of frequency. Lambert's law assumes the sound is scattered in proportion to the sine of the angle of scattering, and the scattering strength is defined as

$$S = 10\log_{10}\mu + 10\log_{10}\sin\theta\sin\phi \tag{2.9}$$

where θ is the grazing angle of the incident wave, and ϕ is the angle, relative to the horizontal, of the direction of scattering. The term $10\log_{10}\mu$ is defined as the mean normalised backscattering strength, or the scattering constant. In the case of backscattered energy where $\theta = \pi - \phi$, equation 2.9 is reduced to produce a sine squared dependence on grazing angle.

$$S_b = 10\log_{10}\mu + 10\log_{10}\sin^2\theta \tag{2.10}$$

The scattering constant, $10\log_{10}\mu$ is usually an empirically defined term, for which Mackenzie [48] has calculated a value of -27dB at frequencies of 530Hz and 1030Hz for a red brick clay seabed. Mackenzie also verified the use of Lambert's law on the basis of older data. Several other studies have obtained reasonable fits of Lambert's law to experimental data at shallow grazing angles (less than 45°). Boehme and Chotiros [49] investigated the scattering from a medium sand seabed in the frequency range 30-80KHz and Stanic *et al.* [50] studied the scattering from a smooth sandy seabed in the frequency range 20-180KHz. Neither of the studies discovered any clear relationship between frequency and the backscattered strength, but both observed that the relationship between backscattering strength and grazing angle was consistent with Lambert's law.

The physical interpretation of Lambert's law is that energy scattered from a matt surface appears equally bright when viewed from any direction. In physical optics this

can be stated as a law for the scattering of light. In the case of scattering of sound from the seabed it is better defined as a *rule*, as it has not been explained theoretically. However it does provide a reasonable approximation for the scattering of sound from certain surfaces at low grazing angles. If the sea bottom has a roughness which is large compared to the wavelength of the incident sound wave, the backscattering will be independent of frequency and Lambert's rule will be applicable. If the roughness of the seafloor is small compared to the wavelength, the scattering strength will increase with frequency. This effect cannot be accounted for with Lambert's rule and a more physically correct model for the scattering of sound from random rough surfaces is required.

2.5.2 Perturbation Theory

The scattering of waves from randomly rough surfaces can be determined from the application of perturbation and related theories. Perturbation theory is a small roughness approximation and is valid for scattering from surfaces when the interface relief is much smaller than the acoustic wavelength. The scattering from the surface is then calculated as the scattering from a smooth surface plus *perturbative* scattering terms due to the slight surface roughness. The solution usually assumes the smooth mean surface is planar, although this can be extended using composite roughness techniques (section 2.5.4).

The conditions for which perturbation theory are valid are expressed in equations 2.11 and 2.12, where $h(x, y)$ is the surface height function at position (x, y) and k is the acoustic wavenumber.

$$k|h(x, y)| \ll 1 \tag{2.11}$$

$$|\nabla h(x, y)| \ll 1 \tag{2.12}$$

The first restriction arises from the assumption that the surface height function can be expanded as a Taylor series about the mean plane. The solution for the scattered field can

then be obtained to first or second order depending on the order of the r.m.s. height terms retained from the Taylor expansion.

The initial studies of scattering from a non-planar surface were performed by Rayleigh [51]. He formulated a solution for the scattering of plane waves at normal incidence from a periodically rough surface, by proposing that the unknown scattered field could be expressed as a sum of outgoing plane waves, the coefficients of which were obtained by consideration of the boundary conditions. The solution is valid if the corrugations are shallow compared to the wavelength of the incident wave. This work was later extended to waves with oblique angles of incidence and then to random rough surfaces by Rice. The resulting perturbation solution is often referred to as the Rayleigh-Rice approximation.

Much of the work on perturbation theory has considered the boundaries as impenetrable and applied Dirichlet or Neumann conditions at the interface. Marsh [52] formulated an expression for scattering from irregular pressure relief surfaces, the Dirichlet boundary condition. He then applied this solution to sea surface scattering using empirical models for the spectra of the rough sea surface [53][54]. Kuo [55] extended the work of Marsh to bistatic scattering from a penetrable two fluid interface, which he applied to scattering from sandy sea bottom surfaces and arctic ice cover. The penetrable boundary has more complex boundary conditions and requires the pressure and the normal component of the particle velocity to be continuous across the interface. Kuperman [56] calculated the forward specular reflection and transmission at a random rough two fluid boundary using a second order perturbation solution.

The accuracy of the perturbation method is dependent on the validity of the restrictions on the r.m.s. surface height, relative to the wavelength and the gradients of the surface, as expressed in equations 2.11 and 2.12. The precision is also affected by the order of the solution, although a first order calculation is normally sufficient for obtaining the scattering cross section, providing the above restrictions are adhered to.

2.5.3 Kirchhoff Theory

Kirchhoff theory provides an alternative solution to the scattering problem, and is widely used for calculating the scattering of waves from rough surfaces. Kirchhoff theory is regarded as producing a more accurate solution than perturbation theory when the radius of curvature of the scattering surface is larger than the wavelength of the incident wave.

Kirchhoff theory provides an approximation to the field on the surface of a scatterer by application of Huygen's principle, which states that every point on the wavefront can be considered as a source of secondary waves. Each point on the surface of the scatterer is treated as though it was part of an infinite plane parallel to the local surface normal at that point. The scattered field is then calculated from the integral over all the elementary sources, from Huygen's principle, using the Helmholtz integral and the tangent plane approximation. The resulting Helmholtz Kirchhoff integral relates the field on the scattering surface to the field at any point.

Due to the tangent plane approximation, Kirchhoff theory is exact if the scattering surface is an infinite smooth plane, but the calculated field is an approximation if the scattering surface is finite sized, non-planar or rough. The accuracy of the approximation diminishes depending on the amount the actual scatterer differs from the ideal infinite smooth plane.

The restrictions on the applicability of the Kirchhoff method are expressed in equation 2.13,

$$kr_c \cos^3 \theta_i \gg 1 \tag{2.13}$$

where r_c is the radius of curvature of the surface, k is the acoustic wavenumber and θ_i is the angle of incidence (complement of the grazing angle). This restricts the roughness of the surface relative to the wavelength of the incident wave. The severity of the restriction

is dependent on the angle of incidence of the wave. Kirchhoff theory is considered to provide a more accurate solution when the incident wave is closer to normal incidence [44].

Kirchhoff theory is sometimes referred to as the "high frequency approximation". Every part of the scattering surface is assumed to be locally planar, where the dimensions of this local plane, over which this assumption is implied, are dependent on the incident wavelength. Therefore, the higher the frequency of the incident wave, the shorter the wavelength and a smaller planar restriction results.

Eckart [57] used the Helmholtz Kirchhoff integral to describe the scattering and reflection of sound at the sea surface. He discussed the solution for incident waves at high and low frequencies, although the method is also applicable for all intermediate frequencies. Clay and Medwin [58] present a similar method to Eckart for calculating the scattering from the sea bottom. This technique has been applied to the analysis of sonar data by Stanton [59], to estimate the roughness and correlation area of the sea bottom.

2.5.4 Composite Roughness Techniques

The two basic methods for calculating the acoustic scattering from rough surfaces, the Kirchhoff approximation and perturbation theory, consider the surface roughness to be of a single scale. Both of these techniques have limitations on this scale of roughness: the perturbation approximation is valid if the r.m.s. roughness is smaller than the wavelength of the incident wave and the surface gradients are small; the Kirchhoff approximation is valid if the radius of curvature of the surface is greater than the incident wavelength. In most practical situations roughness exists over many scales and neither technique is strictly valid. Composite roughness theory provides a method of reducing the effect of this problem. It avoids the shortcomings of perturbation theory and the Kirchhoff approximation by combining the two and treating the interface as the sum of large and small scale surfaces.

The surface is modelled as two independent roughness scales, as illustrated in figure 2.3: a high frequency, small amplitude roughness superimposed on a slowly varying roughness large compared to the incident wavelength, representing the low frequency components of the surface. The perturbation model is applied to calculate the scattering from the high frequency surface and this result is modified to take into account the effect of the larger scale surface.

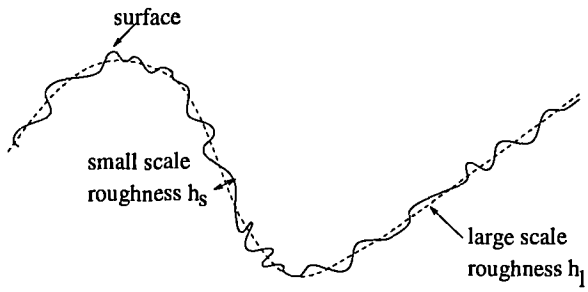

Figure 2.3: Surface with two scales of roughness

One of the first composite roughness models was developed by Kuryanov [60]. Kuryanov calculated the field from the small scale high frequency roughness using perturbation techniques, but instead of using the reflection from a plane as the zeroth approximation, he used the field scattered from the low frequency large amplitude roughness, calculated using the Kirchhoff approximation. Later techniques rely on the separation of the surface roughness spectrum into low frequency and high frequency domains. The problem with these techniques is in determining a suitable frequency at which to separate the two roughness scales. At frequencies above the splitting frequency the perturbation approximation is valid and at frequencies below the splitting frequency the Kirchhoff approximation is valid, hence an incorrect choice of the splitting frequency may result in the application of a scattering model outwith its domain of validity. Several different values for the splitting frequency have been proposed. Bachmann [61] applied this technique to sea surface backscattering.

The majority of the work on composite roughness models has been related to scattering from the sea surface, as several empirical models have been formulated to model the sea surface spectrum as the sum of high frequency capillary waves and the low frequency swell. McDaniel and Gorman [62] have applied the composite roughness model to calculate the backscatter of both acoustic and radar signals from the sea surface. They used the Rayleigh-Rice perturbation approximation to model the Bragg diffraction from the high frequency part of the surface, as the acoustic backscatter from surfaces with roughness small compared to the incident wavelength is dominated by waves with the Bragg wavenumber. To ensure the correct application of the Rayleigh-Rice and Kirchhoff models the cutoff wavenumber at which to partition to two roughness scales was then selected as the Bragg wavenumber.

The complete composite roughness model developed by McDaniel and Gorman includes terms for both the shadowing of the surface and the tilt of the large scale surface. Their model is valid for grazing angles less than 60°, although the shadowing correction has a negligible effect for grazing angles greater than 5°. As discrepancies between the model and data could not be accounted for, even with the inclusion of higher order perturbation terms [63], the scattering from a sub surface bubble layer was proposed. A term for the volume scattering by this layer was then included into the model.

McDaniel [64] has shown that at high grazing angles the scattering strength is highly dependent on the choice of the cutoff wavenumber between the roughness scales. To alleviate this problem McDaniel proposed the addition of diffractive corrections to the high frequency Kirchhoff solution by retaining terms from the series expansion of the scattering integral. The surface correlation function was split into low and high frequency wavenumber domains and the scattering strength was found to be less dependent on the cutoff wavenumber.

The composite roughness model has been extended by Jackson *et al.* [65] to model seafloor backscatter at a two fluid boundary using a heuristic formula based on the sea

surface pressure release case. In a similar argument to McDaniel and Gorman [62] - that interface scattering is not solely responsible for the measured values of scattering, Jackson included the sediment volume scattering as well as the interface scattering. To avoid the problems of the composite roughness technique at steeper grazing angles (near normal incidence) Jackson replaced the composite roughness model with the Kirchhoff approximation to calculate the backscattered energy, rather than applying diffractive corrections of the type proposed by McDaniel. This is possible because the restrictions on the Kirchhoff technique are less strict at steep grazing angles and it is therefore unnecessary to subtract the short wavelength portion of the interface before applying the Kirchhoff approximation.

Jackson's model requires several geoacoustical parameters to describe the water-sediment interface and sediment volume characteristics. The bottom relief at the interface is assumed to obey Gaussian statistics with an isotropic spectrum obeying a simple power law. This assumption is supported by spectral data obtained by Briggs [11] and Fox and Hayes [12], and hence requires only two input parameters to describe the surface roughness in terms of the power spectrum, namely the spectral exponent and the spectral strength. In the absence of experimentally measured sediment properties the surficial input parameters can be estimated from empirical relationships constructed by Mourad and Jackson [66], using bulk measurements of the logarithmic grain size. The physics of the model were also extended by Mourad and Jackson to model the sediment sound absorption due to a lossy fluid at the interface boundary.

Using backscatter data and sediment characteristics measured at several sites [67][68], satisfactory agreement has been achieved between the model and data [65][68]. These results have also increased confidence in the inclusion of sediment volume scattering in the model, and it is argued that for coarse sand bottoms, roughness scattering dominates, but for soft sediments, volume scattering is the dominant scattering mechanism.

2.5.5 Bistatic Models

The majority of the scattering models discussed in the preceding sections calculate the backscatter strength or the forward reflection coefficient, although the scattering from a rough surface will occur over all angles. Bistatic models, which can represent the forward specular reflection lobe, have been developed to model the scattering in three dimensions, including the out of plane scattering. These models allow for the transducer geometry to be bistatic, with the transmitter and receiver in separate locations, or can model hybrid paths rather than monostatic backscattering, where the returning wave follows a different path to the outgoing wave.

Caruthers and Novarini [69] developed the Bistatic Scattering Strength Model (BISSM) to model bistatic scattering. The technique uses Lambert's law to model the random diffuse scattering from small scale roughness and a coherent scattering term, based on the Kirchhoff approximation, to model the forward scattering lobe resulting from the reflections from large scale facets. This approach is similar to that of Ellis and Crowe [70], although the formulation of Ellis and Crowe assumes that each facet is larger than the incident wavelength and smooth, whilst BISSM includes a term for the roughness of the facets. Both of the techniques are applicable to low frequency scattering and both model only the interface scattering, neglecting scattering due to volume inhomogeneities in the sediment.

A bistatic model for high frequency scattering from the seabed has been developed by Jackson [71] as an extension to his earlier backscatter models [65][66]. The extended model again treats the scattering as being composed of two terms: one due to the interface roughness of the seabed and the other due to the sediment volume scattering. The backscattering model used the Kirchhoff approximation to calculate the scattering at near normal incidence, and in a similar manner the bistatic model employs this approximation near the specular direction. The model then interpolates between the Kirchhoff approximation in the near specular direction and the perturbation technique in all other

directions. Unlike the backscatter model, composite roughness corrections are not applied to the perturbation result, partially to simplify the technique and also because the composite roughness corrections are small (fig. 2 [71]). A more physical approach to modelling the volume scattering was also applied using perturbation theory, which requires additional input parameters describing the spectra of the inhomogeneities in the sediment density and compressibility. Although there is a lack of adequate data reported on bistatic scattering, preliminary testing of the bistatic model at one test site has provided a general agreement between experimental data and the model [72]. The bistatic model will be investigated further in chapter 4.

2.5.6 Summary of Scattering Models

Lambert's law provides a simple empirical model from which a satisfactory initial estimate of the scattering from a surface can be obtained. However, the results only provide a reasonable estimate of the scattering strength at low grazing angles. The remaining models for calculating the scattering from a randomly rough surface are based around the solution of the wave equation at the boundaries. Each method of solution is valid for a limited set of circumstances, and these conditions are summarised in figure 2.4.

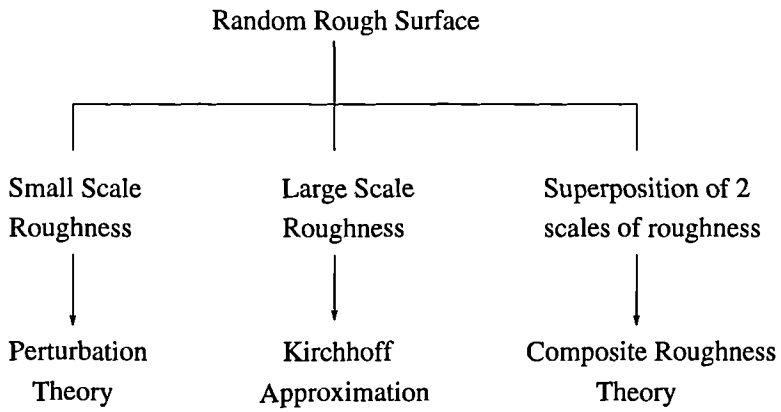

Figure 2.4: Summary of scattering models

The accuracy of the solutions obtained from the application of any of these models to the scattering problem is dependent on the observance of their restrictions of validity. These conditions have emerged due to the simplifying approximations assumed during their derivation, therefore the suitability of a particular scattering model is dependent on the application. For the simulation of sidescan sonar images the natural choice of model is a bistatic composite roughness model. This will permit the calculation of both the direct backscattered energy and also the multi-path reflections from a seabed consisting of the sediment roughness superimposed on the seabed topography.

2.6 Active Sonar Models

The effects of the previously discussed environmental models, propagation models and scattering models can be combined to produce some of the fundamental building blocks of active sonar models, or sonar performance prediction models. This class of active sonar models allows the prediction of the system signal, noise and reverberation levels in response to a particular environment. Reverberation models are often included in this classification of models, as they can be difficult to separate from active sonar models.

As propagation models become more advanced they can include more of the features typically included in active sonar models, although active sonar models tend to be simple applications models as opposed to the complex research orientated propagation models. The propagation terms within active sonar models are most often calculated from the simple intuitive ray tracing approach.

Sonar performance models tend to be based around the sonar equations [1], which were first formulated during World War *II* as the logical basis for calculations of the maximum range of sonar equipment and are similar to the equations used to describe radar performance. The sonar equations provide a simple means of linking together quantitatively the various effects of the target, medium and equipment using simple parameters.

The equations for an active monostatic sonar are expressed in equation 2.14, for the noise limited case and equation 2.15, for the reverberation limited case.

$$SL - 2TL + TS = NL - DI + DT \tag{2.14}$$

$$SL - 2TL + TS = RL + DT \tag{2.15}$$

The individual parameters are expressed in logarithmic form and are defined in table 2.1. This is just one formulation of the sonar equations; similar alternative equations exist for passive sonars or for the bistatic case where the transmission loss is not the same in both directions.

Symbol	Parameter
SL	Source Level
TL	Transmission Loss
TS	Target Strength
NL	Noise Level
DI	Receiver Directivity Index
RL	Reverberation Level
DT	Detection Threshold

Table 2.1: The parameters of the Sonar Equations

The equations are based on the basic equality between the desired signal received and the undesired or background signal. When the undesired signal is due to the steady state background noise already existing in the environment, the noise limited case occurs, but if the background signal is the result of unwanted returns from the emitted acoustic signal, the reverberation limited case occurs.

The primary purpose of these equations and active sonar models is for the analyses of sonar systems and as such they have two main functions: the prediction of the performance of an existing sonar system or in the design of new sonar systems. In their first function they permit the performance of the sonar to be estimated, in a variety of environments, in terms of the detection probabilities or effective range, for example. They can be used either for prediction purposes or after experimental sonar trials to account for performance. In this form active sonar models are often used during minehunting to calculate the effective range at which an object may be detected to reduce the probability of false alarms. Their second function is for the design of new sonar systems, where they can be used to optimise the sonar performance to the particular application, through the investigation and determination of the individual parameters.

The outputs of sonar performance models tend to be in graphical or numerical format, illustrating the effects of the individual parameters against terms such as the range or time or frequency. The output of a simplified prediction model is illustrated in figure 2.5. From this output the effective range at which the signal excess falls below the threshold can be obtained; for the illustrated case the range is 970m.

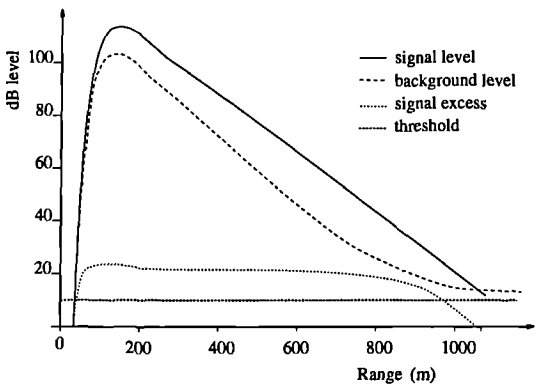

Figure 2.5: Typical output of active sonar model

Weinberg [73] developed the Generic Sonar Model to "*provide sonar systems developers with a comprehensive modelling capability for evaluating the performance of*

sonar systems and investigating the ocean environment in which they operate". This computer program is based on a modular design which incorporates several types of model for each parameter, allowing the comparison of different sub models. Hence, the title "generic".

Several commercially available sonar performance models have been developed. These include INSIGHT [74][75] developed by BAeSEMA and the Minehunting Performance Prediction System developed by GEC-Marconi [76]. The INSIGHT model is based on a fast transmission loss module composed of individual components which calculate the effects of Lloyd's mirror, bottom reflections, bottom refractions, surface ducts and convergence zones. The computer model, which operates on a standard personal computer (PC), permits the graphical display of the reverberation and propagation in complex situations, where the effects of the environment, such as the sound velocity profile and the equipment effects, due to the source level and beam patterns, can be easily altered. The GEC-Marconi Minehunting Performance Prediction System is designed to complement the use of naval minehunting sonars. It produces recommendations for the sonar parameters, and predictions of the classification and detection performance, using information supplied by the operators, data from the minehunting sonar and sound velocity profiles obtained from its integral velocity measuring probe.

SEARAY [77] is a real time performance model approved for naval use; it is an energy model, using an incoherent ray tracing method to calculate the acoustic propagation. Within the model, the bottom reverberation is calculated from empirical equations based on the measurements of McKinney and Anderson [78], where the bottom type is specified in the range 1-5, where type 1 represents a mud bottom and type 5 a rocky sea bottom. The sea surface reverberation is estimated from the empirical expressions of Chapman and Harris [79]. The outputs of this model tend to be in graphical format and typical output plots are displayed in figure 2.6. These include plots of the ray trajectories and reverberation against grazing angle, in addition to displaying reverberation losses

with range to permit the determination of the effective sonar range.

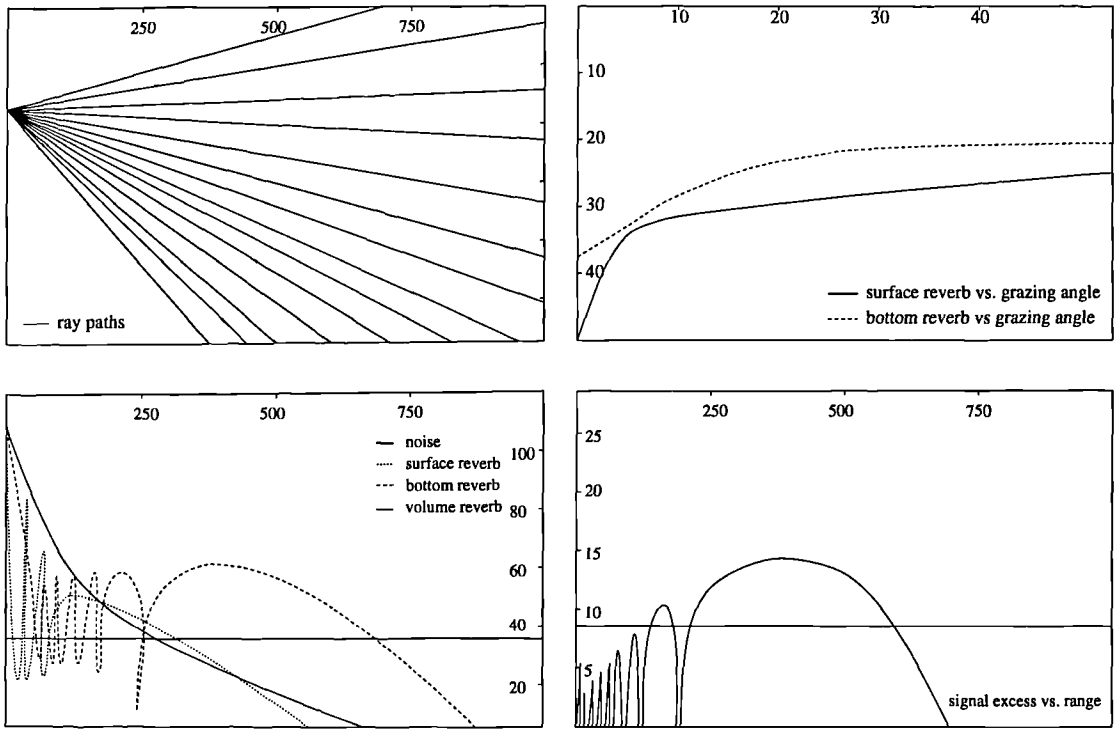

Figure 2.6: Typical output plots from SEARAY

Sammelmann at the US Navy Coastal Systems Station is developing the PC-based Shallow Water Acoustic Toolset, PC-SWAT [80]. This is an alternative ray tracing energy model which is hoped to replace SEARAY. Functionally it is very similar to SEARAY, although it does include multi-path effects which SEARAY cannot compute. Identical results have been obtained during comparison of the two models if multi-path effects are suppressed during the PC-SWAT calculations. In addition to the McKinney Anderson bottom reverberation model, PC-SWAT also includes a more advanced backscatter model, which can model up to 18 different sediment types which are specified using sediment classification terms (for example sand, fine silt).

Within the naval communities several other active sonar models exist. The majority of these are used for minehunting applications and as such the literature tends to remain classified.

2.7 Synthesis of Sonar Images

As well as the development of the PC-SWAT two dimensional energy model, Sammelmann is also developing SWAT, a three dimensional model permitting image synthesis [5]. This model is also intended for use with high frequency sonars in shallow water environments and will be capable of modelling the operation of both real aperture and synthetic aperture sonar, although the model is still at the developmental stage. As far as the author is aware, the SWAT model is the only other model currently in development which is attempting to model the sonar process and generate synthetic sonar images.

The two models, SWAT and PC-SWAT, are being developed to fulfill complementary roles within the research and applications fields. PC-SWAT has been developed as a simple applications model which can rapidly generate energy levels for use by sonar engineers in the field. SWAT is being created for more complex research based applications and its use is foreseen for the design of minehunting sonars and as a sophisticated testbed for the isolation of individual parameters or the simulation of complex processing routines. The run times of the SWAT model on a DEC-Alpha workstation are typically around 18 hours to simulate an image representing an area of seabed 6 metres by 10 metres.

SWAT is based on a three dimensional model of a target which is composed of facets, edges and point scatterers. The Kirchhoff approximation is employed to calculate the scattering from each of the facets which describe the gross shape of the target. Keller's Geometric Theory of Diffraction is used to calculate the scattering from the edges and point scatterers are used to describe the scattering from bolts and protrusions on the surface of the target. The total target strength is then formed as the coherent sum of all the scattering.

SWAT also includes three dimensional coherent beam patterns as well as surface and bottom reverberation, which are treated as zero mean Gaussian random processes.

The surface and bottom are represented as a grid of point scatterers, the amplitudes of which are dependent on the standard deviation of the Gaussian process. This limits the surfaces to representing isotropic seabeds and sea surfaces, and no directional properties are included.

The SWAT model has many features in common with the model presented in this thesis, but each has their own advantages. The features which are treated similarly by both models include the method of incorporation of the beam patterns, which will be discussed for the thesis model in chapter 6, and the pulse length, which will be discussed in chapter 3.

The primary reason for the development of the SWAT model was the simulation of targets for use in minehunting applications for the US Navy. This treatment of target strength is the main advantage of the SWAT model. The model presented in this thesis is also capable of simulating targets but uses a simpler mathematical description of the targets, rather than the complex facet model of SWAT which can require up to 20,000 primitives.

Both models employ a ray tracing approach, but at present the SWAT model assumes a simplified isovelocity environment and hence considers all the rays as straight lines. The model presented in this thesis includes the variation of the sound velocity with depth and traces the actual curved ray paths. Both of the models consider multi-path effects.

The SWAT model considers the sea bottom to have an isotropic distribution of point scatterers on a flat seabed. It is therefore incapable of simulating directional features, such as sand ripples, or larger scale topographic features such as a sloping bottom. Both of these assumptions are removed in the model presented in this thesis.

The SWAT model and the model discussed in this thesis consider the actual physical processes which result in the generation of the sonar image. This is a very

computationally intensive process and alternative statistical methods, which are unrelated to the physical processes, have been proposed to rapidly compute sonar images, requiring only a minimal number of input parameters.

Le Gall [4] has developed such a statistical method to synthesise images of sonar textures. The aim of this work is to rapidly generate textural images, from a minimal number of input parameters, for use in on-shore training systems for mine countermeasures procedures [81]. The synthesis is based on the technique of Gagalowicz and De Ma [82] for simulating natural textures. An artificial sonar texture field can be generated using *a priori* knowledge of the second order statistics, derived from the actual sonar images. The second order statistics of the artificial texture image are then designed to equal those of the original image, so making the two images appear visually similar. This provides a technique to mimic and display sonar-like images without the necessity of storing the actual image, as only its second order statistics are required. However, the statistical technique is unrelated to the physical process and cannot be used to view changes in acoustic parameters or explain the process by which sidescan sonar images are generated.

2.8 Conclusions

This chapter has provided a summary of some of the diverse range of models available within the underwater acoustics field. This review has included the topic of environmental models, the empirically derived set of models used to describe the complex underwater environment and its effect on acoustic signals. In particular, the effect of the environment on the acoustic field as it propagates was considered in the class of propagation models, which calculate the intensity and phase of the transmitted acoustic field. A variety of approaches exist for calculating the field based on the range of simplifying assumptions adopted in order to solve the wave equation, which describes the problem. The range of scattering models employed to determine the acoustical energy scattered from

the random rough surfaces, of which the seabed and sea surface are composed, were also discussed.

Each of these models concentrates on one particular aspect of the subject of sonar systems and produces solutions to particular acoustical problems. The more general range of active sonar models, although incorporating several of the features discussed above, tend to be simpler operations models producing graphical results of the system signal, reverberation and noise levels.

The majority of the models discussed in this chapter produce numerical and graphical results, illustrating the various signal levels or ranges. These results, although describing individual features of the sonar system, tend to bear no direct resemblance to the images output from typical imaging sonar systems. It can be difficult to understand and correlate the relationship between the numerical results and the sonar images generated, particularly for the (often untrained) sonar operators in the field.

A sonar operator may have to rely on a sonar image to make detection and classification decisions. At present there is no direct link between the images and the signal to noise ratios generated by traditional sonar performance models. To bring the two outputs together a model is required that can produce both a sonar type image, recognisable to the operator, and provide the signal levels and detection ranges *etc.* in a numerical form. This type of model will have a variety of applications, including use as a training tool in sonar and tactical simulators and for performance prediction during both the design and operation of sonar systems.

Due to the increasing power and reduced cost of computing facilities, a model which will produce this type of output is now feasible, as the impact on computing requirements of modelling decisions can be largely ignored. At present the only model of this form capable of synthesising the image outputs of a sonar system is the SWAT model, which is currently under development by the US Navy.

The SWAT model concentrates on the simulation of images of targets on the seabed and is based around a target strength model, with a simplified treatment of the seabed. It models the seabed as a Gaussian random distribution of point scatterers and is unable to simulate the effects of anisotropic seabeds. The seabed will also influence both the shadow produced by the target, and the target strength if the seabed itself partially shadows the target. As the shadow produced by the object is often used for detection purposes, the inability to model these effects can result in incorrect detection decisions.

The applications of imaging sonars include remote sensing and classification of the seabed, pipeline inspection, fisheries inspection and channel observation for dredging purposes, as well as object detection. Hence the need for a general sonar model capable of producing images of any seabed structure and objects on the seabed is apparent.

The aim of the model developed in this thesis is to generate synthetic sonar images by modelling the underlying physical processes. These fundamental processes include the propagation of the acoustic signal through the sea water medium and its subsequent scattering from the seabed, both of which are dependent on the complex underwater environment. The proportion of scattered energy received by the transducer is then displayed as an image of the seabed. This illustrates the role of the previously discussed environmental models, propagation models and scattering models in this application. The actual process by which sonar images are generated, including these effects, is discussed in more detail in chapter 3 in order to explain the modelling approach adopted.

Figure 2.7 illustrates the various sub models which are considered in this thesis for the synthesis of the sonar image. The basic principles which are fundamental to the development of the model are presented in chapter 3. Chapter 4 then discusses the methods of generating models to represent the seabed structure and sediment roughness, as well as the scattering models to calculate the interaction of the acoustic waves with the seabed. The propagation of the acoustic signal through the water column, including the effects of the sound velocity profile, the attenuation and the spreading loss are incorporated into the

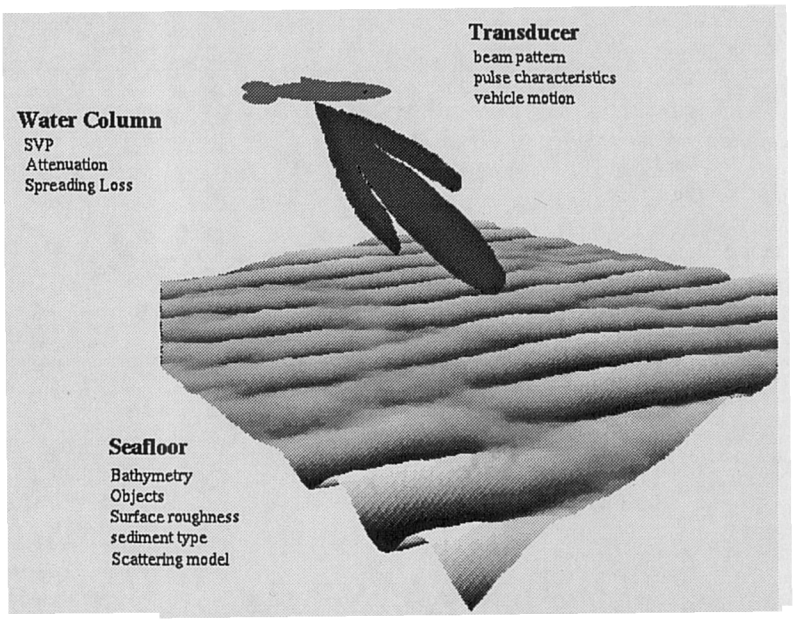

Figure 2.7: Schematic view of the modelling process

model in chapter 5. One topic not mentioned in the review is the modelling of the beam patterns and the directivity of the transducer, as standard equations have been employed initially for this purpose and their derivation is included in Appendix B. The integration of the directivity of the transducer is described in chapter 6.

Chapter 3

Fundamentals of Synthesis of Sidescan Sonar Images

3.1 Introduction

The preceding chapter discussed existing underwater acoustics models and established the requirement for a model to represent the operation of sonar and produce an output recognisable as a sonar image. This chapter presents the fundamentals of the model developed to fulfill this requirement and provide a method of synthesising sidescan sonar images by modelling the underlying physical processes.

The discussion and the model development is centred on the simulation of sidescan sonar, the operation and principles of which will be described prior to the development of the model to justify the fundamental structure adopted for the model. In addition, the accurate synthesis of sidescan sonar images requires an understanding of the sonar process and the ability to interpret sidescan sonar images.

The structure of the model is proposed under very simplistic conditions to lay the foundations for the incorporation, in subsequent chapters, of sub-models for the propagation and scattering effects reviewed in chapter two. To permit the extension of the model to include these effects, a general processing technique is also developed to allow the output of the model to be displayed in an image format, which in itself is one of the motivations behind this thesis.

3.2 Principles of Operation of Sidescan Sonar

The basic principles of sonar and in particular the operation of sidescan sonars will be explained to provide a basis of understanding for the principles of the model developed for synthesising sidescan sonar images. Further details on the operation of sidescan sonar and the generation of sonar images can be obtained from [83][84][85][86].

3.2.1 Basic Sonar Principles

The basic principles which govern the operation of sonar systems are general to all types of active system, from the simplest echo-sounder to the more complex sidescan and bathymetric sonars. The operation involves the transmission of a pulse of acoustical energy into the water medium and the subsequent reception of any returned energy reflected from objects or the seabed.

The initial step in the sonar process is the generation of an electrical pulse, with the desired characteristics of frequency, length and energy, by the transmitter. This electrical signal is then applied to the transducer, which is normally constructed from piezo-electric ceramic which expands and contracts under the application of the electric field to generate an acoustic pulse of oscillating pressure in the water. This pulse propagates through the water column and the sound is reflected and scattered by the seabed or targets present in the water column or on the seafloor. A proportion of this scattered energy will be reflected back to the transducer, which converts the oscillating pressure vibration into an electrical signal which is detected and amplified by the receiver.

The entire process is regulated by the control unit which synchronises the operations and controls the timing for the transmission and reception of the electrical signals. The control unit usually incorporates a device to display and record the returned signals; in the past this device was typically a paper chart recorder, but now the signal is often simultaneously recorded onto magnetic tape, to allow later replay and processing of the

data. Operator controllable functions to select parameters such as the frequency, pulse repetition rate or range are also usually incorporated into the control unit.

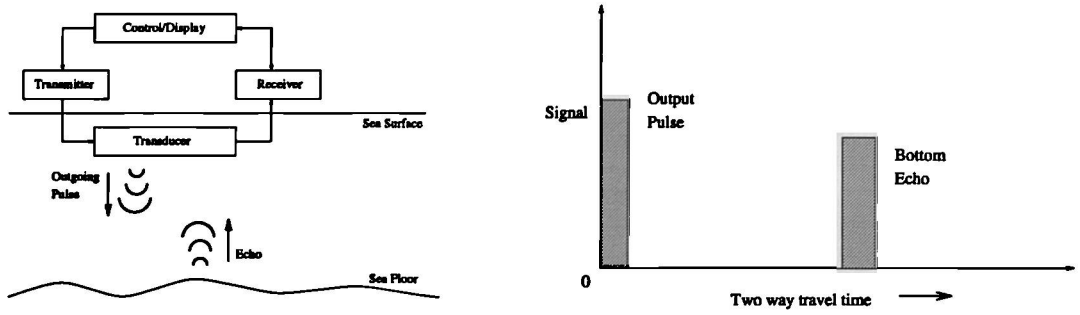

Figure 3.1: (a) Basic elements of sonar system (b) Basic returned signal of sonar system

The entire process is summarised in figure 3.1, from which it should be noted that a sonar does not actually measure depth or distance but is time dependent as it measures and displays the two way travel time. The two way travel time is the time for a pulse of energy to be transmitted through the water column to its interception and reflection from the target and return to the transducer, this is illustrated in figure 3.1(b).

The preceding discussion applied to active sonar systems which transmit energy into the environment and listen for a return. The principles of operation of passive sonar systems are similar, although they do not incorporate a transmitting device, but simply listen for acoustic energy in the environment emitted by other sources.

3.2.2 Sidescan Sonar Characteristics

Sidescan sonar systems are used to provide qualitative images representing large areas of the seabed and the objects on it. As a form of sonar system the basic principles of the operation of sidescan sonar are explained in section 3.2.1, but the actual characteristics of sidescan sonar are determined by the implementation of these basic principles. The main characteristic features of a sidescan sonar are that it is a towed, sideways looking device.

The piezo-electric transducers of a sidescan sonar are usually mounted onto a separate body which is towed through the water behind the survey vessel. This allows the transducer to be decoupled from the motion of the ship and provides a more stable platform from which to operate the transducer. The towed body is often referred to as the towfish, or simply the fish. The transducers can also be mounted on Remotely Operated Towed Vehicles (ROTV), which are "flown" by operators aboard the ship, allowing more accurate control of the position and motion of the vehicle, as it is largely divorced from the motion of the survey vessel.

A sidescan sonar is a sideways looking device, each pulse of acoustic energy emitted causing echoes from an area of the sea bottom perpendicular to the direction of travel of the towfish. Transducers are normally mounted on either side of the towfish to permit it to gather information on two channels, from the seabed on either side of the towfish. The use of two channels allows a larger area of the seabed to be scanned at any time.

The transducers are normally shaped and controlled to produce a beam, for each emitted pulse, which is narrow in the horizontal direction and wide in the vertical direction. Due to the narrow horizontal beam, returned energy is received from only a thin strip of the seafloor. The wide vertical beam permits the ensonification of a large segment of the water column and allows the reception of reflected energy from areas of the seafloor distant from the towfish.

As the transducers are towed along they gather sequential lines of data returned from each pulse, and these lines are displayed sequentially down a vertical trace to generate an image. This systematic sideways scanning is the basic principle of sidescan sonar. The scanning occurs in two directions, both along track and across track. The data is gathered discretely along track as the transducer is towed and pulses are emitted. The along track resolution of the image is therefore a function of the horizontal beam width, the pulse repetition rate and the tow speed. Across track, perpendicular to the towfish, the echoes are received with successively increasing two way travel times due to the passage

of the pulse through the water.

Examples of the typical operating characteristics of commercially available short range sidescan sonars are summarised in table 3.1. Many of the short range, high resolution sonars are dual frequency and can be switched from frequencies around 100KHz to 500KHz in the vicinity of targets or areas of interest to improve the across track resolution. The pulse repetition rate is also increased and the along track resolution is simultaneously upgraded.

System Parameters	Sidescan Sonar Systems			
	EG&G 272	Klein 422S	EDO 4175	Ultra 3050
Frequency	100/400KHz	100/500KHZ	100/520KHz	100/325KHZ
Pulse Length	0.1/0.01ms	0.1/0.02ms	0.1/0.05ms	0.09/0.03ms
Peak Output *	228/222dB	228/216dB	218/217dB	210dB
Horiz. Beamwidth	1.2°/0.5°	1°/0.2°	1°/0.5°	1.6°/0.6°
Vert. Beamwidth	50°	40°	25°	32°
Tilt Angle	20°	10°	-	-
Depth Rating	600m	12000m	60m	300m
Max. swath	1000/200m	1000m/300m	1200m/200m	800m

Table 3.1: Summary of commercially available short range sidescan sonars
*(*Source level in dB re 1 μPa at 1m, - no information available)*

Larger ranges can also be imaged using lower frequencies and longer pulse lengths, and typical characteristics of medium and long range sidescan sonars are summarised in table 3.2. The low frequency sonars produce lower resolution images of larger areas of the seabed, with typical resolution cell dimensions of 50m by 500m from GLORIA images [87]. These sonars are used to form images of large areas of the seabed or large scale topographic features such as oceanic ridges and sea-mounts.

System Parameters	Sidescan Sonar Systems			
	Ultra 60	Klein 422	TOBI	GLORIA MK II
Frequency	60KHz	50KHZ	30-32KHZ	6.5KHZ
Pulse Length	-	0.2ms	2.8ms	2s
Peak Output *	231dB	228dB	-	>225dB
Horiz. Beamwidth	1°	1.5°	0.8°	2.7°
Vert. Beamwidth	35°	10°/20°	50°	35°
Tilt Angle	-	40°	-	20°
Depth Rating	6000m	12000m	6000m	50m
Max. swath	1.2km	1.2km	6km	45km

Table 3.2: Summary of commercially available longer range sidescan sonars
*(*Source level in dB re 1 μPa at 1m, - no information available)*

3.2.3 Sidescan Sonar Images

The interpretation of sidescan sonar images, or records, requires an understanding of the phenomena which result in the generation of the images. The images are composed of bright and dark areas representing features of the seabed and water column.

As previously explained, the transducer, which is towed at a certain altitude above the seabed, emits a pulse of sound which travels away from the towfish until it strikes the seabed or a target. Some of the outgoing sound is then reflected back to the transducer, although the intensity returned is not an absolute value but is dependent on factors such as the angle and direction from which the target was ensonified. In addition, the material properties of the seabed sediments and targets determine their reflectivity, with rock and gravel acting as stronger reflectors than soft sediments such as mud and sand. The intensity of the return is displayed against the two way travel time, or time of flight. Figure 3.2(a) illustrates the geometry of the sidescan sonar system and figure 3.2(b) displays the

returned intensity against the two way travel time in the form of an 'A' scan. An 'A' scan is simply one line of a sonar image corresponding to the returned energy from a narrow strip of the seabed due to the reflections from one emitted pulse.

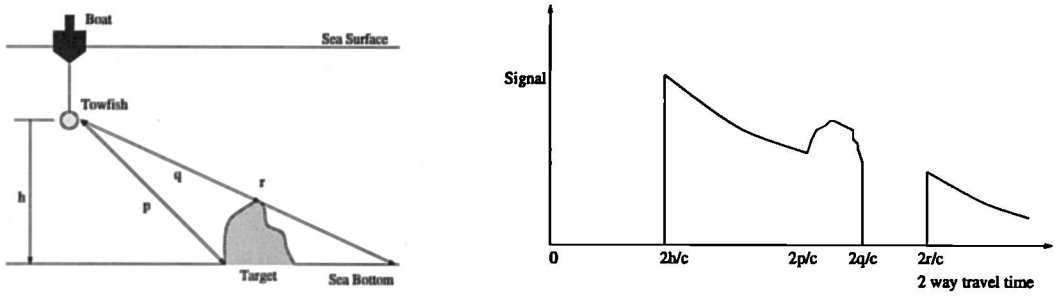

Figure 3.2: (a) Geometry of sidescan sonar system (b) Corresponding 'A' scan

At the beginning of the trace there is a blank area, as the pulse propagates through the water column without returning any echoes. The *first bottom return* is the first echo to return from the sea bottom closest to the towfish. For a relatively flat seabed the first return is from the seabed directly below the towfish and it occurs at time $\frac{2h}{c}$ seconds, where h is the height of the towfish in metres and c is the velocity of sound. (The discussion at present assumes that the velocity of sound is constant everywhere within the water column.) The first return is then followed by echoes at successively greater slant ranges, where the slant range is the actual distance from the sonar to the point on the seabed from which the sound was reflected. These points are displayed at correspondingly greater distances from the start of the trace. This is illustrated in figure 3.2(b) by the return from the target at time $\frac{2p}{c}$, where p is the slant range to the target.

The orientation of the target relative to the direction of the incoming pulse will influence the intensity of the reflected signal. The closer the inclination of the surface normal of the target to the direction of the incoming pulse, the greater the energy reflected back to the the transducer. Objects protruding above the seabed will create high intensity returns but will prevent the sound from reaching the seafloor for some distance behind

them. This will produce an acoustic shadow zone which appears on the trace as a blank area. Shadows can also be generated by depressions on the seafloor, as illustrated in figure 3.3. Depressions result in a dark shadow area on the trace succeeded by a lighter area, caused by the reflections from the face of the depression facing back towards the sonar.

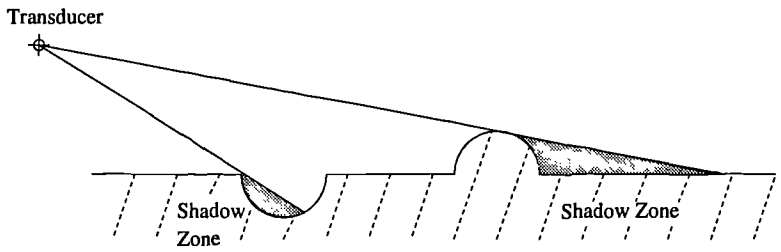

Figure 3.3: Creation of shadow zones

The intensity of the returned energy decreases with range due to the effects of absorption, spreading and scattering. To compensate for these effects and maintain an even intensity across the image to aid in the interpretation, gain is applied to the incoming signal. The gain is normally time dependant and the primary method employed is usually *time varying gain* (tvg). These effects will be investigated further in chapter 5.

The sidescan records are typically displayed as greyscale images. Throughout this text the following convention will be employed: high intensity signals will be displayed on the sonar image as white and no return will be displayed as black. This convention is directly applicable in this situation where computer greyscale images are generated. Sonar records can also be displayed as the inverse to this convention, a practice which stems from the early use of thermal recorders where the strength of the mark was proportional to the intensity.

3.3 Fundamentals of the Basic Model

The fundamentals of the model for simulating the operation of sidescan sonar, through consideration of the physical processes, to generate synthetic sidescan sonar

images, can be developed from the previously described principles of operation of sidescan sonars. The model will initially be developed using very simplistic conditions. These *ideal* conditions should not be regarded as merely academic but as a convenient base from which to develop the model. The performance of the model will be determined under the simplistic conditions and then extended in later chapters to include more complex variables associated with the irregularities of sidescan sonar images.

3.3.1 Simplifying Assumptions

Prior to explaining the basic principles of the model, the assumptions inherent in its derivation will be introduced. These assumptions are related to simplified treatments for the water column, seabed and transducer directivity.

In the water column it is assumed that the isovelocity condition is applicable as the sound is considered to be travelling everywhere at the same velocity. It is also assumed that there is no loss of energy, due to absorption, spreading or scattering, as the acoustic pulse propagates through the water medium, until it is reflected from the seabed. In the initial case the seabed is considered to be a totally flat, horizontal plane.

The final assumption considered is related to the transducer directivity. The energy is emitted from the transducer with the same intensity over all vertical angles, but has an infinitely thin, knife edged horizontal beam. This results in the ensonification of an infinitely thin *line* of the seabed perpendicular to the towfish. At all points along this line the incident intensity is constant, due to the lossless medium and vertical beam pattern assumptions.

Applying these assumptions, the basic principles of the simulation model can be explained.

3.3.2 Basic Principles of the Model

The simulation process will be developed initially in two dimensions, generating as its output an 'A' scan, displaying the intensity versus the time of flight for the energy returned from a single emitted pulse. Only one channel will be considered, so the 'A' scan represents the seabed on one side of the towfish only.

As the pulse of acoustical energy is emitted by the transducer it can be considered vertically as expanding wavefronts. The ray hypothesis can then be applied to represent the propagating waves, where the rays are proposed to be everywhere perpendicular to the wavefronts and illustrate their direction of travel. As a result of the isovelocity assumption, the wavefronts will be spherically spreading, as each point on the wave will advance at a constant rate. This results in the rays following totally straight paths.

For each line of the image or 'A' scan, a pulse of sound is emitted, which is modelled as a set of rays, each of which is emitted from the transducer at a preset angle. The path of each ray is then traced until it intersects the seabed. To generate the 'A' scan, two values are required for each ray traced: the time of flight, or two way travel time, and the intensity of sound reflected.

Due to the simplified conditions of isovelocity and a flat seabed, the slant range of the ray can be calculated by the application of simple pythagorean geometry using knowledge of the towfish altitude and the angle at which the ray was emitted. From the slant range the two way travel time can be calculated, assuming that the reflected ray follows a path back to the transducer identical to that of the original incident ray.

$$2\ way\ travel\ time = \frac{2 \times slant\ range}{c} = \frac{2h}{c \sin\theta} \tag{3.1}$$

where c is the velocity of sound, h is the height of the towfish above the seabed and θ is the angle, relative to the horizontal, at which the ray was emitted.

In the initial phase of the model, the amplitude of the backscattered signal is calculated from Lambert's Law of diffuse reflectivity. This assumes that the incident energy is scattered equally in all directions, and the amount of energy backscattered in the same direction as the incident ray is

$$I_r = I_i \mu \sin^2 \theta_g \tag{3.2}$$

where θ_g is the grazing angle, μ is the empirical reflectivity coefficient, and I_r and I_i are the incident and reflected intensities. As a result of the isovelocity and flat seabed assumptions the grazing angle is equal to the angle at which the ray was emitted. The accuracy of Lambert's Law for calculating the backscatter was considered in section 2.4.1 and will be further investigated in chapter 4.

For each ray the incident intensity, I_i, is constant, due to the assumptions that no losses occur as the ray propagates and that the vertical beam pattern is constant in all directions. The output intensity is then simply a function of the grazing angle and the reflection coefficient. If the reflection coefficient is assumed to remain constant over the entire area ensonified, the output intensity further simplifies to a function of the grazing angle only.

Applying the above assumptions, the intensity and two way travel times for a set of rays can be calculated and is displayed as an 'A' scan in figure 3.4. In obtaining this output from the model, the towfish was positioned at a height of 10m above the flat seabed, and the speed of sound was assumed to be constant at $1500ms^{-1}$. The scattering constant, $10\log\mu$, was selected to be -22dB to represent a sandy seabed. Each of the rays was emitted from the transducer with a constant intensity selected to be unity. The intensity displayed in the 'A' scan is calculated using equation 3.2, and is displayed as an absolute value and not a logarithmic value, to represent the actual output of a sonar system.

The discrete points represent the returned values for each ray. The distribution of these points is dependent on the angles at which the rays were emitted. In figure 3.4, the

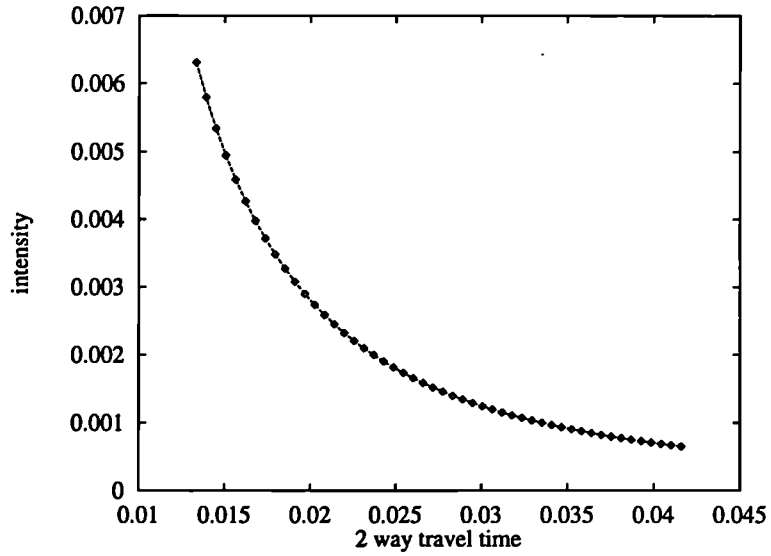

Figure 3.4: 'A' scan illustrating sonar return from flat seabed

time increments between the returns from each ray are constant as the angles at which the rays were fired were calculated to produce constant slant range increments.

The principle of constant slant range increments is illustrated in figure 3.5, where three successive rays have been emitted into the scene. The slant range of the first ray is l_n, and for the second ray is $l_{n+1} = l_n + \Delta l$ and for the third ray is $l_{n+2} = l_{n+1} + \Delta l = l_n + 2\Delta l$. The increment in slant range, Δl, for each successive ray is maintained constant. The time increments between each of the rays returned is also constant, as a linear relationship exists between time and distance due to the isovelocity assumption.

The points at which the rays intersect the seabed will not be evenly spaced, and the distance between the points of intersection for successive rays will decrease with range across the swath. Constant slant range increments are desired since the output of a sonar display is time based and not distance based, as explained in section 3.2.1, and this produces evenly spaced samples in the time domain. The time based display of sonar images will be considered further in section 3.4.

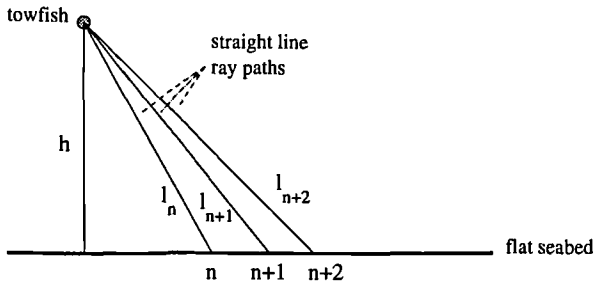

Figure 3.5: Constant increments in slant range

3.3.3 Synthesis of Sonar Images

The initial development of the model considered only two dimensions, generating an 'A' scan as its output. The model will now be extended to three dimensions to produce synthetic sidescan sonar images. Again only one channel will be considered, representing the image returned from the seabed on one side of the towfish.

The basic process of emitting a set of rays to represent each pulse of energy, and tracing these rays to their intersection with the seabed to obtain values of the time of flight and intensity returned for each ray, is essentially repeated for each line of the image. The towfish is positioned at an (x, y, z) coordinate in space, where z represents the height of the towfish, the y axis is orientated in the direction of travel of the towfish and x is the direction perpendicular to the towfish, as shown in figure 3.6. At this position the transducer emits a pulse of acoustical energy and the times and intensities of the rays are calculated. The transducer is then moved along the y axis to a new position, to represent the motion of the towfish, and the process is repeated by the transmission of the next pulse, to obtain the next line of the image.

The successive lines are then displayed next to one another, as with the real sonar process, to create the image. Each line is displayed as a line of pixels across the image, with the greyscale value of each pixel determined by the intensity returned for that ray, with black representing no returned signal and white representing a high intensity return.

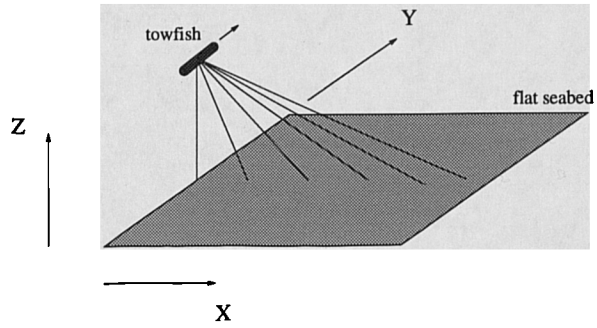

Figure 3.6: Position of towfish in 3 dimensional space

Using the same scenario described in section 3.3.2, with the transducer maintaining a constant height of 10m, a constant speed of sound of $1500ms^{-1}$, and a flat seabed with the reflectivity properties of sand, the image shown in figure 3.7 is obtained. The left hand edge of the image represents the instant of time when the pulses were emitted. The black area then represents the period of no return as the pulse propagates through the water column without reflecting any energy. The first return from the seabed has the highest intensity and represents the sound reflected from directly below the transducer. The intensity returned decreases with time across the trace as a result of the decreasing grazing angle. Each line of the image is identical due to the simplifying assumptions and the constant altitude of the towfish.

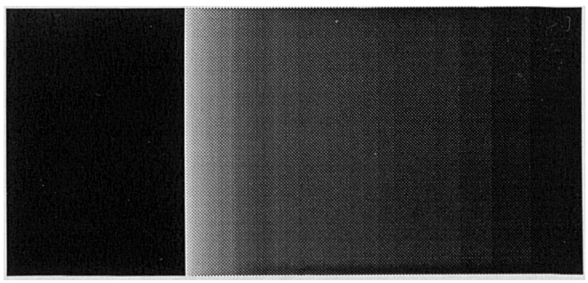

Figure 3.7: Simulated sonar image from flat seabed

Another assumption has been introduced in extending the model to three dimensions: the towfish is assumed not to move between the transmission of the pulse of energy and the reception of the scattered energy for that pulse, as it is assumed that each ray

returns along the same path as the original incident ray. Thus, the motion of the towfish is considered as a series of discrete increments, where the transducer transmits the next discrete pulse after each increment, rather than as a continuous motion with discrete pulses emitted.

The process is not strictly three dimensional but is $N \times 2D$, as it essentially repeats the two dimensional process for each of the N lines of the image. Each line of the image is also composed only of returns from an infinitely thin line of the seabed.

The towfish in the above example followed a straight line path, at constant height parallel to the y axis. The position of the towfish, from which the pulse is emitted, can be altered to represent variations in its height. Figure 3.8 illustrates the output image for the same totally flat seabed but the height of the towfish is increasing linearly. This is reflected in the image as an increase in the time of occurrence of the first bottom return.

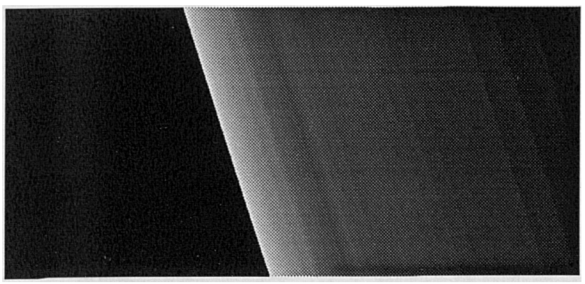

Figure 3.8: Simulated sonar image with increasing fish height

The transducer motion characteristics and their subsequent effect on the sonar image will be considered in more detail in chapter 6.

3.3.4 Optical Ray Tracing and Computer Graphics

As as result of the assumptions, the simplified model for creating sidescan sonar images is similar to optical ray tracing, which is a well known technique in computer graphics. Ray tracing allows realistic simulations of light images to be produced by

calculating the intensity and colour of each individual light ray which is projected into a pre-defined scene. The object of ray tracing is to simulate the propagation of light through an environment by tracing light rays through a scene to determine which objects they interact with. Each light ray is traced back from the receiver (or eye), through each reflection and refraction to the final interaction with an object or surface. This technique models the physical properties of light and the interaction between light and matter.

Computer graphics ray tracing was first developed by Appel [88] and by Goldstein and Nagel [89]. Appel was the first to ray trace shadows, using a sparse grid of rays to determine the shading of a point or if the point was in shadow. Goldstein and Nagel pioneered the use of constructive solid geometry, creating complex scenes from simple mathematical primitives combined using Boolean operators. Whitted [90] and Kay [91] then fundamentally extended ray tracing to include specular reflections and refractive transparency as well as the simple diffuse reflections calculated from Lambert's law.

Optical ray tracing models are now capable of producing realistic simulations of complex scenes as they can calculate both diffuse and specular reflections and trace refracted rays through objects with varying refractive indices [92]. The effects of focussing, texture mapping and the artificial simulation of caustics can also be incorporated. The introduction of radiosity calculations for more realistic modelling of diffuse reflections and the associated colour bleeding effects [93], has also permitted the creation of more authentic shadows and penumbra by removing their unrealistically sharp edges.

The technique of ray tracing in computer graphics has already been applied to the acoustical design of concert halls and auditorea [94], to permit the visualisation of the acoustic fields. Blake [95] investigated the concept of applying ray tracing techniques from computer graphics to the simulation of sidescan sonar images by the alteration of an optical ray tracing program to mimic some of the features of sidescan sonar. The model produced synthetic images but was not physically correct as it failed to rectify many of the limiting assumptions of the computer graphics technique.

Although light and sound can both be considered as waves that transmit energy through a medium, there are several fundamental differences which require the two types of energy to be treated differently and this subsequently affects the modelling process. The main differences are due to the speed of propagation and the wavelength of the two types of wave. Light propagates in air approximately five orders of magnitude faster than sound underwater. As light propagates so quickly that the eye cannot perceive its temporal nature, optical images are presented in the spatial domain, whereas a sidescan sonar image is displayed in the time domain as it is the differences in the times of return of the acoustic energy which generates the image. The resolution of optical images is also much greater than that of sonar images, as sound has a much longer wavelength than light; this also affects the scattering behaviour and the relative roughness of surfaces.

As the model is extended to include more of the factors influencing acoustic energy underwater and the generation of sonar images, the similarities between the two techniques decrease. The one common factor which links the model developed in the thesis and optical ray tracing, is the fundamental principle of the application of geometric ray theory to create synthetic images of complex scenes.

3.4 Display of Data

The basic principles of the model, where an image is generated by tracing rays to their intersection with the seabed was discussed in section 3.3. Several problems arise in displaying the output of the model as an image. These difficulties are related to the modelling of the continuous process of the return of the energy from the transmitted pulse as a discrete number of rays. The technique of displaying the data as an image and the inherent problems will now be considered.

As discussed in section 3.2.1, the sonar is a time based measuring device, as the intensity of the returned signal is displayed against the two way travel time. Each row of the output image is generated from the response from one emitted pulse, where the

beginning of the display for each line is triggered by the transmission of the acoustical pulse into the water column. The emission of each successive pulse acts as a trigger and resets the time measurement, and each line of the image displays the acoustic energy returned to the transducer over a period of time equal to the reciprocal of the pulse repetition rate.

Sidescan sonar generates as its output a band-pass signal centred on the operating frequency. To display the output, the spectrum is shifted to zero frequency and is low pass filtered to obtain the envelope of the signal. The envelope of the signal is then applied directly to an analog recorder, such a thermal chart recorder, where the intensity of the mark left on the paper is proportional to the magnitude of the envelope.

Digital displays and recording devices are becoming increasingly more common, as the availability of computing power and storage facilities continues to expand. Some sonars, such as the Klein System 2000 and the EG&G DF1000, digitise the signal directly at the transducer head, prior to any processing or recording of the signal. With the digital sonar, the shifted low passed amplitude envelope is sampled at uniform time increments, with a frequency greater than twice the bandwidth to satisfy Nyquist's sampling theorem [96]. The uniform time samples are then recorded or displayed directly as an image.

An image displayed on a computer can be considered as a grid of equal sized equidistant pixels. A greyscale value is displayed in each of these pixels to represent the intensity of the signal. As the pixels in each row are equally spaced, they must represent equally spaced time samples on the sonar image. This results in the requirement that the discrete samples returned from each of the rays traced, for each line of the image, return intensity values which occur at constant increments of time.

In the example of section 3.3.2, the returned echoes occurred at equally spaced increments in time, as the firing angles of the rays were calculated to produce constant slant range increments. This was possible due to the simplifying conditions of an

isovelocity medium and a flat seabed. If either of these assumptions is removed it is no longer possible to calculate in advance the time of return and the intensity of the ray simply from knowledge of the height and angle at which it was emitted into the scene.

The isovelocity assumption will be removed by the extension to the basic model presented in chapter 5. The effect of the sound velocity profile in the water column on the times of return of the rays will be briefly discussed here to illustrate the problems of predicting the travel times, and a more detailed discussion of the medium and its effects will be given in chapter 5.

If the velocity of sound is not constant throughout the water column, as was previously assumed, the rays can no longer be modelled as following straight line paths since they are refracted by the changes in velocity. The refraction can be modelled by the simple application of Snell's law at the boundaries between areas with differing velocities, or if the velocity changes are linear the rays will follow the arcs of circles (a result obtained from Snell's law and linear gradients). From the known initial conditions of the towfish position and the angle at which the ray was emitted, the rays are traced incrementally through the water column to their intersection with the seabed. Due to the complex refracting medium, the curved ray paths cannot be predicted in advance, to select a firing angle which will result in the desired time of return. Ray tracing is a trial and error "shooting method", as discussed in section 2.4.2, where the desired ray path characteristics can only be obtained from an iterative selection process.

As the rays follow complex paths, the slant range cannot be calculated from pythagorean geometry, but is obtained from the length of the actual traced path. The time of flight is also no longer directly proportional to the distance travelled as the velocity varies along the ray path. As it is impossible to obtain *a priori* information regarding the time of flight without incrementally calculating the ray path, the returned intensity cannot be calculated at uniform intervals in the time domain due to the refractive nature of the medium.

This is only one of the problems in attempting to obtain reflected signals which are uniformly spaced with time. The above discussion has assumed a perfectly flat seabed without surface texture; the removal of this assumption will be discussed in Chapter 4, but a brief outline of the problems associated with randomly rough seabeds will be presented here. If the topography varies with range, successive returns can no longer be guaranteed to return successively increasing times of flight with increasing horizontal range from the transducer.

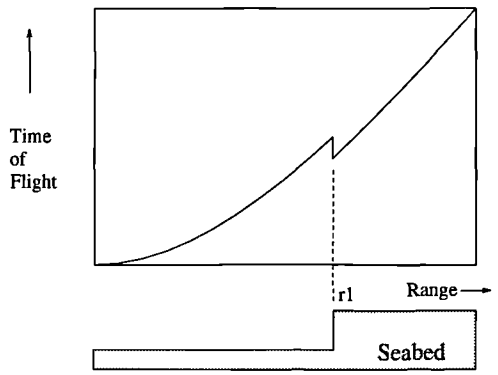

Figure 3.9: Effect of stepped seabed on time of flight

As an example, the isovelocity conditions are again assumed and rays are emitted at successively decreasing firing angles (angle relative to the horizontal) to produce constant slant range increments. If the seabed is totally flat, the time of flight will increase with range. If, though, the seabed consists of a simple step, occurring at range r_1, the time of flight will increase with range until r_1 is reached, it will then decrease, due to the shorter path length resulting from the decreased vertical distance from the transducer to the seabed. At ranges greater than r_1 the time of flight will continue to increase again.

This illustrates the problem for a very simple case, but the actual seabed terrain is very complex due to both the bathymetry and the sediment roughness. The intensity values returned for each ray will therefore occur at random points in time, and the time increments between successive rays will not be constant. The processing technique developed to circumvent this problem will be described in the following sections.

3.4.1 Processing of Data

It is only possible to obtain constant slant range increments between consecutive traced rays if the simplifying conditions of the isovelocity medium and a flat seabed are applied. If either of these conditions are removed, the assumption that the rays produce intensity values at constant time increments will produce unacceptable approximations. A general technique is required to produce equally spaced time samples from the data returned from the emitted rays since both of the simplifying assumptions will be removed in later chapters. The processing technique introduced here permits the output to be displayed as a sonar image without distorting the data by the introduction of errors or the violation of sampling theory.

The processing technique employed to develop the uniform samples will be explained in the following sections. The method is divided into several steps and the principles fundamental to each of the individual processes will be explained. The overall considerations regarding the number of rays to trace and the timing requirements to be satisfied, to minimise potential sources of error, will then be discussed. The model considers only the magnitude of the intensity response in the processing of the data and the phase is neglected within the following discussion.

The first step of the processing is to sort the data into increasing time order. Although the data is generated with increasing horizontal range, this does not necessarily result in increasing times of return, as illustrated in section 3.4. The subsequent processing functions consider the effects of simultaneous returns, shadows, the pulse length and the decimation of the output for display purposes.

3.4.2 Areas of High Illumination

The magnitude of the reflected intensity is dependent on the orientation of the scattering surface relative to the direction of the incoming rays. Objects which have a surface

normal inclined in a similar direction to the incoming wavefront will produce brighter areas on the sonar image. Objects on the seabed, or a non-flat seabed, will also produce areas of high illumination due to the reception of echoes from more than one part of the scene at the same instant of time.

This can be illustrated by considering the simple case of a step on a seabed, each part of which is a totally flat reflecting plane composed of an identical material. The same incoming wavefront will ensonify points on both steps of the seabed, as illustrated in figure 3.10 (a). Considering the equivalent ray representation of figure 3.10(b), the length of ray_1 is equal to the length of ray_2 and both these rays, although emitted at different angles will produce echoes with identical two way travel times.

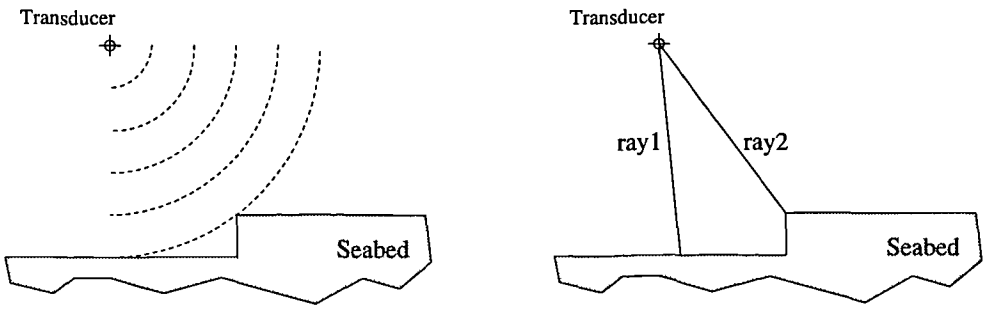

Figure 3.10: (a) Emitted wavefronts (b) Ray representation

In an actual sonar image this will result in an area of high illumination due to the simultaneous reception and summation of the energy. In a similar manner, to facilitate the processing of the data for the simulation, if more than one ray produces a return with equal two way travel times, the total intensity at this time sample will be calculated from the addition of the intensities of these rays. This will result in an area of high illumination on the simulated image, which is analogous to the brighter areas generated on actual sidescan sonar images.

Considering again the stepped seabed situation as described above, the intensity returned is displayed against the time of flight in figure 3.11. During the time period

between the first bottom return at time t_1 and the time t_2, intensity values are received from the reflections of rays from the lower step only. In the time interval from t_2 to t_3 contributions are received from rays which have intersected the upper step in addition to the rays which have been reflected from the lower step. The high intensity points occurring at approximately time t_2 are due to the reflections from the face of the step, because of the inclination of this surface relative to the incoming rays. The intensity of the returned rays from the upper step is less than the echoes from the lower step due to the reduction in the grazing angle. The energy received after time t_3 is the result of echoes from the upper step only. During the time period from t_2 to t_3, the reflected energy from rays with the same travel times is summed together to produce the area of higher intensity shown in the plot of figure 3.11(b).

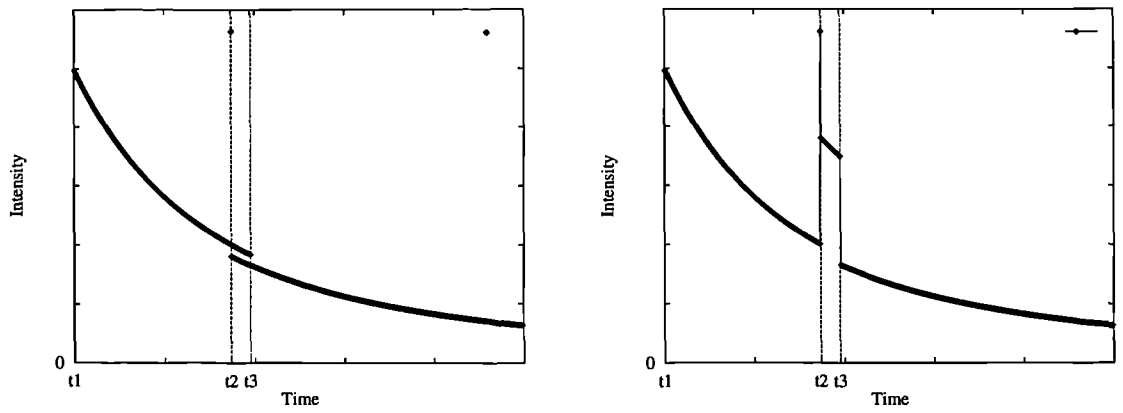

Figure 3.11: (a) Intensity returned with time (b) Processed return illustrating bright spot

The basic principle is extrapolated to the processing of any data, where if any rays return identical two way travel times, the intensity values at this time will be added together to create a higher intensity area on the sonar image.

3.4.3 Shadows

The objects which reflect the acoustic energy will also prevent the energy from ensonifying some part of the seafloor, resulting in acoustic shadow zones. Shadows are one of the primary features which provide three dimensional information from the two dimensional sonar image, and their position and shape contain valuable information for the accurate interpretation of the image. The shadow zone may be created by either an object relieved from, or depressed into, the seabed, or by the self shadowing of the seafloor.

The effect of shadows can be illustrated by considering again the case of a step on a seabed, each part of which is a totally flat reflecting plane, figure 3.12(a). It is assumed for ease of explanation of the basic principle that isovelocity conditions again apply. It is impossible to illuminate the area of the seabed directly below the step. The ray emitted at angle θ will intersect the upper step, but the ray fired at angle $\theta - d\theta$ will intersect the lower step of the seafloor as illustrated below. The difference between the two way travel times for the two rays is significantly greater than the average time increment between successive rays for the flat seabed.

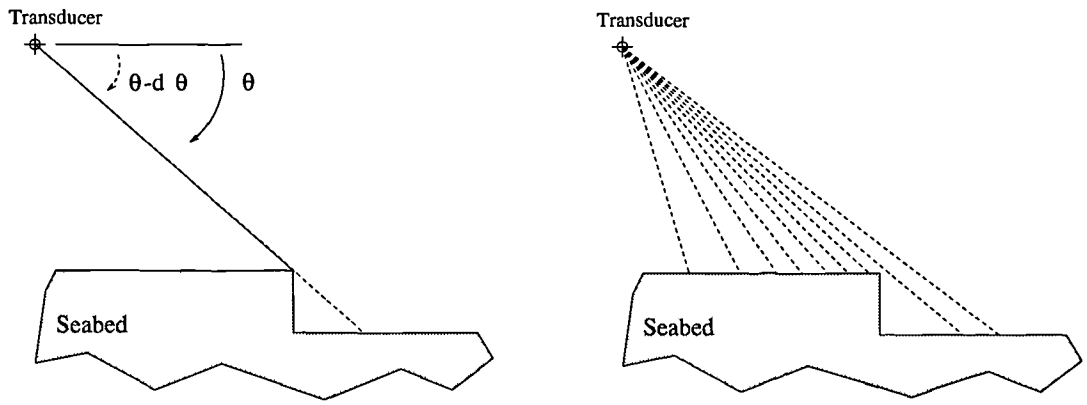

Figure 3.12: (a) Shadow zone (b) Rays intersecting the seabed

The angles at which the rays are emitted from the source can be calculated to produce constant slant range increments by applying the isovelocity and flat seabed

assumptions. For the rays emitted at these angles this produces returns with constant time increments, Δt, between successive rays, for the rays intersecting the upper step as displayed in figure 3.12(b). The first ray to intersect the lower step has a significantly longer two way travel time than the previously emitted ray which intersected the upper step, and the returns are no longer at constant time increments. The intensity returned for each of the rays is displayed against the two way travel time in figure 3.13.

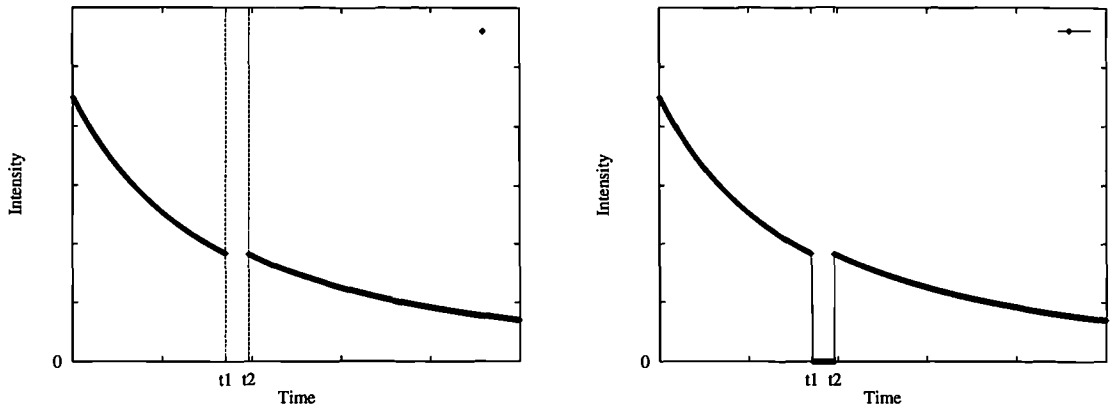

Figure 3.13: (a) Times of flight for illustrated rays (b) Padded with zero intensity

To facilitate the display of the output as an image, the data is required at constant time increments. The signal cannot simply be interpolated, either with a simple linear technique or with the more complex technique of sinc functions [97], to provide values at the omitted time samples. For the above case, this would result in the insertion of intensity values in the time interval from t_1 and t_2, when no ray returned an intensity value. The reason no sample was recorded was because no energy was received by the transducer in this time period because of the shadow zone. The correct intensity value to insert is therefore zero. In the above example, the time samples in the shadow period occurring between times t_1 and t_2 are padded with a value of zero intensity to produce constantly spaced time intervals, figure 3.13.

The explanation for the insertion of a zero value of intensity when no time sample occurred assumed uniformly spaced time samples, apart from in the shadow zone. This

method can be extended to include the effects of the actual seabed topography, the sediment roughness and the refractive seawater medium, where although the rays are emitted at angles which would result in constant time increments if the simplifying assumptions held, the data is returned at varying time increments. A similar argument regarding shadow zones is applied, that is, if no return occurs at a given instant of time, the area of the seabed is in shadow and the intensity value is zero.

In the processing of the data, the smallest time interval which exists between any two returned times of flight is calculated. To provide uniformly spaced samples in the time domain, the data is interpolated to this smallest time interval by the insertion of an intensity value of zero when no sample exists.

3.4.4 Pulse Length

One of the factors influencing the across track resolution of the sonar image is the length of the pulse of acoustical energy emitted by the transducer. The pulse has a physical extent in the water which is determined by the sound speed. By the time the trailing edge of the sonar pulse has left the plate of the transducer the leading edge will already have travelled a distance equal to the pulse length (in seconds) multiplied by the sound speed. The outgoing pulse in the water is thus an expanding wavefront of finite extent.

The length of the pulse affects the range resolution and determines the theoretical minimum separation at which two objects on the seabed can be detected. This minimum separation is half the physical length of the pulse. A longer pulse length will encompass the two objects and the returning echo will resemble a single target, figure 3.14. A shorter pulse will correctly record the two targets separately. The higher frequency 500KHz sidescan sonars with typical pulse lengths of 0.01ms therefore have a theoretical resolution a factor of ten greater than the medium frequency 100KHz systems with pulse lengths of 0.1ms.

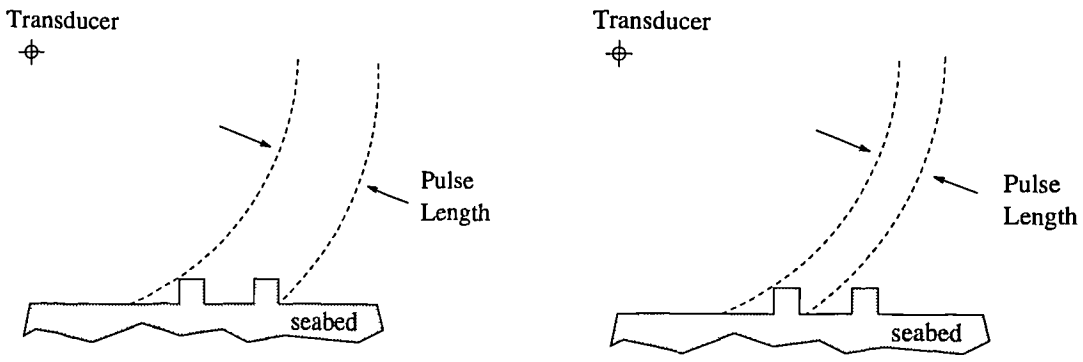

Figure 3.14: Effect of pulse length on range resolution

The previous discussion of the basic principles of the model assumed that the pulse of sound was of infinitesimal duration and each ray returned represents an impulse of acoustic energy returned at the one time instant only. However, each ray intersects with the seabed for a finite duration of time, dependent on the pulse length, and the energy is returned from that ray for a finite duration of time.

To incorporate the effect of the pulse length in the simulation model, and the subsequent loss of resolution, the discrete signal returned is convolved with the pulse length. This is equivalent to assuming that each ray produces a response for the finite duration of the pulse length and models the interaction of these returned pulses.

In figure 3.15(a), a rectangular shaped pulse of length 0.1ms and unity magnitude is displayed in discrete samples in the time domain. Figure 3.15(b) illustrates the intensity returned at the discrete time samples for each ray for the case of a regular box shape object on a flat seabed (combination of the up step and down step examples of figures 3.10 and 3.12). This returned signal has already been processed to add any signals occurring at the same time sample and to pad with zeroes to represent the shadow zones and generate equally spaced time samples. The return for each ray effectively assumes that the return is an infinitesimal duration impulse. Figure 3.16(a) then shows the result of the convolution of the pulse with the signal of figure 3.15(b), and the effect of the pulse on the resolution can be noted. If a longer pulse of length 0.4ms is applied, the across track

resolution decreases further, figure 3.16(b).

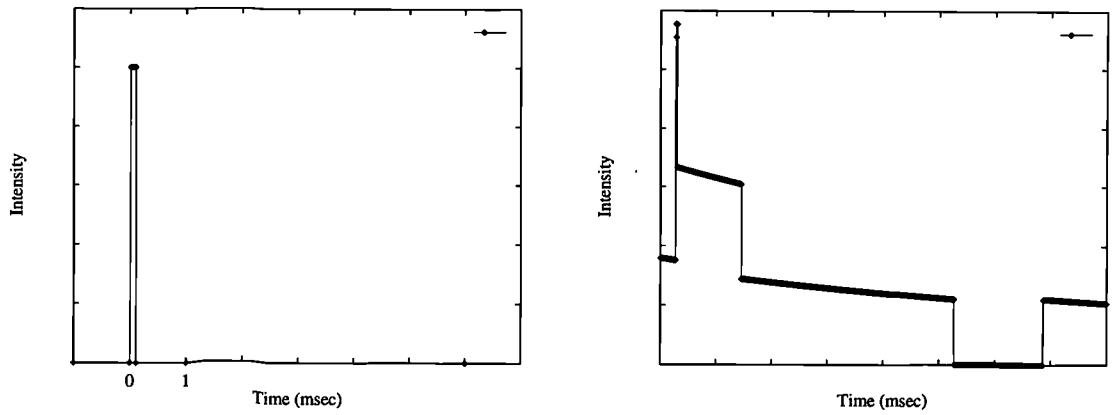

Figure 3.15: (a) Applied pulse of length 0.1ms (b) Data generated assuming infinitesimal pulse

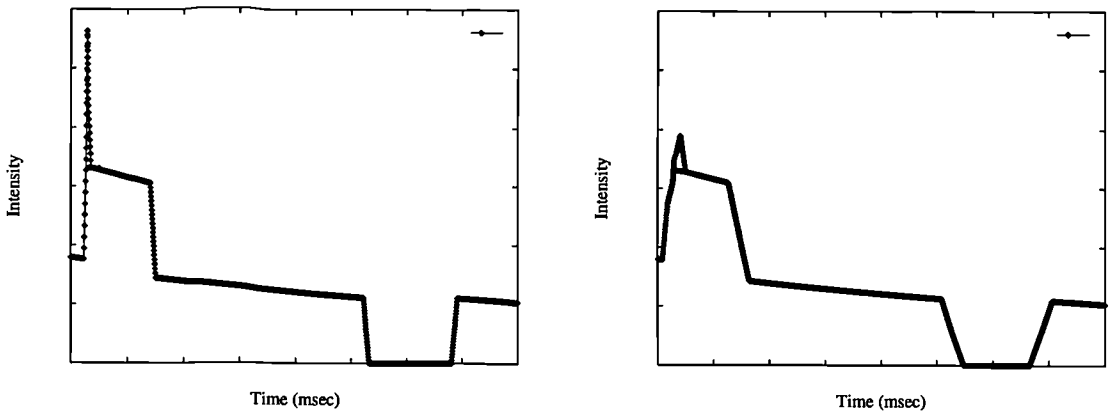

Figure 3.16: (a) Data convolved with 0.1ms pulse (b) Data convolved with 0.4ms pulse

The pulse in this example was assumed to be rectangular, but any shape of pulse may be modelled. Due to the finite bandwidth of the transducer the pulse shape is rarely rectangular; even if a rectangular pulse is applied to the transducer by the transmitter, the pulse emitted into the water will be modified. The inclusion of the pulse length by convolution allows the actual pulse shape to be easily incorporated.

3.4.5 Decimation

The preceding signal generation and processing techniques have generated more samples than will be displayed, as the final output image will consist of fewer pixels per line of the image than samples generated. It is therefore necessary to convert the sampling rate period to that of the display without distorting the data. The number of samples is reduced by decimation.

The process of decimation is illustrated in figure 3.17, where an input signal $x(n)$ is down sampled by an integer factor M. The decimator consists of a digital anti-aliasing filter $h(k)$ and a sample rate compressor. The sampling rate compressor reduces the sampling rate by the factor M, from the original rate F_s to $\frac{F_s}{M}$. To prevent aliasing of the signal at the lower rate, the digital filter is applied to first bandlimit the input signal to frequencies less than $\frac{F_s}{2M}$.

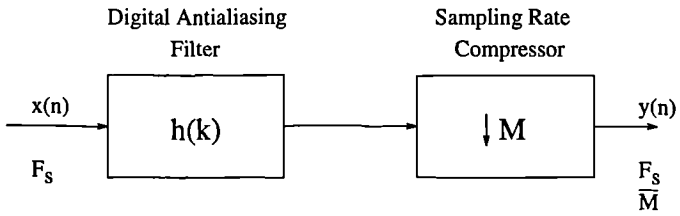

Figure 3.17: Block diagram of decimator

A finite impulse response (FIR) filter was designed to low pass filter the signal. The FIR filter was selected for this application due to its linear phase response, as it maintains the frequencies in phase with each other relative to their original values and does not alter the overall shape of the signal. A filter with a non linear phase characteristic would cause a phase distortion in the signal, as the different frequency components would be delayed by different amounts. The undesired distortion, which precludes the development of a coherent simulation, can be avoided by the use of a FIR filter.

The FIR filter is characterised by equations 3.3 and 3.4 for a discrete input signal $x(n)$ and a filtered output signal $y(n)$, where $h(k)$, for k = 0,1,2,..N-1 are the impulse response coefficients for the filter and N is the number of filter coefficients (filter length). Equation 3.4, defines $H(z)$, the transfer function of the filter, which provides a means of analysing the filter by evaluation of the frequency response.

$$y(n) = \sum_{k=0}^{N-1} h(k)x(n-k) \tag{3.3}$$

$$H(z) = \sum_{k=0}^{N-1} h(k)z^{-k} \tag{3.4}$$

The method of equiripple design based on Chebyshev approximation techniques was used for determining the coefficients of the FIR filter. Filters designed by this method are optimal in the sense that the peak approximation error in the frequency domain, over the frequency range of interest, is minimised. The method also results in an error curve with equal magnitude ripples in either the pass or stop bands.

The application of the Chebyshev approximation method to the design of the digital filter required for the decimation requires the definition of the tolerance scheme of the filter. Figure 3.18 illustrates the tolerance scheme for the low pass filter required for decimation by a factor of M. The passband deviation δ_p, stopband deviation δ_s, the passband cutoff frequency f_p, the stopband cutoff frequency f_s and the number of filter coefficients, N, require to be specified. To satisfy the Nyquist requirements, the passband cutoff frequency is less than half the original sampling rate.

The optimal filter can be designed from this tolerance scheme using a computer based algorithm developed by McClellan *et al.* [98]. The algorithm uses the Remez exchange method to design filters with the minimum weighted Chebyshev error in approximating the desired ideal frequency response. The numerical algorithm requires

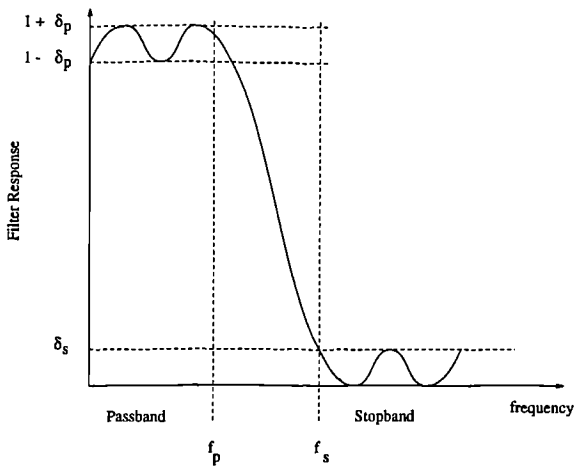

Figure 3.18: Low pass filter characteristics

the number of filter coefficients to be specified. In practice the number of filter coefficients is unknown, but can be estimated from the empirical relationships, specified by equations 3.5, 3.6 and 3.7, which were determined by Hermann *et al.* [99] and generalised by Rabiner [100]:

$$N \approx \frac{D_\infty(\delta_p, \delta_s)}{\Delta F} - f(\delta_p, \delta_s)\Delta F + 1 \tag{3.5}$$

Within this expression ΔF is the width of the transition band normalised to the sampling frequency and D_∞ and $f(\delta_p, \delta_s)$ are defined by equations 3.6 and 3.7.

$$D_\infty(\delta_p, \delta_s) = \log \delta_s[a_1(\log \delta_p)^2 + a_2\delta_p + a_3] + [a_4(\log \delta_p)^2 + a_5 \log \delta_p + a_6] \tag{3.6}$$

where $a_1 = 5.309 \times 10^{-3}$, $a_2 = 7.144 \times 10^{-2}$, $a_3 = -4.761 \times 10^{-1}$, $a_4 = -2.660 \times 10^{-3}$, $a_5 = -5.941 \times 10^{-1}$ and $a_6 = -4.278 \times 10^{-1}$.

$$f(\delta_p, \delta_s) = 11.01217 + 0.51244[\log \delta_p - \log \delta_s] \tag{3.7}$$

This decimation of the signal is analogous to the digitisation process often used in modern sonars, where the analogue signal is low pass filtered and the envelope of the band limited signal is sampled at constant time increments. The digitised output is then

displayed directly as an image where each pixel corresponds to one sample.

3.4.6 Summary of Data Processing and Timing Requirements

It is important to minimise the introduction of sources of error through the processing of the data by considering the timing requirements. Potential sources of error exist through the interpolation of the data with zero values of intensity to simulate the effect of shadows. An area may be padded with zero intensity to represent a shadow zone when the problem is related to a lack of resolution as an insufficient number of rays have been traced. It must also be possible to insert an integer number of time samples to maintain the uniformity requirements.

The second requirement can be fulfilled by specifying the precision to which the two way travel times are calculated and truncating all times to this precision. This value is also the smallest time interval which exists between any two samples, and the data will be interpolated to this sampling interval by the insertion of the value of zero intensity where no sample points exist to create uniformly spaced samples in the time domain.

The number of rays to trace is determined by the frequency of the transducer. To satisfy sampling theory the desired period between rays, Δt, is half the period of the emitted signal. The angles at which the rays are emitted are calculated to produce the constant time increment Δt between them if the isovelocity and flat seabed assumptions are applied. For a 100KHz sonar the desired time increment is $5\mu s$.

The returned data from the rays emitted at these angles is sorted into ascending time order, and the intensities of any samples occurring at the same instant of time are added. The data is then padded with zeros to produce constant time increments at a period equal to one tenth of the period of the input signal ($1\mu s$ for a 100KHz sonar). The number of samples is then decimated back to the original number of rays emitted, which results in equally spaced time samples with a constant increment of Δt. This ensures that

only time periods greater than Δt with no samples are padded with the intensity value of zero and reduces the probability of wrongly defining a shadow zone. The data is then convolved with the pulse, the length of which must be greater than Δt. For a 0.1ms pulse and time increments between samples of $5\mu s$, the response due to each pulse is effectively determined by twenty data points.

The number of data points which the signal is decimated to for display is related to the bandwidth of the sonar system, as the output must be low pass filtered and the envelope sampled at twice the bandwidth. Typical 100KHz sonars have bandwidths of 8KHz, so the data is sampled at a frequency of greater than 16KHz.

The procedure to generate the uniform time samples from the random time samples of the rays traced satisfies the requirements of the Nyquist Sampling Theorem. This minimises the probability of introducing errors by the application of the method described. The images in all subsequent chapters are created by applying this method of processing to generate uniformly spaced time samples from the information returned from the rays traced. Details of the computer program written to implement the data processing are summarised in Appendix D.

3.5 Conclusions

After consideration of the physical characteristics which result in the generation of sonar images, this chapter presented the basic principles of the model developed for simulating the operation of sidescan sonar. The model has been developed initially under simplistic conditions, as it does not consider the actual refractive effects of the seawater medium, or the transducer characteristics, and approximates the seabed as a totally flat reflecting plane. The simplified model is summarised in figure 3.19.

The procedure defines the modular ray tracing approach adopted in the development of the simulation system. This basic model will be extended in later chapters to

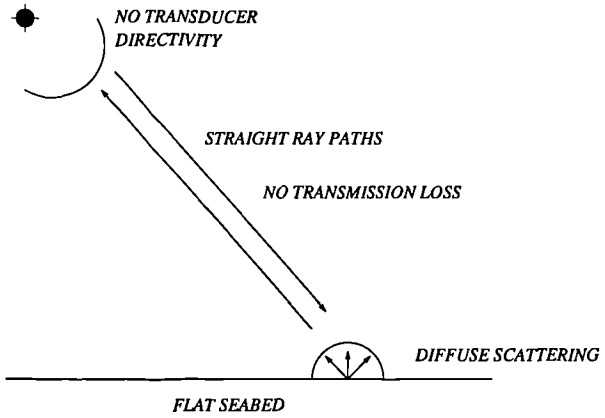

Figure 3.19: Summary of the simplified model

incorporate the complex effects of the medium, the seafloor and the transducer into the framework structure of the model defined here. Chapter 4 will remove the flat seabed assumption and develop realistic images of seafloor texture. The refractive nature of the seawater medium, and its effect on the sonar image will be discussed in chapter 5 and the transducer directivity and motion will be incorporated into the model in chapter 6.

Under simplistic conditions it was possible to determine the intensity values of the rays reflected from the seabed at constant time intervals. As these simple conditions will be removed in the later chapters, a general processing technique was proposed to produce equally spaced samples in the time domain from the random returns from the rays traced. The returned intensity values are required at uniform time samples to allow them to be displayed in image form. It is the visualisation of the output of the model of the sonar process in an image form which is the principle motivation for the development of this model. The processing technique developed in this chapter will be applied to produce the uniform time samples from the data generated under any conditions, and will be used to permit the simulated data to be displayed in image format in all subsequent chapters.

Chapter 4

Seabed Topography and Reverberation

4.1 Introduction

Chapter three discussed the fundamental principles of the technique employed to simulate sidescan sonar images. Several simplifying assumptions were introduced to permit the derivation of the model; one of these assumptions was the existence of a totally flat seabed. Although providing an initial starting point for the model development, this assumption is very limiting, as it is the imaging of the topographic features of the seabed which provides the primary motivation for the majority of sidescan sonar surveys.

This chapter will initially discuss models to provide a source of sufficiently complex and realistic data to represent the seabed topography and sediment roughness. The incorporation of the seabed model into the sonar simulation model will then be discussed. This removes any assumptions regarding a flat seabed and permits the synthesis of sidescan sonar images representing complex seabed structures. The model will then be extended to simulate objects on the seabed or in the water column, to provide a general simulation model which is capable of synthesising many of the other applications of sidescan sonar in addition to route survey.

The original model developed in chapter three considered only the rays backscattered to the transducer along an identical path to the original incident ray. With the introduction of the large scale topographic features and objects, the energy reflected to other

parts of the scene and then scattered back to the transducer must be considered. These multiple path effects will also be included into the simulation model to provide a more accurate model of the physical processes resulting in the generation of sidescan sonar images.

The basic model developed in chapter three applied Lambert's Law to calculate the scattering, but with the inclusion of the multiple reflection paths the limitations of modelling the scattering with this technique become apparent. The second part of this chapter investigates the scattering process and applies a bistatic scattering strength model to the problem. This model permits the scattering to be determined in any direction and includes the properties of the sediment, in terms of both the volume scattering from the penetration of the sediment and the sediment interface roughness.

4.2 Models for Seabed Topography

The simplest form of the model, developed in chapter three, assumed the seabed to be a totally flat reflecting plane. This representation is also used in many of the propagation models discussed in chapter 2, but for this application, where the output of the model synthesises a sonar image, a more realistic representation of the seabed is desired. A seabed model is therefore required which will provide a source of sufficiently complex and realistic information about the seabed topography for the input to the synthesis model.

The contour charts derived from bathymetric data can be regarded as deterministic models of the seabed. Unfortunately, bathymetric data exists only for a few areas of the seabed and is usually of too large a scale to be of direct use for this application. Most of the available contour data has been derived from bathymetry with a resolution of 100m or larger [12] [101], and the data is often only available for the single track below the transducer. The resolution is therefore inadequate when compared to the swath widths of the high frequency sidescan sonars which will be modelled (typically 150m or less), as even

the contour charts provide a smoothed representation of the seabed topography. With the current development and increasing use of high resolution scanning bathymetric sonars, higher resolution bathymetric information may soon become more widely available.

To combat the lack of deterministic data on the topography of the seafloor, several stochastic models have been developed to represent the distribution of features of the seabed in a statistical sense. Many of these models use simple Gaussian statistics to represent the seabed roughness. The SWAT model [5] for synthesising sonar images, employed a grid of point scatterers, each of which had an amplitude and phase determined by the standard deviation of the Gaussian process derived from the reverberation model. This provides the capability of representing an isotropic seabed roughness but it is unable to model topographic features of the seafloor.

A stochastic model based on the power spectral density has been developed to quantitatively characterise the seabed roughness on scales ranging from a few centimetres to several kilometres [12] [11]. The power spectral density relates the spatial energy distribution over the frequency range and provides a simple and concise representation of the seabed topography and surface roughness. This relationship, which is characterised by a roll-off with frequency, is expressed in equation 4.1, where $S(f)$ is the spectral density, f is the frequency and β is the frequency exponent.

$$S(f) \alpha \frac{1}{f^{\beta}} \tag{4.1}$$

This relationship has been investigated and verified for seabed topographies spanning a range a spatial frequencies. Bell [101] discovered the power law relationship for the low spatial frequency topographic data from the abyssal hills of the Pacific Ocean. Fox & Hayes [12] also investigated low spatial frequency data and argued that the data could be extrapolated to higher frequency roughness. Insufficient data exists at present to confirm whether the same power law can be extended over all frequencies or whether the

spectrum should be partitioned into a number of frequency segments, each with a power law relationship characterising the geological features which have resulted in the topographic features of this frequency range.

Small scale, high frequency roughness features have also been characterised with the power law relationship. The high resolution data, depicting detail at scales of less than 1cm, which was employed in the majority of analyses was obtained from stereo photographs of the seabed. Briggs [11] and Jackson & Briggs [68] measured one dimensional spectra of the microtopography from stereo photographs taken at a variety of sites with different sediment types. These spectra could all be represented by the power law relationship, which was dependent on the sediment type. Briggs [11] discovered that the slope of the spectra tended to flatten with decreasing frequency and related this to the data of Fox & Hayes. Jackson *et al.* [67] also measured one dimensional spectra and converted these to two dimensional spectra using relationships between the Fourier transform and the relief covariance. Akal and Hovem [102] have presented a numerical technique to directly obtain the two dimensional power spectrum and auto-correlation function at centimetre resolution, to provide a quantitative description of the seafloor roughness.

The power law relationship, which provides a suitable representation of the seafloor topography and roughness, can be characterised by a Brownian motion stochastic model. Mandelbrot [103] produced a theoretical basis for this relationship in terms of *fractals* and the *fractal dimension*. Fractals have found widespread application in the modelling of natural scenes, permitting complex images to be generated from simple rules. The *fractal dimension* of Mandelbrot is related to the frequency exponent coefficient β by equation 4.2, where D is the fractal dimension and E is the Euclidean dimension.

$$D = E + \frac{3 - \beta}{2} \tag{4.2}$$

Fractal dimensions 0.2 to 0.3 greater than the Euclidean dimension tend to produce the

most realistic synthetic topography [104] and appear to be favoured in nature.

The concept of fractals and fractional Brownian motion (fBm), can be used to generate realistic topographic features on both large and small scales. The concept can even be extended to *multifractals*, where the resultant image is formed by the superposition of several fractal texture images of differing dimensions.

4.3 Inclusion of Seabed Topography into the Simulation Model

The simulation model will employ fractional Brownian motion, or fractal, models to represent the seabed topography. This power law relationship has been verified for a range of scales, from centimetre resolution to several kilometres, as discussed in section 4.2. The use of fractal models, which provide a good representation, both visually and statistically, of the seabed topography, permits the calculation of the interaction of the acoustic pulse with complex, yet controlled surfaces. Linnett [105] discusses the implementation of models to synthesise both isotropic and directional fractal surfaces. These models will be used to generate images to represent the seabed topography for input to the simulation model.

The technique employed to calculate the intersection of the ray with the fractal seabed is similar to the technique of grid tracing developed by Musgrave for ray tracing fractal terrains in computer graphics [106] [107]. Both methods are based on the concept of height fields, where the input fractal terrain is transposed into a two dimensional grid array of altitude values which describe the surface.

The sonar simulation model employs as its input a greyscale image representing the seabed topography and figure 4.3(a) provides an example of such an input seabed image. The intensity of each pixel in the image is related to the height of the seabed at that point, and is stored as the altitude value in the grid array. Scaling factors are applied to determine the range of altitude values over the area of seabed to be imaged. Appropriate

scaling factors are determined from the work of Jackson *et al.* [65] which discusses the typical variations in the magnitude of the seabed topography with range.

The rays are emitted using the procedure described in chapter 3 and are traced as they follow straight line paths towards the seabed. The height of the ray above the seabed is compared to the altitude values at the four corners of the grid cell over which the ray is traversing. If the altitude of the ray is less than any one of the heights within that cell, then the ray is investigated to determine if it has intersected the seabed within that cell. To test for intersection, the terrain within the rectangular cell is partitioned into two triangular planes, or facets, by splitting the cell diagonally. The terrain is represented by triangles as it can only be guaranteed for three points to be coplanar. The intersection test consists of calculating the equations of the triangular planes and determining the point of intersection between the ray equation and the plane equation. The point of intersection, if it exists, is checked to ensure that it lies within the confines of the cell. This process is illustrated schematically in figure 4.1.

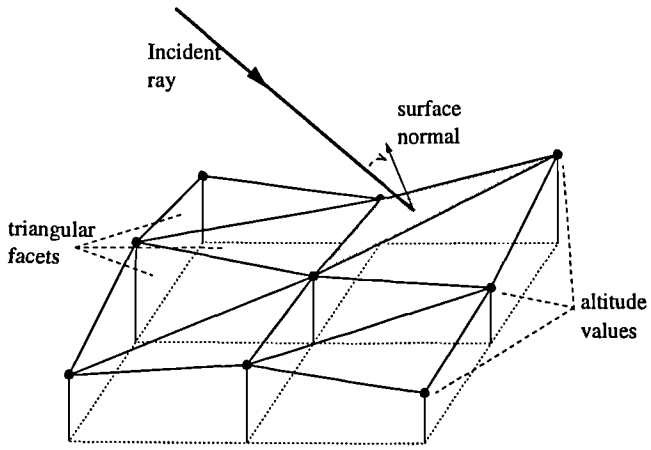

Figure 4.1: Schematic diagram illustrating intersection of ray with triangular seabed facet

Rays grazing past the surface will fail the intersection tests, although most rays will incline directly onto the surface at the first cell tested for intersection. The intersection tests have a greater probability of failure at long ranges, where the ray paths are closer to

the horizontal, or when the ray is traversing over seabed which is sloping away from the transducer.

Once the point of intersection of the ray with the seabed has been determined, the actual slant range to this point can be calculated. The two way travel time is then obtained from the slant range and the velocity of sound, which for the present is assumed to remain constant. The local surface normal of the triangular plane intersected by the ray is calculated from the equation of the plane which was determined previously. The grazing angle of the ray is calculated with respect to the local surface normal, and the scattering strength determined from Lambert's law is therefore dependent on the orientation of the surface at the point of intersection.

The efficiency of this technique is related to the fact that the minimum number of ray intersection tests are performed, and the planar equations of the seabed facets are determined only as required. The execution time can be further reduced by the introduction of a *bounding volume*. The highest point of the seabed terrain is determined, and the altitude of the ray is compared to the altitude values of the cells it is traversing only when the ray altitude is equal to, or less than, the maximum height of the seabed, which constitutes the bounding value.

An image of the height field used to represent an area of the seabed is displayed in figure 4.2(a) as a three dimensional perspective plot. The height field was generated from a fractal model with an isotropic frequency decay of $\frac{1}{f^{\beta}}$, with the frequency exponent β equal to 0.8, which results in a fractal dimension of 2.2, the most common dimension encountered in natural scenes [108] and a scaling factor representing an r.m.s. height variation of 60cm over 100m range was applied [65]. The seafloor has a scattering constant for Lambert's Law of -22dB, to represent a sandy seabed [109]. The simulated sonar return calculated from this seabed is illustrated in figure 4.2(b), where the towfish was flown at a constant height of 10m along the left hand edge of the seabed image. The black

region at the beginning of the trace is the period of no return as the pulse propagates through the water column without reflecting any energy. The seawater is still assumed to be an isovelocity, loss-less medium, and each ray is emitted with constant energy in a knife edged beam, as discussed in chapter three.

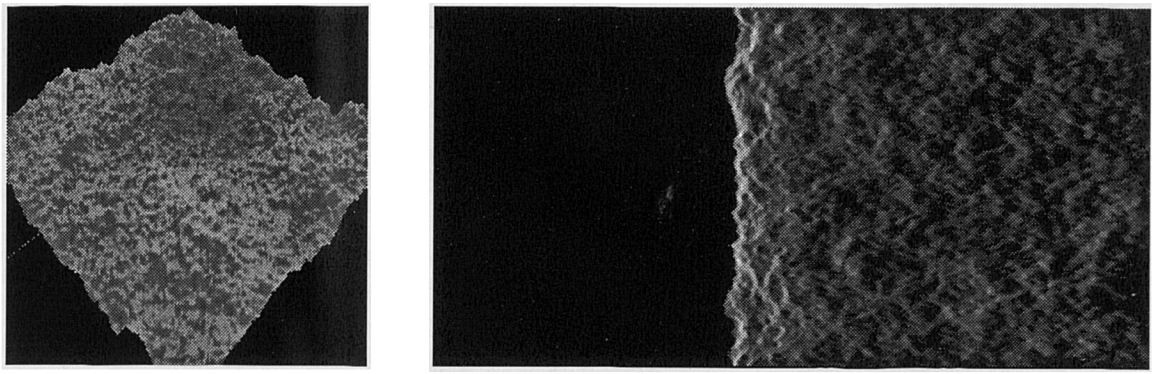

Figure 4.2: (a) Fractal height field (b) Simulated sonar image of fractal seabed

More complex fractal images can be created to represent the input seabed, modelling directional features such as the sand ripples of figure 4.3(a). This image is used to create the height field prior to tracing the rays. The simulated sonar image of this scene is displayed in figure 4.3(b). The transducer is again towed at a constant height of 10m and the seabed scattering parameters represent a sandy surface. The simulated image illustrates the effect of the time based display, resulting in the compression of the sonar image close to the towfish and the expansion with range, an effect known as *slant range distortion*. This causes the period of the sand ripples in the sonar image to increase with range, and distorts the sand ripples at the start of the trace when the towfish is directly above. The effects illustrated in the simulated image of figure 4.3 will be compared to actual sonar images in chapter seven.

The technique can also be used to simulate different seabed textures within the one image. A composite seabed image is created by defining fractal boundaries on an image, since naturally occurring boundaries do not usually occur as straight lines. Each of the segmented areas created by the boundaries are filled with different images to represent

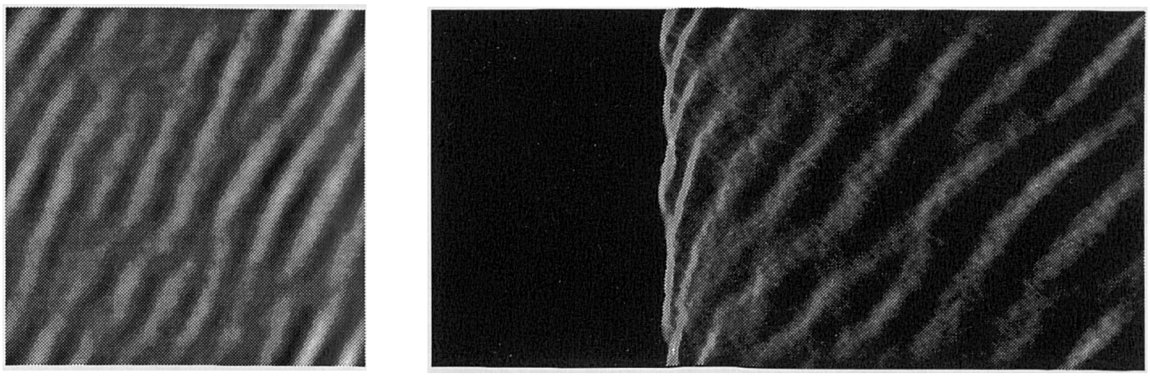

Figure 4.3: (a) Fractal image of seabed topography (b) Simulated sonar image of fractal seabed

different sediment types or structures. The technique for creating these multi-texture fractal images is explained by Linnett [105]. The scattering constant for Lambert's law is then defined for each of the areas. The input image of a multi-texture seabed is illustrated as a height field in figure 4.4(a). The sand ripples are defined with a reflection coefficient of -22dB and the other areas of the image are characterised as clay-mud with coefficients of -29dB. The simulated sonar image of this height field and these sediments is displayed in figure 4.4(b). The period of no return has been removed from this image simply to permit more of the detail of the simulation to be visualised.

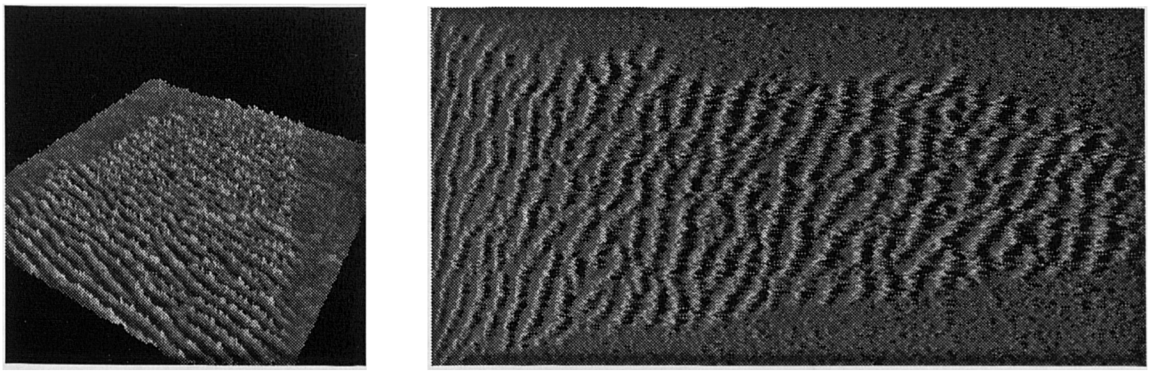

Figure 4.4: (a) Fractal height field (b) Simulated sonar image of fractal seabed

The use of height fields has the advantage that any seabed topography can be simulated, including sloping seabeds, anisotropic and composite seafloor structures, as there is

no underlying assumption concerning a flat, homogeneous seabed. The technique is not limited to fractal terrains as the input seabed; any input height field can be implemented, including gridded bathymetric data. This permits the method to be extended to include real seafloor topographic data when available. If the bathymetric data is of too large a scale, a hierarchical technique could be implemented using fractals to represent the rough seafloor surface between the bathymetric data points. The boundaries between the different sediment types can also be obtained from classified sidescan sonar images, to permit the simulation of realistic areas of the seabed.

4.4 Mathematically Defined Objects

There are numerous applications of sidescan sonar and in addition to surveying the topographic features of the seafloor, the aim of the sidescan survey is often to examine or search for objects on the seabed or in the water column. Such applications include pipeline inspection, where the pipeline on the seabed is examined for underlying spans due to erosion; or mine countermeasures applications where channels are surveyed to detect and classify objects on the seabed. The objects in both of these cases are man-made and as such have a regular shape.

To create a general purpose model, which can be used to simulate a variety of sidescan sonar applications, it is also necessary to synthesise sonar images containing objects on the seabed or in the water column. As the majority of the objects which it is desired to model have a regular structure, mathematical procedures can be used to define their shape. This is similar to the technique used in ray tracing in computer graphics, where complex scenes are created by defining each of the objects in the scene using mathematical primitives. The primitive objects can also be combined to create more complex objects through the use of constructive solid geometry.

The sonar simulation model has the ability to incorporate any number of spheres and cylinders, in any orientation, within the scene. Planar objects on the seabed can also

be modelled by manipulation of the input height field. The spheres and cylinders are defined using mathematical coordinates to specify their position and orientation relative to the other objects in the scene to be synthesised. A spherical object is defined by its centre coordinate in three dimensional space and its radius; a cylinder is specified by the coordinates of the centre points of its end plates and its radius. More complex scenes can be constructed by the superposition of these primitives to model most of the commonly encountered underwater structures, and an example of the combination of cylinders to construct an object to represent a tethered mine is shown in figure 4.11(a).

The incorporation of mathematically defined objects into the simulation program results in an increased number of intersection tests. Each ray traced must be tested to check if it intersects any of the defined objects, as well as testing for intersection of the seabed. The actual point of intersection with an object can be determined from the equation for the ray and the equation defining the object. If the ray can intersect more than one object it must be tested to ensure that it is the first point of intersection which is recorded, as it is assumed that none of the objects are transparent to acoustic energy. The amount of backscattered energy received by the transducer due to the intersection of the object is calculated from Lambert's Law using the local surface normal at the point of intersection to calculate the grazing angle. The speed of execution can again be increased by the use of bounding volumes to minimise the number of intersection tests performed.

Figure 4.5 illustrates the simulation of a sonar image incorporating a cylindrical object representing a pipeline. The input seabed is the fractal sand ripples of figure 4.3(a), and the cylinder is of 0.4m radius positioned at a horizontal range of 20m from the towfish. The simulated image illustrates the higher intensity reflections from the face of the pipeline orientated towards the transducer and the effect of reflections from the pipeline and the seabed occurring at the same instant of time resulting in the higher intensity return. The shadow zone behind the cylinder is determined both by the shape of the cylinder and the topography of the seafloor, as the shadow is influenced by the sand ripples.

The pipe is suspended by the crests of the sand ripples, and at the troughs of the sand ripples the pipe is unsupported by the seabed and a span is formed underneath the pipe. When the pipe is supported by the seabed the shadow is attached to the image of the pipe, but at the troughs where the spans occur, the shadow is located at a distance from the pipe determined by the height of the span.

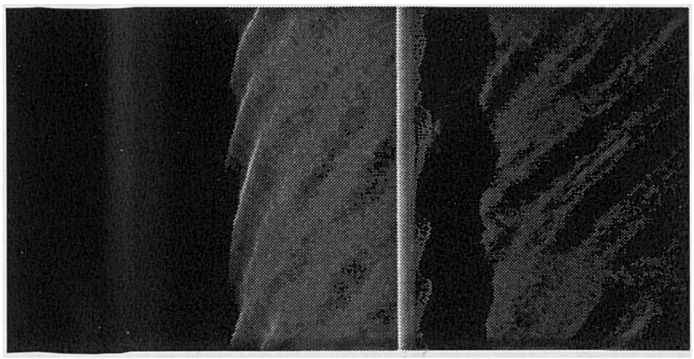

Figure 4.5: Simulated sonar image of pipe on sand ripples

The simulated sonar image of the pipeline and the resulting shadow is uncharacteristically sharp and clear. This is attributed to the calculation of only the backscattered energy and the neglect of the complex scattering effects occurring in the region of the pipe. These effects, and their incorporation into the model, will be investigated in the following section.

4.5 Multiple Reflections

The pulse of acoustic energy transmitted through the water column is scattered in all directions upon interaction with an object or the seabed. The amount of energy scattered in each direction is dependent on the seabed roughness. Up to now the simulation program has calculated only the diffuse energy backscattered along a path identical to the incident ray path. This was a reasonable assumption in the original development of the simulation when the seabed was assumed to be flat, as the energy scattered in the other directions was transmitted away from the transducer and would not have influenced the

sonar image created. With the extension of the simulation model to include objects and more realistic representations of the seafloor topography, some of the energy scattered in the other directions may then be reflected back towards the transducer by other parts of the scene. Therefore the multiple paths of the rays must be incorporated into the the simulation as they influence the sonar image.

4.5.1 Specular Reflection

The acoustic energy scattered from a rough surface is composed of a diffuse field scattered in all directions and a coherent field reflected in the specular direction. The relative magnitudes of the two fields are dependent on the surface roughness; a subjective term which in turn is dependent on the frequency and the angle of the incident energy.

The simulation model previously has considered only the portion of the diffuse energy backscattered to the transducer. The principal direction of the reflected energy tends to be in the specular direction, where the angle of reflection is equal to the angle of incidence. To model this effect, instead of effectively terminating the ray on intersection of the seabed, the ray is traced in the specular direction from the point of intersection, to determine if it interacts with another part of the scene. If this specular ray does intersect an object, or another part of the seafloor, the diffuse energy from this intersection, scattered back to the transducer, will then be calculated.

The reflection loss of the specular ray reflected from the seafloor can be approximated from the Rayleigh formula for the reflection of sound at a plane boundary between two fluids [110]. For a plane wave incident, at a grazing angle θ, upon a boundary between two fluids with densities ρ_1 and ρ_2 and velocities c_1 and c_2, as indicated in figure 4.6, the intensity of the reflected wave I_r is related to the intensity of the incident wave I_i by equation 4.3,

$$\frac{I_r}{I_i} = \left[\frac{m \sin\theta - \sqrt{n^2 - \cos^2\theta}}{m \sin\theta + \sqrt{n^2 - \cos^2\theta}} \right]^2 \tag{4.3}$$

where m is the ratio of the density of the sediment to the density of the water and n is the refractive index or the ratio of the velocity in the water column to the velocity in the sediment, as denoted by the notation of Brekhovskikh [111]. A similar expression can also be derived, in terms of the grazing angle and the ratios m and n, for the energy transmitted into the sediment.

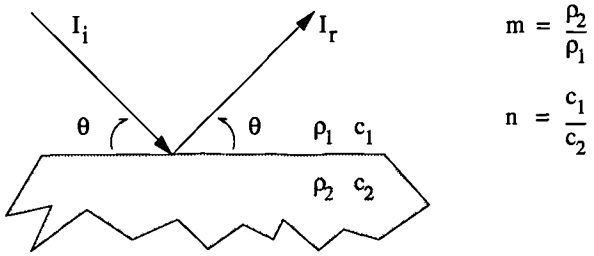

Figure 4.6: Reflection of wave at a plane boundary

The reflection loss is calculated as the logarithmic expression of equation 4.3, $10 \log \frac{I_r}{I_i} dB$, and is a function of the grazing angle and the properties of the sediment-water interface. The above formula has neglected the absorptive effects which are inherent in all sea bottom materials. From experimental measurements, Hamilton [112] has related the attenuation loss of compressional waves in marine sediments to the frequency of the incident wave by the expression of equation 4.4,

$$\alpha_s = kf^n \tag{4.4}$$

where α_s is in decibels per metre, f is the frequency in kilohertz and k and n are empirical constants. The value of n has been determined to be approximately unity for most soft sediments and k is dependent on the porosity and is approximately equal to 0.5 in the porosity range 35-60%. To incorporate the absorption of the sediment into equation 4.3,

the refractive index is replaced by a complex value to model the losses in the sediment. The reflection loss is plotted against the grazing angle in figure 4.7 for the reflection of a plane wave at a water-sand boundary. At grazing angles greater than the critical angle transmission of the acoustic energy into the sediment occurs. The graph illustrates the effect of including the sediment absorption which eliminates the sharp changes occurring at the critical angle, due to the leakage of energy into the sediment.

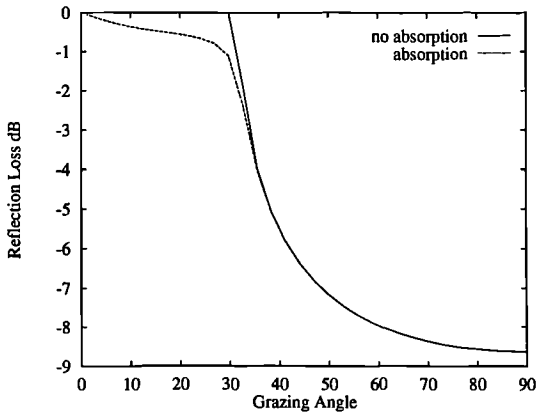

Figure 4.7: Reflection loss at a water-sand boundary

The value for the specularly transmitted energy calculated by this method is only an approximation, as this has neglected the scattering of the acoustic energy due to the assumption of a planar boundary. An alternative method for calculating the energy scattered and reflected at a rough interface will be presented in section 4.6.

4.5.2 Backscatter from Multi-Path

The amount of energy scattered back to the transducer from the subsequent interactions of the ray with the scene must be determined. The procedure to calculate the energy contributions from the multi-paths can be explained by consideration of the schematic diagram of figure 4.8, which represents the scene described previously in section 4.4, of a pipe on a rough seabed.

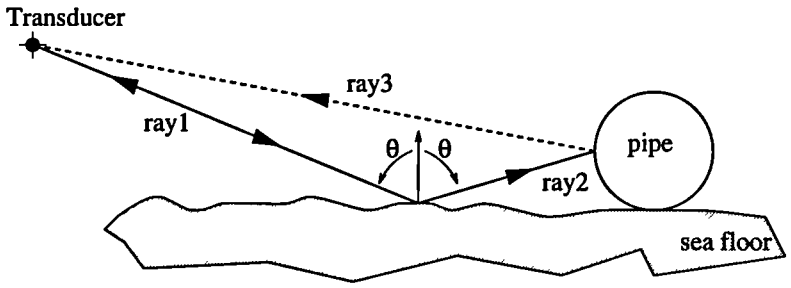

Figure 4.8: Multiple reflections from object

The original ray traced from the transducer, ray_1, has intersected the seabed and the diffuse energy backscattered along the same ray path is calculated using Lambert's Law. This energy is returned to the transducer at a time dependent on the length of the ray path and the velocity of sound. The ray is then traced from the point of intersection in the specular direction to determine if it intersects another part of the scene. The energy reflected in the specular direction, where the reflected angle is equal to the local angle of incidence, is calculated from the Rayleigh reflection formula expressed by equation 4.3. In the situation illustrated, the specular ray, ray_2 intersects the pipe, and the diffuse energy scattered back in the direction of the transducer, along ray path ray_3, is calculated from Lambert's Law. This energy is returned at a time dependent on the total path length of the ray, calculated from the sum of the lengths of ray_1, ray_2 and ray_3. The diffusely reflected ray traced back to the transducer is tested to ensure that its path is not impeded by another object in the scene, which would prevent the reception of the energy by the transducer. The whole procedure can be repeated iteratively for each ray to trace any number of specular reflections and intersections for the one original ray.

4.5.3 Results

The simulated sonar images of figures 4.2, 4.3 and 4.4 traced the single backscattered rays only. This does not noticeably degrade the images, as the majority of the forward reflected rays would have exited the scene without intersecting another part of the

seabed. In figure 4.5, with the incorporation of the pipeline, the effects of the ray multi-paths must be considered and figure 4.9 simulates the identical scene but the multi-paths are also traced, although the across track range of image 4.9 has been altered slightly to illustrate more of the detail.

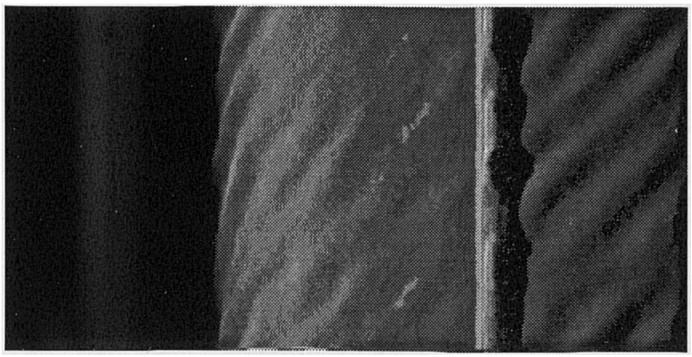

Figure 4.9: Pipeline on sand ripples with multi-paths of rays traced

On comparison of the two images, figures 4.5 and 4.9, several differences can be noted around the cylinder, which represents the pipeline, as a result of tracing the multiple paths of the rays. The forward reflected energy, which has subsequently been reflected from the pipeline, has resulted in a faint second reflection of the pipe particularly in the areas of the seabed spanned by the pipe. The effects of the multiple reflections are most apparent in the region surrounding the pipe, due to the complex scattering of the acoustic energy between the pipe and the seabed.

Another simulated sonar image of a pipeline is illustrated in figure 4.10. The pipeline again has a slight span underneath it, as can be noted from the detachment of the shadow from the pipeline image and the slight multiple reflection of the pipe. The pipeline is of 0.3m radius and is situated at a horizontal range of 20m from a 100KHz transducer towed at 10m above the seabed.

More complex objects can also be created by the combination of the mathematical primitives described in section 4.4. Figure 4.11(a) illustrates a schematic diagram of a tethered mine constructed from three cylinders with the dimensions shown. This mine has

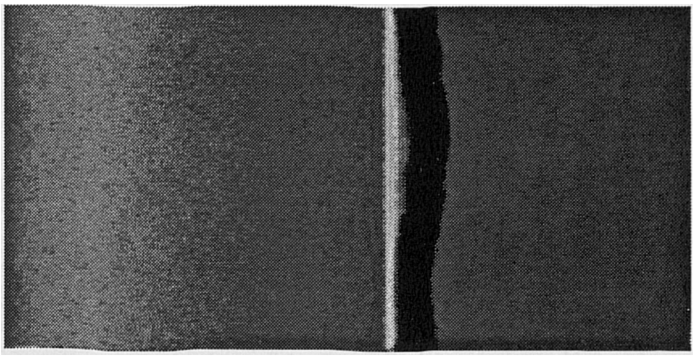

Figure 4.10: Pipe on seabed with unsupported span

then been ensonified at a range of 32m, by a transducer flown at a constant height of 10m.

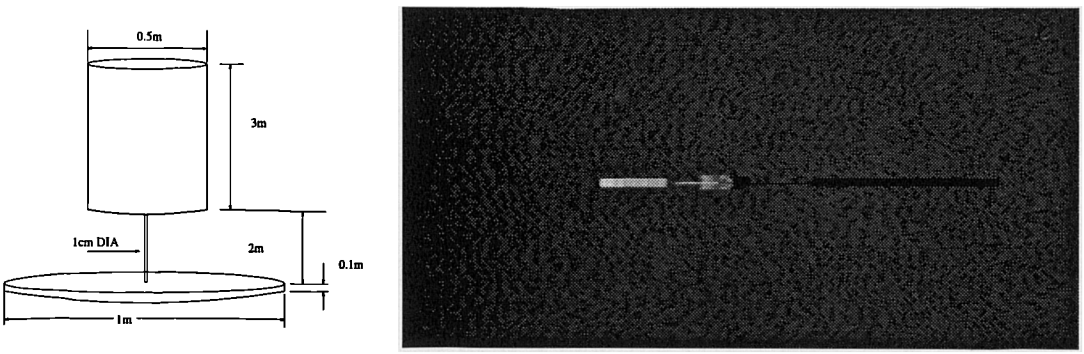

Figure 4.11: (a) Schematic diagram (b) Simulated sonar image of tethered mine

4.5.4 Number of Significant Multi-Paths

The process of tracing the specular ray from each intersection can be repeated iteratively for any number of reflections. For the majority of the rays traced, the specular ray will eventually exit the scene, and will effectively terminate. For the remaining set of rays which remain within the scene, the iterative process requires to be artificially terminated at some stage. The number of multi-paths and the energy contributed by each reflection will therefore be investigated.

Using the scene described in section 4.4, of a pipeline on sand ripples, and considering only one line of the image, figure 4.12(a) plots the percentage of the rays

intersecting the scene a given number of times. The majority of the rays (82%) emitted by the transducer intersect the scene only once, as the specular rays traced from the first intersection point exit the scene without intersecting it again. The majority of the multiple reflections which do occur arise as a result of reflections from the pipe. On removing the pipe from the scene, over 95% of the rays exit the scene after the first reflection from the seabed, and the remainder of the rays exit after the second reflection.

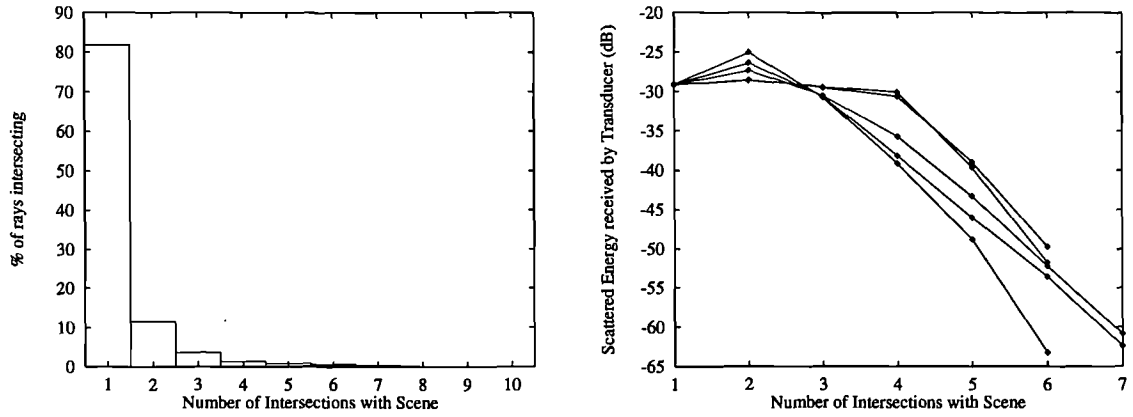

Figure 4.12: (a) Number of ray reflections within scene (b) Energy scattered at each intersection for 5 sample rays

The relative magnitude of the energy contributions received by the transducer for the rays which do interact with the scene several times can be illustrated in figure 4.12(b). This graph illustrates for five rays the energy scattered back to the transducer at each of the points of intersection of the ray with the scene. The energy received by the transducer after five reflections has fallen on average by greater than 20dB from the initial value of the energy backscattered at the first reflection. The energy received by the transducer from subsequent reflections of that ray will have a minimal effect on the output sidescan sonar image. The above graphs have illustrated the problem for the most extreme of the images illustrated in this chapter, as this scene has the largest range of height values for the seabed and the pipe introduces a large reflecting facet. In the generation of the other images the multiple reflection paths of the rays had a lesser effect on the simulated images.

In order to minimise the introduction of errors the sonar simulation program terminates the tracing of the ray once the intensity of the specular ray has decreased by more than 40dB. The scattered energy contributions from this ray therefore have a negligible effect on the image. As discussed above, the majority of rays have already exited the scene by the time the energy contributions have decreased by this amount.

4.6 Seabed Reverberation

The sonar simulation model has used Lambert's law to calculate the diffuse backscatter from the seabed. This simple empirical law has provided a reasonable comparison to experimental data only over a very limited range of shallow grazing angles [48] [49] [50], and appears to be valid for calculating the scattering from rough surfaces only where the scattering is independent of frequency. Although Lambert's law can be used to provide a satisfactory initial estimate of the scattering it should be more correctly regarded as an empirical *rule*.

Lambert's law can also only be used to calculate diffuse scattering and cannot be applied to provide an estimate of the forward scattering in the specular direction. To combat this problem, the sonar simulation model obtains a value for the forward specular reflection from the Rayleigh reflection coefficient, equation 4.3. The Rayleigh coefficient assumes a totally flat interface between the two fluid media, and hence provides only an approximation for the scattering at a rough boundary.

A model is therefore required to determine the reverberation from a rough seabed. This model must have the capability to calculate the scattering from the seabed in any direction, as required by the sonar simulation model. The model must also be valid over the full range of grazing angles, as opposed to Lambert's Law which is valid for a limited range of shallow grazing angles only.

As discussed in chapter two, several solutions to the problem of calculating the scattering at a random rough interface have been formulated as solutions to the wave equation with the appropriate boundary conditions. The two main types of solution are the small roughness perturbation approximation and the Kirchhoff approximation. Both of these techniques have limited domains of validity dependent on the approximations applied in the derivation of their solutions. The Kirchhoff and perturbation theories have been applied to several problems describing the scattering from the seabed, as has the composite roughness technique. The composite roughness technique is formed by the combination of the two techniques to account for the scattering from both large and small scale irregularities, by avoiding the shortcomings of the individual theories. Jackson [65] has developed a composite roughness model to describe the high frequency backscattering from the seabed which has found widespread application. This model, although valid over all grazing angles, cannot provide the specular reflection required by the sonar simulation model. Jackson has extended the backscatter model to calculate the bistatic scattering from the seabed [71] and the sonar simulation model will apply this bistatic model developed by Jackson to the scattering problem inherent in the simulation. Other bistatic models have also been proposed, most notably those by Caruthers & Novarini [69] and Ellis & Crowe [70]. These provide corrections to Lambert's law in the specular direction, but are unsuitable for this application as they are valid only at low frequencies. The model developed by Jackson is valid at the high frequencies required for sidescan sonar simulation and provides a model with a physical basis which has compared favourably to experimental data from several sites.

4.6.1 The Bistatic Scattering Model

The bistatic scattering model implemented in the simulation model was developed at the Applied Physics Laboratory at the University of Washington (APL-UW) by Jackson [71] to calculate the high frequency scattering from a rough seabed. The bistatic

model is an extension to earlier backscatter models proposed by Jackson [65] [66], which have compared favourably to experimental data gathered at seven well characterised sites [65] [66] [68]. Preliminary tests have also been performed on the bistatic model using data gathered off the coast of Florida [72]. The bistatic model, and the equations which characterise it, will be briefly explained prior to discussion of the inclusion of the bistatic model into the sonar simulation model.

The bistatic scattering model is composed of two terms to model the scattering due to the interface roughness and the scattering from volume inhomogeneities in the sediment. The output of the model is expressed in terms of the bistatic scattering strength $S_b(\theta_s, \phi_{s,}\theta_i)$ as stated in equation 4.5, where $\sigma_{br}(\theta_s, \phi_s, \theta_i)$ and $\sigma_{bv}(\theta_s, \phi_s, \theta_i)$ are the roughness and volume scattering cross sections per unit area. At the higher frequencies of interest, 10-100KHz, the acoustic penetration of the seabed is minimal and the volume scattering can be described as a surface process and quantified by the effective cross section, σ_{bv}.

$$S_b(\theta_s, \phi_s, \theta_i) = 10\log_{10}[\sigma_{br}(\theta_s, \phi_s, \theta_i) + \sigma_{bv}(\theta_s, \phi_s, \theta_i)] \tag{4.5}$$

Within this expression the incident grazing angle is defined as θ_i, θ_s is the scattering grazing angle and ϕ_s is the bistatic angle, defined as the difference in azimuth between the incident and scattered directions. Dimensionless geometric parameters derived from these angles are used in the calculation of the scattering cross sections. These parameters, Δ_t and Δ_z, expressed in equations 4.6 and 4.7, are proportional to the transverse and vertical components of the change of the acoustic wave vector upon scattering.

$$\Delta_t = \frac{1}{2}(\cos^2\theta_i - 2\cos\theta_i\cos\theta_s\cos\phi_s + \cos^2\theta_s)^{1/2} \tag{4.6}$$

$$\Delta_z = \frac{1}{2}(\sin\theta_i + \sin\theta_s) \tag{4.7}$$

The magnitude of the change of the acoustic wave vector is denoted by Δ, defined in equation 4.8.

$$\Delta = \sqrt{\Delta_t^2 + \Delta_z^2} \tag{4.8}$$

The model assumes that the sediment can be treated as a lossy fluid, and the effects of elasticity are neglected. The sediment can therefore be characterised in relation to the water column by three dimensionless parameters: the mass density ratio, the sound speed ratio and the loss parameter. These parameters, in addition to the other input parameters for the model, are summarised in table 4.1. The bottom relief is modelled as a Gaussian process with an isotropic spectrum obeying the simple power law discussed in section 4.2. This fractal random process is characterised by the two dimensional roughness spectral density, $W(K)$, expressed in equation 4.9,

$$W(K) = \frac{w_2}{(h_0 K)^{\gamma_2}} \tag{4.9}$$

where K is the magnitude of the two dimensional wave vector. The spectral strength, w_2, has dimensions of $(length)^4$, and the parameter h_0 is a reference length employed to balance the units to maintain the dimensions of w_2 independent from the value of the spectral exponent, γ_2.

The scattering due to the interface roughness is treated by two different approximations. In a manner analogous to the original backscatter model [65], where the Kirchhoff approximation was used to calculate the scattering cross section near normal incidence, the Kirchhoff approximation is employed to calculate the scattering cross section in the near specular direction for the bistatic model. The small roughness perturbation approximation is used to calculate the scattering cross section in all other directions. The roughness scattering cross section $\sigma_{br}(\theta_s, \phi_s, \theta_i)$, is formed by the smooth interpolation between the two techniques.

Parameter			Value	
Symbol	Definition	Short Name	Sand	Silt
ρ	Ratio of sediment mass density to water mass density	Density ratio	1.94	1.15
v	Ratio of sediment sound speed to water sound speed	Sound speed ratio	1.113	0.987
δ	Ratio of imaginary wavenumber to real wavenumber for the sediment	Loss parameter	0.0115	0.00386
γ_2	Exponent of bottom relief spectrum	Spectral exponent	3.67	3.25
w_2	Strength of bottom relief spectrum (cm^4) at wavenumber $\frac{2\pi}{\lambda} = 1cm^{-1}$	Spectral strength	0.00422	0.000518
γ_3	Exponent of sediment inhomogeneity spectrum	Inhomogeneity exponent	3.0	3.0
w_3	Strength of sediment inhomogeneity spectrum (cm^3) at wavenumber $\frac{2\pi}{\lambda} = 1cm^{-1}$	Inhomogeneity strength	0.000127	0.000306
μ	Ratio of compressibility to density fluctuations in the sediment	Fluctuation ratio	-1	-1

Table 4.1: Input parameters for bistatic model

The bistatic Kirchhoff cross section is expressed in equation 4.10, where $J_0(u)$ is the zeroth order Bessel function and k is the acoustic wavenumber of the signal in the water.

$$\sigma_{kr}(\theta_s, \phi_s, \theta_i) = \frac{|R(\theta_{is})|^2}{8\pi}\left[\frac{\Delta^2}{\Delta_z \Delta_t}\right]^2 \int_0^\infty e^{-qu^{2\alpha}} J_0(u) u du \tag{4.10}$$

Within equation 4.10 the parameter q is defined as

$$q = 2k^2\Delta_z^2 C_h^2 (2k\Delta_t)^{-2\alpha} \tag{4.11}$$

The parameters α and C_h are roughness structure parameters related to the spectral

strength and spectral exponent of the bottom relief.

$$\alpha = \frac{\gamma_2}{2} - 1 \tag{4.12}$$

$$C_h^2 = \frac{2\pi w_2 \Gamma(2-\alpha) 2^{-2\alpha}}{h_0^{\gamma_2} \alpha(1-\alpha)\Gamma(1+\alpha)} \tag{4.13}$$

$R(\theta_{is})$ is the complex plane wave reflection coefficient, or Rayleigh coefficient, for a flat boundary between the water column and the sediment layer, as previously discussed in section 4.5.1. The Rayleigh coefficient is evaluated at the angle $\theta_{is} = \sin^{-1}\Delta$, which is the grazing angle at which specular reflection between the transmitter and receiver occurs. For the configuration of a sidescan sonar, where the transmitter and receiver are located at the same position this is the angle at which normal incidence occurs.

The scattering cross section determined by the application of bistatic perturbation theory is stated in equation 4.14,

$$\sigma_{pr}(\theta_s, \phi_s, \theta_i) = \frac{1}{4} k^4 |1 + R(\theta_i)|^2 |1 + R(\theta_s)|^2 |G|^2 W(2k\Delta_t) \tag{4.14}$$

where G is the complex function expressed in equation 4.15.

$$G = \left[\frac{1}{\rho} - 1\right]\left[\cos\theta_i \cos\theta_s \cos\phi_s - \frac{P(\theta_i)P(\theta_s)}{\rho}\right] + 1 - \frac{\kappa^2}{\rho} \tag{4.15}$$

The formulation uses the complex reflection coefficient and the roughness spectral density which were defined previously. Also required is the value κ, which is defined as the complex wavenumber in the sediment divided by the real wavenumber in water, and the complex coefficient $P(\theta)$ which is defined in equation 4.16.

$$P(\theta) = \sqrt{\kappa^2 - \cos^2\theta} \tag{4.16}$$

The volume scattering cross section is calculated from a technique based on perturbation theory. The sediment volume is assumed to contain no gradients only the random fluctuations caused by variations in the density and compressibility produced by the biological and hydrodynamical manipulation of the sediment. The density fluctuation in the sediment due to these inhomogeneities is expressed in the power law form of equation 4.17.

$$W_{\rho\rho}(k) = \frac{w_3}{(h_0 k)^{\gamma_3}} \tag{4.17}$$

The compressibility fluctuations are treated analogously and are assumed to be proportional to the density fluctuations. The spectrum of the compressibility fluctuations is related to the density spectrum by equation 4.18. The selection of the value of -1 for the fluctuation ratio, μ, in table 4.1 amounts to the assumption that the fractional fluctuations in density and compressibility are equal and opposite.

$$W_{KK} = \mu^2 W_{\rho\rho} \tag{4.18}$$

The effective bistatic scattering cross section at the interface, σ_{bv}, due to inhomogeneities in the sediment is related to the sediment volume scattering cross section σ_v, by equation 4.19.

$$\sigma_{bv}(\theta_s, \phi_s, \theta_i) = \frac{\sigma_v \left| 1 + R(\theta_i) \right|^2 \left| 1 + R(\theta_s) \right|^2}{2k^2 \rho^2 \operatorname{Im}\left[P(\theta_i) + P(\theta_s) \right]} \tag{4.19}$$

The volume scattering cross section is determined from perturbation theory and stated in equation 4.20.

$$\sigma_v = \frac{\pi}{2} k^4 \left| \mu\kappa^2 + \cos\theta_i \cos\theta_s \cos\phi_s - P(\theta_i) P(\theta_s) \right|^2 W_{\rho\rho}(\Delta k) \tag{4.20}$$

The spectrum of the density fluctuations in the sediment $W_{\rho\rho}$ is evaluated at the Bragg wavenumber for volume scattering, which is defined by the sediment as the magnitude of the difference between the real parts of the incident and scattered three dimensional wave vectors, equation 4.21.

$$\Delta k = k\left[4\Delta_t^2 + (\mathrm{Re}(P(\theta_i) + P(\theta_s)))^2\right]^{1/2} \tag{4.21}$$

These equations characterise the bistatic scattering strength model and further details of the development of the bistatic model can be obtained from [71] [65] [66]. The application of this model provides a more physically correct basis for the calculation of the scattering at a rough interface and includes the effects of both the interface scattering and the sediment volume scattering.

4.6.2 Inclusion of Bistatic Scattering Model

The bistatic scattering strength model uses the above detailed equations to calculate the scattering, in any direction, from a rough surface. The inclusion of this bistatic model into the sonar simulation model was based on the structure detailed in section 4.3 for determining the intersection of a ray with a rough seabed. For each ray emitted the point of intersection with a triangular plane of the height field was calculated. At this point of intersection on the plane, the scattering is calculated by the bistatic model developed by Jackson. Jackson's model includes the roughness of the sediment on this plane with the two dimensional roughness spectrum.

The energy backscattered to the transducer along an identical ray path to the original ray is calculated by the effective reduction of the bistatic model to the simpler backscatter case. For this case the incident grazing angle, θ_i, is equal to the scattered grazing angle, θ_s and the bistatic angle, ϕ_s is 180° as the scattered ray remains within the same plane as the incident ray, but is travelling in the opposite direction. The local

surface normal to the intersected plane is used to calculate the grazing angle. Therefore, the influence of the larger scale seabed topography on the scattering is also included.

The calculation of the multiple reflection paths also requires the level of energy scattered in the specular direction. This can be calculated from Jackson's model with the incident grazing angle equal to the scattered grazing angle, but the bistatic angle, ϕ_s is now equal to zero degrees. The local surface normal of the intersected facet is again used to determine the local incident grazing angle. The subsequent diffuse scattering from the intersection of the specular ray with another part of the scene, requires the calculation of the energy scattered towards the transducer. The direction of scattering will not be the simple backscatter situation, but will be dependent on the geometry of the scene. The ray is assumed to remain within the original plane and ϕ_s is set to zero, but the scattered grazing angle can be in the range from 0 to 180°.

The bistatic model assumes the sediment to be a lossy fluid and suitable input parameters for the model to represent sand and silt seabeds are listed in table 4.1. The simulation model uses the direct implementation of the equations of section 4.6.1 for the bistatic model developed by Jackson to calculate the scattering cross section. The integral equations for the Kirchhoff approximation are solved by the application of numerical techniques [27]. The selection of the Kirchhoff or perturbation technique to calculate the interface scattering is dependent on the scattering angle. The specular reflection is always calculated with the Kirchhoff technique, but the choice of technique for the backscatter case is dependent on the incident grazing angle; the Kirchhoff method is employed if the ray is at near normal incidence, and the perturbation technique elsewhere. The interpolation point between the two methods is dependent on the sediment type.

4.6.3 Results

The output of the bistatic scattering model will be considered prior to the discussion of the results obtained by the inclusion of the scattering model into the sonar

simulation model. The backscatter results derived from the bistatic model will be considered initially to allow direct comparison to Lambert's Law, and then the bistatic scattering results including the specular reflection will be presented.

Figure 4.13(a) plots the backscatter strength as a function of the grazing angle for a medium coarse sand seabed, where *total* is the total backscattering strength formed as the sum of the roughness and volume scattering. The relative contributions of the roughness and volume scattering are dependent on the sediment type, with roughness scattering dominating with coarser sediments, such as sand, and volume scattering acting as the dominant mechanism for softer sediments, such as silt.

The backscatter output is then compared to Lambert's Law for the same medium sand seabed, figure 4.13(b). Lambert's law provides a reasonable fit to the scattering strength only over a limited range of angles. As the grazing angle increases towards normal incidence, the differences between the two models become apparent. Jackson's backscatter model has compared well to seabed reverberation data in this region and provides a more accurate backscatter model.

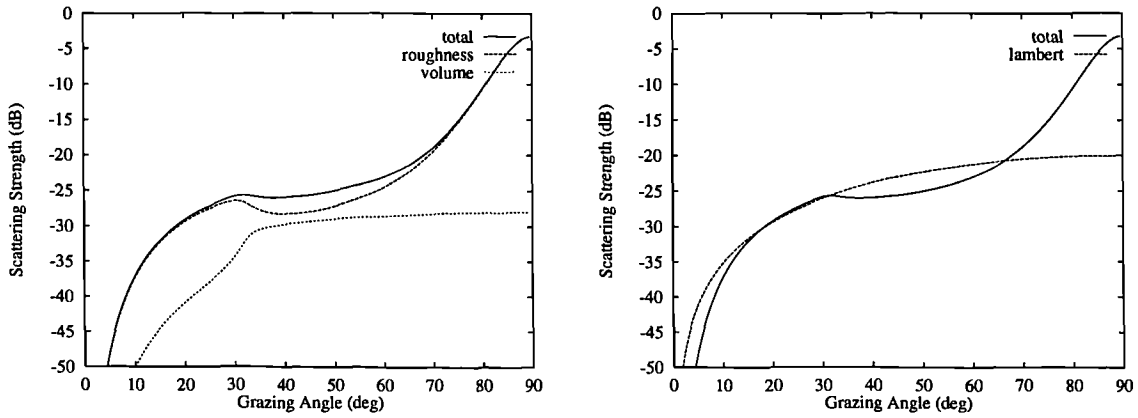

Figure 4.13: (a) Relative contributions to total backscatter (b) Comparison of backscatter to Lambert's Law

To provide an example of the bistatic scattering strength, figure 4.14(a) plots the scattering strength against the scattering angle, θ_s, for a fixed incident grazing angle of

50°. The scattering is calculated within the incident azimuthal plane for a medium coarse sand sediment. A strong scattering lobe exists in the forward specular direction. The width of the lobe affects the scattering strength at the surrounding angles and the comparison to Lambert's law is only valid over a small range of backscatter directions and not for the forward scattered energy. The effect of the sediment type on the specular lobe can also be illustrated, where figure 4.14(b) displays the scattering strength for a silty seabed. The scattering in this case is dominated by the sediment volume scattering except near the specular peak where interface scattering dominates.

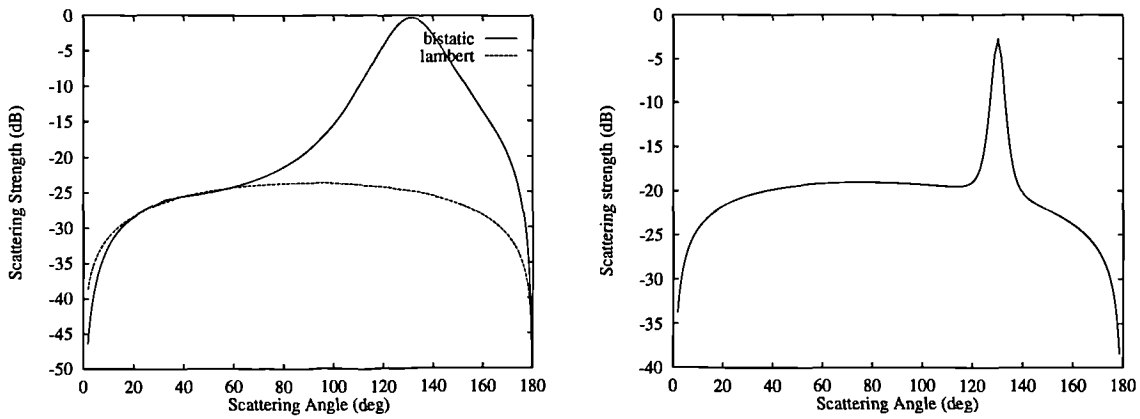

Figure 4.14: (a) Scattering from a sand seabed (b) Scattering from a silt seabed

The results of the inclusion of the bistatic scattering strength model into the sonar simulation model can also be illustrated. Figure 4.15(a) plots as an 'A' scan, of intensity versus time, the monostatic backscattered reverberation from a totally flat seabed, calculated using both Lambert's Law and Jackson's scattering model. Jackson's model predicts a higher backscattering strength than Lambert's Law for the seabed closest to the towfish, where the rays incline on seabed at near normal incidence. The difference between the two models becomes less apparent with range, as the grazing angle reduces. These effects are predicted in the backscattering strength plots of figure 4.13(b).

Figure 4.15(a) illustrates the effect of the scattering model for the simplified case of a totally flat seabed. The scattering from a rough seabed is illustrated in figure 4.15(b) in

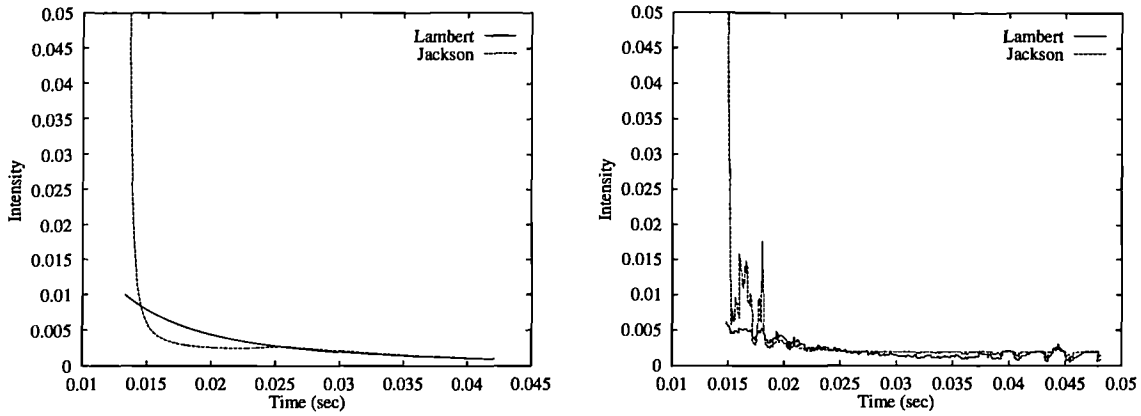

Figure 4.15: (a) Scattering from a flat seabed (b) Scattering from a rough seabed

the form of an 'A' scan, with the monostatic backscatter calculated by the two models for one line of the image representing the sand ripples on the seabed displayed in figure 4.3(a). The grazing angle no longer decreases with range due to the rough seafloor and differences occur between the two models over all ranges, particularly in areas with facets orientated towards the transducer giving rise to greater backscattered energy. The main difference between the two models again occurs in the area closest to the towfish, due to the higher backscattered strength predicted by Jackson's model for this area where the reflection is partially specular.

The effect of the scattering model can also be noted on the simulated sidescan sonar images of the rough seabed used to generate the 'A' scans of figure 4.15(b). The sonar image in figure 4.16(a) was simulated using Lambert's Law to calculate the backscatter, whereas figure 4.16(b) employed Jackson's model to calculate the scattering. In both cases the seabed was assumed to be constructed of a medium coarse sand. The application of Jackson's model calculates higher levels of energy backscattered from the seabed closest to the towfish and results in higher intensity levels for the greyscale values of the pixels in this initial part of the image. The use of Lambert's law resulted in a more even greyscale tone across the image as less of contrast between the highest and lowest intensity existed, as can be observed in the sample 'A' scans of this scene.

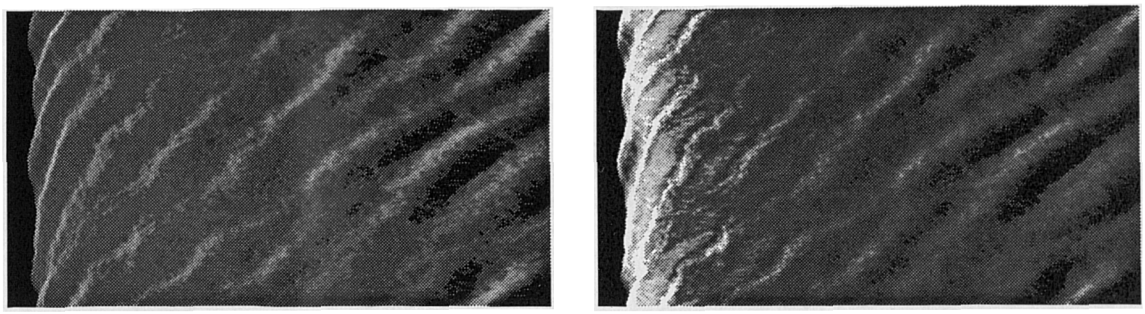

Figure 4.16: (a) Scattering calculated using Lambert's Law (b) Scattering calculated using Jackson's model

4.6.4 Limitations of Scattering Model

The scattering model discussed represents the seabed as a fluid without layering or gradients. The interface between the seabed and the water column is therefore modelled as the boundary between two fluid media. This approximation is suitable for calculating the scattering from sediments such as sand, silt or clay.

The modelling of the sediment as a fluid results in the calculation of only the longitudinal compressional waves in the sediment. In solid media, another type of wave is also supported due to the elasticity of the material and the solid sustains transverse shear waves in addition to the compressional waves [47].

At the high frequencies used in the model, there is only a slight penetration of the sediment due to the high attenuation of the acoustic waves. The penetration is accounted for by the scattering from the volume inhomogeneities close to the interface. The model therefore assumes that the sound does not penetrate to the depths of the underlying basement rock which would be capable of supporting shear waves.

The upper regions of the sediments, with which the acoustic wave interacts, tend to be water filled and tenuous [66]. The generation of shear waves within this region is minimal and it is a reasonable assumption to model only the compressional waves. The scattering model, though, is incapable of representing the scattering from exposed regions of

basement rock or other solid materials. At present the simulation model reverts to the assumption of Lambert's law to approximate the scattering from the solid media, as both techniques produce an approximation to the actual scattering and Lambert's Law is the simpler of the two techniques to implement.

A further assumption of the model is that all the scattering remains within the plane of the incident ray. In reality the acoustic energy will be scattered in all directions, although the principle method by which energy is returned to the transducer is by the monostatic backscatter from the seabed. The main direction in which energy is scattered away from the transducer is the forward specular direction within the plane. The calculation of the in-plane scattering can therefore be regarded as a reasonable approximation.

4.7 Conclusions

This chapter has extended the model to remove the flat seabed assumptions of chapter three. The sonar simulation model now has the capability to model complex seabed topographies through the application of fractal models. Fractal models provide a simple relation between the power spectral density and the frequency of the surface roughness. The use of this relationship to produce quantitative models of the seabed has been experimentally verified for roughness scales from a few centimetres up to several kilometres and provides a simple stochastic representation of the seabed topography.

The complex seabeds created by this method were converted into height fields of the terrain to permit the calculation of the interaction of the acoustic rays with the seabed. The technique of ray tracing with height fields permits the simulation of sidescan sonar images of any seabed structure, including composite images containing more than one seabed structure or sediment type.

The technique of tracing the acoustic rays to their intersection with the seabed was extended to include mathematically defined objects on the seabed or in the water column.

This provides a more general simulation model capable of synthesising sidescan sonar images containing man-made structures such as pipelines or mines.

With the introduction of the large scale topographic features and objects the modelling of the scattering of the acoustic energy at the point of intersection, required to be expanded as it was no longer appropriate to consider only the backscattered energy. Therefore the energy reflected to other parts of the scene and then scattered towards the transducer was included into the simulation. This resulted in the tracing of multiple reflection paths for the one incident ray.

The extension of the scattering to include multiple reflections highlighted the limitations of modelling the scattering with the empirical approximation of Lambert's Law. A bistatic scattering model developed by Jackson was incorporated into the simulation model. The bistatic model is based on the solution of the wave equation at random rough boundaries, and as such has a more physically correct basis than Lambert's Law. The model is also valid over all grazing angles and incorporates the specular scattering lobe.

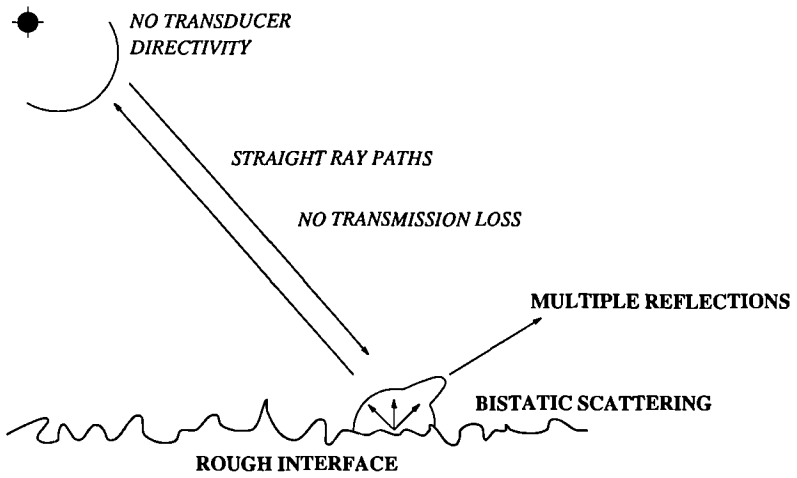

Figure 4.17: Summary of the simulation model

The current status of the model is summarised in figure 4.17, which illustrates the extensions of the model from the simplified structure proposed in chapter three. In summary, this chapter has presented techniques to permit the inclusion of the seabed

topography and the sediment roughness into the simulation model and has incorporated a scattering model with a stronger physical basis. The simulation model still assumes an isovelocity water medium, in which the acoustic energy traverses without incurring transmission losses, and uniform transducer characteristics. The extension of the model to remove these assumptions will be considered in the following chapters.

Chapter 5

Acoustic Propagation and Transmission Losses

5.1 Introduction

The effect of the water medium on the sidescan sonar process has been ignored in the development of the sonar simulation model described in the preceding chapters. The model has previously assumed that the rays followed totally straight line paths from the transducer to the seabed and that they incurred no loss of energy as they propagated through the water.

Neither of these assumptions are valid as a result of the complex characteristics of the water environment and in particular, the effect of the varying velocity of sound with propagation. Environmental models for the water medium were presented in chapter 2, in addition to the discussion of models to represent the propagation of acoustic energy through this complex environment.

The water column has two principal effects on the propagation of acoustic energy, as it influences both the direction of propagation and the losses incurred during propagation. This chapter will discuss the inclusion of a ray based propagation model into the sidescan sonar simulation model, to determine the actual path of the propagation and calculate the losses encountered during the transmission. The relative importance of these effects on the signal returned to the sidescan sonar will be discussed and results presented for the typical underwater environment encountered off the coast of Britain.

Finally, the chapter will consider other sources of loss and distortion of the signal which have not yet been incorporated into the structure of the sidescan sonar simulation model. The effects of these losses, and the justification for their omission at present, will also be considered.

5.2 Acoustic Propagation

The velocity of sound is one of the main physical properties of the water medium which influences the propagation of acoustic energy. The velocity of sound in water is not a constant as assumed in earlier chapters, but is a function of temperature, salinity and pressure. These three parameters vary with factors such as the geographic location, weather, season and time of day. Several empirical relationships have been formulated to quantify the relationship between these parameters and the velocity of sound, as discussed in section 2.3.

The propagation of acoustic energy in the water is described by the wave equation, which is stated in chapter two as equation 2.2. This is a partial differential equation relating the space and time derivatives of the acoustic parameters which describe the wave motion. No direct and general solution to the wave equation exists as a result of the variations in velocity and other complex features of the underwater environment and its boundaries. Instead several different types of solution have evolved for use with different environmental conditions, frequencies and transmission ranges. Each of the solutions is valid for a range of conditions dependent on the simplifying assumptions adopted in their development. The range of propagation models developed includes ray models, normal mode techniques, parabolic equation solutions, finite element methods and fast field solutions. The underlying principles of each of these techniques for calculating the propagation of the acoustic field were discussed in chapter two. The relative advantages and disadvantages in the application of each of the techniques were also highlighted.

The simulation model will apply a ray model to calculate the propagation of the acoustic energy through the water column. The principle motivation for the use of this type of model is its applicability to high frequency problems, as the sonar simulation model is typically synthesising high resolution sidescan sonars with operating frequencies of 100KHz and above. In addition, the ray model provides a simple, intuitive representation of the acoustic field which can be easily incorporated into the structure for the model proposed in the preceding chapters. The range dependence of the seabed topography can also be included in the ray tracing technique. The limitations of the wave based propagation models which precludes their use for this application were discussed in chapter two. These models tend to be more suited to low frequency, long range propagation problems.

5.2.1 Ray Theory

Prior to applying ray theory to the propagation problem, the limitations in the use of the ray solution must be examined. These inherent limitations can be understood by consideration of the derivation of the ray solution to the wave equation.

If the source is assumed to generate a harmonic signal, the wave equation is reduced to the Helmholtz equation, as stated in equation 2.3. The basis of ray theory is the assumption that a solution to the Helmholtz equation exists in the form detailed in equation 5.1,

$$G(x, y, z) = A(x, y, z)e^{iS(x,y,z)} \tag{5.1}$$

where G is the acoustic velocity potential of the field at position (x, y, z). $S(x, y, z)$ is a rapidly varying phase function known as the eikonal, which represents surfaces of constant phase called wavefronts. $A(x, y, z)$ is a much more slowly varying envelope function incorporating the effects of geometric spreading and various loss mechanisms. On substituting the solution, equation 5.1, into the Helmholtz equation and separating the real and imaginary parts, equations 5.2 and 5.3 can be obtained.

$$\frac{\nabla^2 A}{A} - (\nabla S)^2 + k^2 = 0 \tag{5.2}$$

$$2(\nabla A . \nabla S) + A\nabla^2 S = 0 \tag{5.3}$$

These equations can be further simplified by the application of the geometrical optics approximation as expressed in equation 5.4.

$$\frac{\nabla^2 A}{A} \ll k \tag{5.4}$$

This equation is interpreted as the assumption that the amplitude of the phase function varies slowly in range with respect to a wavelength. The substitution of this approximation into equations 5.2 and 5.3 results in the derivation of the eikonal equation, equation 5.5.

$$(\nabla S)^2 = k^2 \tag{5.5}$$

The solution of the eikonal calculates the surfaces of constant phase which represent the wavefronts. The direction of energy travel is along the ray trajectories which are orthogonal to these wavefronts and can be expressed as the direction cosines of $S(x, y, z)$. The amplitude of the field at any point can be obtained from the density of these rays or, alternatively, a more formal solution can be calculated from equation 5.3.

The ray trajectories obtained by this method provide a simple physical interpretation of the acoustic field, where the rays represent the direction of the energy flow. The changes in the direction of these rays are quantitatively related to the changes in the velocity of propagation of the sound wave.

The limitations in the use of ray tracing to calculate the acoustic propagation are related solely to the application of the geometrical optics approximation, as no other

approximations were introduced in obtaining the solution. The physical implications of the approximation can be summarised in three statements:-

1. The curvature of the ray over a wavelength must be small.

2. The fractional change in sound speed over a wavelength must be small.

3. The fractional change in A over a wavelength must be small.

These three statements limit the ray solution to the calculation of high frequency propagation and the technique can typically be regarded as valid for frequencies above 200Hz. The application of ray theory to the simulation of sidescan sonar lies well within the domain of validity.

5.2.2 Ray Tracing in Stratified Media

Ray theory can in principle be used to calculate the acoustic field in an environment where the velocity varies in three dimensions. The ray solution is more commonly applied to the two dimensional case where the velocity is a function of range and depth only, and the ray is assumed to remain within the vertical plane in which it was emitted. This is partially due to the lack of environmental information in three dimensions and also to reduce the computational overheads.

If the medium is assumed to be horizontally stratified, in that the physical characteristics depend only on depth, the ray solution is further simplified as Snell's Law is applicable [21]. The horizontal stratification assumption is commonly applied in propagation models and tends to hold for the majority of the oceanic areas provided that it is not applied in the presence of oceanic fronts or eddies.

Using the assumption that the sound speed is a function of depth only, Snell's law can be applied to calculate the refraction of a ray as it crosses the boundary between two layers with differing velocities. If the thickness of the layers of constant velocity

becomes infinitesimal, the sound speed, c, becomes a continuous function of depth, $c(z)$. The direction of the ray at a depth z can then be obtained from equation 5.6 for a ray with a grazing angle, θ_i at the initial depth, z_i,

$$\frac{\cos\theta}{c(z)} = \frac{\cos\theta_i}{c(z_i)} = a \tag{5.6}$$

where a is the Snell's law constant for the ray. This method can be applied in a piecewise manner to the sound velocity profile to calculate the ray path. The travel time and horizontal displacement of the ray trajectory can then be obtained by forming continuous integrals along the ray path.

The velocity profiles in the sea are often measured and sampled at a number of discrete depths, using devices such as profiling CTD (Conductivity Temperature Depth) probes. If a linear interpolation of the sound speed between the depth points is applied, this defines a number of layers of constant gradient velocity. The use of this approximation simplifies the evaluation of the ray path integrals, and the calculation of the ray parameters using this method will now be discussed.

The actual sound velocity profile, $c(z)$, is replaced by a series of layers where the velocity gradient, g, in each layer is constant. Within each of the layers the velocity can then be expressed as the linear equation of equation 5.7, using the notation of figure 5.1.

$$c_2 = c_1 + g\Delta d \tag{5.7}$$

It can then be demonstrated that the path of a sound ray through a layer with constant velocity gradient can be represented by the arc of a circle [113], as illustrated in figure 5.1. The radius of curvature of the ray, R_c, is related to the difference in depth, Δd, between two points on the ray P_1 and P_2 by equation 5.8.

$$\Delta d = R_c(\cos\theta_2 - \cos\theta_1) \tag{5.8}$$

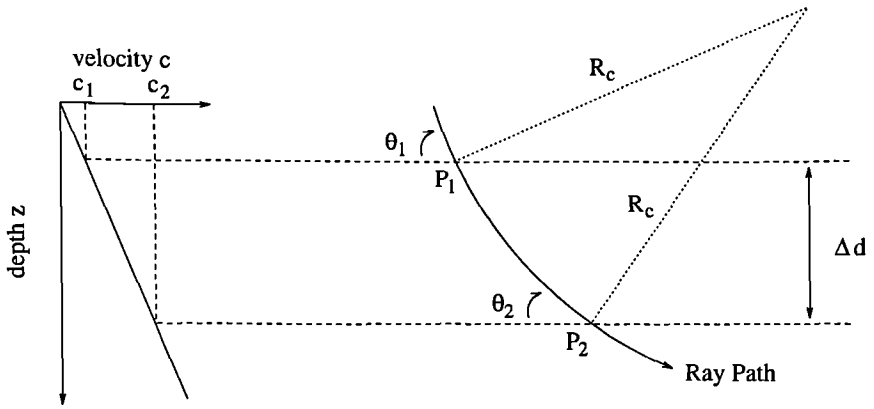

Figure 5.1: Ray path geometry in constant velocity layer

Equations 5.7 and 5.8 can then be combined with Snell's law to permit the radius of curvature for each ray to be calculated directly, using knowledge of the angle of the ray, θ, at a depth where the velocity is c. This equation can also be expressed in terms of the vertex velocity, c_0, which is the velocity, real or extrapolated, at which the ray would become horizontal within this gradient.

$$R_c = \frac{c}{g \cos\theta} = \frac{c_0}{g} \tag{5.9}$$

For underwater applications it is usual to consider a velocity gradient as positive when the velocity of propagation increases with depth. The radius of curvature is then also positive and the ray is refracted upwards towards the surface. When the velocity gradient is negative, the radius of curvature is also negative and the ray is bent downwards. This relationship can be expressed as the fact that the ray always bends towards the region of minimum velocity.

The radius of curvature and hence the ray path through each of the layers can then be calculated incrementally through the water column. This permits the calculation of the ray trajectories, ray lengths and travel times within the horizontally stratified media.

5.2.3 Implementation of Ray Theory

The technique applied to incorporate the effects of the actual ray trajectories into the simulation model for sidescan sonar images is a modification to the technique proposed in section 4.3, where straight ray paths were assumed. The simplified form of ray theory for stratified media is employed to facilitate the incorporation of the effect of the velocity profile into the simulation model. The assumption of horizontal stratification was applied primarily for simplicity, as the ray trajectories can then be calculated using the principle of circularity of rays in a linear gradient. The consequences of this assumption will be considered in section 5.2.5.

The input sound velocity profile, which is assumed to apply over the entire area ensonified, is segmented into layers of constant velocity gradient. The majority of the experimental sound velocity profile data employed in the simulations existed as velocity measurements at discrete depth intervals, and a linear gradient was assumed to apply between each of the samples.

Each individual ray path is traced incrementally from the transducer until its interaction with the seabed. The rays are emitted from the transducer at angles which would have resulted in constant slant range increments if the isovelocity and flat seabed assumptions were applicable. With the knowledge of the altitude of the fish, and hence the initial velocity, in addition to the angle of emission, the ray can be traced as it follows the arc of a circle in the layer in which it was emitted.

The ray paths are then traced through each successive layer until the altitude of the ray is equal to, or less than, the bounding volume of the seabed, as explained in section 4.3. Only the initial entry point of the ray and the angle at which it enters each layer and the subsequent exit point require to be calculated. This reduces the execution time of the process for each ray. The rays may be refracted from the scene without ever penetrating the bounding volume.

Once the altitude of the ray is equal to the bounding value, the ray path is then calculated in small increments. The vertical coordinate of the ray is decremented by *dz* and the corresponding horizontal coordinate is calculated using the equation for the arc of the circle in that layer. Using the new position of the ray, the altitude of the ray is compared to the grid cell which it is traversing, using the height field method previously described. If this test for intersection is negative, the incremental ray tracing process is continued. If the test is positive, the exact point of intersection is obtained. The intersection point is now calculated from the equation for the intersection of the triangular plane representing the seabed and the equation for the arc of the circle in that velocity layer, as the ray is no longer represented as a straight line. The calculation of the exact point of intersection in this manner should minimise any errors introduced by testing for intersection only at discrete increments along the ray path. The value for *dz* is also selected to ensure that the resulting increment in the horizontal displacement is always much smaller than the grid size of the seabed height field.

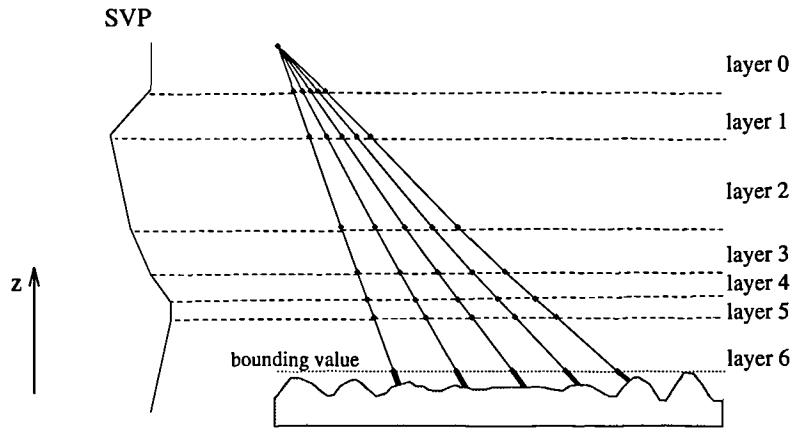

Figure 5.2: Calculation of ray paths

The process of tracing the rays is summarised in figure 5.2, which illustrates the individual points which need to be calculated to fully describe the ray path. Above the bounding value, the position of the ray is required to be calculated only on the intersection between two constant gradient layers, as the exact ray path within each layer is fully

described as the arc of a circle. Below the bounding value many points are calculated and tested for intersection with the seabed.

At the point of intersection between the ray and the seabed, the grazing angle is a function of the curvature of the ray trajectory and the local surface normal to the intersected facet. The backscattered energy is calculated using the grazing angle determined by consideration of the actual ray path and the seabed orientation. The backscattered energy can be proven to follow an identical ray path back to the transducer as the original emitted ray [114].

The exact travel time for the ray is summed incrementally as the path of the ray through each layer is calculated. The changes in velocity as the ray propagates are therefore included in the two way travel time calculations.

The specular ray reflected in the forward direction can then be traced from the point of intersection. Whilst the altitude of the ray remains below the bounding volume, the ray position is calculated incrementally using the method of small increments to the altitude position, and is continuously tested for re-intersection with the seabed. The ray continues to be traced until it exits the scene, independent of its position relative to the bounding volume, as it may subsequently be refracted back towards the seabed.

The calculation of the energy contributions from the multi-paths introduces an approximation to the technique. If the specular traced ray intersects another point in the scene, the energy scattered from this point of intersection back to the transducer must be calculated. The ray path from this point to the transducer must therefore be determined. Since the coordinates of the start and end points of the ray are known, the eigenray joining them must be determined, which can only be calculated by trial and error. This is one of the disadvantages of the ray tracing technique when the rays through specific points are to be determined and was not evident in the preceding application where only the start point of the ray was specified. This calculation of the eigenrays is a time consuming

repetitive process, especially if several velocity layers separate the two points. To speed up the execution time, the ray is assumed to follow a straight line path between the two points. In the case of the multi-path reflections, the errors introduced to the travel time calculations should be minimal, as the difference in path length between the actual ray path and the straight line approximation is small, especially over short ranges. The difference in the scattering angles between two rays should also be small and will not significantly affect the calculation of the scattered energy. The errors introduced by this assumption will be discussed further in section 5.2.4.

5.2.4 Effect of Ray Curvature

The resulting curvature of the ray paths due to the sound velocity profile affects both of the parameters displayed in a sidescan sonar image, as it can influence both the two way travel times and the intensity values. The two way travel time, or time of return, is influenced by the actual path of the ray through the water column, which is related to the curvature of the ray within each layer. The two way travel time is also no longer directly proportional to the path length due to the variations in the velocity of propagation along the ray path. The second effect on the image is due to the alteration of the intensity values which are dependent on the grazing angles of the rays at the point of intersection and are therefore related to the curvature of the ray paths.

The effect of the sound velocity profile is difficult to quantify in a general sense as it is dependent on the individual situation and varies non linearly with parameters such as the towfish height and the range of interest. However, the effect of one sound velocity profile (SVP) can be compared to another by keeping the other parameters constant, and general trends of the effects can be noted. The relative magnitude of the effects on the sidescan sonar images are also difficult to quantify as it depends on features of both the sidescan sonar and the display of the image. The effect of the difference in the time of return from the same point on the seabed for different sound velocity profiles will depend

on the amount of time each pixel represents. This depends on the number of pixels per line of the image and the pulse repetition rate, which is related to the maximum range. The time duration of each pixel, in an image which has not been slant range corrected, can be calculated using the expression of equation 5.10.

$$pixel\ duration = \frac{1}{no.\ of\ pixels} \times \frac{1}{pulse\ repetition\ rate}\ seconds \qquad (5.10)$$

The effect of the intensity variations depends on the number of grey levels used to display the image, as the output image is quantised to this number of levels, which has already introduced errors to the process. The range of intensity values represented by each grey level is determined by the maximum range of intensity values across the image, which is related to the scene which is ensonified.

To illustrate the actual effect of the ray curvature, real sound velocity profiles gathered by the Dunstaffnage Marine Laboratory in the Clyde Estuary will be examined [115]. The profiles were measured at four sites in the Clyde: East of Kintyre, South End of Arran Deep, Cumbrae and Dunoon, at approximately ten minute intervals over periods of up to 24 hours. The data was collected in early February 1993, at a time of strong winter freshwater influence, and in mid August 1993, at a time of surface water heating and well developed thermoclines. The general trend in the location of the maximum velocity in the data resulted in a maximum velocity close to the surface in the summer and close to the bottom in the winter.

The velocity profiles were determined from temperature, pressure and salinity measurements obtained using a profiling CTD (Conductivity Temperature Depth) system. The velocity was then calculated using the empirical relationship formulated by Medwin [7] and expressed in equation 2.1. The available data had been averaged over 1 metre bins and interpolated to obtain values every metre.

A sample of the velocity profiles measured is displayed in Appendix A. The profiles SVP1 to SVP5 were obtained in February, whilst profiles SVP6 to SVP9 were measured in August. The variation in the location of the maximum velocity over the two sets of data is apparent. The profiles SVP1 and SVP6 were measured in water with a maximum depth of 50m, whereas the other profiles were measured in water with depths of greater than 80m. The profile labelled "ISO", is the isovelocity profile of constant value $1483.5 ms^{-1}$, the average velocity of all nine profiles. These profiles are representative of the general trends obtained at the four sites in both winter and summer. The trends in the effects of the ray curvature will be investigated using these profiles.

The curvature of the ray path will influence where a ray, which was emitted at a specific angle, will intersect the seabed. This is illustrated in figures 5.3(a) and (b) for the ten profiles, where the rays were emitted at 10° from the horizontal in each of the profiles. The ray paths were calculated for the towfish positioned at 20m and 70m above a totally flat seabed. (Two different towfish altitudes, 20m and 70m, are used throughout the following examples to illustrate the dependence of the effect of the sound velocity profile on the towfish position.) The point of intersection varies from a horizontal range of 113.95m to 116.18m for the towfish at 20m above the seabed and from 368.42m to 499.49m for the towfish at an altitude of 70m.

Although a single ray will appear to move, the actual position of a specific point on the seabed in the sonar image must be considered. The position of a specific point or object on the sidescan sonar image is determined by the time of return for the ray intersecting this point. The value for the time of return is determined by the ray curvature and the variation in the velocity along the ray trajectory as previously explained. The effect of the variation in time due to the actual ray path does not appear to be very significant. Using the profiles displayed in Appendix A, tables 5.1 and 5.2 summarise the variation in the time of return values, with the various profiles, for rays intersecting a totally flat seabed at horizontal ranges of 50m, 100m, 200m and 500m, for towfish positioned at

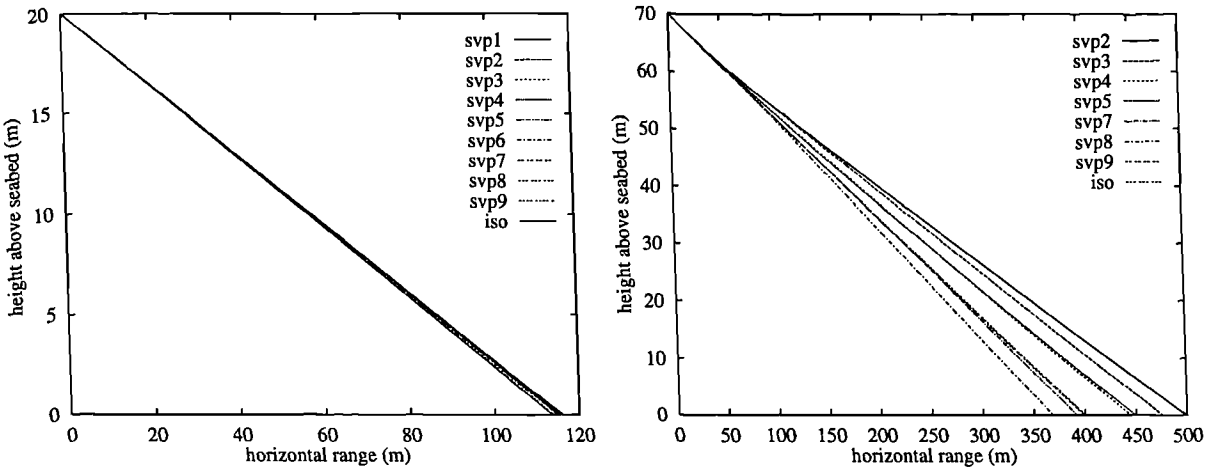

Figure 5.3: Rays emitted at 10 degrees from fish at (a) 20m (b) 70m altitude

altitudes of 20m and 70m respectively. The actual time of return values and grazing angles for the rays in each of the profiles considered are tabulated in Appendix A.

Horizontal Range	50m	100m	200m	500m
Max. Difference (msec)	0.907	1.717	3.383	8.422
Average Time (msec)	72.6	137.48	270.97	674.59

Table 5.1: Variation in time of return values for fish at altitude of 20m

Horizontal Range	50m	100m	200m	500m
Max. Difference (msec)	1.269	1.798	3.122	7.441
Average Time (msec)	116.060	164.688	285.883	681.144

Table 5.2: Variation in time of return values for fish at altitude of 70m

The variation in the time of return values increases with increasing horizontal range for either situation. This is to be expected as the further the ray propagates in the medium the greater effect the medium is able to exert on the ray path.

The variation in the times of return will result in the variation in which pixel of the output image represents a specific point on the seabed. In severe cases this could effectively cause the position of a specific point or object to appear to "move" in the image dependent on the sound velocity profile of the water column. For the cases considered above the variation is slight and represents approximately 1% of the average time of return at each of the ranges. To relate this to the output image, the pulse repetition rate of a 100KHz sonar is typically around 1.25 pulses/second and the typical output of a commercial sidescan sonar system is displayed across 800 pixels. Each pixel therefore represents 1 msec. The variation in the time of return can therefore result in the apparent motion of an object over 1 pixel, when the object is situated at 50m horizontal range, to the motion over 8 pixels at 500m range. A variation of only a few pixels in 800 can be difficult for the human eye to detect.

The second effect of the ray path is to alter the intensity values due to the variation in the grazing angle. The magnitude of the effect in the variation in the grazing angle on the backscattered energy is dependent on the actual grazing angle. Considering figure 4.13, which displays the backscattered energy against the grazing angle, the variation will have a greater effect at very shallow grazing angles and at very steep grazing angles, close to near normal incidence. The effect will be related to the sediment type, as the backscattering strength curve is dependent on the properties of the sediment.

Tables 5.3 and 5.4 display the variation in the grazing angle and the average values of the grazing angles through water columns with the profiles SVP1 to SVP9. The rays were traced from a towfish situated at both 20m and 70m above a flat seabed, to their intersection with the seabed at horizontal ranges of 50m, 100m, 200m and 500m.

The variation in the values calculated for the grazing angle at the point of intersection again increased with increasing horizontal range. The backscattering strengths for the sand and silt seabeds were also calculated for the case when the towfish was positioned at an altitude of 20m. At a horizontal range of 50m the variation in the backscattered

Horizontal Range	50m	100m	200m	500m
Max. Difference (degrees)	0.124	0.249	0.503	1.323
Average Time (degrees)	21.78	11.266	5.616	2.07

Table 5.3: Variation in grazing angle values for fish at altitude of 20m

Horizontal Range	50m	100m	200m	500m
Max. Difference (degrees)	0.009	0.217	0.425	1.077
Average Time (degrees)	54.444	34.956	19.218	7.811

Table 5.4: Variation in grazing angle values for fish at altitude of 70m

strength was approximately 0.052dB for a sandy seabed and 0.027dB for a silt seabed. This increased to a variation of 13.78dB at a horizontal range of 500m for the sand seabed. This is the maximum range of most 100KHz sidescan sonars, as the signal tends to become noise limited as the average backscattering strength has fallen to -62.5dB, and the transmission losses, which will be discussed in section 5.3, further reduce the signal strength.

The effect of the typical sound velocity profiles examined for the Clyde estuary have produced very little effect on the output sonar image. To illustrate the relative magnitude of the effect, figure 5.4 shows the simulated sonar image of a cylindrical object at 300m range for two different sound velocity profiles. The cylinder had dimensions of 0.3m radius and 3m length. The images display only a small area of the total sidescan image, representing approximately 6.5m by 9m, and within these enlarged sections of the images only very slight variations are noted in the relative positions of the cylinder and in the intensity values of the images. Within the complete sidescan image, over the full range, the apparent motion of the cylinder was negligible.

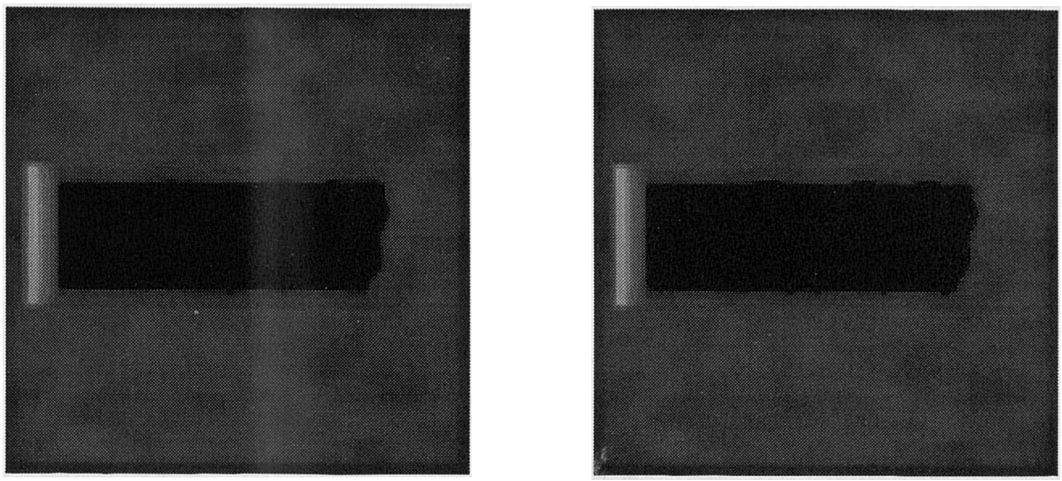

Figure 5.4: Simulated sidescan sonar images of cylinder in two different sound velocity profiles

In section 5.2.3, when the method of calculating the scattering from the multiple reflections was introduced, the assumption that the scattered energy from subsequent reflections could be calculated by assuming a straight line ray trajectory back to the transducer was proposed. The effect of this assumption will be illustrated using the Clyde velocity data. For each of the profiles the average velocity over the vertical range of interest was calculated. The time of return and the grazing angle for the rays intersecting the seabed at horizontal ranges of 50m, 100m, 200m and 500m were calculated using the fish heights of 20m and 70m for each of the profiles.

The times of return and grazing angles for the actual ray trajectories can then be compared to the isovelocity straight ray approximations, calculated using the average velocity. The differences between the times of return calculated for the isovelocity assumption and the actual ray trajectories are displayed in figure 5.5(a) for the towfish at an altitude of 20m and in figure 5.5(b) for the towfish at 70m, where the error bars indicate the range in the values calculated for each of the profiles. The errors between the two times are always less than 0.074msec, and as each pixel of the sidescan image typically represents 1msec, the effect of the assumption is virtually negligible.

The errors in the grazing angle between the isovelocity approximation and the actual ray are typically less than 0.5°, rising to a maximum of 1.1°. This will have only a very small effect on the scattering strength, as the larger errors only occurred at long ranges, where the scattering strength contributions were very small, as previously discussed.

The assumption that the energy contributions from the multiple reflections follow straight line ray paths back to the transducer will therefore not introduce significant errors in the calculation of the sonar image. The actual sound velocity profile will still be used in all other situations to produce the most accurate image and to provide energy calculations for numerical display.

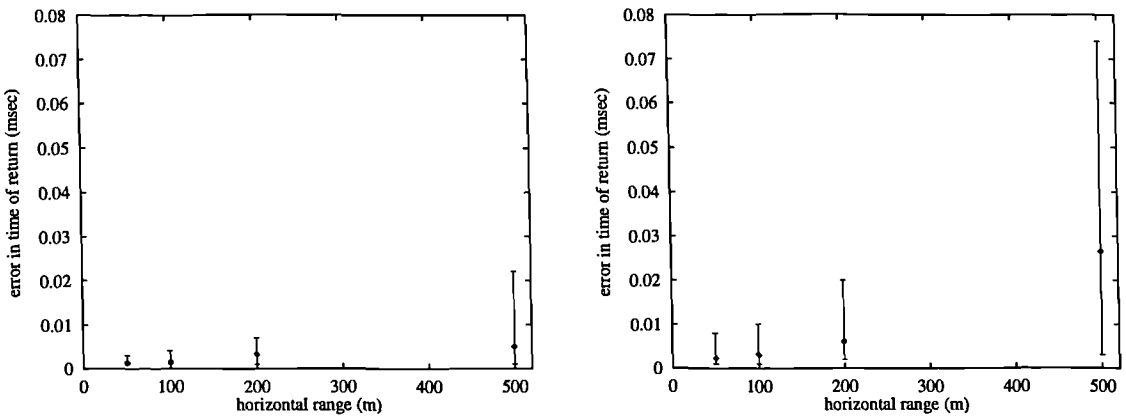

Figure 5.5: Errors in time of return values for (a) fish at 20m (b) fish at 70m

The above discussion has illustrated that the anisovelocity water column typically does not significantly alter the sidescan sonar images generated. In a few cases however, the sound waves may be subject to severe ray bending including extremes of ray convergence to create acoustic channels which can propagate signals over very long distances, and ray divergence whereby all the acoustic energy is directed away from a certain area creating a shadow zone.

Severe refraction can alter the range to which the sonar can ensonify the seabed and will affect the sidescan sonar image. Figure 5.7(a) shows the path of the rays through

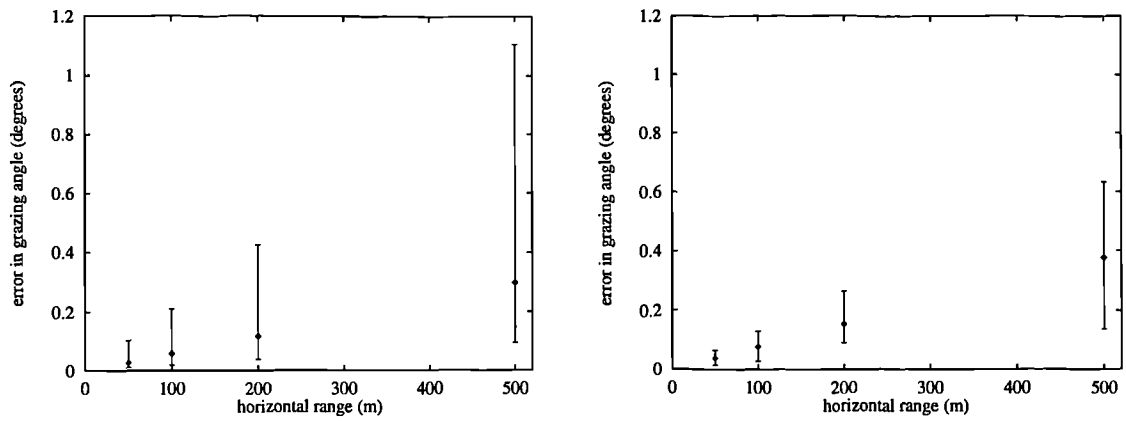

Figure 5.6: Errors in calculated grazing angles for (a) fish at 20m (b) fish at 70m

a water column with an isovelocity sound velocity profile. The rays all follow straight line paths due to the uniform velocity throughout the water column. Figure 5.7(b) illustrates the ray paths for a severe thermocline where the velocity at the water surface is much greater than at the seafloor. The rays have been refracted towards the region of minimum velocity and have been unable to ensonify the seabed to the same range as the isovelocity case.

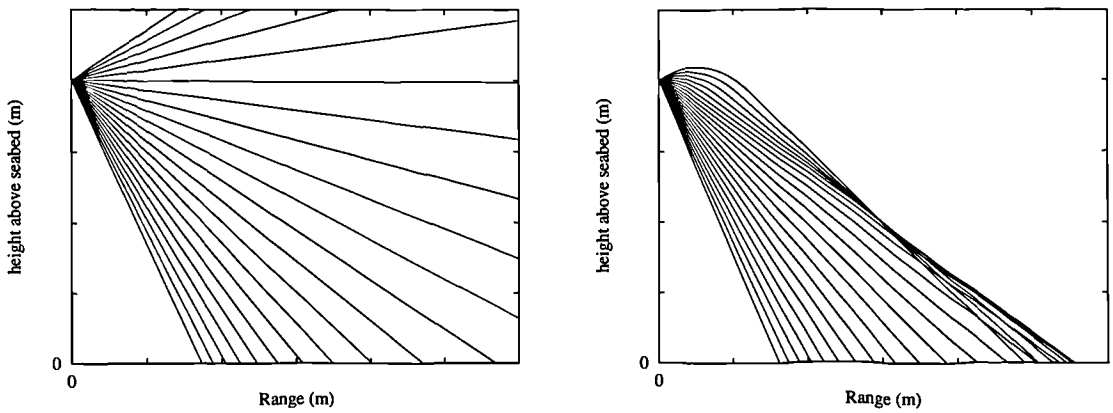

Figure 5.7: (a) Ray paths in isovelocity media (b) Ray paths through severe thermocline

The effect of this ray curvature on the sidescan sonar images which are generated when the acoustic pulse propagates through media with these same sound velocity profiles is then illustrated in figure 5.8. Figure 5.8(a) displays the sidescan sonar image for

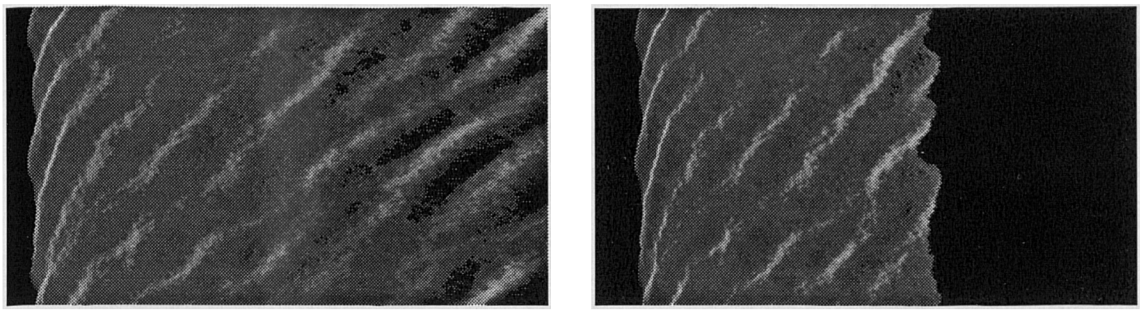

Figure 5.8: Simulated sidescan sonar image (a) isovelocity (b) thermocline

the isovelocity situation illustrated in the ray trace of figure 5.7(a). In figure 5.8(b) where the severe thermocline in the velocity profile was used, the signal is unable to propagate over the same horizontal range and the sidescan sonar has ensonified a smaller area of the seabed. The signal has therefore been returned over a shorter period of time and no intensity is returned from the greater ranges resulting in the blank area on the trace where the sonar is still 'listening' for the reflected signal, prior to emitting the next pulse.

As previously discussed the velocity profile has a greater effect in determining which part of the seafloor is ensonified, rather than on the actual image generated of the same area of seabed. This is illustrated in figure 5.8, where the sidescan images for the region closest to the towfish, which is ensonified in both cases, are very similar.

An effect of this severity is not frequently encountered and is often misinterpreted when it does occur. The thermocline required to produce this type of effect tends to occur in areas where high daytime temperatures have significantly raised the temperature of the upper layers of the water but very little mixing of the water has occurred. An example of this type of refraction effect on a sidescan sonar image obtained during a survey of Lake Erie is shown in figure 109 of reference [84].

5.2.5 Horizontal Stratification Assumption

The calculation of the ray trajectories assumed a horizontally stratified media where the velocity of propagation was a function of depth only. Unfortunately, insufficient data was available to fully investigate the effect of this assumption on the simulated sonar images.

The curvature of the ray path was illustrated, in section 5.2.4, to have a minimal effect on the time of return and intensity values returned for a ray intersecting a specific point on the seabed. A high probability therefore exists that the variation of the velocity profile with range will also have a minimal effect, apart from in the presence of severe horizontal variations in the vicinity of oceanic fronts or eddies.

Data sets exist for the short term variation of the sound velocity profile at one specific point in the sea [115]. The magnitude of these variations was proven to produce only a very small effect on the sonar image [116]. Extrapolating these variations and assuming they occur with range over the entire environment, the effect on the sonar image will be small. The use of the horizontal stratification assumption therefore appears reasonable, especially over the relatively short ranges of the high resolution sidescan sonar.

5.3 Transmission Loss

In addition to governing the direction of the propagation, the water medium has a second principal effect on the transmission of acoustic energy: this is to determine the loss of energy experienced by the acoustic signal as it propagates. The magnitude of the losses are particularly important in the simulation of sidescan sonar as the propagation losses must to be considered in two directions, both for the propagation of the emitted signal to the seabed and for the return propagation of the signal reflected from the seabed.

The loss of acoustic energy due to propagation through the media can be considered as the sum of the spreading loss and the absorption loss. The spreading loss is a geometrical effect representing the loss of energy as the wave spreads outward from the source. The absorption loss is a frequency dependent loss related to the conversion of energy to heat by the non-ideal medium. There is also a loss of energy due to the scattering by inhomogeneities in the water column and leakage from the propagation duct. This section will consider the deterministic spreading and absorption losses which are the principal causes of propagation loss at the frequencies of interest for the simulation of high resolution sidescan sonar.

5.3.1 Absorption Loss

Absorption loss is a frequency dependent loss which occurs because of the non ideal nature of the propagating medium, as energy is converted into heat by the frictional forces occurring during the repeated compressions and rarefactions of the wave propagation. When a plane wave travels through an absorbing media the fractional reduction in intensity per unit distance is constant. On integration over the entire length of the transmission path and then expressing the result in logarithmic form, as stated in equation 5.11 the absorption loss is proportional to the range, r. The constant of proportionality in equation 5.11, is the absorption coefficient, α, which is usually expressed in units of dB/km. The range, r is typically measured from a reference point 1m distant from the source [1].

$$absorption\ loss = \alpha r\ dB \tag{5.11}$$

The absorption of acoustic energy by the seawater is caused by three main effects: the shear viscosity, volume viscosity and ionic relaxation. The first two effects are present with propagation in both pure water and salt water and are related to the energy extracted from the acoustic wave to overcome the viscous forces which partially oppose the

stresses set up by the acoustic pressure wave. It is the ionic relaxation which results in different absorption coefficients for pure water and seawater. This is due to the presence of magnesium sulphate and boric acid ions in seawater which disassociate due to the applied acoustic pressure and then after a finite time, reassociate. The loss of energy depends on the duration of this finite relaxation time of the process compared to the period of the acoustic wave and is at a maximum value when the two times are approximately equal.

Several empirical relationships have been proposed to quantify these relationships and the effects of temperature, pressure and salinity on the absorption. The majority of the models calculate the absorption in seawater as that of pure water plus an excess absorption due to the presence of the salts. Schulkin and Marsh [13] developed a model which is valid even when the salinity is not a standard, but it neglects the effect of the boric acid relaxation. Fisher and Simmons [14] later proposed a different form of the expression using data obtained from laboratory experiments, which incorporated the effect of boric acid. Francois and Garrison [117] [118] have developed a refinement to the model of Fisher and Simmons but have maintained the same notation in the expression for the absorption coefficient, α, as expressed in equation 5.12.

$$\alpha = \frac{A_1 P_1 f_1 f^2}{f_1^2 + f^2} + \frac{A_2 P_2 f_2 f^2}{f_2^2 + f^2} + A_3 P_3 f^2 \tag{5.12}$$

The first two terms in equation 5.12 represent the chemical relaxation processes for boric acid and magnesium sulphate respectively. The third term is the absorption which is present in pure water. The pressure dependencies are expressed by the terms P_1, P_2 and P_3. The relaxation frequencies for boric acid and magnesium sulphate are given by f_1 and f_2, while f is the frequency of the acoustic wave. The terms A_1, A_2 and A_3 are dependent on the temperature, salinity and pH properties of the water.

The relative contributions of the three terms over the frequency range from 100Hz to 1MHz is illustrated in figure 5.9(a), using the model of Francois and Garrison. Above 200KHz, the absorption effects present in pure water are the largest contributor to the absorption, whereas between 10KHz and 200KHz the relaxation of magnesium sulphate ions dominates. Below 10KHz the absorption is also due to the effect of boric acid. At frequencies below 100Hz the effects of scattering by inhomogeneities in the water influences the attenuation of the acoustic wave.

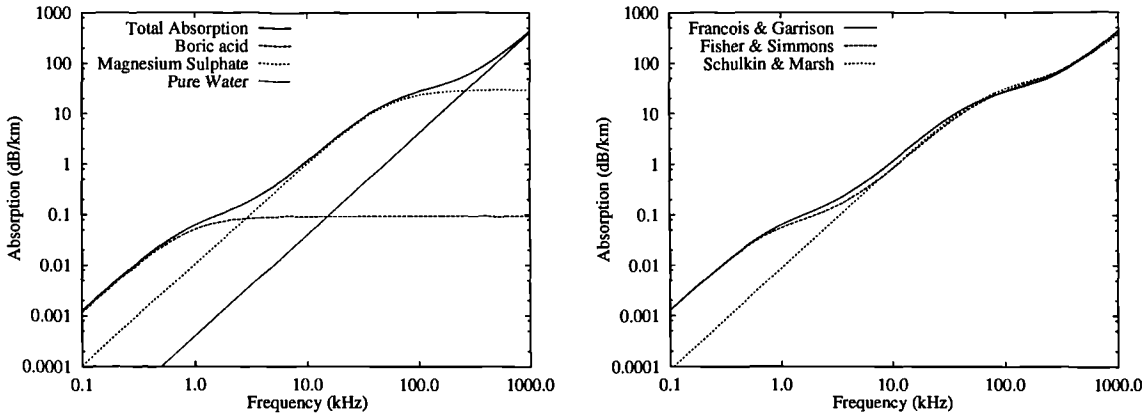

Figure 5.9: (a) Relative contributions of absorption processes (b) Comparison of absorption models

The sonar simulation model will implement the model of Francois and Garrison to calculate the absorption loss. This model has been developed from a theoretical basis using data from absorption experiments performed at sea over a variety of conditions. It is viewed as a refinement to the model of Fisher and Simmons, as it includes the effects of salinity and the pH, which affects the boric acid relaxation process. The model is valid over the frequency range from 100Hz to 1MHz, which includes the frequency range of interest for high resolution sidescan sonar. The three models which have been discussed are compared in figure 5.9(b). At the high frequencies of interest there appears to be very little difference between the three models for the case illustrated which was calculated for a water temperature of 4°C and a pressure of 1 atmosphere.

5.3.2 Spreading Loss

The second principle form of loss during propagation is the spreading or divergence loss. This is a geometrical effect related to the regular weakening of the sound signal as it spreads outwards from the source.

If the acoustic signal is emitted into a lossless, unbounded, homogeneous medium, its energy is radiated equally in all directions. The wavefronts are spherical due to the constant velocity of propagation and the energy is equally distributed over the surface of the sphere. Considering at present, that there is no loss of energy to attenuation, the power over each sphere is constant. The spreading loss can then be represented as the inverse square law of equation 5.13, where I_1 is the intensity at range r_1, and I_2 is the intensity at range r_2.

$$spreading\ loss = 10\log\frac{I_1}{I_2} = 10\log\left(\frac{r_2}{r_1}\right)^2 \tag{5.13}$$

The assumption of an unbounded medium is invalid for the ocean due to the presence of the upper and lower bounds of the sea surface and the seabed. For medium to long range propagation, the power then becomes distributed over a cylinder with a height equal to the water depth and a radius determined by the range. The spreading loss can then be represented as the inverse first order power law of equation 5.14.

$$spreading\ loss = 10\log\frac{I_1}{I_2} = 10\log\left(\frac{r_2}{r_1}\right) \tag{5.14}$$

As the assumptions of the cylindrical or spherical spreading laws neglect the variability of the water medium, and the subsequent refraction of the rays, the power law is often modified to the form of equation 5.15, where $1 \leq n \leq 2$.

$$spreading\ loss = 10\log\frac{I_1}{I_2} = 10\log\left(\frac{r_2}{r_1}\right)^n \tag{5.15}$$

A more accurate method of computing the spreading loss is to employ the information previously calculated in the ray diagrams to determine the ray trajectories. The loss can then be estimated from the change in separation of closely spaced rays [114]. This is the method employed in the sonar simulation model and the calculation of the spreading loss in this manner will now be explained, using the technique described by Horton [114].

If the medium is horizontally stratified, the ratio of the acoustic intensity at an index point, at unit distance from the source, to the ratio at point P, can be expressed in equation 5.16, using the notation of figure 5.10. The horizontal distance between the source point and the point P is represented by the parameter S_h.

$$\frac{I_0}{I_P} = -S_h \frac{\sin\theta_P}{\cos\theta_0} \frac{dS_h}{d\theta_0} \tag{5.16}$$

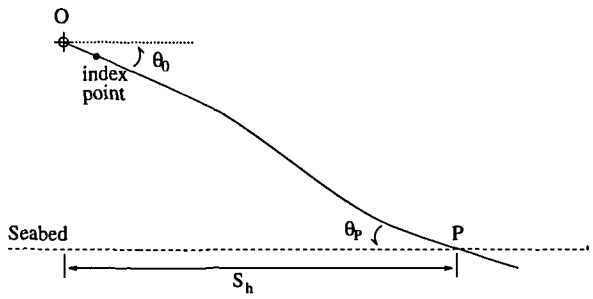

Figure 5.10: Divergence along sound ray

Equation 5.16 is independent of the sound velocity profile employed on the condition that the profile varies with depth only. This is the horizontal stratification assumption applied in the original calculation of the ray trajectories by the sonar simulation model. Therefore the equation is valid for any ray path between point 0 and P, provided the ray remains within a single vertical plane. The calculation of the spreading loss in this manner assumes that there is no leakage of energy, or scattering by inhomogeneities in the water medium, therefore the energy that is emitted between two rays remains within the confines of these rays.

For a medium composed of several horizontal layers, each with a constant velocity gradient, a numerical solution to the term $\frac{dS_h}{d\theta_0}$ in equation 5.16 can be computed. Within a constant gradient layer, the horizontal increment ΔS_h, from points m to n, on the ray path, can be differentiated to obtain equation 5.17.

$$\left[\frac{d}{d\theta_0}\Delta S_h\right]_m^n = R_c \tan\theta_0\left(\frac{1}{\sin\theta_m} - \frac{1}{\sin\theta_n}\right) \tag{5.17}$$

In equation 5.17, R_c is the radius of curvature of the ray within this layer and θ_m and θ_n are the angles, relative to the horizontal, of the ray at points m and n respectively. The total value of $\frac{dS_h}{d\theta_0}$ for the entire ray path is obtained by summing the increments through each layer calculated using equation 5.17.

The sonar simulation model calculates the spreading loss for the ray travelling from the transducer to the seabed using this technique. Although the backscattered ray follows an identical path to the outgoing ray back to the transducer, the spreading loss is not independent of the direction of energy flow. A factor dependent on the velocity of propagation at the start and end points of the ray is included to calculate the divergence of the energy on the return path, and is expressed in equation 5.18. The velocity at the intersection of the ray with the seabed at point P is c_p, and c_0 is the velocity of propagation at the source. The spreading loss is calculated from a reference point at unit distance from the effective source and hence the scattering on the return path is calculated from the point $P+1$.

$$\frac{I_{0+1}}{I_P}\frac{I_{P+1}}{I_0} = \frac{\cos^2\theta_p}{\cos^2\theta_0} = \left(\frac{c_p}{c_0}\right)^2 \tag{5.18}$$

The scattering strength calculated using the bistatic method presented in chapter 4 is calculated at unit distance from the seabed and incorporates the spreading loss over this

distance, so the complete spreading loss over the entire ray path is calculated. The spreading losses incurred by the forward reflected specular rays are calculated incrementally along the ray path, in the same manner as presented above.

5.3.3 Total Propagation Loss

The total losses incurred during the propagation of the acoustic energy can be calculated as the sum of the absorption loss and the spreading loss. The relative magnitudes of the two components of the loss are plotted against range in figure 5.11, where an isovelocity medium has been assumed. The absorption loss has been calculated for a 100KHz acoustic signal with an absorption coefficient of 29.8 dB/km. In figure 5.11(a), the range is displayed on a logarithmic scale, and the spreading loss decreases linearly at a rate of 20dB per decade due to the constant spherical spreading. Figure 5.11(b) plots the range in linear coordinates and the direct proportionality between the absorption loss and the range can be observed.

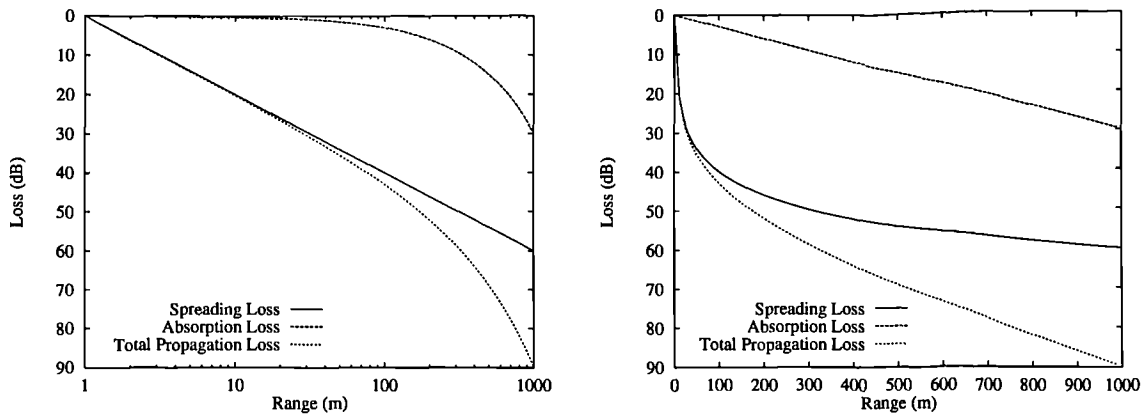

Figure 5.11: (a) Propagation loss vs. range on logarithmic scale (b) Propagation loss vs. range on linear scale

At short ranges the spreading loss dominates the propagation loss. The absorption loss increases with increasing range, and eventually at the transition range the absorption loss is equal to the spreading loss. Above this transition range, the absorption loss

dominates. The position of the transition range is determined principally by the frequency of propagation which determines the absorption coefficient.

5.3.4 Effect of Sound Velocity Profile on Losses

The sound velocity profile of the water column can affect both the absorption loss and the spreading loss. The velocity profile will influence the absorption loss in two manners, as it can alter both the absorption coefficient, due to its dependence on the temperature and salinity, and the path length of the ray. The spacing of the rays, from which the spreading loss is calculated, is also dependent on the velocity profile. The velocity profiles measured in the Clyde Estuary and displayed in Appendix A will be examined to illustrate the magnitude of the effect revealed by calculating the propagation loss using the actual sound velocity profile.

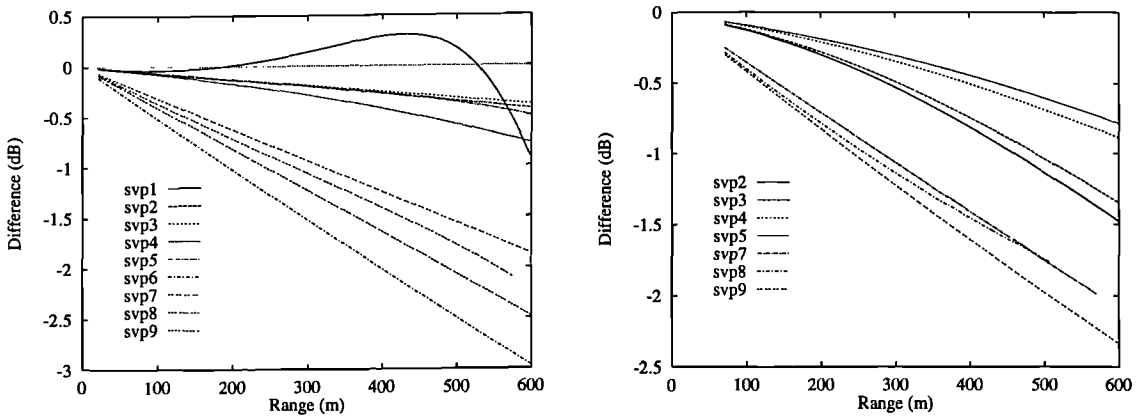

Figure 5.12: Error between calculating the propagation loss using isovelocity assumption and actual SVP for fish at (a) 20m altitude (b) 70m altitude

Figure 5.12 plots the difference between calculating the total propagation loss assuming isovelocity conditions and spherical spreading with a constant absorption coefficient, and the total propagation losses calculated by consideration of the actual ray spreading and variation of the absorption due to the variation of sound velocity with depth. Figure 5.12(a) is calculated for the fish at an altitude of 20m and figure 5.12(b) is

calculated for the towfish at 70m altitude, as the ray trajectories are dependent on the source position. In both cases, the difference increases with range, with a difference of 2.5dB at 500m, the effective maximum range of a 100KHz sonar. At ranges of less than 200m the error tends to remain below 1dB.

5.3.5 Effect of Losses on Sonar Image

The loss of energy experienced by the signal during its propagation through the water medium will affect the sonar image produced. Since the propagation loss occurs when the signal is travelling in both directions, both away from and back to the transducer, the propagation loss from the path length of a ray can be regarded as approximately double those of figure 5.11. This results in the rapid attenuation of the signal with range, and the resulting increase in the range of intensity values returned for each emitted pulse.

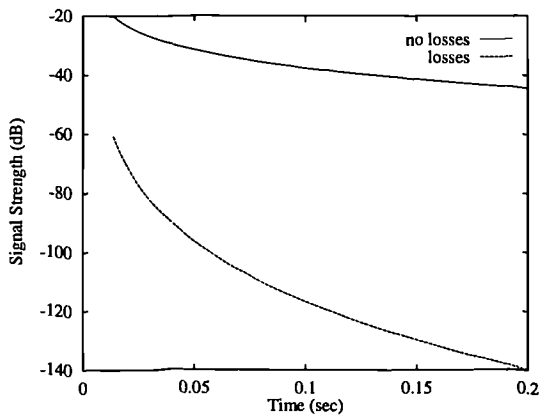

Figure 5.13: Comparison of signal strengths

The effect of the losses on the signal is illustrated in figure 5.13. This displays the intensity returned against time, for one line of a sonar image, where the signal has been reflected from a totally flat planar seabed. The intensity values are displayed in decibels to permit the visualisation of the full range of intensity values and allow direct comparison on one scale. When the returned signal has been calculated ignoring the propagation

loss and calculating only the backscattered energy, the signal spans an intensity range of approximately 20dB. With the inclusion of the propagation loss, the signal is attenuated by a minimum of 40dB and this attenuation increases with range. The returned signal is therefore spread over a greater range of intensity values. This results in a very non-uniform intensity image with very bright areas at the beginning of the trace and produces difficulties in distinguishing features at long ranges where the contrast in grey levels is minimal. Figure 5.14(a) displays the sonar image calculated if the propagation losses are neglected and figure 5.14(b) displays the sonar image of the same flat seabed if the propagation losses are included. A more uniform intensity image is generated when the losses are removed from the calculations. The increase in the intensity range to be displayed results in an increase in the quantisation errors as each grey level represents a broader band of intensity values.

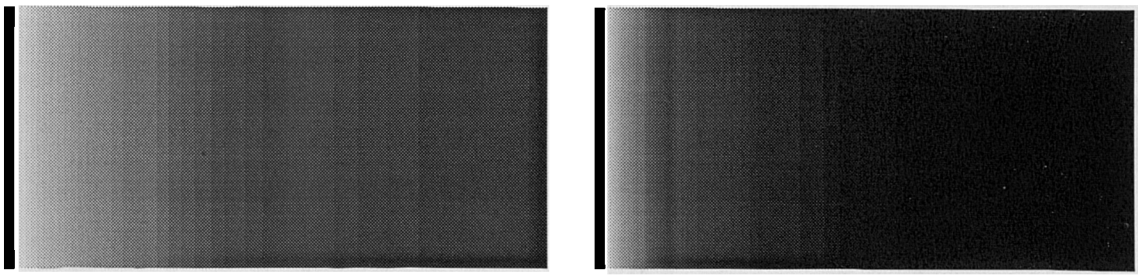

Figure 5.14: Sonar image of flat seabed (a) neglecting propagation loss (b) propagation loss included

5.4 Compensation of Losses

The problem discussed in section 5.3.5, of the rapid decay in the image intensity levels, can be minimised by the application of a gain function to the returned signal. The applied gain produces a more uniform intensity image, where the intensity variations due to the features of the seabed are easier to distinguish.

The primary method of compensation is time varying gain (tvg). Higher intensity reflections are returned from the seabed closest to the towfish and the reflected signal then

decreases rapidly with range (or time from the start of transmission), due to the increased losses. This rapid decrease of the signal strength is displayed in figure 5.15(a). To compensate for the decrease in signal strength, time varying gain applies a gain which increases rapidly with time, from the time of transmission of the pulse. The gain is reset to zero on the emission of every pulse and increases in an inverse manner to the losses, as shown in figure 5.15(b).

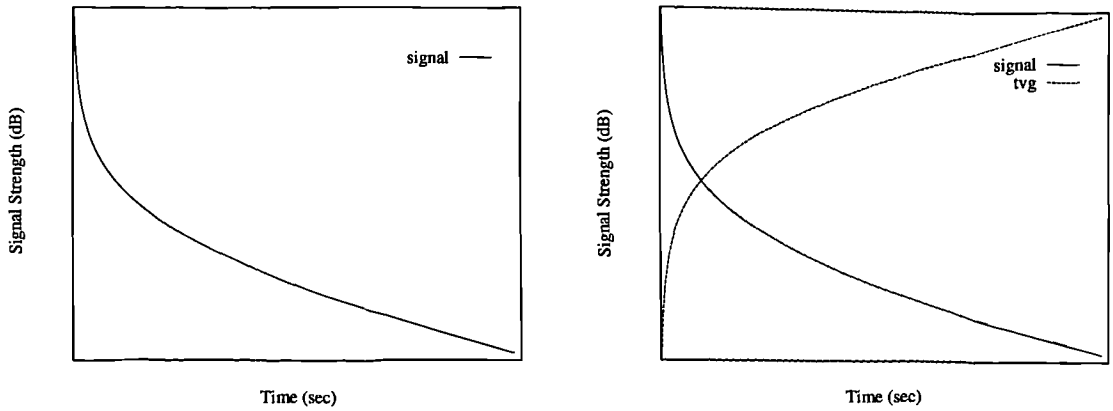

Figure 5.15: (a) Signal strength (b) Time varying gain

The simplest compensation accounts for the losses due to the propagation loss only. The typical gain applied assumes spherical spreading and is computed as $40\log r + \alpha r$, where r is the range from the transducer and α is the absorption coefficient. The range is calculated from the linear relationship, $r = velocity \times time$, and is calculated for the time from the start of the transmission of the pulse. Some time varying gain curves include terms to account for the decrease in backscattering strength with range also.

The time varying gain is usually applied directly by circuitry in the sonar head and the data is therefore recorded with the gain already included. In some sonar systems the gain can be adjusted by the operator to produce a visually more uniform image, or to highlight certain features, but often the actual level of the gain applied is not recorded.

The sonar simulation model will apply the standard representation of the time varying gain, calculated using $40\log r + \alpha r$ and assuming a constant velocity of $1500ms^{-1}$.

The absorption coefficient is calculated from equation 5.12 for the standard conditions of salinity and temperature for the operating environment. This gain will be applied to all further simulated sidescan sonar images generated, to compensate for the propagation losses and produce images with more uniform intensity characteristics.

The gain is not equal to the propagation loss due to the application of the assumption of an isovelocity medium with constant velocity of $1500ms^{-1}$ in calculating the gain. The difference between the tvg and the propagation loss will be determined by the sound velocity profile of the water column. A representation of the difference can be obtained from figure 5.16 which plots the difference between the time varying gain applied and the total propagation losses for the profiles displayed in appendix A. Figures 5.16(a) and (b) plot the calculated difference against the time of return, for the towfish at altitudes of 20m and 70m respectively.

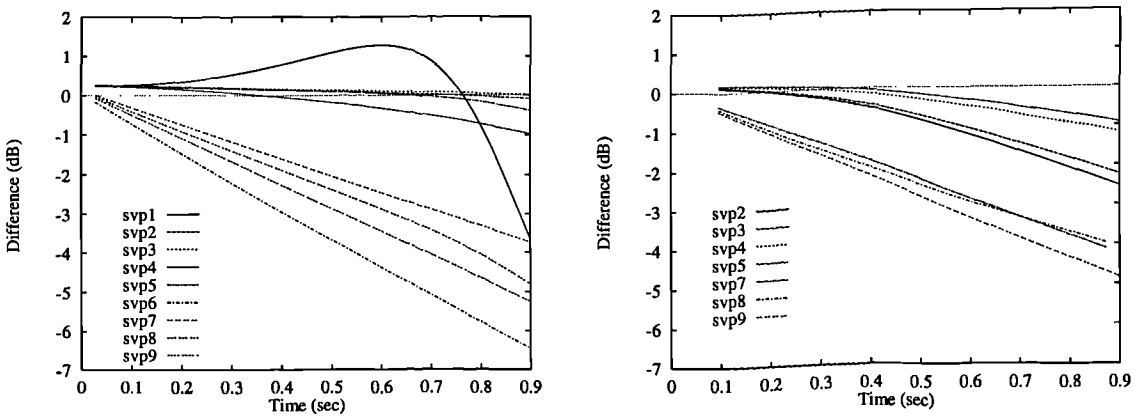

Figure 5.16: Difference between tvg and total propagation loss for fish at (a) 20m (b) 70m altitude

The curves are similar to those displayed in figure 5.12, but the differences are greater. This is partially due to the calculation of the two way losses in figure 5.16 and also because of the assumption of a velocity of $1500ms^{-1}$ when calculating the range for the application of the time varying gain.

The difference between the tvg curve and the total propagation loss makes it necessary to calculate the actual losses and then apply the time varying gain. The approximation that the time varying gain is equal to the losses could be applied to permit fewer calculations to be performed and hence increase the execution rate, but the accuracy of the output is reduced. The simulation model will therefore sacrifice speed for greater accuracy in the calculation of the output images. This also provides a more general model from which propagation loss information can be derived numerically.

5.5 Sources of Loss and Interference

In addition to the spreading and absorption losses discussed in section 5.3, other sources of loss exist within the complex underwater environment. As the sound propagates outwards from the transducer it is reflected and scattered in different directions by the uneven water surface, the inhomogeneities of the water column and the rough seabed. Some of this scattered energy is returned to the transducer, and may influence the image generated.

The scattering of the acoustic energy has two primary effects on the sonar system. The first of which is the reduction of the amount of energy reaching the sea bottom. This results in an additional factor to the attenuation loss, which is usually defined as the sum of the absorption and the scattering losses.

The second effect of the scattering is to produce a constant level of unwanted energy at the transducer. The desired signal must then exceed this level to be visible. The scattering of the emitted energy is known as *reverberation*. The portion of the scattering from the sea surface is called surface reverberation, and that portion scattered by the inhomogeneities in the water is known as volume reverberation. Also present is the reverberation from the sea bottom, which was discussed in chapter 4. This bottom reverberation is the desired signal from which the image of the seabed is generated, but the volume and surface reverberation can produce unwanted distortions on the image.

In addition to the unwanted reverberation, other unwanted noise signals will be present at the transducer. This acoustic energy is already present in the environment and is not the result of the acoustic signal applied by the transducer. The noise and reverberation can result in the appearance of "clutter" in the images and may even mask the signal from the desired target.

The sonar simulation model, in its current state, considers only the deterministic spreading and absorption losses. Noise and reverberation are random signals which cannot be specified with regard to time or space, and therefore stochastic models must be applied to account for the unwanted random energy. The determination and incorporation of these stochastic models forms part of the proposed future work for this project, which will be discussed in chapter 8. However, a brief description of the qualitative effects of the noise and reverberation on sidescan sonar images will be presented in the following sections.

5.5.1 Sea Surface Reverberation

The effect of the interaction of the acoustic energy with the sea surface is dependent on the position of the towfish and the sea state. If the sea surface is calm, the most obvious effect of the surface is usually the first surface return which appears as a thin line of high intensity. The position of this line is determined by the towfish position relative to the seabed and the sea surface. If the towfish is closer to the sea surface, the surface return will appear as a white line prior to the first bottom return. If the towfish is closer to the seabed, the surface return will appear after the first bottom return and will be superimposed on the seafloor image. However, if the sonar is operating in deep water, the first surface return may not be visible on the sidescan image.

If the sea surface is rough, reflections from the under-sides of the waves and from air bubbles will occur. This will result in a mottled appearance on the sonar record, and will produce clutter in the image. This clutter will appear on the image immediately after

the first surface return. It can be minimised by directing the beam away from the sea surface.

The sea surface can also produce interference effects on the sonar images. This is caused by multiple ray paths reaching the target, either through the direct ray path or the surface reflected ray path. The effect occurs more frequently in calm seas when the operating frequency is less than a few kilohertz.

The effect of neglecting the surface reverberation in the calculations for the sonar simulation model is dependent on the sea state, which in turn is determined by factors such as the weather and tidal conditions. Generally, neglecting the surface reverberation will result in the generation of an image with slightly less speckle and clutter. In calm waters when the transducer is relatively close to the seabed, and directed away from the sea surface, the effect of the surface reverberation is minimised, and it is under this condition that the simulated sonar images will be generated.

5.5.2 Volume Reverberation

The oceans and seas are full of unidentified scatterers that clutter and obscure the backscattered signal. The scatterers may absorb the incident acoustic energy as well as reflecting it.

The inhomogeneities of the water which scatter sound have a variety of sources, and can consist of suspended sediments, air bubbles or marine organisms. At the operating frequencies of sidescan sonar, the dominant biological scatterers are zooplankton, although larger fish with air filled swim bladders can also cause the reflection of sound. Problems arise in modelling the volume reverberation as the density and position of marine organisms in the water column is difficult to quantify, as it varies with factors such as the light intensity and time of day. In general though, the volume reverberation increases with increasing depth.

The volume reverberation will also add increased speckle and clutter to the image. The reverberation is present at all ranges with a power proportional to the transmitted power, but it will decrease with time after the start of transmission. In severe cases it may even obscure the target echo, although this generally only occurs at the outer ranges of the image, where the target echo is greatly attenuated. If the volume reverberation is not severe, the neglect of its calculation will result in a slightly "cleaner" image of the seabed with less speckle. The volume reverberation is impossible to quantify generally and is different for every situation, so it could not be included with any accuracy unless experimental data for the site of interest was available. The sonar simulation model therefore assumes the operation of the sonar in relatively homogeneous waters, where the effects of volume reverberation are minimal.

5.5.3 Noise

The previous discussion has centred on the reception of scattered acoustic signals which are the result of the energy transmitted by the sonar system. Also present in the oceans are a variety of noise sources which emit acoustic energy. This energy may also be received by the sonar system. These producers of acoustic energy can be broadly partitioned into self-made and ambient noise sources.

Self-made noise is the noise which arises as a direct result of the presence of the survey vessel, and may be due to the deployment of other instruments, the ship's machinery or the flow of water past the towing vessel. The ambient noise is the noise inherent in the environment regardless of whether the survey vessel is present or not. There are a variety of sources of ambient noise, both man made and natural, all of which have different frequency characteristics. The sources of noise consist of surface waves, oceanic turbulence, seismic disturbances, ships traffic, thermal sources, rain, wind and biological noise. The ambient noise is at its lowest levels at the typical operating frequencies of high resolution sidescan sonar transducers, where the principle sources of ambient noise are

wind noise and thermal noise due to molecular interactions.

The ambient noise is frequently modelled as a gaussian process of zero mean and specified variance, since the noise originates from a number of sources with random amplitude and phase. This model is inaccurate for man made or localised noise sources.

The presence of noise will also result in the degradation of the sonar image with speckle and clutter, and may even prevent the differentiation of a desired target signal, in a similar manner to the reverberation effects. The relative effects of noise and reverberation are determined by their amplitudes at the range of interest.

The sonar simulation model neglects the effects of noise and reverberation in the environment. This assumption is reasonable provided there are only very low levels of noise and reverberation present, and the simulated images are of the regions of the record before the signal has become noise or reverberation limited. The model concentrates, at present, on modelling the deterministic processes which influence the generation of the image. The effect of the random processes due to the noise and reverberation can then be investigated and quantified using suitable stochastic representations, to determine their influence on the simulated sidescan sonar image.

5.6 Conclusions

This chapter has presented the extension of the sonar simulation model to incorporate the effects of an anisovelocity water medium. A ray based propagation model has been included to calculate the exact ray curvature due to the variation of the velocity of propagation in a horizontally stratified medium.

The exact ray curvature was shown to produce very little effect on the simulated sonar images for the majority of situations. Its incorporation does, however, produce a more physically correct and general model, which can be applied to a wide range of situations. The simulation model can also be applied to calculate the exact energy levels, in

addition to generating the images. With the inclusion of the exact propagation paths, the model has the ability to simulate the effect of anomalies in the sound velocity profile, which is a powerful feature for the application of the model as a training and visualisation tool, as it permits the visualisation and explanation of these anomalies in the images.

The simulation model has also been extended to calculate the propagation loss incurred by the signal. This loss is composed of the absorption and spreading losses, which were calculated from the actual ray trajectories determined by the propagation model. The inclusion of the loss in the simulation model resulted in the rapid attenuation of the image intensity with range. This attenuation could be partially compensated for by the application of a time varying gain, in a similar manner to the actual process occurring in the sonar system.

The scattering losses, due to the volume and surface reverberation, were neglected from the calculations. This provides a reasonable assumption, provided the images are only generated at ranges where the signal will not be limited by noise or reverberation.

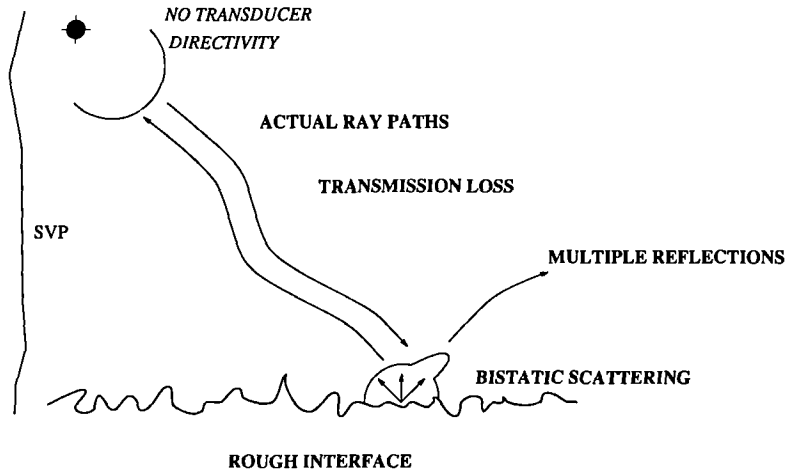

Figure 5.17: Summary of simulation model

A summary of the model status is presented in figure 5.17. The simulation model now incorporates the sound velocity profile of the medium, which influences the ray trajectories and the propagation losses. The inclusion of models for the rough seabed and

the bottom reverberation were presented in the previous chapter. The simulation model still neglects the effect of the transducer characteristics on the simulated sidescan sonar image, although the remainder of the simplifying assumptions introduced in chapter three have now been removed.

Chapter 6

Transducer Directivity and Motion Characteristics

6.1 Introduction

The sonar simulation model developed in the preceding chapters has neglected the directional properties of the sidescan sonar transducer. To simplify the model development the assumption that the energy was emitted with equal intensities within one vertical plane was introduced. This resulted in the computation of each line of the simulated sidescan sonar image by tracing rays which intersected one infinitesimally narrow line of the seabed perpendicular to the direction of travel of the towfish.

This chapter will investigate the directional response of transducers for underwater acoustics applications, during both the transmission and reception of signals. The subsequent effect of incorporating the three dimensional directivity response of the transducer into the sonar simulation model will then be considered.

The sidescan sonar image is generated by towing the transducer through the water and sequentially scanning the seabed to the side. The towing motion produces instabilities which can alter the trajectory, speed and orientation of the towfish. The translational and rotational motion instabilities will therefore alter the directivity properties and consequently the sidescan sonar image generated. This chapter will also investigate these motion characteristics of the transducer and simulate their effect on the sidescan sonar images.

6.2 Directivity of Transducers

A transducer is a device for converting energy from one form to another and within the context of a sonar system its role is to convert between acoustical and electrical signals. Transducers can typically be categorised depending on whether magnetic or electrical fields are employed in the conversion process [119]. The commonest form of transducer for underwater acoustics applications is created from piezoelectric ceramics and utilises the electric field.

For the operation of a sidescan sonar system, the functions of the transmitter and receiver, or hydrophone, are combined within the one transducer. The transducer is therefore required to possess linear and reversible characteristics, to facilitate the dual purposes of signal transmission and reception. A linear transducer has the ability to produce an exact equivalent, in electrical terms, of the applied acoustic signal. The reversible condition implies that the transducer can convert energy in either direction between electrical and acoustical forms. This is also frequently expressed in the more specialised form of the *reciprocity theorem*, which states that the transmit and receive responses are identical [119].

The majority of transducers are directional in that they can transmit and receive energy effectively only over a certain angle of space. The concept of a *beam* is often introduced to express this directionality, since during transmission the acoustic energy is thought of as confined to a beam, and by analogy, the receiving system is considered as having a beam. In the reception case, the beam refers to the solid angle over which the transducer can detect the signal.

Even within the beam, the distribution of energy is not uniform in magnitude or direction. The area in front of the transducer can be separated into the near field zone and the far field zone to explain the energy distribution. In the near field area the phases of the pressure waves from different parts of the transducer are significantly different, and this

results in regions of constructive and destructive interference. The magnitude of the waveform in any given direction varies unevenly with range from the transducer. The extent of the near field is determined by the near field distance, r_0, which is dependent on the transducer dimensions and operating frequency. The accepted approximation for the calculation of the near field distance is stated in equation 6.1, where A is the area of the transducer and λ is the wavelength of the transmitted wave [120].

$$r_0 = \frac{A}{\lambda} \tag{6.1}$$

Beyond the near field distance the far field zone exists. In this area, the signals from the transducer with the greatest differences in path length can no longer destructively interfere and the overall energy field is summed from the individual contributions. The result of this summation leads to the formation of the acoustic beams. The remainder of this chapter will assume far field conditions, since the range to any intersection is assumed to be large compared to the physical dimensions of the transducer and the high frequencies of interest.

The use of a directional system has several advantages as it enables the direction of signals to be determined and permits the differentiation of closely spaced signals. It also improves the noise selectivity of the system, as the ambient noise arriving from other directions will be discriminated.

The directional response of the transducer in the far field is specified in terms of the *beam pattern*. The response is usually specified in terms of the angles θ and ϕ in polar coordinates, where θ is the angle in the vertical plane and ϕ is the angle in the horizontal plane. The response of the transducer, $R(\theta, \phi)$, can then be stated in equation 6.2, where $R(0,0)$ is the response on the acoustic axis where $\theta = \phi = 0^o$, and $v(\theta, \phi)$ is the normalised response function. The beam pattern, $B(\theta, \phi)$, is then defined as the square of the normalised response function [1].

$$R(\theta, \phi) = R(0,0)v(\theta, \phi) \tag{6.2}$$

A theoretical point transducer with infinitesimal dimensions has a uniform beam pattern which is equal in all directions. However, any transducer with finite dimensions will possess directional properties. A desired beam pattern can then be generated by shaping a single transducer, or by combining several transducers to generate an array.

The transducers employed within a sidescan sonar system are required to possess a particular form of beam pattern or directionality. In this case, a beam pattern is required which is wide vertically, to transmit uniform intensities out to all ranges. The horizontal beam should be very narrow, to ensure each line of the image is generated from the returns from only a narrow strip of the seabed.

Prior to explaining the actual implementation of the beam pattern within the sonar simulation model, the following sections will consider the theory for the generation of a beam pattern with the desired characteristics.

6.2.1 Response of Linear Arrays

For simplicity, the basic principles of the relationship between the directivity and the transducer characteristics will be investigated initially for linear arrays. The concepts will then be extended to planar arrays in the following section.

A linear array is an array with a specified length but no width. The array therefore has directional properties along its length, but in the perpendicular direction with zero width, it appears as a point source with uniform directionality. It is the beam pattern along the array length which will be investigated, and this is represented as $B(\theta)$.

In its simplest form, the beam pattern of a single element array can be calculated from the Fourier transform of the acoustic aperture. Since the array usually consists of more than one element, the beam pattern is calculated by summing the contribution from

each element of the array, taking into account the phase differences due to the acoustic path lengths which result from the positions of the elements within the line array. The directivity response for a linear array of point elements is derived in this manner in Appendix B. The resulting beam pattern for a linear array of n point transducers, each equi-spaced by a distance d is expressed in equation 6.3.

$$B(\theta) = \left[\frac{\sin\left(\frac{n\pi d \sin\theta}{\lambda} \right)}{n \sin\left(\frac{\pi d \sin\theta}{\lambda} \right)} \right]^2 \tag{6.3}$$

In a similar manner, the response of a continuous line array can be derived. In this case, the elements are so close together as to form a continuous line, and the response is formed by the integration, rather than by the summation of the individual contributions. The beam pattern for a linear array of length L, obtained by this technique is expressed in equation 6.4.

$$B(\theta) = \left[\frac{\sin\left(\frac{\pi L \sin\theta}{\lambda} \right)}{\frac{\pi L \sin\theta}{\lambda}} \right]^2 \tag{6.4}$$

The derivation of the above beam patterns has assumed that each of the elements has a uniform response. Since each of the elements will have a finite length, they will also have a directional response. The total response of a linear array of finite sized elements can be obtained from the *product theorem* [1]. This theorem states that the beam pattern is the product of the directional pattern of each element alone and that of the corresponding linear point array. This is expressed in equation 6.5 for an array of n elements each of length a, spaced apart by a distance d. The first term of this equation is the response of each element alone and the second term is the array factor.

$$B(\theta) = \left[\frac{\sin\left(\frac{\pi a \sin\theta}{\lambda}\right)}{\frac{\pi a \sin\theta}{\lambda}}\right]^2 \left[\frac{\sin\left(\frac{n\pi d \sin\theta}{\lambda}\right)}{n \sin\left(\frac{\pi d\theta}{\lambda}\right)}\right]^2 \tag{6.5}$$

Figure 6.1(a) plots the beam pattern $B(\theta)$, calculated for a linear array consisting of 6 elements each of length 6mm spaced apart by 7mm. The beam pattern consists of a main lobe, at right angles to the surface of the array, and several smaller side lobes. The same beam pattern is displayed in figure 6.1(b) in logarithmic form, where the beam pattern is expressed in decibels. The use of the logarithmic form permits the visualisation of the relative magnitudes of the side lobes, the first of which have a response 13dB below the main lobe.

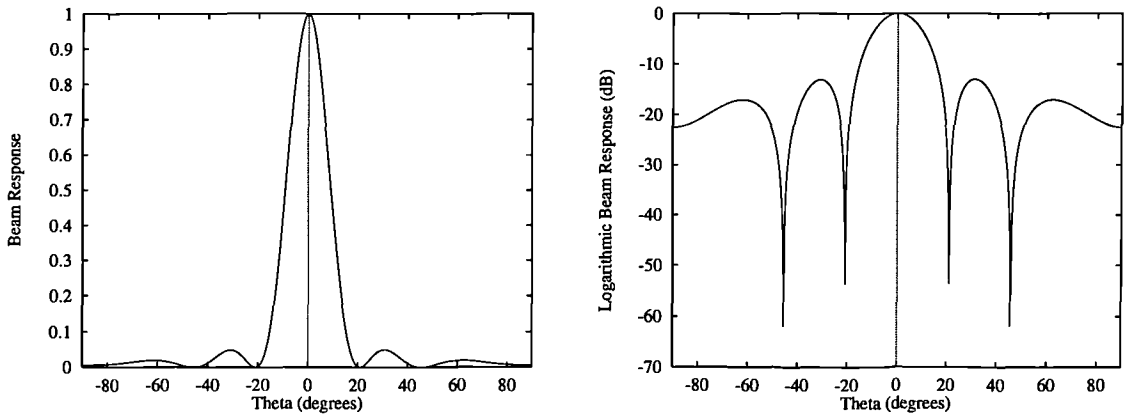

Figure 6.1: (a) Beam pattern for linear array of 6 elements (b) beam pattern in logarithmic form

The beam width can be determined from the beam patterns of figure 6.1. The beam width is usually defined as the angle between the two half power points on the main lobe. On the logarithmic scale this is the angle between the -3dB points and for the case illustrated above the beam width is 18.2°.

The width of the main lobe and the number and position of the side lobes is dependent on the number of elements in the array and their dimensions. As the number of

elements is increased, the width of the main lobe is decreased and the number of side lobes is increased. The beam pattern of the array can also be modified by the application of amplitude or phase shading. Shading techniques are often applied to reduce the response of the side lobes.

The above expressions for the beam patterns have all been calculated for broadside arrays, where the main lobe is at right angles to the surface of the array. The array can also be steered, either mechanically or electrically, to direct the main lobe and deflect the beam. The commonest and most flexible method of steering is to electrically adjust the phase relationships of the elements of the array. The process of steering will result in a distorted non-symmetrical beam pattern where the centre of the main lobe will occur at the steering angle and not at θ equal to 0°.

6.2.2 Response of Planar Arrays

The above discussion centred on linear arrays with finite dimensions on only one axis. However, all transducers have finite dimensions on more than one axis, and the linear array provides only a useful analogy and starting point for the extension of the theory to planar arrays.

The commonest types of transducer array are planar, where the elements lie on a single plane. To calculate the directivity response, the product theorem can then be extended to two dimensions. For a rectangular planar transducer, the directional pattern in any plane normal to the surface of the the transducer can be expressed as the product of the patterns of two orthogonal line arrays.

Transducers are normally composed of several elements, to permit greater control to be exerted over the directivity response. The beam pattern for a grid array of rectangular transducer elements can be obtained by the application of a similar technique, where the beam pattern at any point is formed by the product of the directivity patterns

calculated from the two orthogonal line arrays composed of finite length elements.

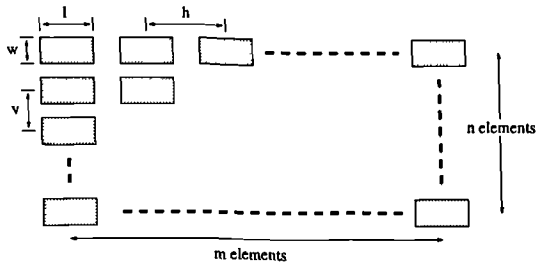

Figure 6.2: Rectangular grid array of transducer elements

Figure 6.2 illustrates a grid composed of m by n rectangular transducer elements. Each element has dimensions of l by w and is spaced apart by a distance h horizontally and v vertically. The horizontal beam pattern is expressed in equation 6.6 and the vertical beam pattern is given by equation 6.7.

$$B_h(0,\phi) = \left[\frac{\sin\left(\frac{\pi l \sin\phi}{\lambda}\right)}{\frac{\pi l \sin\phi}{\lambda}}\right]^2 \left[\frac{\sin\left(\frac{m\pi h \sin\phi}{\lambda}\right)}{m\sin\left(\frac{\pi h \sin\phi}{\lambda}\right)}\right]^2 \tag{6.6}$$

$$B_v(\theta,0) = \left[\frac{\sin\left(\frac{\pi w \sin\theta}{\lambda}\right)}{\frac{\pi w \sin\theta}{\lambda}}\right]^2 \left[\frac{\sin\left(\frac{n\pi v \sin\theta}{\lambda}\right)}{n\sin\left(\frac{\pi v \sin\theta}{\lambda}\right)}\right]^2 \tag{6.7}$$

The total beam pattern at any angle (θ, ϕ) can then be calculated from the product of these two beam patterns as stated in equation 6.8.

$$B(\theta,\phi) = B_h(0,\phi) \times B_v(\theta,0) \tag{6.8}$$

The directivity response of a rectangular grid array of transducers calculated using this technique is displayed in figure 6.3. The array consisted of a grid composed of 6 elements by 25 elements, each with dimensions of 5mm by 6mm spaced apart by 6mm

horizontally and 7mm vertically. Figure 6.3(a) displays the beam pattern, expressed in decibels, in cartesian coordinates and figure 6.3(b) displays the pattern in polar coordinates, the form in which it is more usually visualised.

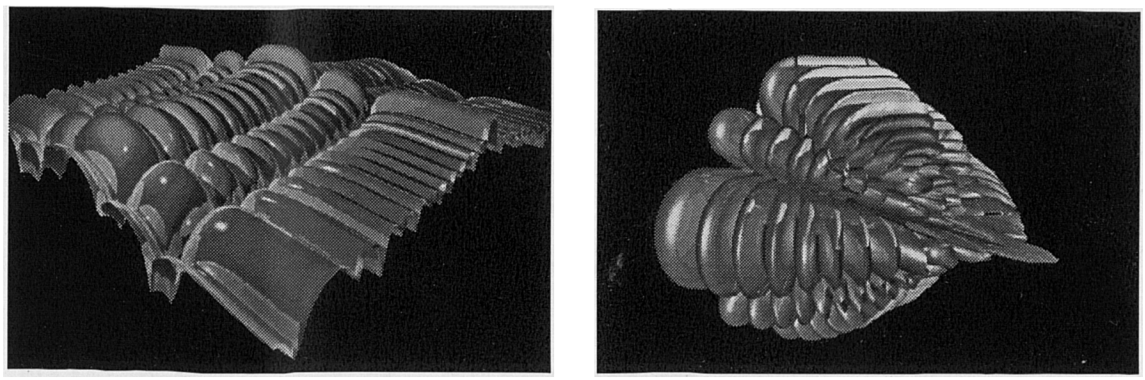

Figure 6.3: Three dimensional beam pattern from rectangular grid array (a) cartesian coordinates (b) polar coordinates

The resulting beam pattern from this arrangement of transducer elements has a main lobe which is wide in one direction, 18.2°, and narrow in the perpendicular direction, 5.1°. The wide lobe occurs due to the use of 6 elements on one axis and the narrow lobe results from the employment of 25 elements on the other axis. The number of side lobes is also related to the number of transducer elements.

6.2.3 Source Level

The previous discussion has considered only the normalised response function. The total response in any direction is also a function of the axial response, which is the response $R(0,0)$, in the direction $\theta = \phi = 0^o$ for an unsteered array. This relationship was expressed in equation 6.2.

The maximum axial pressure is related to the maximum acoustic pressure applied by the transducer to the water. The maximum pressure level is limited by cavitation effects and the interactions between transducer elements within closely packed arrays. The cavitation effects are related to the compressions and rarefactions of the pressure

wave, which produce bubbles on the face of the transducer and can eventually cause the water to rupture. The pressure at which this breakdown, or cavitation, occurs is related to the properties of the water and the operating frequency.

The sonar is typically operated to produce maximum source intensity levels to extend the maximum operating ranges. The maximum level is just below the cavitation threshold and is typically of the order of 228dB re 1μPa at 1m for commercial 100KHz sidescan sonars, as summarised in table 3.1.

6.3 Inclusion of Directivity into Simulation Model

The incorporation of the transducer directivity into the sonar simulation model is a direct extension to the model structure developed in the preceding chapters. This extension will permit the simulation of sidescan sonar images which include the effects of the transducer beam pattern.

The simulation model will calculate the beam pattern of the transducer assuming it is generated by a rectangular grid array. The number of elements within the array and the dimensions of the elements are specified as input parameters to the model. Referring to table 3.1, the beam widths of typical commercially available sidescan sonars tend to be approximately 1° in the horizontal dimension and between 25° and 50° vertically. The parameters used within the simulation model will tend to generate beam patterns with dimensions within this order of magnitude. The other input parameter required to fully describe the beam pattern is the tilt or depression angle. This is the angle, relative to the horizontal, at which the acoustic axis of the vertical lobe is orientated towards the seabed.

The simulation model assumes that the range to any point of intersection is always greater than the near field distance, and the directivity response is calculated for the far field condition. Using the technique discussed in section 6.2.2, the beam pattern for the rectangular grid array is calculated for the range of horizontal and vertical angles. The

vertical angle will be denoted by θ, where θ equal to zero is the horizontal direction. The angle in the horizontal plane will be referred to as ϕ, where ϕ equal to zero is the direction perpendicular to the horizontal axis of the array. The notation adopted for the horizontal and vertical angles is displayed schematically in figure 6.4. The directivity response calculated for the angular range $0 \leq \theta \leq 90^o$ and $-90^o \leq \phi \leq 90^o$ is stored within a two dimensional look up table. A look up table is employed to improve the execution time of the computer program for the simulation model, to prevent the repeated calculation of the directivity response at the same angles.

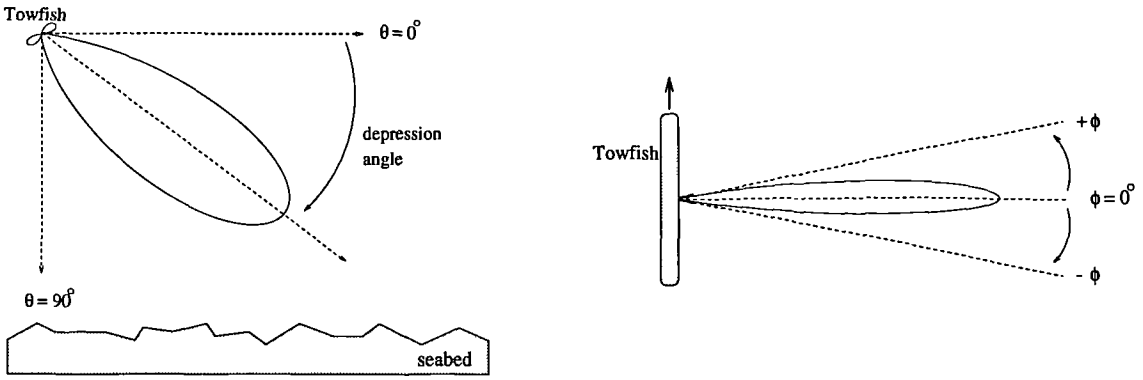

Figure 6.4: (a) Beam angles in vertical plane (b) Beam angles in horizontal plane

Identical directional responses for the transmission and reception of signals are obtained for a sidescan sonar transducer as a result of its reciprocity properties. The one look up table can therefore be employed to calculate both of the responses.

The inclusion of the vertical beam pattern will be considered initially, where it is assumed that the horizontal beam is infinitely thin and knife edged. This assumption results in the effective ensonification of only one line of the seabed perpendicular to the direction of travel of the towfish. A weighting factor is then applied to the intensity value of each of the emitted rays to account for the transmit response of the transducer. The weighting factor is obtained from the look up table, where the vertical angle, θ, is equal to the angle of emission of the ray and the horizontal angle, ϕ, is equal to zero. The

maximum response is obtained for the ray emitted at an angle equal to the depression angle.

The receiver response is included in a similar manner, where the weighting factor due to the receiver beam pattern is obtained from the look up table for the vertical angle of the incoming ray. The weighting factors for the transmit and receive responses are equal for backscattered rays, where the reflected rays returning to the transducer have followed an identical ray trajectory to the outgoing rays. For rays which are the result of scattered energy from multiple reflections the receiving angles, and hence weighting factors, differ from the transmit angles and weighting factors for the emitted rays.

A more realistic transducer will generate a beam with a finite width in the horizontal plane as well as in the vertical dimension. This would result in the ensonification of an area of the seabed, rather than a line, for each pulse of acoustic energy emitted. The area of the seabed ensonified is referred to as the *footprint* of the sonar beam pattern.

To include the full three dimensional directivity response of the transducer, rays must be emitted over a range of horizontal angles and not just perpendicular to the horizontal plane of the transducer. Therefore, in addition to calculating the returns from rays traced with the vertical plane ϕ equal to 0°, rays will be traced within other vertical planes, as illustrated in figure 6.5. The rays remain within the vertical plane in which they are emitted as a result of the horizontal stratification assumption adopted in the development of the model in the previous chapter. Within each vertical plane, the exact curvature of the ray trajectories is determined from the sound velocity profile, using the technique described in section 5.2.3.

Each ray is traced to its point of intersection within the scene and the intensity and time of return are calculated as described previously in section 4.3. The path of the ray is now a function of three dimensions, (x, y, z), since the y coordinate now alters along the ray path. As a result of the horizontal stratification assumption, the y coordinate will

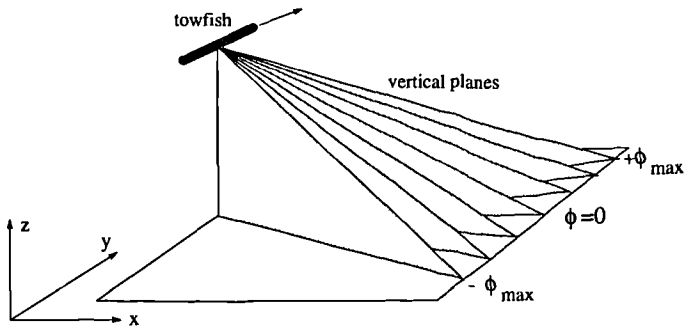

Figure 6.5: Rays traced in vertical planes over full 3 dimensional beam pattern

increase linearly along the ray path, with a linear gradient determined by the tangent of the horizontal angle at which the ray was emitted. The components of the ray trajectory in the x and z planes are determined by the ray curvature.

For each ray traced, a weighting factor for the transmit sensitivity is included. The weighting factor is determined from the look up table for the angle (θ_t, ϕ_t) at which the ray was emitted. The receive directivity factor is incorporated in a similar manner for the reflected ray arriving at the transducer at an angle (θ_r, ϕ_r).

The range of horizontal angles over which the rays are traced, ($-\phi_{max}$ to ϕ_{max}), is determined by the horizontal beam pattern. The minimum angular range is selected to cover at least the beam width defined as the angular width between the half power points. The angular range is generally selected as double this value, unless significant power exists within the side lobes. The number of vertical planes over which to trace rays is also dependent on the beam pattern. The relationship between the simulated image and the number of planes and angular range over which the rays are traced is investigated in section 6.4.3.

The method presented above is not limited solely to the use of rectangular grid arrays but can be extended to any beam pattern. Calibration information from the directivity of actual sidescan transducers can be employed provided the data is first stored in a suitable two dimensional look up table. The directivity responses are often only available

for the vertical and horizontal planes, and the data would need to be interpolated to obtain the weighting factors at other angles.

6.4 Effect of Directivity

Section 6.2 investigated the directional responses of various transducer architectures. The effect of this directional response on the simulated sidescan sonar images will now be considered.

6.4.1 Effect of Vertical Beam Pattern

Initially, only the effect of the vertical beam pattern on the simulated sidescan sonar image will be investigated. This vertical beam pattern will determine the energy distribution incident along a line of the seabed, perpendicular to the direction of motion of the transducer.

The incident energy distribution is dependent on the vertical beam pattern, and in particular the beam width of the main lobe. The side lobes have a smaller response and tend to be orientated away from the main area of interest on the seabed. Since only the seabed reverberation is calculated within the sonar simulation model, and the sea surface reflections are neglected, the effect of the side lobes orientated towards the sea surface is not included. The underlying assumption is that the side lobes directed towards the sea surface possess only a very small magnitude response, and their effect on the image is negligible.

Figure 6.6(a) illustrates the effect of the vertical beam pattern on the intensity incident at the seabed over a range of horizontal distances from the towfish. To permit the visualisation of the influence of the effect of the transducer characteristics, the incident intensity is expressed as a function of the directivity only and the propagation losses are neglected. The incident intensity is plotted for transducer beam patterns with widths of

50°, 40° and 25°, selected from the example transducer characteristics summarised in table 3.1. In all three cases the transducer was situated at an altitude of 10m and a depression angle of 35° was used. A more uniform intensity distribution is obtained across a greater range of the seabed for the wider beam patterns, which is desirable for the application of the transducer as a sidescan sonar. The effects of the side lobes on the intensity distribution can be observed at ranges close to the towfish, near normal incidence.

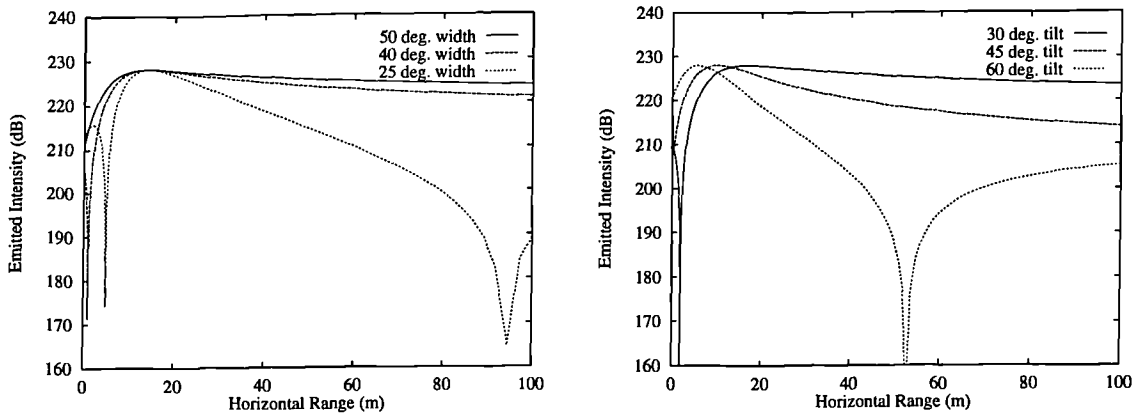

Figure 6.6: (a) Incident intensity as a function of beam width (b) Incident intensity as a function of depression angle

The depression angle of the main lobe will also influence the incident intensity as illustrated in figure 6.6(b). This plots the incident intensity for a transducer at an altitude of 10m with a beam width of 40°, angled at 30°, 45° and 60° from the horizontal. The closer the acoustic axis to normal incidence, the smaller the area of the seabed ensonified by the main lobe. Although it is desirable to steer the transducer towards the seabed to avoid sea surface reflections, a more uniform intensity distribution is obtained with shallower depression angles. The optimum depression angle for a particular application is a function of the maximum operating range. The majority of commercially available sidescan sonars have operator controllable steering angles.

The transducer response will also influence the reception of the signal reflected back to the transducer. The total effect of the transmit and receive responses on the signal

backscattered from a flat planar seabed is illustrated in figure 6.7. Figure 6.7(a) displays the received signal if unity transmit and receive responses are assumed. Figure 6.7(b) then displays the received signal for a transducer with a vertical beam pattern with a width of 50° and a depression angle of 15°. The maximum return is no longer dominated by the near normal backscattering from directly below the towfish, due to the lower directivity response of the transducer in this area. This is a result of the finite beam width and the orientation of the side lobes. In figure 6.7(b) a null point exists between the response of the main lobe and the first side lobe; such null points are normally removed in actual sidescan sonar directivity patterns by the application of techniques such as shading. At greater ranges, where the directivity response is more uniform, the difference between the uniform beam pattern and the directional response is less apparent.

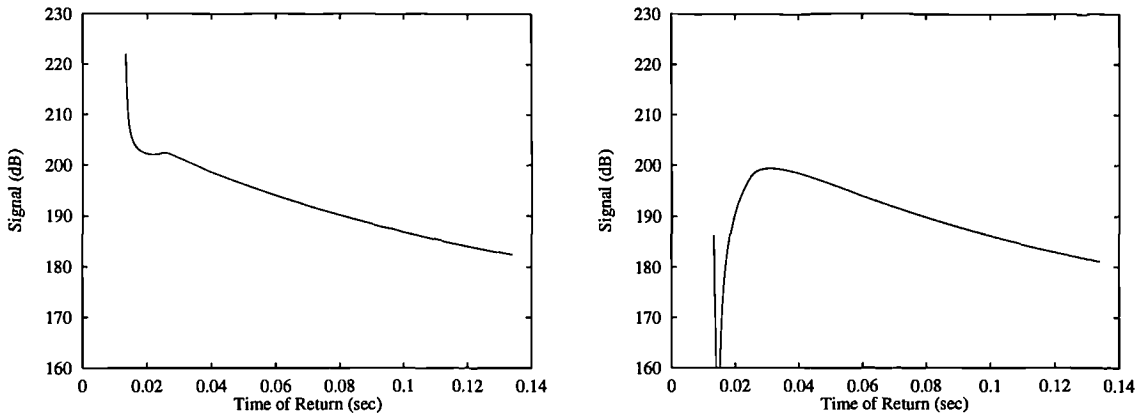

Figure 6.7: (a) Received signal with unity beam pattern (b) Received signal with actual beam pattern

The position of the maximum response is now determined by the depression angle and towfish altitude. The overall signal received at the transducer is therefore influenced by the vertical directivity response. This is also illustrated in the simulated sidescan sonar images of a totally flat seabed as displayed in figure 6.8. Figure 6.8(a) is simulated using a uniform beam pattern and figure 6.8(b) is simulated using a transducer with a beam width of 50° and a depression angle of 15°. The alteration in the intensity distribution between the two simulated images as a result of the vertical directivity response can be

observed.

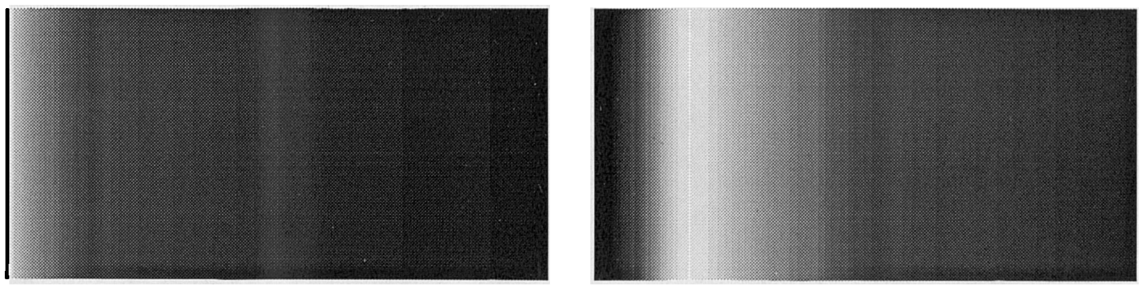

Figure 6.8: (a) Simulated image with unity beam pattern (b) Simulated image with actual beam pattern

6.4.2 Effect of Three Dimensional Beam Pattern

The previous section has considered the effect of only the vertical beam pattern on the simulated signal. The transducer will emit and receive energy over three dimensions, and this resulting effect of ensonifying an area of the seabed, rather than a single line, will influence the image produced.

The along track, or transverse, resolution of the sidescan is influenced by the finite dimensions of the transducer directivity in the horizontal dimension. The effect of tracing rays emitted over a three dimensional beam pattern rather than in the plane perpendicular to the transducer is illustrated in figure 6.9. Figure 6.9(a) displays the simulated sidescan sonar image of a box on a seabed with a sand ripple structure. The simulation has assumed a knife edged beam and each line of the image is composed from the returns calculated from a single line of the seabed scene. This results in a simulated sidescan image where the edges of the box perpendicular to the direction of travel of the towfish are sharply imaged as straight lines. The simulation of an identical scene which has been ensonified by a transducer with a horizontal beam width of 1° is displayed in figure 6.9(b). The along track resolution of the image is degraded by the effect of the horizontal beam width and the edges of the box and the associated shadow are blurred.

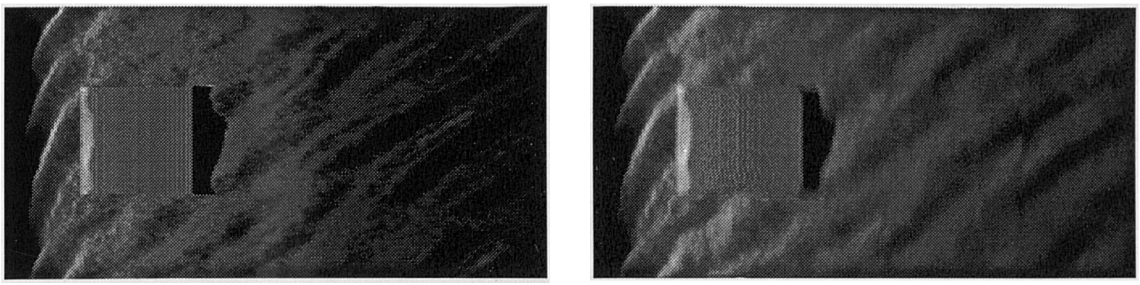

Figure 6.9: (a) Simulation using knife edged beam (b) Simulation using three dimensional beam pattern

The effect of the horizontal beam width and the beam spreading with range is illustrated in figure 6.10. Both images are simulated sidescan records of spherical objects on a flat seabed. Figure 6.10(a) has been simulated with a horizontal beam width of 0.5° and figure 6.10(b) with a horizontal beam width of 1°. The resolution of the images clearly degrades with increasing horizontal beam widths, and this can result in the inability to distinguish two targets which are spaced closely together in the along track direction. The transverse resolution also degrades with increasing range from the transducer due to the beam spreading.

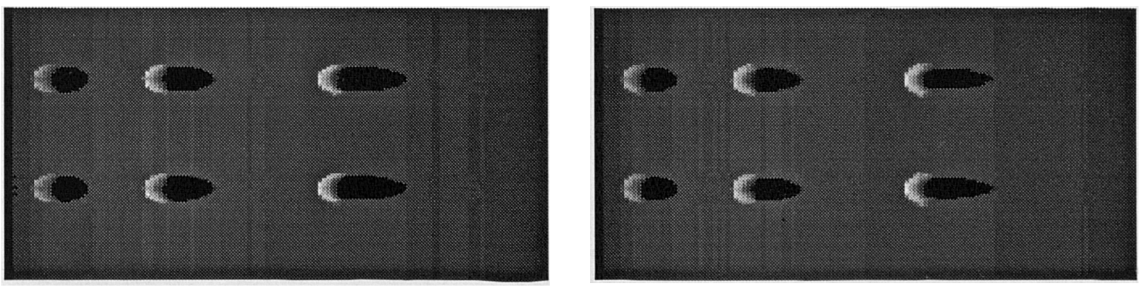

Figure 6.10: (a) Simulated image using 0.5° beam width (b) Simulated image using 1° beam width

The along track resolution is a function not only of the horizontal beam width but also of the tow speed and the pulse repetition rate. The latter two factors are operator controllable and their effect on the image can be minimised or at least quantified. The beam pattern is dependent on the transducer design and it is therefore important to be able to

visualise its effect on the sidescan sonar image.

6.4.3 Assumptions

To incorporate the effect of the horizontal beam width within the simulation model, rays are emitted and traced over the horizontal angular range, $-\phi_{max} \leq \phi \leq \phi_{max}$, displayed in figure 6.5. If rays are traced over the entire horizontal range from ϕ equal to -90° to +90°, the execution time of the model is prohibitively slow. For rays traced at angles greater than a certain angular limit, the energy contributions are virtually negligible, due to the directional response, and no significant contribution is made by them to the received intensity. Within the model the "rule of thumb" was applied that rays traced at horizontal angles greater than twice the angle of the half power point result in no significant energy contributions.

This assumption can be justified with consideration of figure 6.11. This displays the relative intensity contributions for rays traced within vertical planes where the horizontal angle, ϕ, is equal to the angles stated in degrees. The seabed was assumed to be a totally flat planar surface. The horizontal beam pattern employed had a total beam width of 1° between the half power points, and the maximum emitted intensity was set to unity. The graph displays the relative intensity values including the transmit and receive responses and the bottom reverberation, but the propagation loss is assumed to be fully compensated by the time varying gain.

Increasing values of horizontal angle resulted in decreasing intensity contributions, with approximately half the intensity received at ϕ equal to 0.5°, the half power point of the beam width. As the angle increased to 1°, the intensity contributions were reduced by a factor of approximately 500 and produced no significant contribution to the total received intensity. For angles greater than 1°, the intensity contributions were even smaller, even from the first side lobes centred at 1.6°. This is displayed in figure 6.11(b) where the different scale on the y axis should be noted.

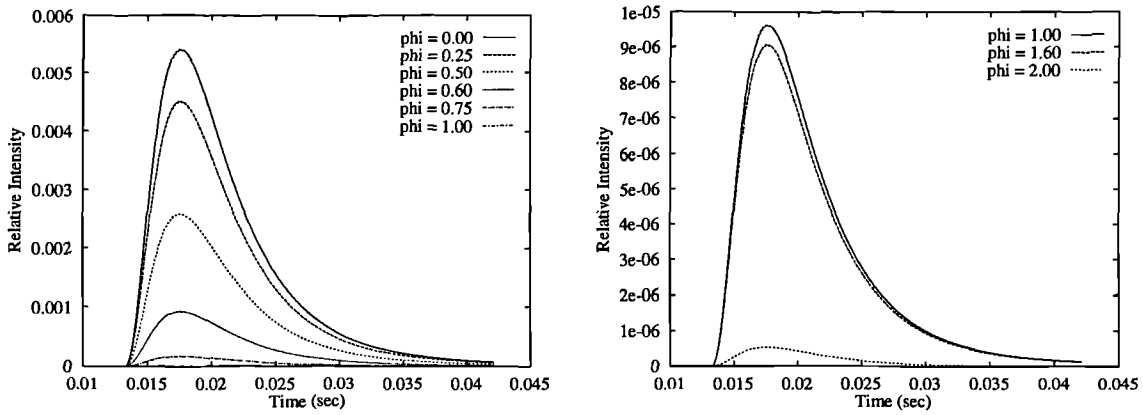

Figure 6.11: Intensity returned against time for rays emitted in vertical planes at horizontal angles stated

The model therefore calculates the intensity contributions within the angular range $-\phi_{max} \leq \phi \leq \phi_{max}$, where ϕ_{max} is equal to the horizontal beam width. The simulation model is flexible in its construction and this value may be altered if significant power exists within the side lobes.

The second assumption is introduced by tracing rays only within a finite number of vertical planes for each line of the image. This arises as a result of the problem of modelling a continuous process with a finite number of rays. The number of rays to emit and trace in each vertical plane was discussed in section 3.4.6. The number of vertical planes within the horizontal angular range, over which to trace rays, also needs to be specified.

The number of vertical planes required is a function of the beam width and the maximum range, which determines the spreading of the beam. The larger the value of either parameter, the greater the number of planes required. The number of planes must always be sufficient to ensure the separation between the planes at the maximum range is not greater than the dimensions of any feature or of the triangular planes representing the facets of the seabed.

Typically within the images simulated, the planes were equally spaced at angles of approximately 0.25°. This selection was made with consideration of both the execution

time and the visual effect on the simulated image. Figure 6.12 displays the same scene ensonified by a transducer with a horizontal beam width of 1°, but simulated using planes equally spaced at 0.5° intervals, 0.25° intervals and 0.125° intervals. Visually very little difference can be distinguished between the images, although the differences are slightly more apparent at greater ranges.

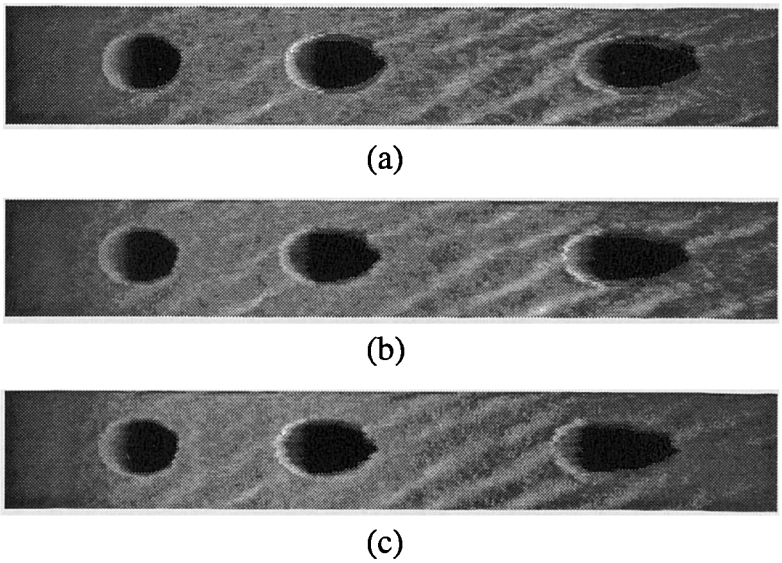

(a)

(b)

(c)

Figure 6.12: Rays traced in vertical planes equally spaced at (a) 0.5° intervals (b) 0.25° intervals (c) 0.125° intervals

The number of planes to trace rays over provides an input parameter to the simulation model and is therefore easily altered. The value selected is a function of both the scene to be simulated and the parameters employed in the simulation to represent the sidescan sonar.

6.5 Motion Characteristics of Transducer

The model developed in the preceding chapters has assumed that the transducer follows a straight line path at constant speed. This is the ideal case, but it rarely occurs due to the effects of towing the sidescan transducer. The towing effects can alter the

trajectory, speed and orientation of the towfish.

The sidescan transducer is normally towed by a cable behind a survey vessel, and the motion of the survey vessel therefore influences the movement of the towfish. The speed and course of the vessel can be altered as a result of wind and sea currents and this motion is communicated to the towfish via the cable. The towfish motion can also be directly affected by underwater currents or eddies. These currents will also affect sidescan transducers mounted on ROTVs, flown remotely by operators aboard ship. It is also difficult for the operator to maintain a constant straight line trajectory for the ROTV as a result of the problems of visualising the remote position of the vehicle.

The motion instabilities of the towfish can be separated into the two categories of translational and rotational motion. The translational motion describes the towfish position in three dimensional space and its velocity. The vertical motion of the transducer is depicted as *heave* and the lateral motion as *sway*. The rotational motion characterises the orientation of the towfish and is expressed in terms of the *roll*, *pitch* and *yaw*.

The motion instabilities of the transducer will further distort the images of the seabed generated by the sidescan sonar. Roll results in intensity distortions on the image, and pitch and yaw produce geometric distortions. Geometric distortions are the discrepancies of object locations on the sidescan image compared to the actual location of features on the seabed. The effects of these motions and the subsequent distortions must be understood to allow accurate interpretation of sidescan sonar images. The effect of these distortions is discussed by Flemming [121], while Cobra *et al.* [3] have presented processing techniques to estimate and correct the geometric distortions on sidescan sonar images.

Within the simulation model, these translational and rotational motions influence the actual position of the towfish from which the rays are traced and the orientation of the beam. This will alter the area of the seabed ensonified by each emitted pulse of acoustic

energy. The following sections will consider the implementation of these motions within the sonar simulation model and their resulting effects on the images produced. Since the translational motion will generally result in a corresponding rotational motion, or vice-versa, it can be difficult to isolate the individual aspects of the motion. The following sections therefore consider the combined effects of the yaw and sway and the pitch and heave, although any of the motions can be considered in isolation.

The discussion of the implementation assumes the towfish trajectory, in three dimensional space, is read from an input file. The (x, y, z) coordinates within the file describe the position of the towfish from which each pulse of acoustic energy is emitted. The angular orientation of the towfish is obtained from the angular displacements between the consecutive points at which the signal is emitted.

6.5.1 Yaw and Sway

Yaw describes the rotational movement produced by the side to side towing instabilities. This is generally the result of the off course motion of the survey vessel automatically producing a corresponding towfish motion. The translational movement of the towfish in the lateral direction is depicted as the sway.

The sideways motion results in the sonar beam periodically scanning ahead and then behind on each channel. This motion is illustrated schematically in figure 6.13 using a plan view of the motion.

With reference to the coordinate system defined previously in figure 6.5, this sideways motion will alter the x coordinate of the towfish, which was previously assumed to remain constant. The towfish coordinates are therefore updated when each set of rays are traced. The rotational movement will alter the horizontal angle at which the acoustic axis of the beam is centred. The simulation model traces the rays emitted in vertical planes along the acoustic axis and those in planes offset by up to $\pm\phi_{max}$ from the axis which

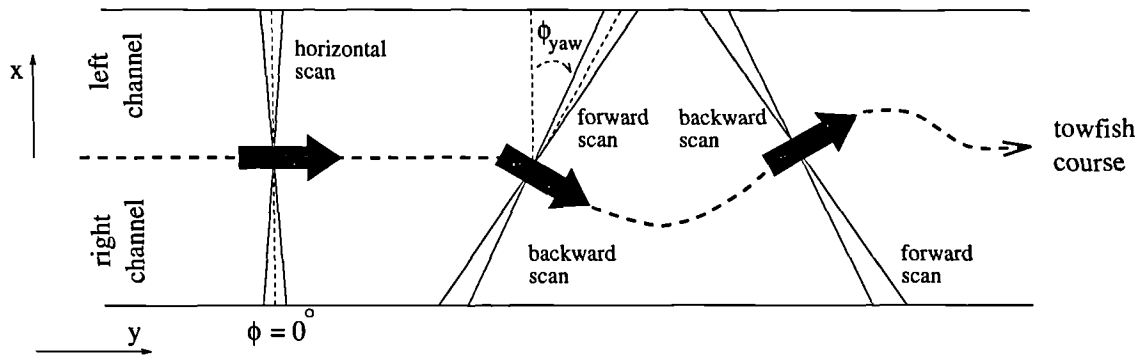

Figure 6.13: Schematic of distortional effects of the yaw and sway motions

describe the beam pattern, as explained in section 6.3. An offset angle to account for the yaw, ϕ_{yaw}, is added to the horizontal angles since the acoustic axis is now centred on ϕ_{yaw} and not on ϕ equal to 0° as for the horizontal scan. The orientation of the acoustic axis in the horizontal plane and the corresponding offset angle will alter dependent on the ray trajectory.

The effect of this sideways motion is illustrated in figure 6.14. Figure 6.14(a) displays schematically a plan view of the scene in addition to the sway and yaw of the towfish trajectory. The scene consists of 9 spherical objects arranged in a grid format on a flat seabed and is ensonified by a sonar at a constant altitude of 10m. The simulated sidescan sonar image of this scene is then displayed in figure 6.14(b). The spheres in the first row, row_1, perpendicular to the ideal towfish path, appear in triplicate as they were scanned during the forward scan, the horizontal scan and the backward scan of the beam. The image of the sphere closest to the towfish is altered least, since it is ensonified over a shorter period of the towfish motion. The other two rows of spheres are imaged only once due to the transducer motion. The spheres in each of these rows do not appear in parallel lines, as illustrated in the schematic of the scene, since row_2 is backward scanned and row_3 is forward scanned during this part of the trajectory.

Although the spheres in each row are located at the same horizontal ranges from the transducer, their positions are distorted on the image due to the lateral horizontal

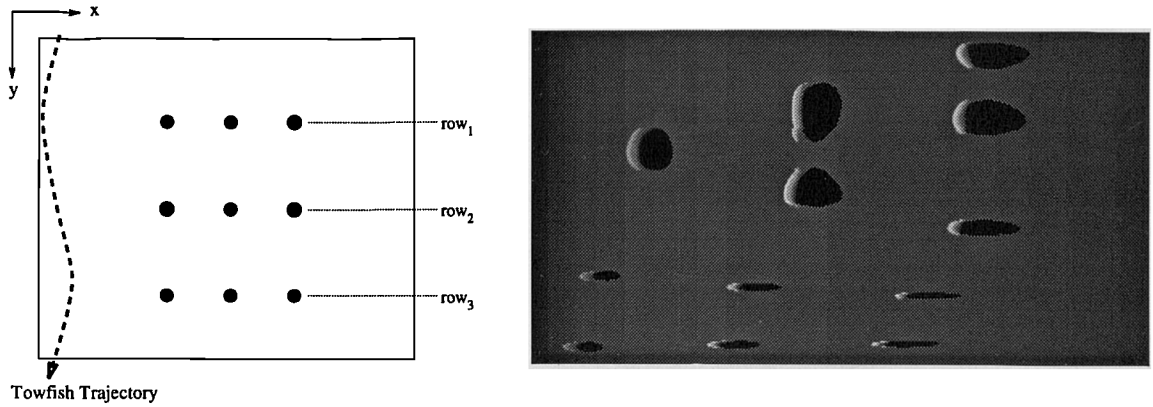

Figure 6.14: (a) Schematic of scene (b) Simulated sidescan sonar image of scene

motion, or sway, of the transducer.

The effect of yaw is also encountered when the vessel turns to change the direction of survey. An example of this turning effect on sand ripples is illustrated in figure 6.15. Figure 6.15(a) illustrates a simulated sidescan sonar image of sand ripples where the tow-fish has followed a straight line path and no distortion has occurred. Figure 6.15(b) and (c) simulate the effects of a shallow turn or curved trajectory. The inward turn and resulting compression of the image is displayed in figure 6.15(b) and (c) simulates the reverse outward turn, which would be encountered by the opposite channel, and the resulting sweeping and expansion of the sand ripples.

6.5.2 Roll

The roll of the transducer produces intensity distortions on the sidescan sonar image, as a result of the alteration of the orientation of the beam within the vertical plane. This rotational motion is displayed schematically in figure 6.16, for a transducer with no roll, rolled backwards and rolled forwards. The rolling alters the depression angle at which the acoustic axis is orientated within the vertical plane and the horizontal range of the seabed ensonified by the main lobe of the beam. This results in a variation in the intensity distribution with horizontal range, of the form displayed in figure 6.6(b) for

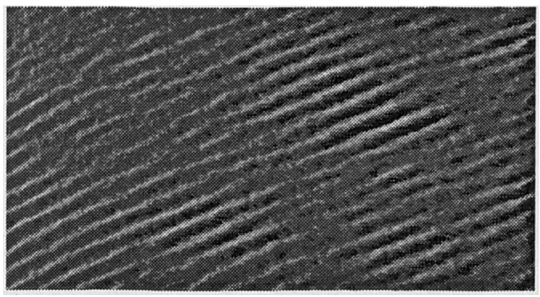

(a)

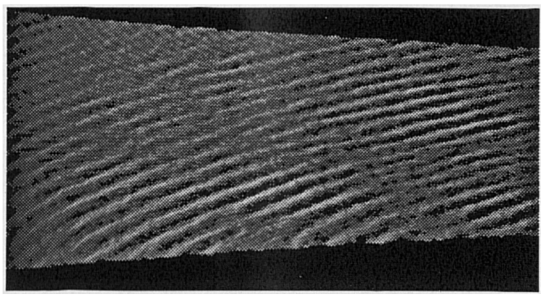

(b)

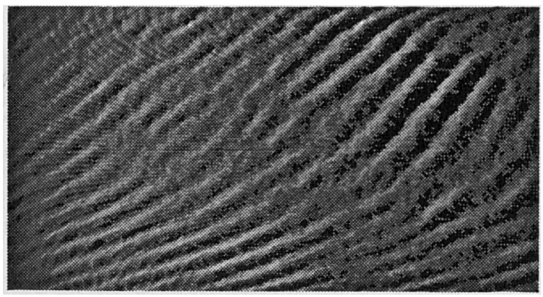

(c)

Figure 6.15: Simulated sidescan sonar images with towfish trajectory in (a) straight line (b) inward turn (c) outward turn

differing depression angles.

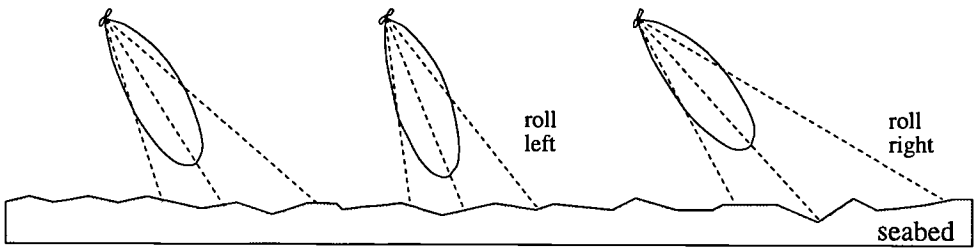

Figure 6.16: Schematic of distortional effects of rolling motion of the transducer

To incorporate the effect of the roll within the sonar simulation model, the depression angle of the beam is varied. The subsequent distortion effect is illustrated in figure 6.17, where figure 6.17(a) is a simulated sidescan sonar image with a constant depression angle of 30° and figure 6.17(b) includes a low frequency rolling motion. The original depression angle of the beam was 30° and this was increased in a sinusoidal manner to a maximum of 40° and then decreased again. The location of the maximum intensity from

the axis of the main lobe correspondingly moved toward the start of the trace and then out to the original range again. The inverse effect would be observed on the opposite channel, with the maximum intensity moving out to greater ranges and then back inwards again.

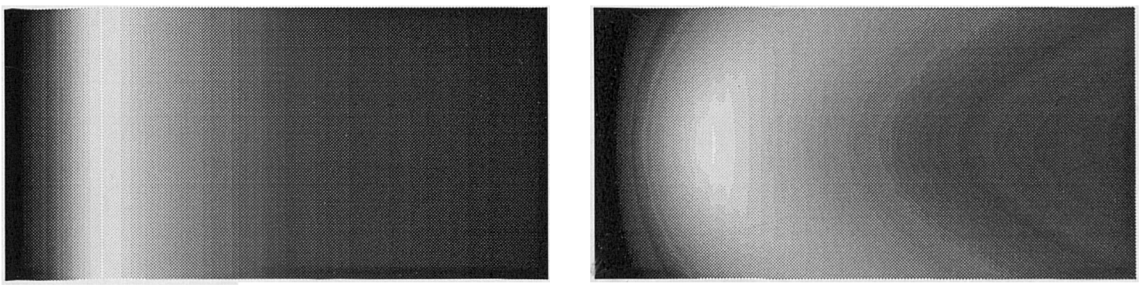

Figure 6.17: (a) Flat seabed ensonified with no roll of transducer (b) Rolling effect included

The rotational effect of roll does not frequently occur in isolation, but more commonly in addition to other motion related distortions. In particular, the towfish will often bank during turns, rolling the transducer. Roll can also result from the survey track running parallel to the crestlines of prevailing swells or waves.

6.5.3 Pitch and Heave

The pitch and heave of the towfish are related to its vertical motion. The increase and decrease of the towfish altitude is described by the heave and the subsequent rotation forwards and backwards within this vertical plane is defined as pitch. This motion is displayed schematically in figure 6.18. As the towfish tilts upwards it scans forwards and as it tilts downwards it scans backwards. Unlike yaw and roll motions, pitch results in identical distortional effects on both channels.

The fluctuations in the towfish height have a direct effect on the first bottom return. This is displayed in the simulated sidescan sonar image of figure 6.19(a), where the towfish altitude has varied from 10m to a maximum of 11m and a minimum of 9m in a sinusoidal manner. The variation in fish altitude is apparent in the first bottom return, where

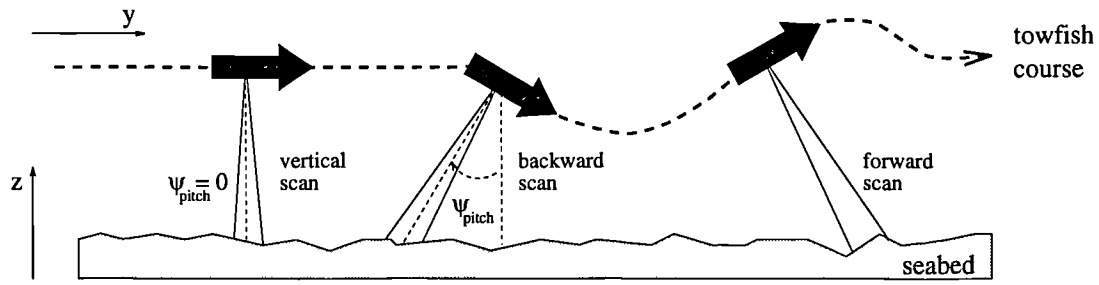

Figure 6.18: Schematic of distortional effects of the pitch and heave motions

the greater the altitude, the longer the period of no return. The effect of the heave on the sidescan image reduces with increasing range, an effect which can be directly visualised in figure 6.19(a). The fish altitude has a lesser effect on the image of the cylindrical pipeline on the seabed, which appears straighter than the first seabed return. The pipeline is lying parallel to the direction of travel, or y axis, but at a horizontal range of 15m from the towfish.

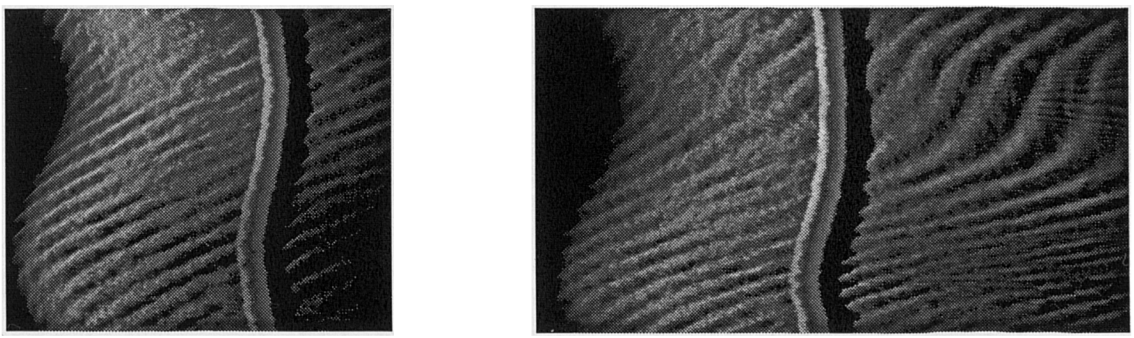

Figure 6.19: (a) Simulated image calculating heave distortions only (b) simulated image including heave and pitch distortions

Figure 6.19(a) has neglected the distortional effects of the towfish pitch and assumed the body of the towfish does not rotate as it rises or sinks. The towfish is liable to pitch as the altitude changes and scan forwards or backwards. The sonar simulation model calculates the pitch angle, ψ_{pitch}, from the change in altitude between two consecutive points on the towfish trajectory. As the towfish pitches, the acoustic axis of the beam is rotated in both the horizontal and vertical planes. Therefore, the depression angle

alters, as does the angle, ϕ, at which the acoustic axis is located in the horizontal plane. If the pitch angle is denoted by ψ_{pitch}, the angle of the acoustic axis in the horizontal plane, ϕ_{pitch}, can be calculated from equation 6.9 and the new depression angle, θ_{pitch}, can be obtained from equation 6.10. The original depression angle is denoted by θ and the acoustic axis is assumed to centred on $\phi = 0^o$ in the horizontal plane when no pitching motion occurs.

$$\phi_{pitch} = \frac{\pi}{2} + \tan^{-1}\left(\frac{\tan\theta}{\sin\psi_{pitch}}\right) \tag{6.9}$$

$$\theta_{pitch} = \frac{\pi}{2} - \sin^{-1}\left(\cos\theta\cos\psi_{pitch}\right) \tag{6.10}$$

The changing horizontal angle, ϕ_{pitch} is included in the simulation model in a similar manner to the effect of yaw, as described in section 6.5.1. The distortional effect of the alteration in the depression angle is similar to the roll of the towfish.

Including the pitching of the transducer into the simulation model, figure 6.19(b) illustrates the subsequent geometric distortion in the simulated image. The images of the sand ripples are compressed and elongated in the along track direction due to the forward and backward scanning.

Pitching does not often occur in isolation, but is encountered more commonly in association with the heave. The fluctuations in the towfish height are normally related to the survey vessel moving up and down in heavy swell. The vessel speed will also alter with the swell and this can result in the towfish sinking and rising.

6.5.4 Speed of Transducer Motion

The features of the sidescan image in the along track direction are affected by the speed of the towfish. If the other display factors such as the range scale and feed rate

remain constant, the effect of speed distortions can be directly visualised in the sidescan image. The distortions result in the compression or elongation of the features in only one dimension, in the along track axis. Flemming [122] discusses these speed distortions and presents methods for their graphical correction using distortion ellipses.

The faster the towing speed, the shorter the objects or features will appear in the along track direction. The objects will also appear on the image with less detail since fewer echoes will be received from each target.

All of the simulated images generated previously have assumed that the transducer is moving through the water at a constant velocity, and the distance between consecutive points on the towfish trajectory from which the pulse was emitted also remained constant. By varying this distance, the effective speed of the towfish can be altered within the simulation model.

The effect of the towfish speed on the ensonification of a spherical target is illustrated in figure 6.20(a). The four identical spherical targets on a flat seabed have been ensonified from a constant range, but each at different speeds. The four speeds are illustrated on the figure in relative terms, where each of the four sections of the image represent the same distance over the ground. The faster the towfish travels the more compressed the target appears in the along track direction.

The speed variations will also distort the apparent angles of features on the seabed. It is therefore difficult to determine the orientation of targets or sediment boundaries on the seafloor. This is illustrated in figure 6.20(b), where an area of sand ripples was traversed at each of the four speeds stated on the figure. This figure can be compared to the undistorted image traversed at constant speed which is displayed in figure 6.15(a). The angles of the sand ripples relative to the towing direction alter depending on the speed. The greater the speed, the closer the sand ripples appear to the perpendicular.

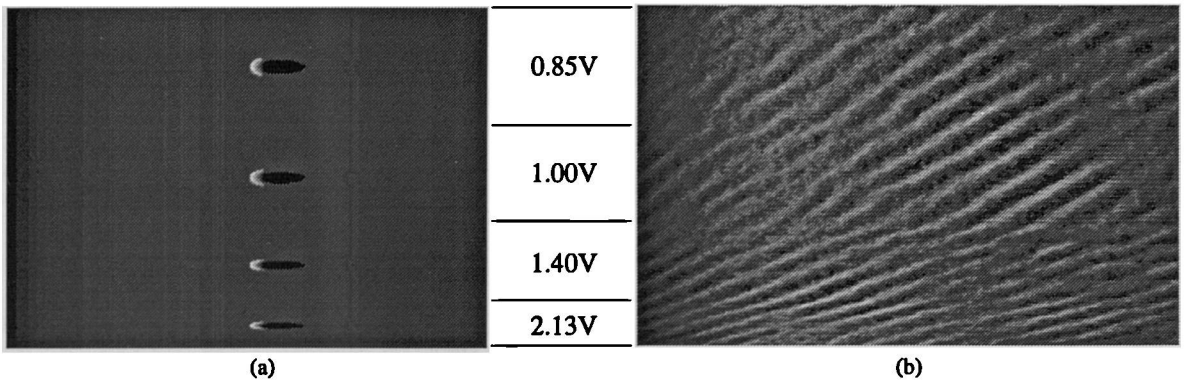

Figure 6.20: Speed distortions

With the recent advances in technology, many commercial sidescan sonar systems have integrated navigational and sensor data. From the navigational data, the survey data collected is correlated directly with the vessel's speed over the ground and the speed distortions on the sidescan images are minimised.

6.6 Towfish Motion Assumption

It has been assumed throughout the development of the simulation model that the towfish remains stationary from the moment a pulse is fired until the return from the maximum range is received. The towfish is then moved to the next position and the process is repeated. This implies that the scan lines, defined as the intersection of the acoustic axis of the beam pattern with the seabed, are approximated as straight lines. This is illustrated schematically in figure 6.21(a), for a towfish following a straight line trajectory.

The towfish motion is continuous in the actual sidescan sonar process and the receiving beam pattern keeps moving ahead during the acquisition of each line of the image. The scan lines from the maximum received signal are bent forward as the acoustic axis of the receiver beam pattern moves forward. The bending of the scan lines is illustrated in figure 6.21(b).

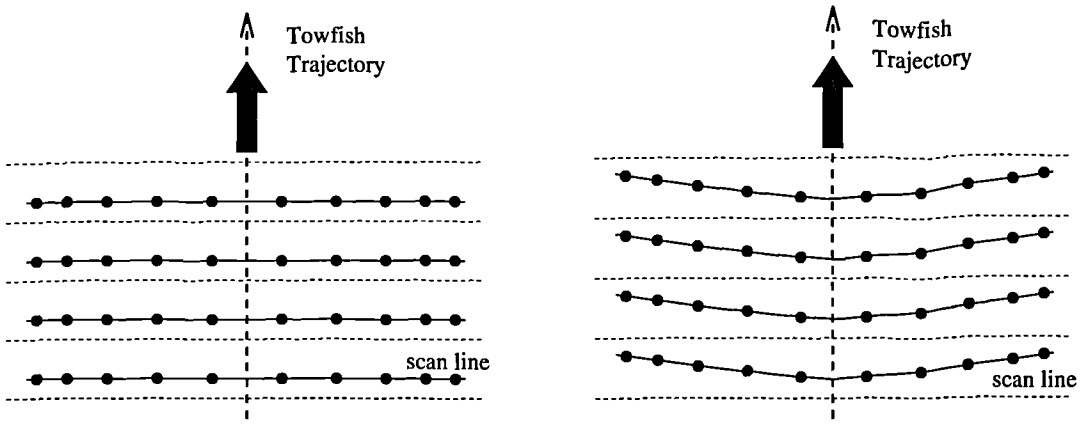

Figure 6.21: (a) Towfish stationary between transmit and receive (b) Towfish moves continuously between transmit and receive

Since the maximum range of the sonar is much larger than the spacing between scan lines in the along track direction, the error resulting from approximating the scan lines as straight is minimal. The magnitude of the error depends on the towfish speed and the pulse repetition rate, which is determined by the operating range of the sonar. The slower the towing speed, the smaller the error introduced.

The typical towing speed of a high resolution sidescan sonar with a range of 100m is of the order of 4.5 knots, (2.25 ms^{-1}). This results in the towfish moving approximately 0.3m in the time period until it receives the signal from the maximum range of 100m. The signal from any range is received offset from the main acoustic axis of the receiver by 0.172°. For the transducer with a 1° beam width, as employed in the previous simulations, the receiver directivity response is 0.351dB below the response of the acoustic axis at this point.

The ray from the seabed returning to the transducer is no longer the backscattered ray, but is scattered in the bistatic plane at an azimuthal angle of 0.172°. Using the bistatic model of Jackson [71], the implementation of which was discussed in chapter 4, the scattering strength from a sandy seabed for the azimuthal orientation of 0.172° is less than 10^{-4}dB below the in-plane backscattering at any scattering angle.

The main error introduced is therefore related to the receiver beam pattern, and can be considered as minimal for the simulation of high resolution sidescan sonar. The curvature of the scan lines will have a stronger influence on long range sonars operating at low pulse firing rates. The extension of the model to remove the assumption of the discrete motion of the towfish and the subsequent approximation of straight scan lines provides part of the future work of this project.

6.7 Conclusions

This chapter has investigated the directivity responses of the standard configurations of sidescan sonar transducers. The directional response can be visualised in terms of the beam pattern, displaying the response as a function of the solid angle in three dimensional space. The finite dimensions and reciprocity principles of sonar transducers produce identical three dimensional responses for both the transmission and reception of signals.

Sidescan sonar transducers typically produce beam patterns with a main lobe which is wide in the vertical dimension and narrow horizontally. The acoustic axis of the centre of the lobe is normally perpendicular to the horizontal axis of the transducer and steered towards the seabed in the vertical axis. The beam pattern of the transducer will result in the ensonification of an area of the seabed, and not a single line perpendicular to the direction of travel, as previously assumed. The vertical response of the transducer characteristics results in a non uniform intensity distribution with range in the across track direction, whilst the horizontal beam width degrades the resolution of the image in the along track direction, an effect which increases with increasing range due to the beam spreading.

The effect of towing the transducer through the water produces rotational and translational instabilities in the towfish, which can alter its trajectory, speed and orientation. These instabilities produce geometrical and intensity distortions on the sidescan sonar

image, and the simulation model was extended to include the effects of the rotational and translational motions of the towfish. This produces a powerful tool for investigating the effects of the motion characteristics of the transducer, which could be employed for the testing of complex algorithms for the motion compensation of sidescan sonar images.

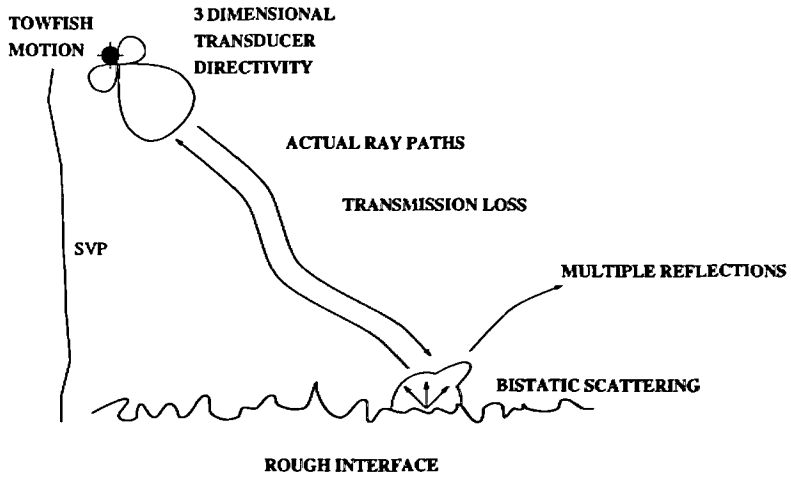

Figure 6.22: Summary of simulation model

The current status of the model is summarised in figure 6.22. All of the simplifying assumptions introduced in chapter 3 have now been considered. The simulation model now includes the directivity responses for both the transmission and reception of the acoustic signal, the effects of the acoustic propagation through the water medium, and the reverberation from realistic models of the seabed topography. The model now incorporates the main deterministic factors influencing the sidescan sonar process. However, the sidescan process is very complex and the simulation model developed within this thesis to represent it could be further extended by the incorporation of stochastic models and other features. Proposed extensions to the features of the simulation model will be considered in chapter 8.

Chapter 7

Investigation of Simulated Images

7.1 Introduction

The previous chapters of this thesis have concentrated on the development of the sonar simulation model, and little consideration has been given to determining the accuracy of the model output. The verification of the output has been purely visual, in that visually realistic sidescan sonar images could be generated. The simulation model has also been demonstrated to correctly represent artifacts and effects of the sidescan sonar process, such as shadows, beam effects and motion characteristics.

The sidescan sonar process produces a qualitative representation in image form of the seabed. No closed form analytic expression exists to represent this complex process. This chapter will discuss the resulting problems of testing and verifying the qualitative output of the sonar simulation model and will consider visual, statistical and spectral techniques for verification. The statistical techniques are applied to verify primarily that the treatment of the seabed roughness by the simulation model appears to be correct, whereas the spectral methods investigate the sediment type. Although a definitive test cannot be constructed to quantitatively verify the model output, the chapter will investigate techniques to further increase confidence in the results generated by the model.

7.2 Problems of Model Verification

Unfortunately, no simple test exists to check the validity of the output of the sonar simulation model. This is partially related to the fact that the sidescan sonar process produces images which are a qualitative and not quantitative representation of the seabed. There are several approaches available for testing the output of a model to gain confidence in the result. These methods include comparing the model output with real data, comparing the output with other models or benchmarks, and the verification of the submodels. Each of these methods will be considered in the following sections.

7.2.1 Comparison with Real Data

Normally, the ideal method of verifying the output of a model is to perform an experiment under controlled conditions and attempt to replicate the experimental outcome using the model with the experimentally derived parameters as inputs. Unfortunately, during the period of study, no access to the range of the experimental facilities required was available. In addition, very little information accompanied the existing sidescan data which was available, since no ground-truthed data or information about factors such as the environmental conditions or transducer characteristics was included with the majority of the datasets. However, even if experimentation were possible, the problem of obtaining a definitive data set to fully describe the experimental environment renders the task prohibitive.

The main problem lies in obtaining information on the seabed topography and structure. The parameters describing the transducer can be calibrated in advance and attitude sensors attached to determine the rotational, translational and altitude characteristics of the towfish motion. If the assumption of a horizontally stratified media is applied, the velocity of sound needs to be measured with a CTD device at only one location, but ideally the velocity should be determined at several sites to ensure the assumption is satisfactory.

To accurately characterise the seabed structure for the area ensonified, information is required to describe the topography and sediment characteristics. The topography information must be determined on a scale comparable to the pulse length of the sonar. However, it is virtually impossible to obtain high resolution topographic information over a large area. Bathymetric sonars generate coarse, low resolution information, which is subject to the errors of the approximations in the calculations. Briggs [11] discusses techniques to obtain high resolution roughness measurements over an area of less than $1m^2$, and concludes that stereo photography is optimal when the water clarity permits. It is, however, difficult to obtain large area coverage with this technique due to the problems of maintaining a reference frame. As a result of the mismatch in resolution between different sensors, it is difficult to co-register data from sensors measuring the topography at different resolution scales.

The sediment characteristics can be obtained using core samples, but the area of the seabed over which this sediment structure is representative must be determined. Typically, this is one of the functions of sidescan sonar surveys. However, the boundaries of the sediments detected within the sidescan image cannot be directly correlated to the actual sediment boundaries on the seafloor, as a result of the distortional effects of the sidescan process.

Difficulty also arises in performing experiments under controlled conditions. The use of laboratory tanks is impracticable due to the multiple paths created by the reflections from the tank sides which can mask the actual bottom reverberation. Limitations also arise in performing experiments at sea, since the seabed and the surrounding environment are not static, but can alter with factors such as the tides and weather conditions. All of the environmental data must be monitored continuously to ensure it is valid at the time when the sidescan image was generated; the process of experimentally determining the environment is therefore subject to high costs and operational difficulties. In addition it is difficult to determine if differences between the image synthesised by the model and the

actual sidescan sonar image arise due to the limitations of the simulation model or as a result of the inaccurate specification of the input data set.

The problem of how to compare the output of the simulation model to the actual sidescan sonar image also occurs, since qualitative images are generated by both the simulation model and the sidescan sonar process. Is a visual comparison of the images suitable in this instance or should techniques such as statistical analysis be performed? The comparison of images will be considered further in sections 7.3 and 7.4.

7.2.2 Comparison with Other Models

Inter-model comparisons provide a recognised technique for the testing of computational schemes, such as the sidescan sonar simulation developed in this thesis, where no closed form analytic solution is available. This technique, though, requires access to alternative models applicable to the problem, and no directly comparable models exist at present. It is hoped that comparisons may be possible with the SWAT [5] model in the future, but this model remains classified at present and is still under development.

Inter-model testing has gained acceptance within fields such as propagation modelling, where several numerical solutions to low frequency propagation problems have been formulated. Benchmark solutions have been computed as standard reference solutions against which the propagation codes can be tested [39]. These benchmarks have been created to permit meaningful comparisons of models and improve confidence in the published results.

7.2.3 Verification of Sub-Models

A common technique in the testing of complex models, created from several subsidiary models, is to test each of the sub-models independently and assume the interaction of the sub-models does not affect their validity. This technique is frequently applied in the

testing of computer based models, although difficulties can arise in testing individual sub-models experimentally as a result of the problems of isolating individual parameters. This technique is applied by Sammelmann in the testing of the SWAT model [80], where the target strength model has been compared to experimental data, but the subsequent incorporation of the target strength model into the image synthesis model was assumed not to affect the validity.

In examining the sub-models and their interactions, it is important to ensure that any approximations introduced are valid in all of the sub-models. The major sub-models of the sonar simulation model are the bottom reverberation, acoustic propagation and transducer models. The results obtained from each of these models after implementation were checked against published data to ensure no errors were introduced during programming, but the underlying assumption is that the models have been thoroughly tested by the originators.

The bistatic reverberation model has been tested by Jackson *et al.* [71] [72] [66] [68] at several sites for various sediment types and good experimental comparisons were obtained. The implemented reverberation model has the ability to replicate Jackson's results using sediment properties and parameters specified by him.

The ray tracing model implemented to calculate the path of the acoustic propagation was also compared to published results of ray traces within horizontally stratified media. The absorption loss characteristics were also reproduced accurately. The spreading loss model was verified for the isovelocity situation and the obvious increase and decrease in spreading loss was observed for divergent and convergent profiles respectively. The ray tracing solution is a high frequency approximation to the wave equation, and is therefore valid for the operating frequencies of sidescan sonar. The reverberation model was also developed specifically to model high frequency scattering. The approximations inherent in the ray tracing solution and the result of the horizontal stratification assumption were discussed in chapter 5.

Throughout the development of the model, all possible steps were taken to minimise the introduction of possible sources of errors, and the consequences of any assumptions introduced in deriving the model were considered.

The above discussion has highlighted the problems in directly verifying the model output. Visual, statistical and spectral methods to increase confidence in the output of the simulation model will now be presented.

7.3 Visual Comparison

Sidescan sonar images can be considered as representing textures, with complex images composed of a number of regions of different textures, corresponding to different seafloor structures or sediments. The majority of image and texture analysis and processing produces subjective results where visual inspection and perception is often the most satisfactory method of testing.

The concept of texture is intimately related to the human observer and the nature of the psychological information perceived by the human visual system remains unknown. Therefore, no precise definition of texture exists, since texture is a purely qualitative phenomena which cannot be translated into quantitative terms [123].

Julesz [124] has verified that the pre-attentive discrimination of texture depends mainly on the difference in second order statistics. Gagalowicz *et al.* [82] confirmed this by synthesising natural textures using only the second order statistics and neglecting the third and higher order statistics, which were considered to have no effect on the visual appearance of the textures. The verification condition applied by Gagalowicz was that two textures were considered *identical* if they were perceived visually as identical.

Visual comparison of images and features therefore provides a powerful tool within the fields of image synthesis and analysis. The human visual system provides a

recognised system for the comparison and discrimination of the qualitative information contained within images.

In the previous chapters, visual inspection of the synthesised sonar images provided the primary method of testing. Synthetic sidescan sonar images were created which appeared visually realistic on comparison with actual sidescan sonar images. Artifacts of the sidescan process, such as the beam effects, shadows and motion characteristics were also correctly represented within the sidescan sonar images.

Unfortunately, it was difficult to synthesise images identical to the existing sidescan sonar images, since insufficient information accompanied the real sidescan data. The quantitative input parameters required by the model cannot be derived in an inverse process from the qualitative sidescan image. Instead, only estimates of the seabed topography and typical medium characteristics and towfish characteristics can be applied. Although identical images cannot be synthesised, the correct representation of artifacts can be illustrated, and several examples will now be presented.

Sand ripples are commonly formed on the seafloor as a result of the current and tidal actions. These ripple features can produce distinctive features on sidescan sonar images. Figure 7.1(a) displays the sidescan sonar simulation of sand ripples, where fractals have been employed to represent the seafloor topography. Figure 7.1(b) displays a section of an actual sidescan sonar survey of an area of sand ripples. Similar features of highlights and shadows can be observed on both images. The images are not identical, though, as insufficient details regarding the height, composition, wavelength and shape of the ripple features on the seabed were available.

Figure 7.2(a) illustrates the simulated sidescan sonar image of larger scale ripples on the seabed. At the beginning of the trace, when the towfish is directly above the area of the seabed ensonified, the ripples appear to bend, or curve, over. This is due to the slant range effects and the subsequent compression of the seabed features at close ranges. A

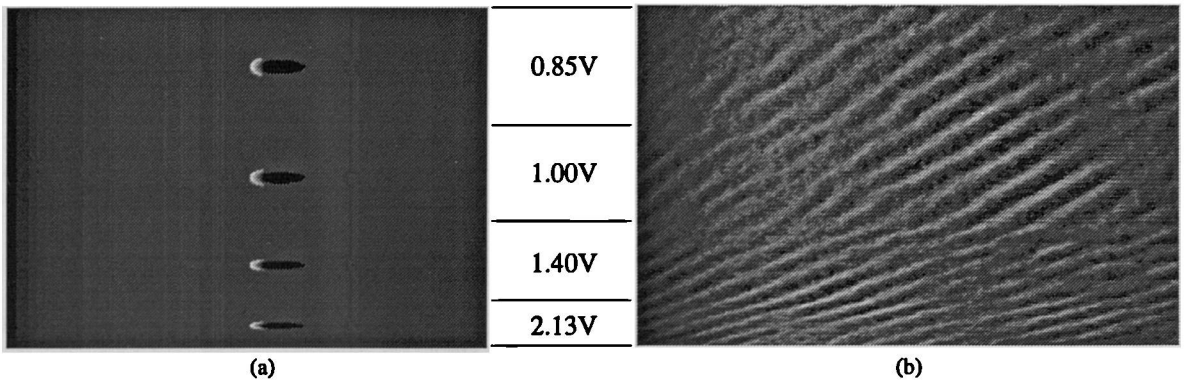

Figure 6.20: Speed distortions

With the recent advances in technology, many commercial sidescan sonar systems have integrated navigational and sensor data. From the navigational data, the survey data collected is correlated directly with the vessel's speed over the ground and the speed distortions on the sidescan images are minimised.

6.6 Towfish Motion Assumption

It has been assumed throughout the development of the simulation model that the towfish remains stationary from the moment a pulse is fired until the return from the maximum range is received. The towfish is then moved to the next position and the process is repeated. This implies that the scan lines, defined as the intersection of the acoustic axis of the beam pattern with the seabed, are approximated as straight lines. This is illustrated schematically in figure 6.21(a), for a towfish following a straight line trajectory.

The towfish motion is continuous in the actual sidescan sonar process and the receiving beam pattern keeps moving ahead during the acquisition of each line of the image. The scan lines from the maximum received signal are bent forward as the acoustic axis of the receiver beam pattern moves forward. The bending of the scan lines is illustrated in figure 6.21(b).

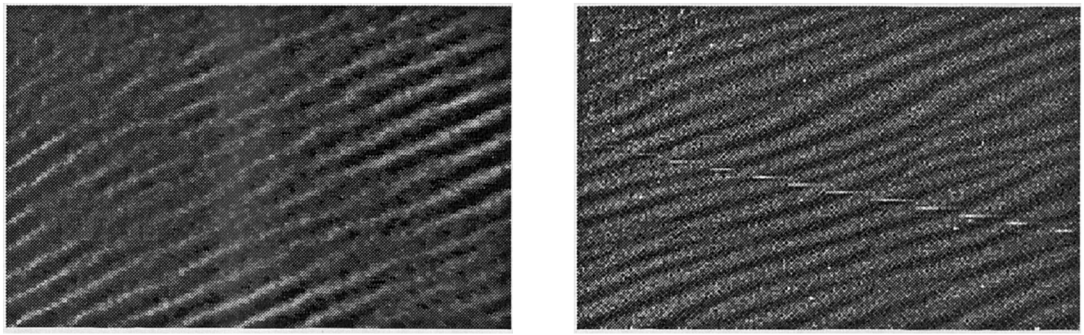

Figure 7.1: (a) Simulated image of sand ripples (b) Real sidescan image of sand ripples

similar effect is illustrated in figure 7.2(b) which represents an actual sidescan sonar trace of a sand ripple structure on the seafloor. The ripples again appear to bend at the beginning of the trace. Again, as a result of the previously described problem of insufficient data, the images of the sand ripples are not identical but do display similar features.

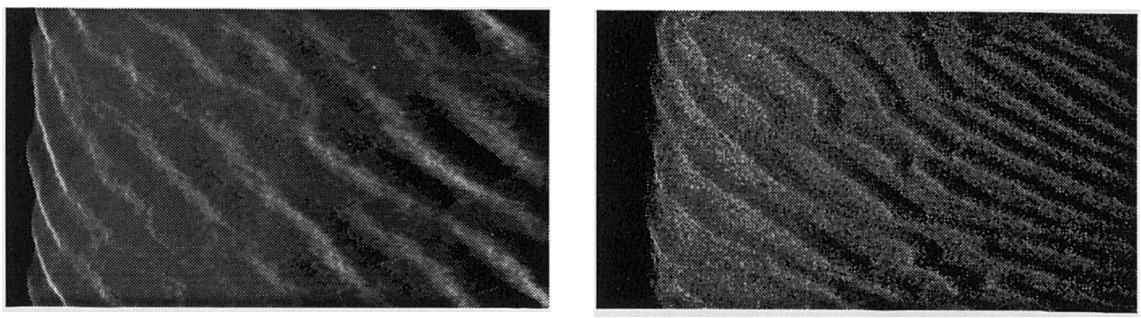

Figure 7.2: (a) Simulated image illustrating curvature of sand ripples below towfish (b) sidescan image representing similar effect

Sidescan sonars are frequently employed to survey pipelines on the seabed. The objective of the surveys is to ascertain where sections of the pipe are unsupported by the seabed and spans have formed in the pipeline. This effect is simulated in figure 7.3(a) which represents a pipe on the seabed with an unsupported span in the centre of the image. The image of the pipeline and the associated shadow alters in this area. This is similar to the image of the span illustrated in figure 7.3(b), which displays the actual sidescan survey of a pipeline in the North Sea.

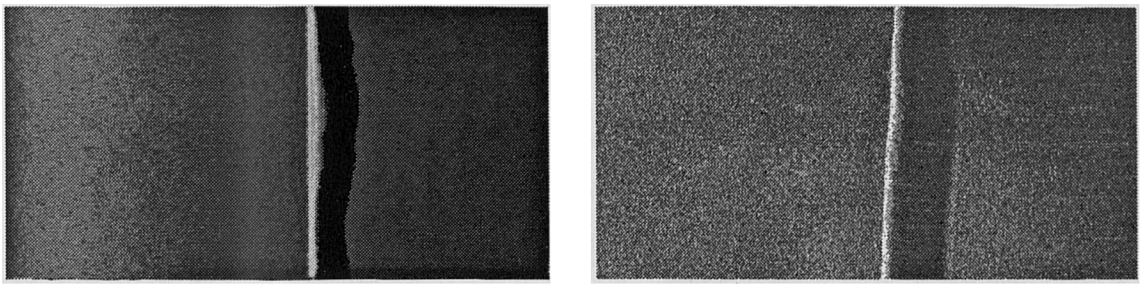

Figure 7.3: (a) Simulated image of span underneath pipeline (b) sidescan image representing a similar effect

Sidescan sonar surveys frequently produce images where different regions of sediment can be observed. The regions can appear similar in topography, but be composed of sediments with different reflectivity and scattering properties, as illustrated in figure 7.4(b) for a section of a real sidescan trace. Within this image the regions are composed of sand with different reverberation levels. Figure 7.4(a) displays a simulated image also containing a boundary between two types of sand.

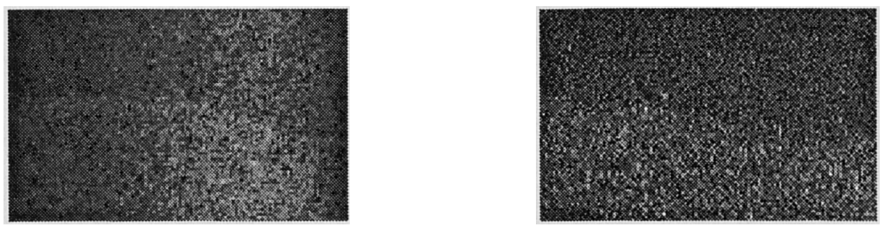

Figure 7.4: (a) Sediment boundary on simulated sidescan image (b) boundary on real image

Effects such as the aspect dependency of sidescan sonar can also be visualised. The sidescan image is dependent on the orientation of the seabed features relative to the direction of travel of the towfish. This is illustrated in figure 7.5, where the same area of sand ripples was ensonified by a transducer towed in four different directions. The image of the sand ripples changes depending on the orientation and this produces a commonly occurring problem in the classification of sidescan surveys, since the sand ripples no longer appear distinctive when orientated with their crests orthogonal to the direction of

travel.

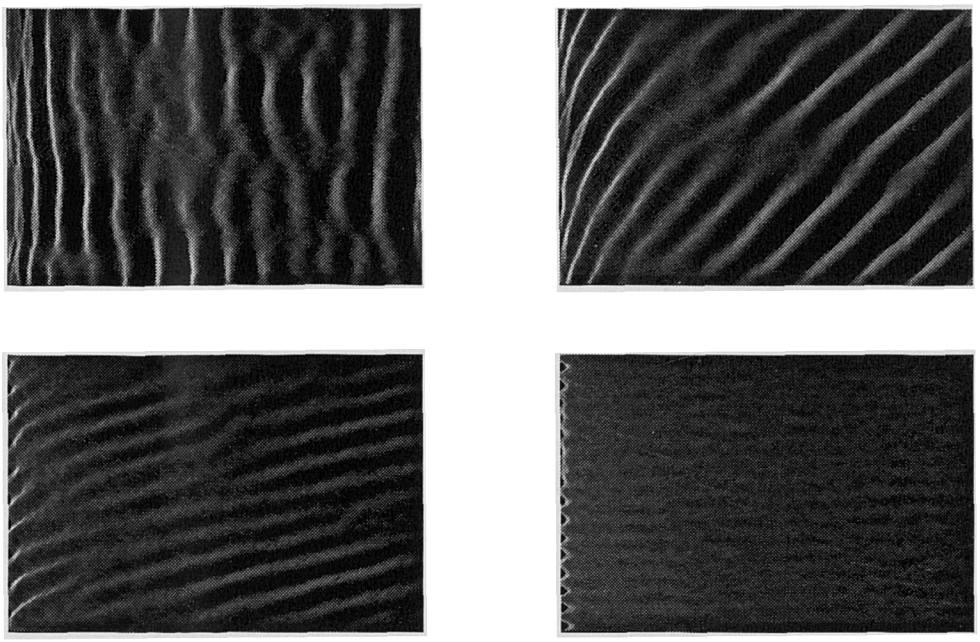

Figure 7.5: Sand ripples ensonified from four different directions

The simulated sonar images displayed in previous chapters can also be compared to real sidescan data. In particular, the effects of the beam and motion characteristics in the simulated images of chapter 6 can be observed to realistically represent the effects illustrated in real sidescan images contained within the sidescan sonar interpretation manuals produced by Klein [84] and EG&G [85].

7.4 Statistical Analysis

Statistical analysis of the images provides an alternative method to the visual comparison, which can provide confirming evidence of the model's reliability.

7.4.1 Sidescan Image Probability Distributions

Sidescan sonar senses and displays the amplitude of the signal reflected from the seabed or objects in the water column. Although the direct display of the echo amplitude

in image format provides a qualitative representation of the seabed, the signal can also be investigated statistically to yield information on the seafloor topography.

The acoustic field scattered from a random rough surface, such as the seabed, is the sum of many elementary waves scattered by points along the surface. The field, which is a complex quantity, will possess approximately Gaussian distributions in the limit as the number of scattering events tends to infinity [44]. An analytical study of Gaussian fields arising from wave scattering from random rough surfaces is provided by Beckmann [45].

If the real and imaginary parts of the scattered field are uncorrelated and independent, the amplitude of the field is reduced to a Rayleigh distribution and the phase to a uniform distribution, as a result of the quadrature addition of the complex components. This is for the assumption of a diffuse scattered field. Beckmann [45] states the result: "Outside a narrow cone (or wedge) about the direction of specular reflection, the amplitude of the field scattered by a rough surface is always Rayleigh distributed; if the surface is very rough, and grazing incidence is excluded, the amplitude of the scattered field is Rayleigh distributed everywhere".

The sidescan sonar image displays the backscattered energy from the seabed. This energy will be modified by the medium and transducer characteristics but the signal is dominated by the seabed reverberation, provided the sonar is operated in an environment with low noise and volume reverberation levels. The signal is composed primarily of the diffuse scattered energy, apart from in regions of near normal incidence occurring from the seabed below the towfish. The sidescan sonar images can therefore be expected to be approximated by Rayleigh statistics.

The distribution of the sonar reverberation has been investigated by Stanton [59] and Alexandrou *et al.* [125]. Stanton related the probability density function (pdf) to scattering theory to estimate the seafloor roughness, and noted that the shape of the pdf of the echo amplitude was dependent on the seafloor roughness.

The probability density functions of several sidescan sonar images were investigated. These images represented a range of sediment types and seafloor structures and were gathered with a variety of sidescan sonar systems with different operating characteristics. The probability density functions obtained from the images were observed to follow Rayleigh distributions for isotropic regions of the seabed.

A maximum likelihood estimator was employed to determine the parameters of the Rayleigh distribution which best represented the sidescan sonar image statistics. The properties of the Rayleigh probability density function are summarised in appendix C. The actual distributions were then compared to the fitted Rayleigh distribution using a Chi-Square test. This test is employed to determine the consistency of two distributions, and a low valued result indicates a high probability that the two distributions are consistent. Equation 7.1 states the chi-square statistic for the comparison of a binned data set to some known distribution, where N_i is the observed number of events in the i^{th} bin, and n_i is the number expected, according to the known distribution.

$$\chi^2 = \sum_i \frac{(N_i - n_i)^2}{n_i} \tag{7.1}$$

In this situation, N_i represents the probability of pixels within the image possessing a grey level i, and n_i is the expected value of the Rayleigh distribution. For this test, and all following results, there are 255 degrees of freedom, corresponding to the number of grey levels minus one [27].

Two representative results are displayed in figures 7.6 and 7.7. Figure 7.6 is a section of a sidescan sonar survey of Bigbury Bay in the English Channel and figure 7.7 is extracted from a survey in the North Sea. In both cases, the pdf can be visually observed to follow a Rayleigh distribution. On fitting a Rayleigh pdf to the data, the chi-square values of 0.0756 and 0.0522 respectively were observed. In both cases the chi-square probability function was approximately equal to one, indicating a strong consistency between

the Rayleigh and the sidescan sonar pdfs.

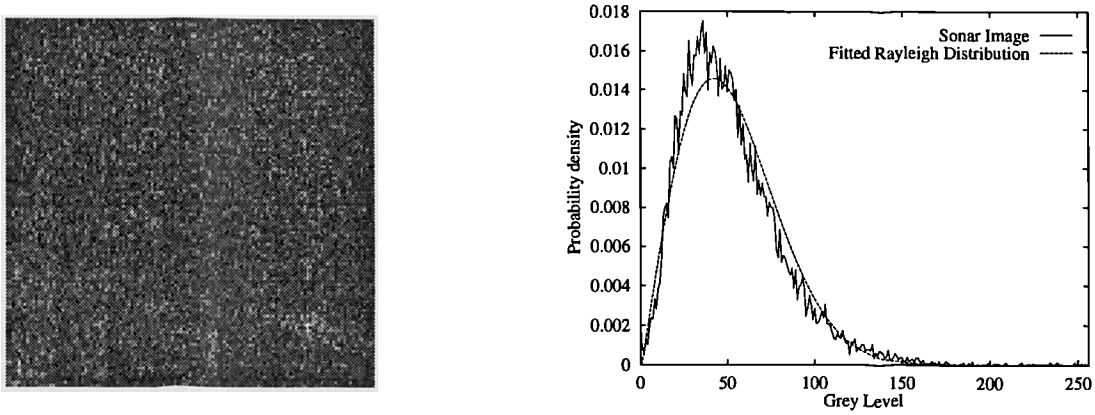

Figure 7.6: (a) Sidescan image of data from English Channel (b) Probability density function of image and fitted Rayleigh

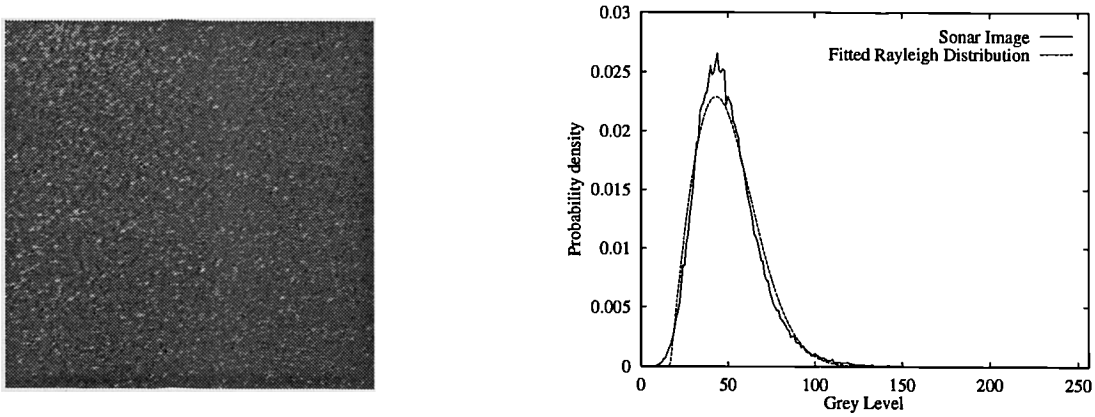

Figure 7.7: (a) Sidescan image of data from North Sea (b) Probability density function of image and fitted Rayleigh

This effect was also noted by Stewart *et al.* [126] for echo envelopes from areas with relatively flat bottom features. In areas with more complex seafloor topography and multi-scale roughness, Stewart observed statistical distributions with longer tails, which required multimodal Rayleigh pdfs to accurately describe. This can be illustrated for the sidescan image of sand ripples on the seafloor, as displayed in figure 7.8. The pdf in this instance can no longer be represented by a single Rayleigh function.

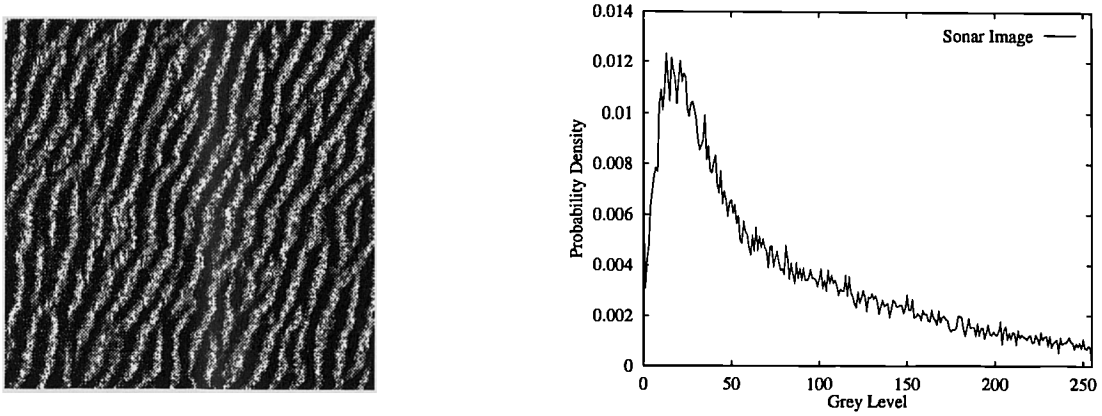

Figure 7.8: (a) Sidescan image of data from English Channel (b) Probability density function of image

7.4.2 Simulated Image Probability Distributions

Section 7.4.1 ascertained that homogeneous, isotropic regions of the seabed produced sidescan sonar images which can be represented with Rayleigh statistics. This section will investigate the statistics of simulated sidescan sonar images of isotropic seabeds.

A similar process to that described in section 7.4.1 was repeated, where a maximum likelihood estimation procedure was employed to calculate the parameters describing the Rayleigh function which approximated most closely the image statistics. A chi-square test was then applied to determine the consistency between the Rayleigh pdf and the probability density function of the simulated image.

A Rayleigh distribution was observed to provide a good representation of the statistics of the simulated images. The statistics of the images for different seabed roughness and sediment types were investigated, and a representative sample of the results are displayed within this section.

The results presented in figures 7.9, 7.10 and 7.11 illustrate the sidescan simulation of a similar scene, but with increasing seabed roughness. An isotropic fractal was employed to represent the seabed topography and by variation of the fractal dimension, the effective roughness of the seabed was altered. The simulated sidescan sonar images of

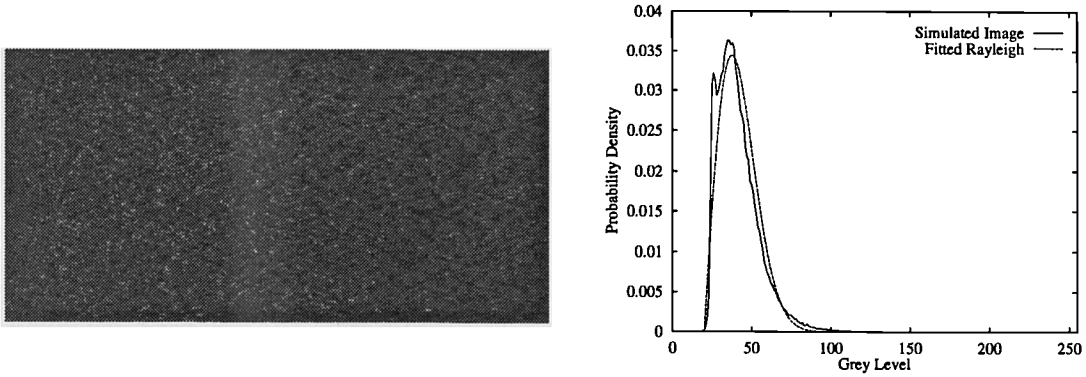

Figure 7.9: (a) Simulated sidescan image from fractal seabed (b) Probability density function of image and fitted Rayleigh

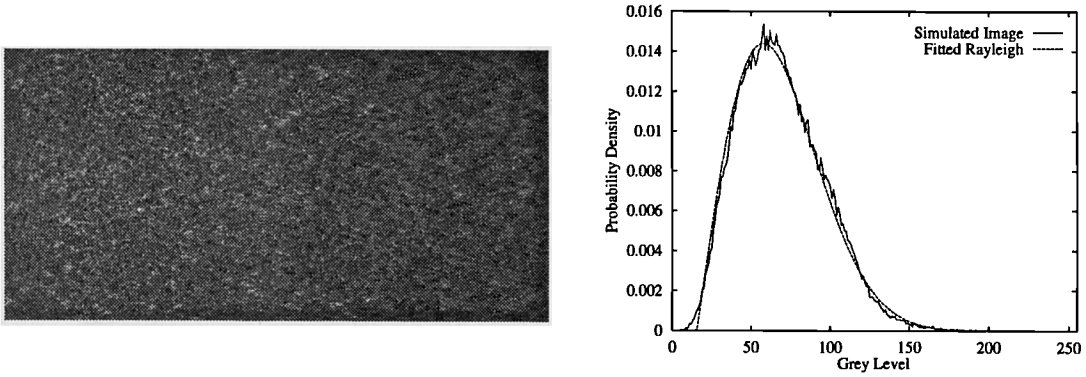

Figure 7.10: (a) Simulated sidescan image from fractal seabed (b) Probability density function of image and fitted Rayleigh

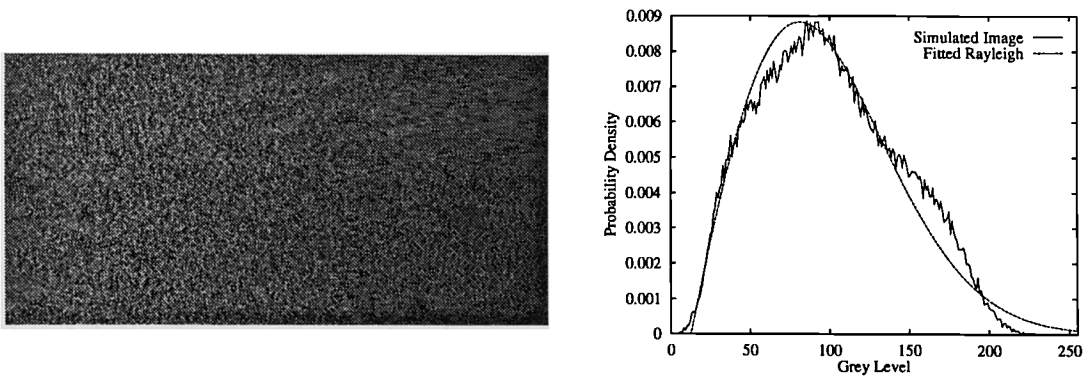

Figure 7.11: (a) Simulated sidescan image from fractal seabed (b) Probability density function of image and fitted Rayleigh

each of the three scenes could be represented by Rayleigh statistics.

The chi-square values for the comparison of the fitted Rayleigh distributions to the actual distributions were 0.205, 0.0126 and 0.035 respectively. The probability function in all three cases was approximately equally to unity, indicating a strong consistency between the two distributions. The resulting alteration of the shape of the pdf of the echo with the seabed roughness was suggested by Stanton [59].

The effect of the sediment type was then investigated, where a scene with identical topography, but with different sediment characteristics was ensonified. The sediment types were specified as silt and sand, and the parameters of table 4.1 were employed to characterise the sediments. The resulting images, and probability density functions, are displayed in figures 7.12 and 7.13 for sand and silt respectively. Again Rayleigh distributions could be fitted to the data with chi-square results of 0.057 and 0.024, and the probability functions for both cases were approximately equal to unity.

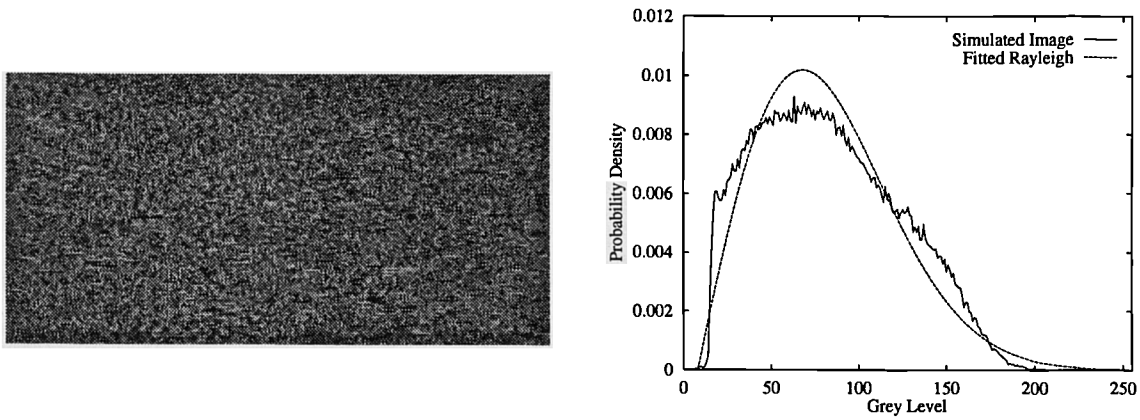

Figure 7.12: (a) Simulated sidescan image from sand seabed (b) Probability density function of image and fitted Rayleigh

The distributions for both sediment types appear similar, and this is suggested by the use of the same seabed topography in both cases. The topography though is liable to be related to the sediment type. The simulated images for the sand and silt appear visually similar, due to the dynamic range of the images. The ensonification of a composite region

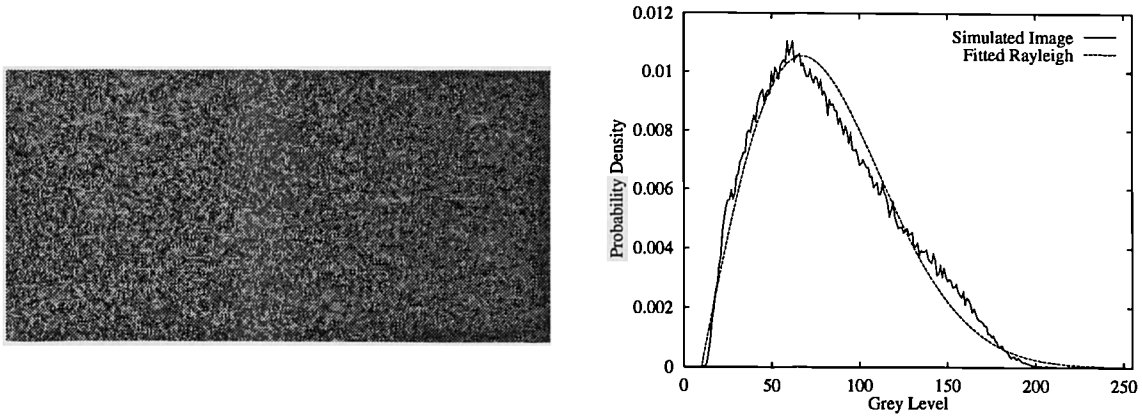

Figure 7.13: (a) Simulated sidescan image from silt seabed (b) Probability density function of image and fitted Rayleigh

of the seabed composed of separate areas of sand and silt is displayed in figure 7.14. The difference in the relative intensity levels of the two regions then becomes apparent.

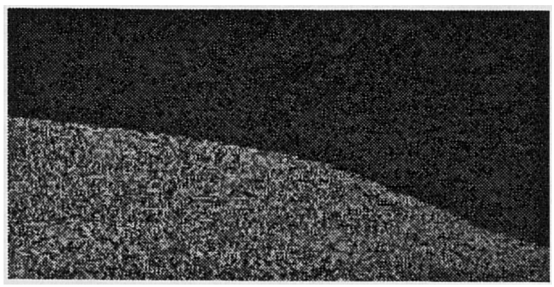

Figure 7.14: Simulated image illustrating sand and silt

The statistics of simulated regions of the seafloor composed of more complex topological features were also investigated. Figure 7.15 displays the simulated sidescan sonar image of a region of sand ripples. The pdf of this image, as for the real sidescan image of sand ripples in figure 7.8, can no longer be represented by a single Rayleigh distribution due to the longer "tail" on the distribution. Although the simulated image is not visually identical to the actual sidescan image, similar characteristics can be observed in the statistical distribution.

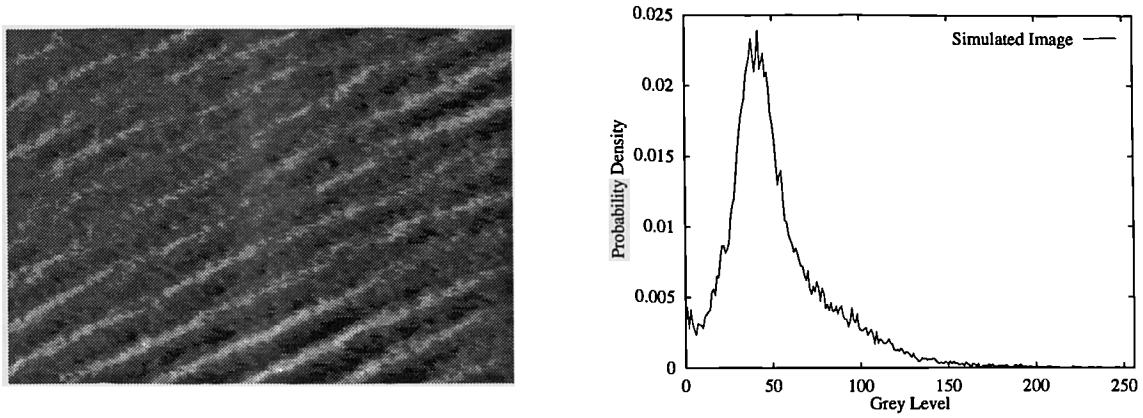

Figure 7.15: (a) Simulated sidescan image (b) Probability density function of image

7.4.3 Comparison of Simulated and Sidescan Image Statistics

By careful estimation of the input parameters it was possible to simulate sidescan sonar images which compared favourably by visual inspection to real sidescan sonar images. From knowledge of the sidescan sonars employed, representative transducer characteristics, including the beam and depression angles, frequency and pulse length, could be applied within the simulation model. The chosen regions of the real sidescan sonar images appeared to represent relatively flat, isotropic zones of the seabed. Isotropic fractals, with fractal dimensions representative of natural scenes, were used to represent the seafloor and were scaled to represent typical seabed roughness.

Figure 7.16(a) illustrates a section of a sidescan sonar image from a survey of Bigbury Bay and figure 7.16(b) represents a visually similar simulation of a sidescan sonar image of a sandy seabed. The statistics of the two images are compared in figure 7.17.

Figure 7.17(a) compares a Rayleigh distribution with a mean of 83.4 and a variance of 1534.8 to the pdf of the actual image. The chi-square statistic for this comparison was 0.0418. The same Rayleigh distribution was then compared to the statistics of the simulated image in figure 7.17(b) and the chi-square statistic of 0.058 was obtained. The Rayleigh provided a better approximation to the real image since its parameters were

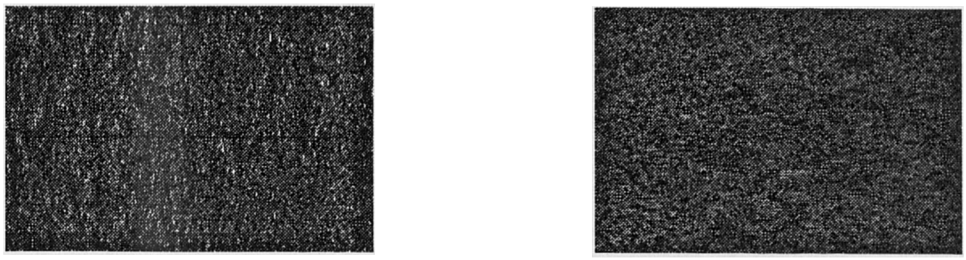

Figure 7.16: (a) Sidescan image of data from English Channel (b) Simulated sidescan image

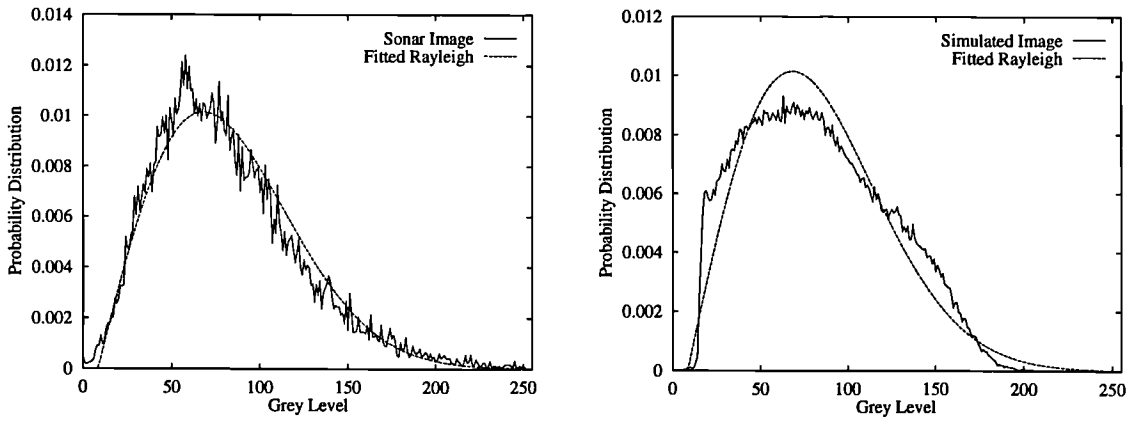

Figure 7.17: (a) Real sidescan statistics (b) Simulated sidescan image statistics

estimated to fit this data set. The probability function for both comparisons approached unity, indicating a strong consistency between the image density functions and the Rayleigh function.

A chi-square test was also applied to compare directly the probability density functions of the two images. Both of the data sets now contained binned values representing the probability of an image pixel having a certain grey level value. The chi-square statistic is calculated using equation 7.2, where R_i is the number of events in bin i for the first data set and S_i is the number of events in the same bin i for the second data set.

$$\chi^2 = \sum_i \frac{(R_i - S_i)^2}{R_i + S_i} \tag{7.2}$$

For the direct comparison of the statistics of the two images illustrated in figure 7.16, the chi-square statistic was 0.0578, indicating that a strong consistency existed between the two data sets.

Figure 7.18(a) illustrates a section of a sidescan sonar image from a pipeline survey in the North Sea. A 100KHz sidescan sonar was employed during this survey and was deployed approximately 10m above the seabed. Figure 7.18(b) represents the simulated sidescan sonar image of an isotropic seabed. The pdfs of the two images are compared to a Rayleigh function with a mean value of 68.53 and a variance of 763.8 in figure 7.19. The chi-square statistic for the comparison of the real image to the Rayleigh function was 0.037 and for the comparison with the simulated image was 0.0126. A better chi-square result was obtained for the simulated image as the Rayleigh function parameters were estimated with the maximum likelihood technique to fit this data. The direct comparison of the two images produced a chi-square statistic of 0.0298.

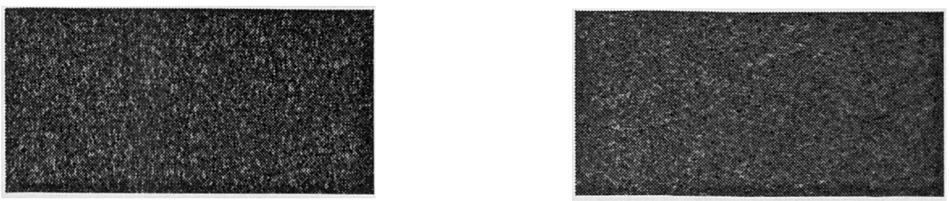

Figure 7.18: (a) Sidescan image of data from North Sea (b) Simulated sidescan image

The simulated sidescan sonar images can therefore be illustrated to possess similar statistical properties to real sidescan sonar images, indicating that the model's treatment of seabed roughness and scattering is consistent with real sidescan sonar. The probability density functions for both the real and simulated images can be approximated by a Rayleigh function, as predicted by the statistics of diffuse scattering from a random rough surface.

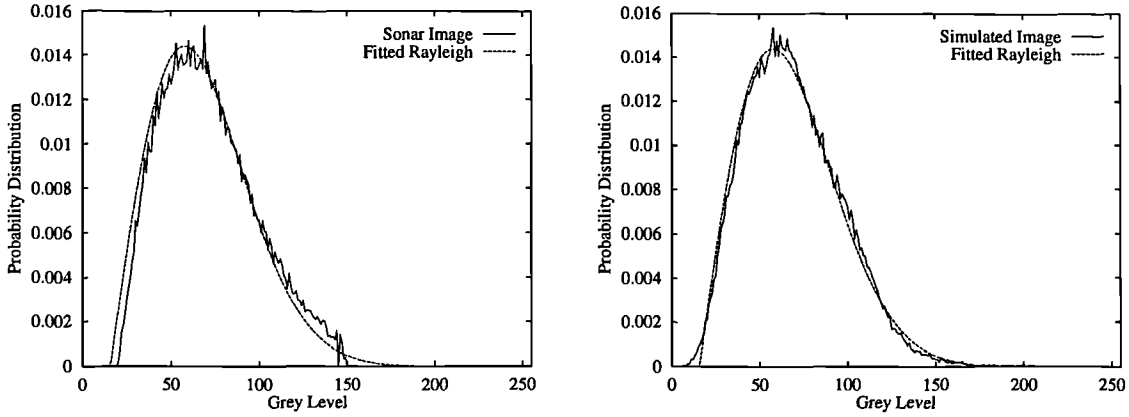

Figure 7.19: (a) Real sidescan statistics (b) Simulated sidescan image statistics

7.5 Power Spectral Density Analysis

The previous section investigated the probability distribution of the sidescan sonar signal. A relationship was observed between this probability response and the roughness of the seabed. The shape of the distribution, however, appeared less sensitive to the sediment type and hardness of the seabed. This is observed in figures 7.12 and 7.13, where similar probability density functions are obtained for the sidescan images of similar sand and silt seabeds. This section will investigate the power spectral densities for these sidescan sonar images with the same topography but with different sediment characteristics, with the aim of demonstrating that like real sidescan data the images are dependent on the seabed type, and that power spectral density analysis can be used to distinguish regions composed of different sediments.

The method applied to extract and investigate the power spectral density was developed by Pace *et al.* [127] [128] [129] for the classification of sediment types from sidescan sonar images. Their classification technique involves the definition of features to classify the spectral response of the sediments. The method for obtaining the log power spectra required for the analysis will be outlined initially in section 7.5.1, and results and features extracted from this spectra will be explained in the following sections.

7.5.1 Calculation of Normalised Log Power Spectrum

The frequency content of the signal is obtained with a Fourier transform (operator F) for each line of the sample trace, where $g_i(t)$ represents the windowed signal amplitude of the i^{th} digitised line. The power spectrum of the i^{th} line is represented by equation 7.3, where t is time and f is frequency.

$$P_i(f) = |F(g_i(t))|^2 \tag{7.3}$$

The average power spectrum is then obtained by averaging $P_i(f)$ over all values of i, for the n selected lines of the trace.

$$P(f) = \frac{1}{n}\sum_{i=1}^{n} P_i(f) \tag{7.4}$$

The log power spectrum was defined to produce a maximum of one and a minimum of zero, and is calculated from equation 7.5,

$$P_L(f) = \frac{1}{\log(A+1)} \log\left[\frac{A(P(f) - P_{\min})}{P_{\max} - P_{\min}} + 1\right] \tag{7.5}$$

where A is defined as a constant equal to 10^4 and $P_{\max}$ and $P_{\min}$, are respectively, the maximum and minimum values of the average spectrum $P(f)$.

The log power spectrum is then normalised, by the division of the integral, as expressed in equation 7.6.

$$P_{NL}(f) = \frac{P_L(f)}{\int_0^{f_{NY}} P_L(f)df} \tag{7.6}$$

7.5.2 Comparison of Sand and Silt

The spectra of the simulated images displayed in figures 7.12 and 7.13 were investigated using the technique of Pace summarised above. These images were simulated with all parameters identical except the sediment type, this included using the same underlying sediment topography, which resulted in the generation of images with similar statistical distributions. The two sediment types employed were sand and silt using the parameters of table 4.1.

The average power spectral density was calculated for 256 lines of each image using equation 7.4 and the result is displayed in figure 7.20(a). Figure 7.20(b) displays the normalised log power spectra, obtained using equation 7.6, for each of the images.

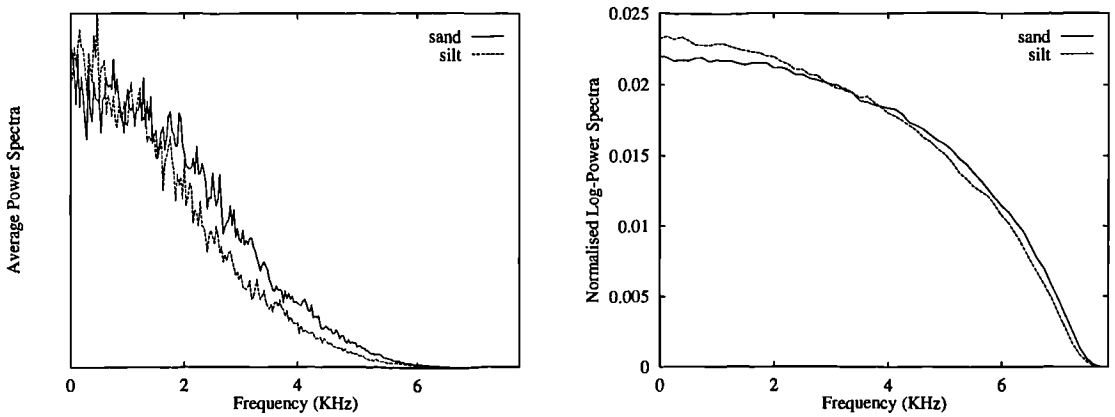

Figure 7.20: (a) Average spectra (b) Normalised log power spectra for sand and silt

On visual inspection a difference exists between the normalised log power spectra for the ensonified regions of sand and silt. The difference between the two spectra is plotted in figure 7.21, and the result can be observed to change from a positive difference to negative. These results are consistent with those suggested by Maguire and Pace [129] for the power spectra obtained from real sidescan sonar data, where a similar general trend of a decrease in power with increasing frequency exists.

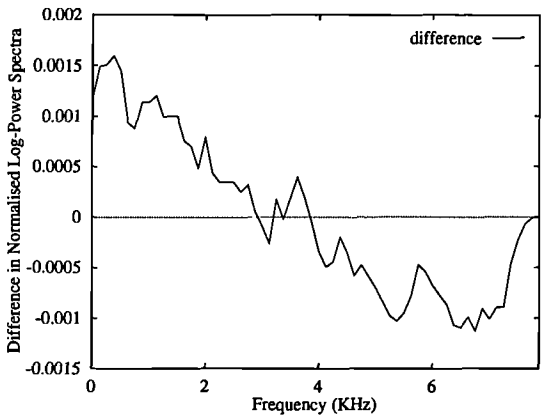

Figure 7.21: Difference between normalised log power spectra for sand and silt

7.5.3 Features of Normalised Log Power Spectrum

To characterise the power spectra and determine if the sediment types are distinguishable within the sidescan sonar image, Pace and Gao defined the three integral features stated in equations 7.7 to 7.9, which are extracted from the normalised log power spectra. The features are employed to quantify the changes in the spectrum and express the ratios of the power in the low and high frequency bands.

$$D_{f_1} = \frac{\int_{0}^{1/2 f_{NY}} P_{NL}(f)df}{\int_{1/2 f_{NY}}^{f_{NY}} P_{NL}(f)df} \tag{7.7}$$

$$D_{f_2} = \frac{\int_{0}^{1/16 f_{NY}} P_{NL}(f)df}{\int_{1/2 f_{NY}}^{f_{NY}} P_{NL}(f)df} \tag{7.8}$$

$$D_{f_3} = \frac{\int_{0}^{1/16 f_{NY}} P_{NL}(f)df}{\int_{3/4 f_{NY}}^{f_{NY}} P_{NL}(f)df} \tag{7.9}$$

Within the above expressions, f_{NY} is the Nyquist frequency, which is equal to half the rate at which the signal is sampled. Using these features it is possible to demonstrate that there is sufficient information to separate regions of the same topography and different sediment types.

Following the procedure of Pace and Gao, the image was segmented into regions of n consecutive lines, where n was selected equal to 8, 16 or 32. The values of the three features were calculated for each of the regions and are summarised within table 7.1.

Feature		Sediment					
		sand			silt		
		n=8	n=16	n=32	n=8	n=16	n=32
D_{f_1}	mean	2.059	2.0188	1.988	2.2833	2.2221	2.190
	std. dev	0.0473	0.0298	0.0235	0.0610	0.0348	0.0242
D_{f_2}	mean	0.2552	0.2503	0.2464	0.2939	0.2848	0.2804
	std. dev	0.0072	0.0038	0.0039	0.0134	0.0072	0.0050
D_{f_3}	mean	1.0733	1.0233	0.9840	1.3516	1.2577	1.2103
	std. dev	0.0459	0.0258	0.0198	0.1058	0.0571	0.0403

Table 7.1: Summary of feature values D_{f_1}, D_{f_2} and D_{f_3}

To quantify the ability of each feature to discriminate between the two sediment types, the separation parameter s was defined [127],

$$s_{ij} = \frac{E_i - E_j}{\sigma_i + \sigma_j} \tag{7.10}$$

where E is the mean and σ is the standard deviation for the sediment types i and j. Using this parameter, the separation values of table 7.2 were obtained for the three features. These values indicate that a high probability exists that regions of sand and silt within a sidescan image can be segmented with a high degree of accuracy, since, as observed by Pace and Gao [127], if the separation parameter is greater than 1.96, the probability of misclassification of each sediment type is less than 2.5%. This is also suggested by the visual inspection of figure 7.14, illustrating the sidescan simulation of adjacent regions of sand and silt.

Feature	Separation		
	n=8	n=16	n=32
D_{f_1}	2.071	3.144	4.423
D_{f_2}	1.879	2.856	3.822
D_{f_3}	1.834	2.827	3.765

Table 7.2: Values of separation parameters for the three features

The values obtained for the features and separation parameters appear consistent with those reported by Pace for real sidescan data. The performance of D_{f_3} is poorer than the other two spectral features, as expected from the definition and previously observed by Pace. The separation parameters also increase with increasing sample size as the features are calculated for larger areas as n increases from 8 to 16 and 32.

The system and environmental dependence of the backscattered signal precludes the direct comparison of the simulated data and the reported sidescan data, since even different sets of real sidescan data cannot be directly compared [129]. In addition, the

simulated images cannot represent an identical situation to the real data due to the lack of environmental information, as previously described in section 7.3. The same general trends though can be observed in both the real and simulated data upon investigation of the spectral characteristics.

7.6 Conclusions

This chapter has investigated the qualitative images produced by the sidescan sonar simulation model and techniques for the verification of the model output. The chapter initially described the problems inherent in the verification of the simulation model, since no closed form analytic solution for the sidescan process exists. Alternative techniques, including visual, statistical and spectral analysis of the simulated images were then examined and a representative sample of results were presented for each technique. The statistical and spectral techniques permitted the investigation of the treatment by the model of both the seabed roughness and sediment type.

The human eye is a powerful analytic tool within the fields of image processing and synthesis. Inspection of the simulated images confirmed that visually realistic results could be produced. The simulation model was also demonstrated to correctly represent artifacts of the sidescan sonar process including slant range, motion and aspect dependency characteristics.

The probability density functions of the simulated and real sidescan sonar images were then examined. It was illustrated that both the real and simulated data sets exhibited Rayleigh statistics, as predicted by the theory of scattering from random rough surfaces.

Finally, the effect of the sediment characteristics was investigated using power spectral density techniques. The simulated data again exhibited similar characteristics and trends to published data on sediment classification from sidescan sonar images.

In conclusion, the motivation for this chapter was to investigate the output produced by the simulation model. No definitive test can be applied to determine the accuracy of the model as a result of the qualitative images produced by the sidescan sonar process and the model. Instead, the model has been demonstrated to produce consistent results on comparison to real sidescan data using visual, statistical and spectral tests. This increases confidence in the model, which is the maximum extent to which it is possible to verify the output.

Chapter 8

Conclusions and Future Work

8.1 Summary

This thesis has presented the initial development of a model for the simulation of sidescan sonar images. The model considers the main underlying physical processes including seabed reverberation, acoustic propagation through the water media, and the transducer characteristics. The output of the model is a simulated sidescan sonar image, comparable to the actual image which would be generated by a sidescan sonar operating under the specified conditions.

The computer model has been created in a structured and easily extensible form. The model requires a quantitative description of the environment and operating conditions from which to generate a qualitative sidescan sonar image. These input parameters are specified by the user when starting the operation of the simulation model.

The fundamental structure of the model was proposed in chapter 3, and the following chapters extended this model through further investigation of the sidescan sonar process. The main features of the model will now be summarised.

The simulation model calculates the propagation of the acoustic signal through the water column using a ray tracing approach. The sound velocity profile, although varying with depth, is assumed to remain constant with range. The spreading losses incurred during propagation are calculated from the actual ray trajectories and the absorption loss is

obtained using the empirical model of Francois & Garrison [117] [118]. The losses can also be compensated for by the application of a time varying gain.

To compute the interaction of the acoustic signal with the seabed, a suitably complex and realistic representation of the topography is required. Fractal models, manipulated to yield height terrain fields, were employed to represent the seabed topography and sediment roughness. The fractal images can be combined to produce complex regions of seabed composed of the boundaries between different sediment types or topographies. The simulation model can also include procedurally defined objects to represent man-made objects in the water column or on the seabed.

The scattering from the seabed can be calculated using Lambert's Law, which provides a simple empirical model. The operator can also specify the use of the bistatic scattering strength model developed at APL-UW by Jackson [71]. This model has a stronger physical basis than Lambert's Law and calculates both the roughness and volume scattering. The calculation of the scattering with either model includes contributions from multiple reflections in addition to the direct backscatter.

The three dimensional directional response of the sonar transducer during transmission and reception of the acoustic signal is also included. The directional response, and the subsequent sidescan images generated, are dependent on the motion of the transducer as it is towed through the water. The effects of rotational and translational instabilities of the towfish, in addition to the towing speed, can also be simulated.

The computer model developed for the simulation of all the above mentioned features of the sidescan sonar process has been implemented in the C programming language and operates in a Unix environment. The *manual pages* describing the operation of the model and the user selectable features are included in appendix D.

8.2 Conclusions

The desired properties for the new simulation model developed in this thesis were determined following an examination of the current literature. The requirement for a simulation model with the following characteristics was highlighted:-

1. The model should consider the underlying physical processes.
2. The model should generate synthetic sidescan images as the primary output.
3. The model should permit the visualisation of the influence of individual parameters on the sidescan sonar image.

These objectives were identified because existing models were observed to model individual features of the sonar process in detail or to produce only representative graphical or numerical results. Difficulties arise in attempting to relate the results of either type of model to the sidescan image generated during sonar surveys.

The model developed within this thesis is felt to fulfill these objectives since it models the underlying physical processes of sidescan sonar, generating as its output synthetic sidescan sonar images. The model presents several advantages which will now be discussed, prior to the consideration of the current limitations of the model. The model will then be compared with the only other similar model known to be in development.

The main advantage of this model is the direct visualisation of the output of the simulated sidescan sonar process in image form. The model is one of the first to generate visually realistic sidescan sonar images of complex seabed topographies and features of the seafloor. This provides a direct advantage over existing models which generate only numerical or graphical results which are difficult to relate to the actual sidescan images.

A further advantage of the model is that it permits the visualisation of the influence of individual parameters on the sidescan sonar image. The parameters can either be explored in isolation or as a complex combination of phenomena. The model has proved

to be a useful analysis tool in this respect and the effect of the sound velocity profile on the sidescan sonar images has already been investigated [116].

It is also envisaged that the model will provide a valuable tool for both training and visualisation, as it will permit the simulation of complex environments and artifacts of the sidescan sonar process. On a more sophisticated scale, it can provide a suitable platform for testing complex algorithms to improve the interpretation of sidescan sonar images.

Visual inspection showed that the output image was able to correctly represent artifacts of the sonar process and produce visually realistic images. Statistical and spectral analysis of the output images also produced results comparable with sidescan images. It is, however, difficult to devise methods of accurately verifying the qualitative images generated by this process, but the techniques presented have attempted to increase confidence in the model output.

On evaluation, the model has been demonstrated to replicate the deterministic aspects of the sidescan sonar process. Every simulated sidescan sonar image of a defined scene is therefore identical. However, sidescan records of a specified area have been observed to change slightly with time. This has been attributed to stochastic processes, such as volume reverberation, surface reverberation and noise, which can also result in the addition of speckle and clutter on the images. The model is currently limited in that it is unable to model these stochastic processes, but the framework of the deterministic model was necessary before stochastic features could be incorporated.

A further limitation of the model, at present, is that it is only capable of representing sidescan sonar. However, the propagation and reverberation sub-models are general for any sonar process and a recombination of the sub-models should permit the simulation of sonar systems with other architectures.

The SWAT model [5] is the only other model known to be under development with the similar objective of generating a physically correct sonar image. With the ever

increasing availability of computer power, a wider range of similar models is becoming more feasible. However, like SWAT, this model can take several hours of computing time to generate a single image, as a result of the iterative calculation process.

The SWAT model is being developed specifically for the simulation of targets on the seabed, and is more advanced in this aspect than the model described within this thesis. SWAT has been demonstrated to predict target strength characteristics including features such as those generated by individual nuts and bolts on the target. The model described within this thesis provides a more general simulation tool which can produce synthetic sidescan sonar images from a variety of complex seabed topographies and sediment types without the flat seabed assumption of SWAT. In addition, the model can incorporate man-made targets using procedurally defined objects rather than the facet based approach adopted by SWAT.

The model also includes the effect of the sound velocity profile on the propagation and transmission losses, unlike SWAT which neglects the effect of the curvature of the propagation paths as a result of its application of the isovelocity assumption. The SWAT model however, is able to alter the beamformer algorithms to simulate synthetic aperture as well as sidescan sonar, but it is unable to simulate the motion characteristics resulting from the towing effects, which are included in this model.

In conclusion, the model has been demonstrated to fulfill the objectives of simulating the sidescan sonar process by modelling the underlying physical processes and producing realistic synthetic sidescan records as the output. The model also presents several advantages, as previously discussed, over the only comparable model currently available. The simulation model is still in its initial development stages and much further work is foreseen, as will be described within the following section. However, the work presented in this thesis has illustrated that the concept of simulating the sidescan sonar process in this manner is feasible.

8.3 Future Work

As previously noted the work in this thesis has proved the concept of the model and other features of the sidescan sonar process can still be added. The structured form of the model should permit the easy addition of further procedures and functions.

As discussed in the previous section, the development of the model has considered the deterministic aspects of the sidescan sonar process. Phenomena, such as the noise and reverberation, which are better described by stochastic models, need to be incorporated. The actual process by which the noise and reverberation interfere with the signal and the levels of interference would require investigation prior to their implementation within the model.

Other extensions to the model, such as the removal of the horizontal stratification or the discrete transducer motion assumptions, could also be investigated. The removal of the discrete transducer motion assumption would permit the simulation of longer range sidescan sonars, such as GLORIA.

The sub-models incorporated within the simulation model for the calculation of the acoustic propagation and scattering are general for any sonar system. The model could therefore be extended to simulate the operation of other sonar systems, such as sector scan, forward looking or synthetic aperture, by the re-linkage of the sub-models with the appropriate transducer characteristics. A more general form of the model could be created by considering the signal returned to each individual element of the array and then applying the appropriate beamforming techniques for the desired sonar architecture.

One of the main objectives in any processing of sidescan sonar images is to obtain quantitative information about the seafloor from the sidescan sonar images. As well as the application of the model for the testing of interpretation and processing algorithms, the model may eventually help provide the basis for the long term goal of developing a form of inverse technique for the extraction of information from the sidescan sonar image.

Appendix A

A. Sound Velocity Profiles

A.1 Sound Velocity Profiles from Clyde Estuary

The following sound velocity profiles (SVP) were measured in the Clyde Estuary and were extracted from the data summarised in reference [115]. These profiles were used to illustrate the effect of the sound velocity profile on the sidescan sonar image.

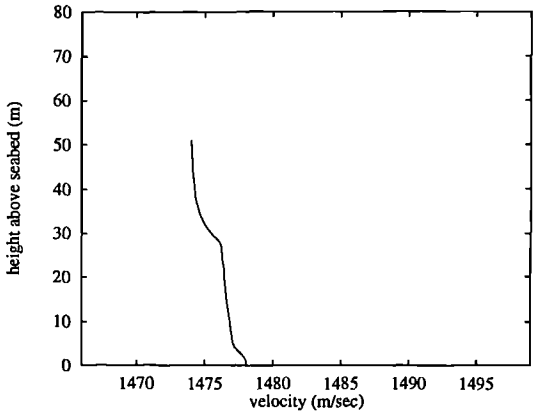

Figure A.1: SVP1

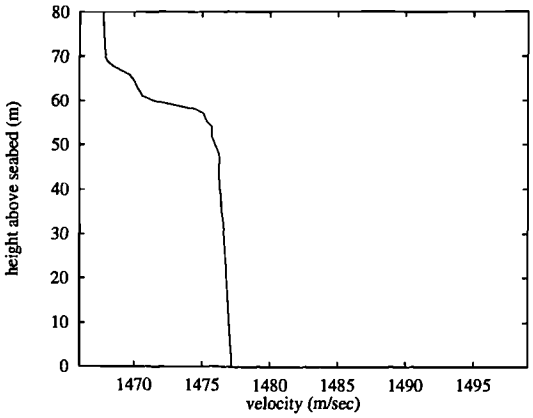

Figure A.2: SVP2

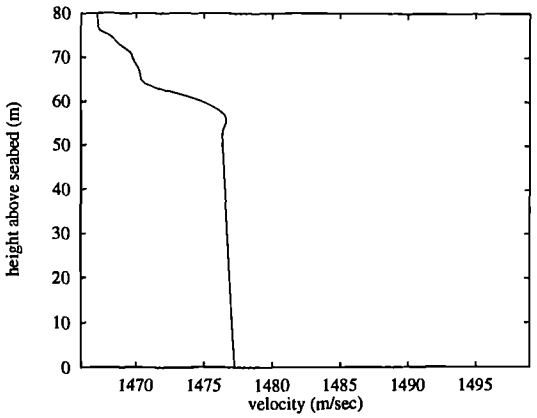

Figure A.3: SVP3

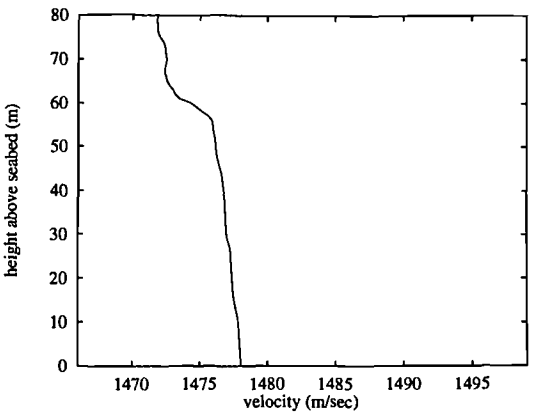

Figure A.4: SVP4

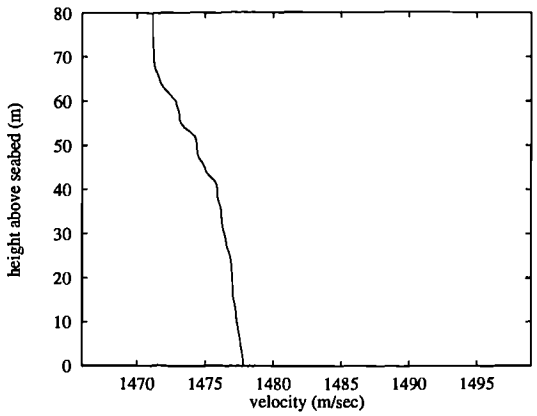

Figure A.5: SVP5

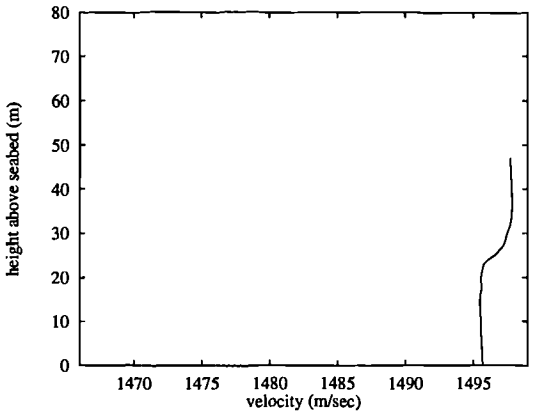

Figure A.6: SVP6

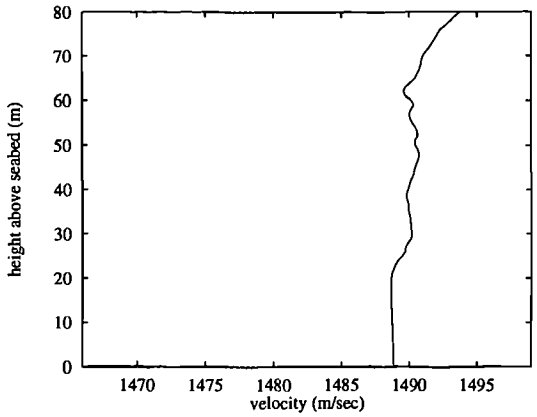

Figure A.7: SVP7

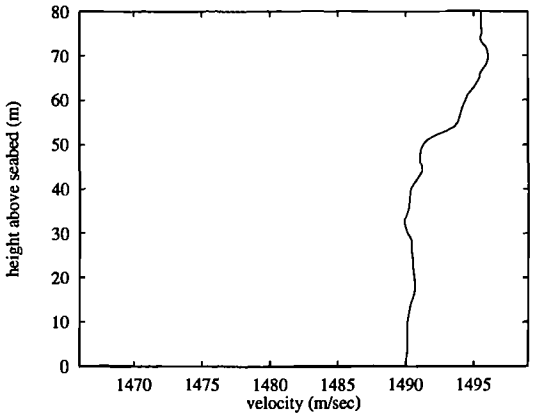

Figure A.8: SVP8

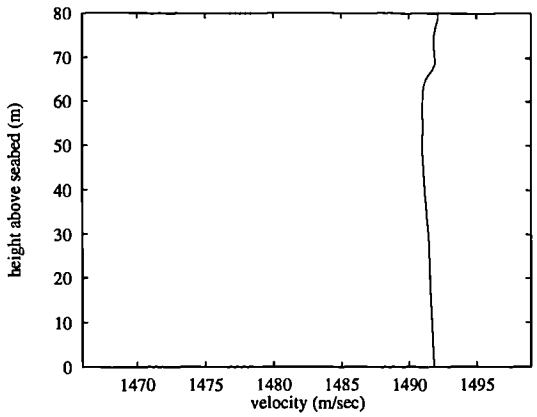

Figure A.9: SVP9

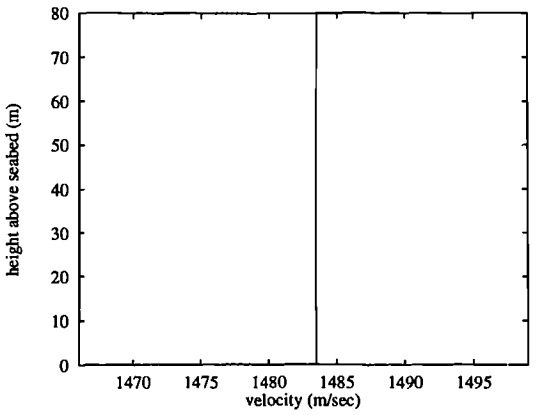

Figure A.10: ISO

A.2 Tabulated Results of Ray Calculations

Tables A.1 and A.2 display the grazing angles and times of return calculated for rays emitted in each of the sound velocity profiles SVP1 to SVP9. The values are calculated for rays emitted from transducers at 20m and 70m above a flat seabed which intersect the seabed at horizontal ranges of 50m, 100m, 200m and 500m.

	Range 50m		Range 100m		Range 200m		Range500m	
	Angle degrees	Time msec	Angle degrees	Time msec	Angle degrees	Time msec	Angle degrees	Time msec
SVP1	21.697	72.922	11.101	138.093	5.288	272.172	1.186	677.575
SVP2	21.786	72.919	11.276	138.092	5.643	272.170	2.122	677.591
SVP3	21.784	72.920	11.277	138.087	5.644	272.162	2.214	677.569
SVP4	21.776	72.883	11.259	138.019	5.545	272.029	2.049	677.231
SVP5	21.760	72.902	11.227	138.057	5.545	272.103	1.885	677.412
SVP6	21.792	72.015	11.291	136.376	5.673	268.789	2.197	669.169
SVP7	21.790	72.345	11.288	137.000	5.666	270.023	2.181	672.247
SVP8	21.821	72.273	11.350	136.861	5.791	269.742	2.509	671.537
SVP9	21.788	72.202	11.282	136.732	5.654	269.491	2.150	670.923
ISO	21.801	73.019	11.310	138.278	5.710	272.539	2.291	678.508

Table A.1: Effect of ray curvature on grazing angle and time of return for fish at an altitude of 20m

	Range 50m		Range 100m		Range 200m		Range500m	
	Angle degrees	Time msec	Angle degrees	Time msec	Angle degrees	Time msec	Angle degrees	Time msec
SVP1	-	-	-	-	-	-	-	-
SVP2	54.413	116.609	34.896	165.463	19.101	287.228	7.546	684.330
SVP3	54.427	116.567	34.921	165.407	19.149	287.135	7.650	684.124
SVP4	54.417	116.532	34.901	165.356	19.109	287.049	7.534	683.918
SVP5	54.394	116.610	34.860	165.466	19.028	287.235	7.338	684.357
SVP6	-	-	-	-	-	-	-	-
SVP7	54.484	115.488	35.037	163.875	19.381	284.469	8.200	677.790
SVP8	54.503	115.341	35.077	163.668	19.453	284.113	8.415	676.916
SVP9	54.447	115.363	34.964	163.697	19.236	284.163	7.834	677.058
ISO	54.462	115.973	34.992	164.564	19.290	285.671	7.970	680.656

Table A.2: Effect of ray curvature on grazing angle and time of return for fish at an altitude of 70m

Appendix B

B. Derivation of Beam Pattern for Line of Equally Spaced Point Transducers

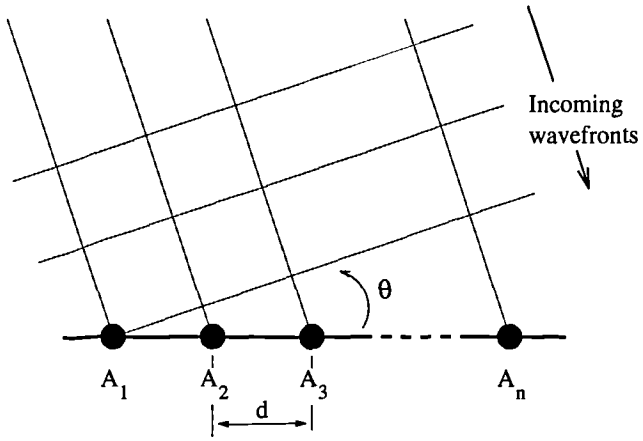

Figure B.1: Acoustic waves incident on a multi-element array

The beam pattern of a line of equally spaced elements can be derived with consideration of figure B.1, where a plane sinusoidal sound wave of unit pressure is incident at an angle θ to a line of n elements. The phase delay between adjacent elements is expressed in equation B.1, in radians.

$$u = \frac{2\pi d}{\lambda} \sin\theta \tag{B.1}$$

The output voltage from element m, which has a voltage response A_m is given by equation B.2.

$$V_m = A_m \cos(\omega t + mu) \tag{B.2}$$

Hence, the overall voltage received at the array from a signal incident at angle θ is obtained as the sum of all such terms for each element.

$$V = A_0 \cos\omega t + A_1 \cos(\omega t + u) + . + A_m \cos(\omega t + mu) + . + A_{n-1} \cos(\omega t + (n-1)u) \tag{B.3}$$

If the array elements all possess a uniform response, where A_m is equal to 1, equation B.3 can be simplified to B.4, where the output is expressed in complex notation.

$$V = \left(1 + e^{ju} + \ldots\ldots\ldots + e^{(n-1)ju}\right) e^{j\omega t} \tag{B.4}$$

If equation B.4 is multiplied through by e^{ju}, and equation B.3 is subtracted from the output, equation B.5 is obtained.

$$V = \frac{e^{nju} - 1}{e^{ju} - 1} e^{j\omega t} \tag{B.5}$$

Equation B.5 can then be manipulated and the time dependence neglected to obtain equation B.6

$$V = \frac{\sin\left(\frac{nu}{2}\right)}{\sin\left(\frac{u}{2}\right)} \qquad where \quad u = \frac{2\pi d}{\lambda} \sin\theta \tag{B.6}$$

The normalised beam pattern, which is the square of this function, normalised to unity at $\theta = 0^o$, is then expressed in equation B.7.

$$B(\theta) = \left(\frac{V}{n}\right)^2 = \left[\frac{\sin\left(\frac{n\pi d}{\lambda} \sin\theta\right)}{n \sin\left(\frac{\pi d}{\lambda} \sin\theta\right)}\right]^2 \tag{B.7}$$

Appendix C

C. Rayleigh Density Function

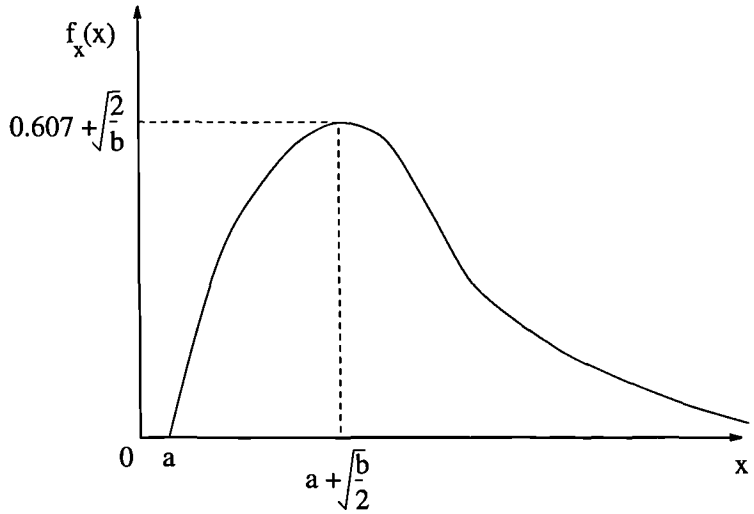

Figure C.1: Rayleigh density function

The Rayleigh density function is expressed in equation C.1 for real constants $-\infty < a < \infty$ and $b > 0$. The function is plotted in figure C.1.

$$f_x(x) = \begin{cases} \frac{2}{b}(x-a)e^{-\frac{(x-a)^2}{b}} & x \geq a \\ 0 & x < a \end{cases} \tag{C.1}$$

The mean value and variance are expressed in equations C.2 and C.3, respectively.

$$E[X] = a + \sqrt{\frac{\pi b}{4}} \tag{C.2}$$

$$\sigma_x^2 = b\frac{(4-\pi)}{4} \tag{C.3}$$

Appendix D

D. Computer Programs

To simulate a sidescan sonar image using the model described within the thesis, three computer programs require to be run in the order listed below :-

sim_sidescan ...

proc_sim_data ..

make_image .....

The parameters required to run the programs and a description of the function of each is detailed in the following *manual pages*.

NAME

sim_sidescan - acoustic ray tracer returning time and intensity for each ray emitted into scene, full 3D version.

SYNOPSIS

sim_sidescan [-?] [-m] [-n #] [-a] [-s] [-l] [-d] [-j] [-t] [-b] [-r] scene_file seabed_file seabed_type_file fish_file SVP_file beam_file output_file

DESCRIPTION

sim_sidescan traces the path of acoustic rays through a water column with a sound velocity profile given by *SVP_file*. It then calculates the point of intersection of the ray with the seabed, or an object on the seabed or in the water column, calculating the intensity of sound scattered using the specified scattering model. The transducer beam pattern is determined from the rectangular grid array with parameters as given in *beam_file*.

As well as tracing the backscattered signal, the ray scattered in the specular direction is also traced until it intersects another object, the backscattered energy from this object is then calculated. The backscattered rays resulting from the multiple reflections are tested for intersection with other objects on return path to transducer.

Calculates the spreading loss from the exact paths of the rays, which is dependent on the SVP. Calculates the absorption loss from Francois and Garrison's Law.

Can include any number, or combination, of spheres and cylinders.

Calculates optimum number of rays to emit to meet sampling requirements. These rays are emitted at angles which would result in constant increments in slant range if isovelocity and flat seabed conditions occur.

Input files:

scene_file — The scene descriptor file. The following input information is required:

start x y z	(start coordinates of seabed grid - default 0,0,0)
size x y z	(size of the seabed grid - default 30.0 30.0 1.0)
beam a b c	(beam information default 45 0 1, a=depression angle,b = horizontal width of beam over which to trace, c = no. of vertical planes over which to trace rays (NB: default gives knife edged beam))
cylinder num	If there are cylinders in the scene how many
x1 y1 z1	(start coords of cylinder)
x2 y2 z2	(end coords of cylinder)
r	(radius of cylinder)
index	(refractive index of cylinder)
sphere num	If there are spheres in the scene how many
x1 y1 z1	(centre coords of sphere)
r	(radius of sphere)
index	(refractive index of sphere)
sed_params n	Number of tiles n on seabed
seabed_type1	(seabed type (sand/silt/med_sand etc) of tile 1)
seabed_type2	(seabed type (sand/silt/med_sand etc) of tile 2)
etc.	

seabed_file — A scope input file representing the seabed height field - usually a 256x256 fractal image

seabed_type_file — A scope image showing the different sediment types to be used - use fracjig programs to create. If only 1 sediment type this image will be totally black.

fish_file — The fish trajectory input file, contains the (x,y,z) coordinates of the transducer position from which each pulse of energy is emitted.

SVP_file — The sound velocity profile of the water column. In the form :

velocity height_above_seabed temperature

for each layer.

beam_file — The parameters to define a rectangular grid array:

frequency
height of each element
length of each element
vertical spacing
horizontal spacing
no. of elements vertically
no. of elements horizontally

Flags include:

-m	trace multiple reflections
-n	number of rays to trace (default calculates optimum, else specify fewer for quick trace)
-a	trace an a-scan from one ping only
-s	include spreading loss
-l	include absorption losses
-d	calculate results in dB, but print to file as absolute intensity
-j	use Lambert's law (default is Jackson's bistatic model)
-b	use uniform beam intensity
-r	print ray trajectory coordinates to stdout
-t	include time varying gain (tvg)
-?	print brief help information.

This version of the program has the following features incorporated
three dimensional transmit and receive beam patterns.
uses SVP to calculate ray paths.
rotational and translational fish motion.
cylinders and spheres in water column or on seabed.
multiple reflections.
spreading loss from SVP.

absorption loss.
time varying gain
inclusion of different seabed types on one image
bistatic model or Lambert's law.
fractal seabed topography.

EXAMPLE

sim_sidescan -n512 -m scene.in fractal.sco black.sco fish_10.in SVP.in beam.in output

where:

scene.in
start 0 0 0
size 30 3 10
sphere 1
15 15 0.2
0.2
1.0
sed_params 1
sand

fish_10.in
0 1 10
0 2 10
0 3 10

etc
0 30 10

beam.in
100000
0.005
0.006
0.006
0.007
3
50

SVP.in
1500 50 7
1500 0 7

calculates the intensity and corresponding times for each line of the seabed image fractal.sco by tracing 512 rays to their intersection with the seabed. The full 3D beam pattern is traced. A sphere is included in the scene, centred at (15,15,0.2) with a radius of 0.2m. The seabed is all the same type and is specified as sand. Multiple reflections are traced.

BUGS

?

SEE ALSO

proc_sim_data, make_image

AUTHOR

Judith Bell.

NAME

proc_sim_data - processes the output from *sim_sidescan*

SYNOPSIS

proc_sim_data infile outfile no_of_pixels_to_convolve no_of_samples

DESCRIPTION

proc_sim_data processes the output file from *sim_sidescan* to create a file ready to be made into an image by *make_image*. It sorts the output times into sequential order, adds the intensities if any times are the same, pads with zeros to create shadows when there is no return, convolves over the pulse length (the number of samples to convolve over is specified in program call) and finally decimates the output to the number of samples specified. It repeats this for each row of the image.

BUGS

?

SEE ALSO

make_image,sim_sidescan

DIAGNOSTICS

none

AUTHORS

Judith Bell

NAME

make_image - creates a scope image from the output from proc_sim_data

SYNOPSIS

make_image infile outfile width height

DESCRIPTION

proc_sim_data prints out 2 columns of numbers, the time and the intensity. *make_image* reads in this file and creates and output float scope image of dimensions width × height, where width is the number of columns in the image and height is the number of rows.

BUGS

Doesn't check that there are width × height numbers in file to create image.

SEE ALSO

proc_sim_data, sim_sidescan

DIAGNOSTICS

none

AUTHORS

Judith Bell

References

1. R.J. Urick, *Principles of Underwater Sound,* McGraw-Hill Book Company, New York (1975).

2. L.M. Linnett, S.J. Clarke, C. St.J. Reid, and A.D. Tress, "Monitoring of the Seabed using Sidescan Sonar and Fractal Processing," *Proc. Inst. Acoustics,* 15(2), pp. 49-64 (1993).

3. D.T. Cobra, A.V. Oppenheim, and J.S. Jaffe, "Geometric Distortions in Side-Scan Sonar Images: A Procedure for Their Estimation and Correction," *IEEE J. Oceanic Eng.,* 17(3), pp. 252-268 (1992).

4. J. Le Gall, "Analysis and simulation of side scan sonar image texture," *Proc. Inst. Acoust.,* 15(2), pp. 75-82 (1993).

5. G.S. Sammelmann, J.T. Christoff, and J.D. Lathrop, "Synthetic Images of Proud Targets," *Oceans '94 Conf.,* 2, pp. 266-271, Brest, France (1994).

6. R.B. Lauer, "Applications Modeling - Status and Trends," *MTS/IEEE Oceans 82 Conf.,* pp. 192-198 (1982).

7. H. Medwin, "Speed of sound in water: A simple equation for realistic parameters," *J. Acoust. Soc. Am.,* 58(6), pp. 1318-1319 (1975).

8. W.D. Wilson, "Speed of sound in sea water as a function of temperature, pressure and salinity," *J. Acoust. Soc. Am.,* 32, p. 641 (1960).

9. C.C. Leroy, "Development of simple equations for accurate and more realistic calculation of the speed of sound in sea water," *J. Acoust. Soc. Am.,* 46, p. 216 (1969).

10. E.L. Hamilton, "Geoacoustic modelling of the sea floor," *J. Acoust. Soc. Am.,* 68(5), pp. 1313-1340 (1980).

11. K.B. Briggs, "Microtopographical Roughness of Shallow-Water Continental Shelves," *IEEE J. Oceanic Eng.,* 14(4), pp. 360-367 (1989).

12. C.G. Fox and D.E. Hayes, "Quantitative Methods for Analyzing the Roughness of the Seafloor," *Rev. Geophysics,* 23(1), pp. 1-48 (1985).

13. H.W. Marsh and M. Schulkin, "Sound Absorption in Sea Water," *J. Acoust. Soc. Am.,* 34, pp. 864-865 (1962).

14. F.H. Fisher and V.P. Simmons, "Sound Absorption in Sea Water," *J. Acoust. Soc. Am.,* 62(3), pp. 558-564 (1977).

15. M.J. Buckingham, "Ocean Acoustic Propagation Models," *J. Acoustique,* 3, pp. 223-287 (June 1992).

16. M.B. Porter, "Acoustic Models and Sonar Systems," *IEEE J. Oceanic Eng.,* 18(4), pp. 425-437 (1993).

17. P.C. Etter, "Underwater Acoustic Modeling Techniques," *Shock and Vibration Digest,* 16, pp. 11-20 (1981).

18. P.C. Etter, "Underwater Acoustic Modeling Techniques," *Shock and Vibration Digest,* 13, pp. 17-23 (1984).

19. F.B. Jensen, "Numerical Models in Underwater Acoustics" in *Hybrid Formulation of Wave Propagation and Scattering,* ed. L.B. Felsen, pp. 295-335, Martinus Nyhoff, Dordrecht (1984).

20. C.H. Harrison, "Ocean Propagation Models," *Applied Acoustics,* 27, pp. 163-201 (1989).

21. G.V. Frisk, *Ocean and Seabed Acoustics: A theory of wave propagation,* Prentice Hall, New Jersey (1994).

22. J.J. Cornyn, "GRASS: A digital computer ray tracing and transmission loss prediction system Volume 1 Overall Description," *NRL Report 7621,* Naval Research Laboratory, Washington D.C. (1973).

23. R.M. Jones, T.M. Georges, and J.P. Riley, "Modelling Acoustic Remote Sensing and the Florida Straits with Ray Tracing," *IEEE Trans on Geoscience and Remote Sensing,* GE-22(6), pp. 633-640 (Nov. 1984).

24. T.M. Georges, R.M. Jones, and J.P. Riley, "Simulating Ocean Acoustic Tomography Measurements with Hamiltonian Ray Tracing," *IEEE Journal of Oceanic Engineering,* OE-11(1), pp. 58-71 (Jan. 1986).

25. A.E. Newhall, J.F. Lynch, C.S. Chui, and J.R. Daugherty, "Improvements in 3D Ray Tracing Codes for Underwater Acoustics" in *Computational Acoustics 1,* pp. 169-185, Elsevier Science Publishers B.V., North Holland (1990).

26. M.B. Porter and H.P. Bucker, "Gaussian beam tracing for computing ocean acoustic fields," *J. Acoust. Soc. Am.,* 82(4), pp. 1349-1359 (1987).

27. W.H. Press, S.A. Teukolsky, W.T. Vetterling, and B.R. Flannery, *Numerical Recipes in C: The Art of Scientific Computing,* Cambridge University Press, Cambridge (1992).

28. M. Porter and E.L. Reiss, "A numerical method for ocean acoustic normal modes," *J. Acoust. Soc. Am.,* 76(1), pp. 244-252 (1984).

29. R.B. Evans, "A coupled mode solution for acoustic propagation in a waveguide with stepwise depth variations of a penetrable boundary," *J. Acoust. Soc. Am.,* 74(1), pp. 188-195 (1983).

30. F.B. Jensen and C.M. Ferla, "Numerical solutions of range dependent benchmark problems in ocean acoustics," *J. Acoust. Soc. Am.,* 87(4), pp. 1499-1510 (1990).

31. F.D. Tappert, "The Parabolic Approximation Method" in *Wave Propagation and Underwater Acoustics,* ed. J.B. Keller and J.S. Papadakis, Springer-Verlag, Berlin (1977).

32. M.D. Collins, W.A. Kuperman, and W.L. Siegmann, "Recent Progress in Parabolic Equation Modeling," *Proc. Second European Conf. on Underwater Acoustics,* 1, pp. 325-331, Copenhagen (1994).

33. M.D. Collins, "Benchmark calculations for higher order parabolic equations," *J. Acoust. Soc. Am.,* 87(4), pp. 1535-1538 (1990).

34. H. Schmidt and F.B. Jensen, "A full wave solution for propagation in multilayered viscoelastic media with application to Gaussian beam reflection at fluid-solid interfaces," *J. Acoust. Soc. Am.,* 77(3), pp. 813-825 (1985).

35. H. Schmidt and J. Glattetre, "A fast field model for three-dimensional wave propagation in stratified environments based on the global matrix method," *J. Acoust. Soc. Am.,* 78(6), pp. 2105-2114 (1985).

36. J.A. DeSanto, *Ocean Acoustics,* Springer-Verlag, Berlin (1979).

37. D.E. Weston, "Horizontal Refraction in a Three-dimensional Medium of Variable Stratification," *Proc. Physics. Soc. London,* 78, pp. 46-52 (1961).

38. G. Rabau, J. Piraux, J. Leandre, and R. Holtzer, "A new simulation in underwater acoustics," *Proc. Second European Conf. Underwater Acoustics,* 1, pp. 351-357, Copenhagen (1994).

39. L.B. Felsen, "Benchmarks: An option for quality assessment," *J. Acoust. Soc. Am.,* 87(4), pp. 1497-1498 (1990).

40. M.J. Buckingham and A. Tolstoy, "An analytical solution for benchmark problem 1: The "ideal" wedge," *J. Acoust. Soc. Am.,* 87(4), pp. 1511-1513 (1990).

41. E.K. Westwood, "Ray model solutions to the benchmark wedge problems," *J. Acoust. Soc. Am.*, 87(4), pp. 1539-1545 (1990).

42. D.J. Thomson, G.H. Brooke, and J.A. DeSanto, "Numerical implementation of a modal solution to a range dependent benchmark problem," *J. Acoust. Soc. Am.*, 87(4), pp. 1521-1526 (1990).

43. D.J. Thomson, "Wide-angle parabolic equation solutions to two range-dependent benchmark problems," *J. Acoust. Soc. Am.*, 87(4), pp. 1514-1520 (1990).

44. J.A. Ogilvy, *Theory of Wave Scattering from Random Rough Surfaces,* Adam Higer, Bristol (1991).

45. P. Beckmann and A. Spizzichino, *The Scattering of Electromagnetic Waves from Rough Surfaces,* Macmillan, New York (1963).

46. L. Fortuin, "Survey of literature on reflection and scattering of sound waves at the sea surface," *J. Acoust. Soc. Am.*, 47(5), pp. 1209-1228 (1970).

47. I. McColl, "Reflection and Transmission of Acoustic Signals at the Sea Bottom," *Heriot Watt University Research Memo.* (1994).

48. K.V. Mackenzie, "Bottom Reverberation for 530 and 1030 cps sound in Deep Water," *J. Acoust. Soc. Am.*, 33(11), pp. 1498-1504 (Nov. 1961).

49. H. Boehme and N.P. Chotiros, "Acoustic Backscattering at low grazing angles from the ocean bottom," *J. Acoust. Soc. Am.*, 84(3), pp. 1018-1029 (1988).

50. S. Stanic, K.B. Briggs, P. Fleischer, R.I. Ray, and W.B. Sawyer, "Shallow water high frequency bottom scattering off Panama City, Florida," *J. Acoust. Soc. Am.*, 83(6), pp. 2134-2144 (1988).

51. J.W. Strutt (Lord Rayleigh), *The Theory of Sound,* 272a, pp. 89-96, Macmillan & Co., London (1929).

52. H.W. Marsh, "Exact Solution of Wave Scattering by Irregular Surfaces," *J. Acoust. Soc. Am.,* 33(1), pp. 330-333 (1961).

53. H.W. Marsh, M. Schulkin, and S.G. Kneale, "Scattering of Underwater Sound by the Sea Surface," *J. Acoust. Soc. Am.,* 33(1), pp. 334-340 (1961).

54. H.W. Marsh, "Sound Reflection and Scattering from the Sea Surface," *J. Acoust. Soc. Am.,* 35(2), pp. 240-244 (1963).

55. E.Y.T. Kuo, "Wave Scattering and Transmission at Irregular Surfaces," *J. Acoust. Soc. Am.,* 36(11), pp. 2135-2142 (1964).

56. W.A. Kuperman, "Coherent component of specular reflection and transmission at a randomly rough two-fluid interface," *J. Acoust. Soc. Am.,* 58(2), pp. 365-370 (1975).

57. C. Eckart, "The scattering of sound from the sea surface," *J. Acoust. Soc. Am.,* 25(3), pp. 566-570 (1953).

58. C.S. Clay and H. Medwin, *Acoustical Oceanography: Principles and Applications,* Appendix 10, John Wiley and Sons, New York (1977).

59. T.K. Stanton, "Sonar estimates of seafloor microroughness," *J. Acoust Soc. Am.,* 75(3), pp. 809-815 (1984).

60. B.F. Kuryanov, "The scattering of sound at a rough surface with two types of irregularity," *Soviet Physics - Acoustics,* 8(3), pp. 252-257 (1963).

61. W. Bachmann, "A theoretical model for the backscattering strength of a composite-roughness sea surface," *J. Acoust. Soc. Am.,* 54(3), pp. 612-716 (1973).

62. S.T. McDaniel and A.D. Gorman, "Acoustic and Radar Sea Surface Backscatter," *J. Geophys. Res.*, 87(C6), pp. 4127-4136 (1982).

63. S.T. McDaniel and A.D. Gorman, "An examination of the composite-roughness scattering model," *J. Acoust. Soc. Am.*, 73(5), pp. 1476-1486 (1983).

64. S.T. McDaniel, "Diffractive Corrections to the high frequency Kirchhoff approximation," *J. Acoust. Soc. Am.*, 79(4), pp. 952-957 (1986).

65. D.R. Jackson, D.P. Winebrenner, and A. Ishimaru, "Application of the composite roughness model to high frequency bottom backscattering," *J. Acoust. Soc. Am.*, 79(5), pp. 1410-1422 (1986).

66. P.D. Mourad and D.R. Jackson, "High Frequency Sonar Equation Models for Bottom Backscatter and Forward Loss," *MTS/IEEE Oceans 89 Conf.*, 4, pp. 1168-1175 (1989).

67. D.R. Jackson, A.M. Baird, J.J. Crisp, and P.A.G. Thomson, "High frequency bottom backscatter measurements in shallow water," *J. Acoust. Soc. Am.*, 80(4), pp. 1188-1199 (1986).

68. D.R. Jackson and K.B. Briggs, "High frequency bottom backscattering: Roughness versus sediment volume scattering," *J. Acoust. Soc. Am.*, 92(2), pp. 962-977 (1992).

69. J.W. Caruthers and J.C. Novarini, "Modeling Bistatic Bottom Scattering Strength Including a Forward Scatter Lobe," *IEEE Journal of Oceanic Eng.*, 18(2), pp. 100-107 (April 1993).

70. D.D. Ellis and D.V. Crowe, "Bistatic reverberation calculations using a three dimensional scattering function," *J. Acoust. Soc. Am*, 89(5), pp. 2207-2214 (May 1991).

71. D.R. Jackson, "Models for scattering from the seabed," *Proc. Inst. Acoustics,* 16(6) (Dec 1994).

72. K. Williams and D. Jackson, "Monostatic and Bistatic Bottom Scattering: Recent Experiments and Modelling," *Oceans '94 Conf.,* Brest, France (1994).

73. H. Weinberg, "Generic Sonar Model," *MTS/IEEE Oceans 82 Conf.,* pp. 201-205 (1982).

74. M.N. Packman, C.H. Harrison, and M.A. Ainslie, "INSIGHT - A fast, robust, propagation loss model with physical intuition," *IOA Acoustics Bulletin,* 17(4), pp. 21-24 (1992).

75. M.A. Ainslie and C.H. Harrison, "Reverberation modelling with INSIGHT," *Proc. Inst. Acoustics,* 16(6), pp. 105-113 (1994).

76. GEC-Marconi, "Minehunting Performance Prediction System," *Commercial Information* (1993).

77. S.M. Tuovila, "SEARAY Sonar Simulation Model," *NCSC Technical Note,* 946-88, Panama City (March 1989).

78. C.M. McKinney and C.D. Anderson, "Measurements of Backscattering of Sound from the Ocean Bottom," *J. Acoust. Soc. Am.,* 36(1), pp. 158-163 (1964).

79. R.P. Chapman and J.H. Harris, "Surface Backscattering Strengths Measured with Explosive Sound Sources," *J. Acoust. Soc. Am.,* 34(10), pp. 1592-1597 (1962).

80. G.S. Sammelmann, *Personal Communication* (11th October 1994).

81. D. Jan, "Towards a high degree of realism in sonar image simulation," *UDT,* London (Feb. 1990).

82. A. Gagalowicz and S. De Ma, "Sequential Synthesis of Natural Textures," *Computer Vision, Graphics and Image Processing,* 30, pp. 289-315 (1985).

83. M.L. Somers and A.R. Stubbs, "Sidescan Sonar," *IEE Proceedings,* 131 part F (3), pp. 243-254 (1984).

84. C. Mazel, *Sidescan Sonar Training Manual,* Klein Associates, Salem (1985).

85. J.P. Fish and H.A. Carr, *Sound Underwater Images: A guide to the generation and interpretation of side scan sonar data,* EG&G Marine Instruments.

86. W.G.A. Russell-Cargill, *Recent Developments in Side Scan Sonar Techniques,* Central Acoustics Laboratory, Cape Town, South Africa (1982).

87. R.C. Searle, T.P. Le Bas, N.C. Mitchell, M.L. Somers, L.M. Parson, and P.H. Patriat, "GLORIA Image Processing: The State of the Art," *Marine Geophysical Researches,* 12, pp. 21-39 (1990).

88. A. Appel, "Some Techniques for Shading Machine Rendering of Solids," *AFIPS Conference Proceedings,* 32, pp. 37-45 (1968).

89. R.A. Goldstein and R. Nagel, "3D Visual Simulation," *Simulation,* 16(1), pp. 25-31 (Jan. 1971).

90. T. Whitted, "An Improved Illumination Model for Shaded Display," *Communications of the ACM,* 23(6), pp. 343 - 349 (June 1980).

91. D.S. Kay and D. Greenberg, "Transparency for Computer Synthesised Images," *SIGGRAPH '79, Computer Graphics,* 13(2), pp. 158-164 (1979).

92. J.D. Foley, A. van Dam, S.K. Feiner, and J.F. Hughes, *Computer Graphics Principles and Practice,* Addison Wesley, Reading, Massachusetts (1990).

93. C.M. Goral, K.E. Torrance, D.P. Greenberg, and B. Battaile, "Modeling the Interaction of Light Between Diffuse Surfaces," *Computer Graphics,* 18(3), pp. 213-222 (July 1984).

94. A. Stettner and D.P. Greenberg, "Computer Graphics Visualisation for Acoustic Simulation," *Computer Graphics,* 23(3), pp. 195-206 (July 1989).

95. V.S. Blake, "The Application of Ray Tracing Techniques from Computer Graphics to the Simulation of Side Scan Sonar Images," *M. Phil. Thesis,* Heriot Watt University, Edinburgh (1994).

96. R.O. Nielsen, *Sonar Signal Processing,* Artech House, Boston (1991).

97. J.G. Proakis, C.M. Rader, F. Ling, and C.L. Nikias, *Advanced Digital Signal Processing,* pp. 31-44, Maxwell Macmillan, New York (1992).

98. J. H. McClellan, T. W. Parks, and L. R. Rabiner, "A Computer Program for Designing Optimum FIR Linear Phase Digital Filters," *IEEE Trans on Audio and Electroacoustics,* AU-21(6), pp. 506-526 (Dec. 1973).

99. O. Hermann, L.R. Rabiner, and D.S.K. Chan, "Practical Design Rules for Optimum Finite Impulse Response Low Pass Digital Filters," *The Bell System Technical Journal,* 52(6), pp. 769-799 (July 1973).

100. L. R. Rabiner, "Approximate Design Relationships for Low Pass FIR Digital Filters," *IEEE Trans on Audio and Electroacoustics,* AU-21(5), pp. 456-460 (Oct. 1973).

101. Bell T.H., "Statistical features of sea-floor topography," *Deep Sea Research,* 22, pp. 883-892 (1975).

102. T. Akal and J. Hovem, "Two-Dimensional Space Series Analysis for Sea-Floor Roughness," *Marine Geotechnology,* 3(2), pp. 171-182 (1978).

103. B.B. Mandelbrot, *The Fractal Geometry of Nature,* W.H. Freeman, New York (1983).

104. R.F. Voss, "Fractals in nature: From characterization to simulation" in *The Science of Fractal Images,* ed. H. Peitgen and D. Saupe, pp. 21-71, Springer-Verlag, New York (1988).

105. L.M. Linnett, "Multi-Texture Image Segmentation," *Ph.D Thesis,* Heriot Watt University, Edinburgh (1991).

106. F. Kenton Musgrave, "Grid Tracing: Fast Ray Tracing for Height Fields," Research Report Dept. of Mathematics, Yale University (Nov. 1990).

107. F. Kenton Musgrave, C. E. Kolb, and R. S. Mace, "The Synthesis and Rendering of Eroded Fractal Terrains," *Computer Graphics,* 23(3), pp. 41-50 (July 1989).

108. P. Burrough, "Fakes, facsimiles and facts: fractal models of geophysical phenonmena" in *Science and Uncertainty, Proceedings of a Conference,* pp. 150-169, IBM UK Ltd., Science Reviews Ltd., London (1984).

109. M. Gensane, "A Statistical Study of Acoustic Signals Backscattered from the Sea Bottom," *IEEE J. Oceanic Eng.,* 14(1), pp. 84-93 (1989).

110. J.W. Strutt (Lord Rayleigh), *The Theory of Sound,* pp. 78-86, Macmillan & Co., London (1929).

111. L.M. Brekhovskikh, *Waves in Layered Media,* Academic Press, New York (1980).

112. E.L. Hamilton, "Compressional Wave Attenuation in Marine Sediments," *Geophysics,* 37(4), pp. 620-646 (1972).

113. L.E. Kinsler and A.R. Frey, *Fundamentals of Acoustics,* John Wiley & Sons, New York (1950).

114. J.W. Horton, *Fundamentals of Sonar,* United States Naval Institute, Annapolis (1957).

115. A. Edwards, C.R. Griffiths, N. MacDougall, D.T. Meldrum, and D. Livingstone, "Sound Speed Variability in the Clyde Sea, February and August 1993," *DML Marine Physics Group Report 99* (1993).

116. J.T. Wickenden, A. Burgess, D.N. Langhorne, L. Linnett, and J. Brown, "Visualising the Effect of Short Term Temperature Variation on Sonar Signals," *TTCP Conference Proceedings* (1994).

117. R.E. Francois and G.R. Garrison, "Sound absorption based on ocean measurements. Part I: Pure water and magnesium sulphate contributions," *J. Acoust. Soc. Am.,* 72(3), pp. 896-907 (1982).

118. R.E. Francois and G.R. Garrison, "Sound absorption based on ocean measurements. Part II: Boric acid contribution and equation for total absorption," *J. Acoust. Soc. Am.,* 72(6), pp. 1879-1890 (1982).

119. D.G. Tucker and B.K. Gazey, *Applied Underwater Acoustics,* Pergamon Press Ltd., Oxford (1966).

120. C.S. Clay and H. Medwin, *Acoustical Oceanography: Principles and Applications,* John Wiley and Sons, New York (1977).

121. B.W. Flemming, "Causes and effects of sonograph distortion and some graphical methods for their manual correction" in *Recent Developments in Side Scan Sonar Techniques,* ed. W.G.A. Russell-Cargill, pp. 103-138, Central Acoustics Laboratory, Cape Town (1982).

122. B.W. Flemming, "Side-Scan Sonar: A Practical Guide," *International Hydrographic Review,* 53(1), pp. 65-92 (1976).

123. S.J. Clarke, "The Analysis and Synthesis of Texture in Sidescan Sonar Data," *Ph.D. Thesis,* Heriot Watt University, Edinburgh (1992).

124. B. Julesz, "Visual Pattern Discrimination," *IRE Trans. Information Theory,* 8, pp. 84-92 (1962).

125. D. Alexandrou, C. de Moustier, and G. Haralabus, "Evaluation and verification of bottom acoustic reverberation statistics predicted by a point scattering model," *J. Acoust. Soc. Am.,* 91(3), pp. 1403-1413 (1992).

126. W.K. Stewart, D. Chu, S. Malik, S. Lerner, and H. Singh, "Quantitative Seafloor Characterization Using a Bathymetric sidescan Sonar," *IEEE J. Oceanic Eng.,* 19(4), pp. 599-610 (1994).

127. N.G. Pace and H. Gao, "Swathe Seabed Classification," *IEEE J. Oceanic Eng.,* 13(2), pp. 83-90 (1988).

128. Z. Reut, N.G. Pace, and M.J.P. Heaton, "Computer classification of sea beds by sonar," *Nature,* 314(4), pp. 426-428 (1985).

129. P.M. Maguire and N.G. Pace, *Pattern Recognition Techniques for Swathe Seabed Classification,* School of Physics, University of Bath (October 1993).